ISSN: 2153-1196 Volume 11, Number 6, June 2020

Scientific Research Publishing

Journal of Modern Physics

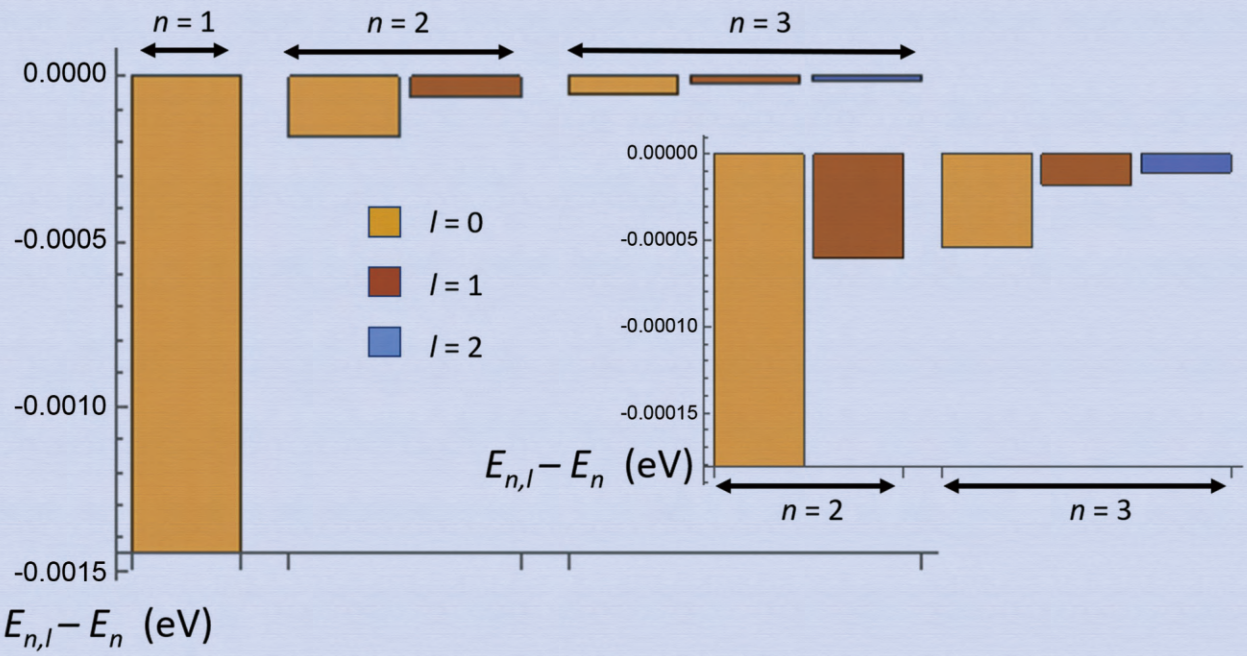

ISSN: 2153-1196

https://www.scirp.org/journal/jmp

Journal Editorial Board

ISSN: 2153-1196 (Print) ISSN: 2153-120X (Online)
https://www.scirp.org/journal/jmp

Editor-in-Chief

Editorial Board

Scientific Research Publishing

Journal of Modern Physics, 2020, 11, 767-966
https://www.scirp.org/journal/jmp
ISSN Online: 2153-120X
ISSN Print: 2153-1196

Table of Contents

Volume 11 Number 6 June 2020

The figure on the front cover is from the article published in Journal of Modern Physics, 2020, Vol. 11, No. 6, pp. 788-802 by Luis Grave de Peralta.

Journal of Modern Physics (JMP)
Journal Information

SUBSCRIPTIONS

The *Journal of Modern Physics* (Online at Scientific Research Publishing, https://www.scirp.org/) is published monthly by Scientific Research Publishing, Inc., USA.

Subscription rates:
Print: $89 per issue.
To subscribe, please contact Journals Subscriptions Department, E-mail: sub@scirp.org

SERVICES

Advertisements
Advertisement Sales Department, E-mail: service@scirp.org

Reprints (minimum quantity 100 copies)
Reprints Co-ordinator, Scientific Research Publishing, Inc., USA.
E-mail: sub@scirp.org

COPYRIGHT

PRODUCTION INFORMATION

For manuscripts that have been accepted for publication, please contact:
E-mail: jmp@scirp.org

Journal of Modern Physics, 2020, 11, 767-778
https://www.scirp.org/journal/jmp
ISSN Online: 2153-120X
ISSN Print: 2153-1196

Use and Abuse of General Criterion for Discrimination of Causal Correlations from Individual Peculiarities and Provisional Correlations

Maria K. Koleva

Institute of Catalysis, Bulgarian Academy of Sciences, Sofia, Bulgaria
Email: mkoleva_1113@yahoo.com

How to cite this paper: Koleva, M.K. (2020) Use and Abuse of General Criterion for Discrimination of Causal Correlations from Individual Peculiarities and Provisional Correlations. *Journal of Modern Physics*, **11**, 767-778.
https://doi.org/10.4236/jmp.2020.116049

Received: April 20, 2020
Accepted: May 23, 2020
Published: May 26, 2020

Abstract

A fundamentally novel approach to the issue about existence of a general criterion for autonomous discrimination of causal correlations from individual peculiarities and provisional correlations at stable complex systems is put forward. It is grounded on a recently proven by the author decomposition theorem whose subject has no cross section with the subject of the Central Limit Theorem. The fundamental advantage of that criterion lies in insensitivity to the details of the underlying dynamics and to the details of the hierarchical structure regardless of the nature of the corresponding system. It holds in an unspecified ever-changing environment. It also holds when information is incomplete and/or uncertain. Another advantage of the criterion is the ability to forecast a change in a system. The limitation of the criterion is substantiated as a ban over predictability whether that change would develop in an adaptation or in destruction. It is worth noting that while the criterion itself holds in the frame of the recently proposed theory of boundedness, the ban over prediction of the nature of a change is model-free.

Keywords

Causality, Correlations, Decomposition Theorem, Central Limit Theorem

1. Introduction

Complex systems viewed as a single matter is relatively new subject of interdisciplinary science. It encompasses a huge variety of systems such as social, biological, climate, ecological systems etc. They all share the answer to the question: how parts of a system give rise to collective behavior and how the system inte-

racts with its environment. Thus, social systems are constituted by people; brains are constituted by neurons, and weather consists of flows of atoms and molecules. The scope of this study encompasses all fields of traditional science as well as engineering, medicine and management.

Such huge variety of systems and behaviors prompts to suggest that the common properties of the behavior of those systems must appear rather as general protocol than as a law and/or rule. To remind, a law in its traditional meaning implies specific relation among variables characterizing a given phenomenon which re-occurs on repetition. What is tacitly presupposed, however, is that the conditions must re-occur the same as well. The latter implies pre-determination of the environment and its permanent constancy. Thus, if exists, such general protocol must hold in an ever-changing environment and must be insensitive to the details of the underlying dynamics and structure of any system. Further, other properties of any such protocol must be its ability to distinguish between common and individual properties of the species. For example, such criterion, applied to DNA, must distinguish a common part, that part shared by all humans, from the part related to the peculiarities of any individual. A crucial requirement for successful distinguishing between common and individual properties is whether such general protocol is able to eliminate provisional correlations. A very illustrative example comes from the weather: when a short-term weather pattern implies climate change and when it is just a provisional fluctuation.

The major goal of the present paper is to demonstrate that such protocol does exist and it is a direct consequence of the basic theorem, called decomposition theorem, derived in the frame of recently put forward by the author theory of boundedness [1]. Its fundamental difference with the Central Limit Theorem is discussed below. Decomposition theorem is derived on account of another common property shared by all complex systems, that is, their stability. Indeed, we humans live in an ever-changing environment where changes vary from pico-seconds to days and nights, up to several decades for individuals and more than 100,000 years as a kind. Thus, the decomposition theorem proves that there is presentation basis (Fourier transform of the autocorrelation function) where the power spectrum of any bounded irregular sequence (BIS) is decomposed into 3 parts: specific discrete pattern, continuous band of universal shape $1/f^{\alpha(f)}$ where f is the current component and $\alpha(f)=1$ for the first component and monotonically increases on the increase of the number of the component. The 3rd component is an irrational component which is always in the infra-red (to the most left in the power spectrum) and which originates from the highly non-trivial interplay between the discrete and the continuous band. A decisive property of that decomposition is that it is robust to the details of the variations in the corresponding BIS and it maintains constant accuracy of separation between discrete and continuous band. This property prompts me to call the discrete band homeostatic pattern. A highly non-trivial consequence of the additivity of the decomposition implies that the specific properties of each and every homeostatic

pattern are robust to the individual responses and/or the current environmental impact. Another decisive property of that decomposition is that the provisional correlations drop out automatically since they are eliminated by definition from the autocorrelation function.

To remind, the autocorrelation function is a measure of the average correlation between any two points separated by an interval which is scanned to vary in an interval from zero to up to the length of the corresponding time series. An exclusive property of boundedness is that it provides correlations of radius equal to the length of time series because every "deviation" from the average inevitably "turns back" in a specific yet bounded interval. Further, major move forward is the assumption that all time scales contribute uniformly which yields lack of any special frequency to be signaled out. Put in other words, the power spectrum of such contribution would appear as a continuous band whose envelope smoothly approaches universal shape famous as $1/f$ noise. It is worth noting, that the uniform contribution of all time scales is very different from random contribution which is characterized by lack of any systematic correlations. Then, the corresponding power spectrum consists of random lines, famous as "white noise".

At this point a question arises: how and why a specific discrete band (homeostasis) appears and why it is superimposed over a band of shape $1/f$ noise. Discrete band appears when the functionality in a system is synchronized so that to produce a stable pattern whose adaptability to an ever-changing environment is consistent with the boundedness of rates and amplitudes. Then, as proven in [1], the general condition for avoiding resonances (which is condition for avoiding "shaking up" a system beyond its thresholds of stability) yields additive decomposition of the power spectrum to specific discrete band and a continuous band of shape $1/f^{\alpha(f)}$. An exclusive for stable systems property of that decomposition is that both discrete band and the shape of the continuous band are insensitive to the statistics of environmental variations. This is easy to track out by means of taking time series of different length and partitioning in sub-time series of appropriate length. If no new line(s) appear, the corresponding system is stable.

In my previous paper [2] I have demonstrated that correlations presented in a homeostatic pattern are namely the causal relations in the corresponding system while the presence of a smooth continuous band implies that the corresponding individual peculiarities are consistent with notion of the corresponding kind. Needless to mention: provisional correlations are eliminated. An illustration why namely the homeostatic pattern represents the corresponding causal relation is presented in the next section.

In order to make the above statement clear let me present an example of three raw time series representing temperature variations in the course of time in an experiment on HCOOH oxidation over Pt catalyst (**Figure 1(a)**, **Figure 2(a)**, **Figure 3(a)**) and their power spectra (**Figure 1(b)**, **Figure 2(b)** **Figure 3(b)** correspondingly). Details can be found in [3]. It is worth noting that the Fourier transform of the autocorrelation function is applied to the raw time series themselves.

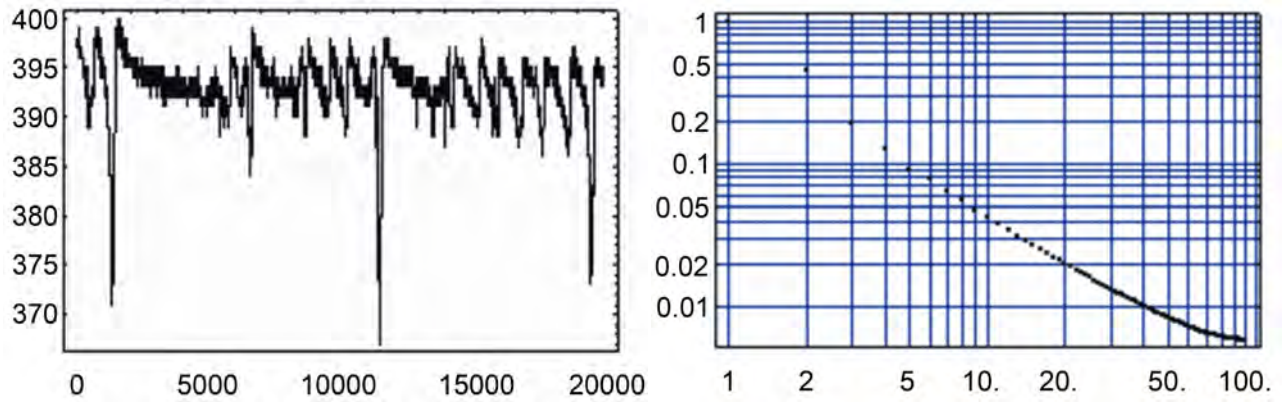

(a) (b)

Figure 1. (a) Temperature variations (in relative units) in the time course (in relative units) of catalytic oxidation of HCOOH over Pt catalyst example 1; (b) Power spectrum of the temperature variations presented in (a).

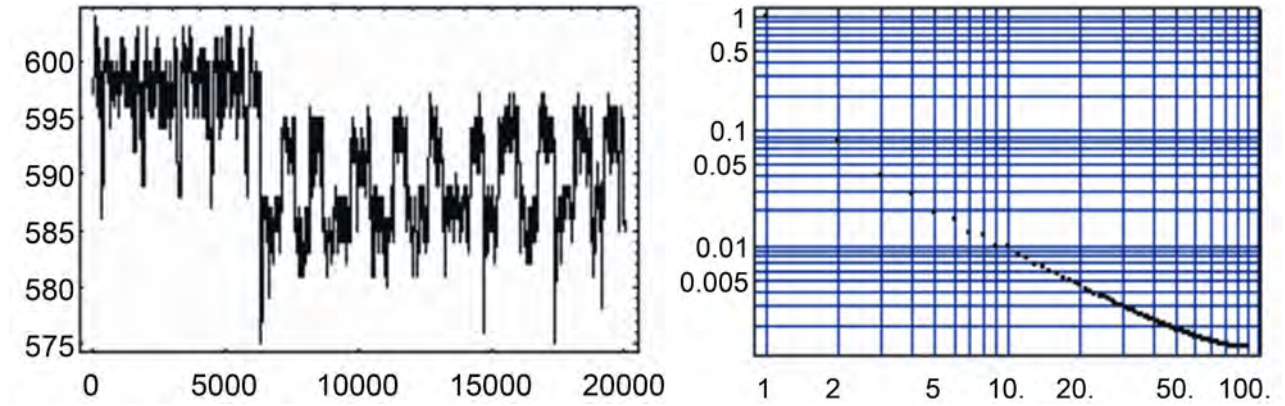

(a) (b)

Figure 2. (a) Temperature variations (in relative units) in the time course (in relative units) of catalytic oxidation of HCOOH over Pt catalyst example 2; (b) Power spectrum of the temperature variations presented in (a).

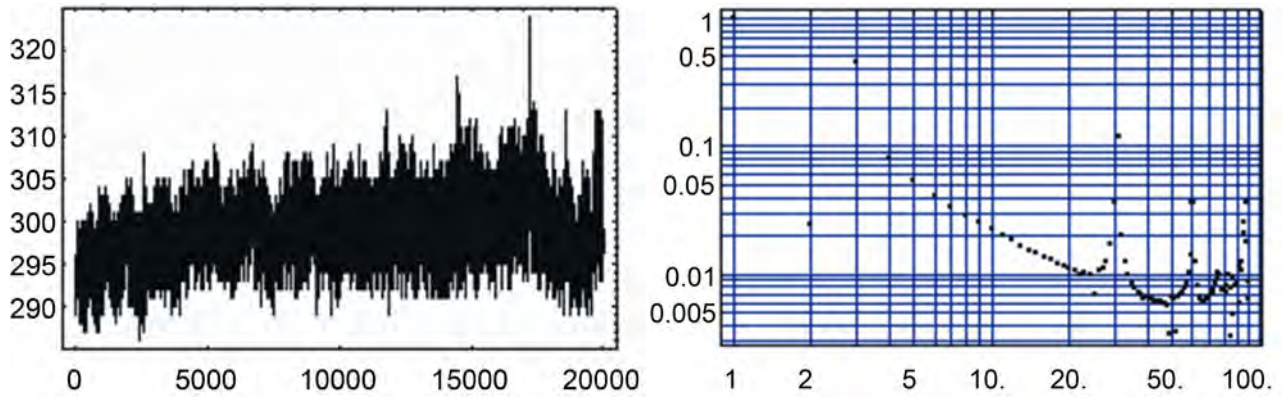

(a) (b)

Figure 3. (a) Temperature variations (in relative units) in the time course (in relative units) of catalytic oxidation of HCOOH over Pt catalyst example 3; (b) Power spectrum of the temperature variations presented in (a).

The power spectra are represented in relative units: each component in a power spectrum is divided to the first component of that power spectrum. The log-log

scale in **Figure 1(b)**, **Figure 2(b)** **Figure 3(b)** makes apparent that the shape of the continuous band is $1/f^{\alpha(f)}$ where $\alpha(f)=1$ for the first component and $\alpha(f)$ gradually increases with the frequency.

The comparison between the above raw time series and their power spectra reveal how inconclusive and deceptive is the judgement of the time series alone and what an unexpected behavior reveal the power spectra.

Yet, this is not surprising when taking into account the fundamental difference between the Central Limit Theorem (CLT) and the decomposition theorem. The fundamental difference lies in their subjects: while the subject of the Central Limit Theorem is independent random variables (yet unbounded), the subject of the decomposition theorem is bounded irregular variables (yet, not independent). Thus, they have no cross-section. The Central Limit theorem serves as grounds for the probabilistic theory which so far is the dominant concept for modeling of any behavior exhibiting any form of variability. However, this scenario suffers a common setback: it lacks generality, that is, it requires specific modeling in each and every case which turns very sensitive to the details of that modelling. On the contrary, the most powerful advantage of the decomposition theorem is insensitivity to the particularities of the dynamics let alone the system is bounded so that the amplitude of variations is confined to vary within specific margins and the rate of exchange of matter/energy/information with the environment is kept also permanently bounded. The most illustrative example of that power comes from application to social networks where the input information is most probably uncertain. The latter comes from the fact that human behavior is rather irrational and because of the variety of reasons people are reluctant to say the truth. However, if a network as a whole is stable, it would reveal a steady pattern which could be substantiated by means of applying the proposed general criterion. Moreover, through making inverse Fourier transform of the homeostatic pattern itself, that is, by means of removal of the continuous band from the corresponding power spectrum, one can find the pattern itself. In the next section it is presented the methodology of how to find out hierarchy in any such pattern.

The criterion could be applied to a large variety of systems where the current knowledge about it is incomplete, uncertain and/or clumsy, or hazardous to be obtained. Thus, the criterion is available for archeological data, meteorological data, medicine (EEG and EKG), urban engineering, financial engineering, DNA sequences, etc. To compare, the method of discrimination between competing models, based on the probability theory, does not provide qualitative difference between competing models and says nothing about the stability of any of them. On the contrary, the proposed by the author criterion provides not only a qualitative difference between different types of correlations but reveals their stability as well. One way is to monitor the power spectrum and to see whether the pattern stays intact or some extra line(s) appear. If stays intact, the corresponding system is stable even in an ever-changing environment, if extra line(s) appear it implies changes. At this point the major question arises whether these

changes yield adaptation or they yield destruction. In Section 3 I will demonstrate that this is undecidable problem by any means of computation, neither by traditional algorithmic computing nor by proposed by me in [1] semantic computing.

Thus, the major goal of the present paper is to outline the general theoretical backgrounds for existence of that criterion and its limitations.

2. Why Homeostatic Patterns Represent Causal Relations? How the Hierarchy Is Revealed in Homeostatic Patterns?

The rigorous considerations why homeostatic patterns represent steady causal relations are represented in [2]. Here I will present them by means of a comparison to the network theory.

Up-to-now there is not established view on the difference between causal and provisional correlations but still pre-dominant view is to associate causality with the covariance in all variety of its forms. The weak point of that idea is the lack of general criterion allowing autonomous demarcation between causal relation, steady correlation and provisional ones. Indeed, the same physical mechanisms provide both causality and provisional correlations. Thus, up-to-now, complex networks, which serve as major implement for modelling complex systems, share common features the major of which consists in assigning probabilities and weights to both inputs and outputs. The role of dynamics and the environment is to rearrange those probabilities and/or weights. Yet, crucial flaw of this scenario is that it does not allow distinguishing causal correlations from provisional ones. Indeed, the probabilistic approach considers causality as a system of binary asymmetric in succession relations. However, this viewpoint does not allow any discrimination between causal and provisional correlations since the latter is also supposed binary and there is no general rule about whether a provisional or a causal relation comes next. So, a sequence of provisional and causal correlations exactly matches a random sequence of "0" and "1" thus justifying the application of CLT.

However, the formal logic grounded on the idea that there exists steady state whose characteristics are defined as specific steady quantal relations among certain variables for each and every specific set of steady environment, is not able to decide whether any given sequence of corresponding "0" and "1" assigned to each and every sequence of "yes-no" answers is indistinguishable from a random sequence of "0" and "1" because there is no general criterion which provides that the answers are always true; moreover there is no general protocol which provides that questions are posed always correctly.

The core of the problem is to be traced up to the Central Limit Theorem where the variables are supposed random independent ones. Thus, the very idea of long range ones is contradictive to the Central Limit Theorem. To compare, boundedness introduces long-range correlations of practically infinite radius while the correlations which are consistent with CLT are only those of bounded radius.

It is worth noting that the above setbacks of the CLT do not allow any robust to the environmental statistics additive separation of a power spectrum to a specific discrete band and universal continuous one. Indeed, the unboundedness of the random variables implies strong sensitivity of the shape of the corresponding power spectrum to the statistics of those variables. Thus, although the provisional correlations are eliminated, no discrimination between causal correlations and the individual peculiarities is available. In turn, the notions of an individual and the notion of a kind turn out blurred. Consequently, the latter renders pattern recognition (e.g. discrimination between cats and dogs) uncertain especially around the demarcation line between qualitatively different subjects (cat or dog).

Outlining, the additive separation of a power spectrum to a specific discrete band and a universal continuous one so that both bands are robust to the statistics of variations, is an exclusive property of the proposed by the author [1] concept of boundedness.

At this point the power of the proposed in the present paper discrimination criterion becomes evident: it is model independent in the sense that there is no need to know, for example, how exactly our bodies work in full details to be positive and certain whether a body is stable or not. Thus, the notion of homeostasis turns insensitive to all kinds of variations, daily variations of temperature for example. Alongside, it turns out that bounded within specific margins deviations from that homeostasis constitutes individual peculiarities in a way consistent with the notion of a kind. Moreover, the insensitivity of the shape of the continuous band to the environmental variations (which are associated with the individual peculiarities) implies that all individuals sharing the same homeostatic pattern share the same evolutionary value as well.

A very important matter in the study of complex systems such as societies, ecological systems and climate is the matter of their hierarchy and its stability. The question is what type of hierarchy is stable and how it is represented in the power spectra. So far, the dominant concept is that about one-directional hierarchy. The latter serves as grounds for the reductionist approach which sits in the very core of the science: thus it implies that complexity goes from elementary particles to cosmological objects via self-organization. However, reductionist approach is not able to provide any qualitative difference among the subjects of self-organization: in the above example it represents emergent patterns in the same terms (in the example of reaction networks those are the concentrations of different sorts of output products compared to the concentrations of the input reagents).

I explicate the qualitative difference between successive hierarchical levels by the use of general mechanism for leveraging the stability of complex systems. Its protocol is grounded on the idea that the environmental impact is distributed onto different levels so that to diminish the load on each level thus increasing the overall stability. Then, since the levels are interconnected by feedbacks (note that levels are parts of the same system), the hierarchy turns bidirectional: it goes both bottom up and top down. This is in sharp contrast with the reductionist

approach where the hierarchy is unidirectional: it goes only bottom up. Yet, the question remains: how different patterns occur on different levels and what is the condition for their stable consistency.

The matter of self-organization is one of the most challenging problems in modern interdisciplinary science and is still far from resolution. My contribution to the problem consists of the fact that the structure of power spectra could reveal the presence of hierarchy and conditions for their stable consistency although different patterns occur on different levels.

In my previous paper [4] I have defined general condition for stable coexistence of patterns that come from different hierarchical levels. In general, this is again the condition for avoiding resonances. To remind, the notion of a resonance implies that a system is "shaken" up to very large amplitudes by means of relatively small driving force (not necessarily periodic). So there are two types of resonances: 1) those which keep the system within the current margins of stability (that is adaptation); 2) those resonances which bring a system beyond current thresholds of stability (that is destruction). In order to avoid destruction, the general protocol applies and it consists of the requirement that the homeostatic patterns of a lower level appear as "satellite" lines superimposed onto each and every line of the higher level pattern.

Then, stable systems reveal a specific "behavioral" pattern on applying operation of coarse-graining (that is partitioning of the corresponding spatio-temporal BIS into cells of almost equal size): it implies that the details of lower level structure are "smoothed out" and appear rather as broadening of the higher level lines so that the higher level patterns remain intact when the system is stable.

Outlining, stable systems are characterized by power spectra which consist of specific steady homeostatic pattern and noise component of universal shape. The homeostatic patterns and the shape of the noise component remain intact on monitoring and/or applying coarse-graining. The latter operation allows revealing of stable self-consistent bidirectional hierarchy.

Another advantage of the proposed general criterion is that causal relations (homeostatic patterns) are distinguishable for steady correlations ($1/f^{\alpha(f)}$ noise) regardless of the decoding algorithm. This is in fundamental opposition to the traditional algorithmic theory where the separation of causal, steady and provisional correlations is impossible to be accomplished by any spontaneous natural mechanism in a non-ambiguous way; instead, it is subject to supervision of our human mind and thus it is highly subjective to current beliefs and understandings of the decoding mind. Accordingly, the latter makes the classification highly sensitive to the ingenuity of the decoder. To compare, the boundedness provides self-sustaining boundedness of logical and quantal errors [5] in a long run which is expressed in a non-ambiguous separation of causal, steady and provisional correlations for each and every BIS substantiated by means of the general discrimination criterion proposed in the present paper.

Summarizing, a general criterion for discrimination between causal and steady correlations at stable complex systems is proposed. It consists of carrying out the

power spectra of any time series which monitor the behavior of a complex system. The use of power spectra implies as well an automatic elimination of the provisional correlations presented in the corresponding time series. An exclusive property is of that criterion is the robustness to the details of the statistics of variations which appear as a response to an ever-changing environment. Another exclusive property is provided by the constant in the time accuracy of separation of both bands in the power spectra. In turn, this suggests a new role of a homeostatic pattern, namely: it serves as bearer of identity for the functionality of the corresponding complex system. This yields a question how the appearance of a new line(s) affects the identity of a complex system in the sense whether it implies adaptation or destruction?

3. Ban over Computation of Predictability of Whether a New Line(s) Is Adaptation or Destruction: Role of Human Mind

In the Introduction it was mentioned that decomposition theorem gives rise to 3 types of components in the power spectrum of a raw time series representing the behavior of a stable complex system. The first two components are a specific discrete pattern and a continuous component whose shape is universal. An exclusive property of the decomposition theorem is that both the pattern and the shape of the continuous band are robust to both the length of the time series and/or the statistics of the environmental variations. This renders an enormous power of the discrimination criterion for discrimination of causal relations, encapsulated in the corresponding discrete pattern, and the steady correlations, encapsulated in the continuous band, which commence from the unique individual response consistent with the "survival of the kind". The discussion about the role of the 3rd component has been postponed to the present section since its computability plays a decisive role for the entire issue about computability of any prediction whether a new line(s) yields destruction or adaptation. The 3rd component comes as a result of highly non-trivial interplay between both other bands. It is a result of confinement of the variation not to exceed specific margins called thresholds of stability. Thus, the 3rd component appears as a result of that confinement and it is displayed at bounded distance to the left of the entire other parts of a power spectrum. And here comes a conundrum: from the point of view of stability, the condition for avoiding resonances renders the line to be irrational. However, another general aspect of the theory of boundedness claims that exchanged matter/energy/information with the environment, exerted by natural processes, is specific yet bounded. An immediate consequence of this claim is that the only computable numbers are those which are represented as bounded sequences of digits so that the precision is dictated by the boundedness. Another group of computable numbers is the zeroes of the unity, e.g. 3/7. The zeroes of unity are of use for the representation of Ramanujan sums which are in the grounds of Ramanujan-Fourier transform. The latter implements a spontaneous mechanism of processing Fourier transform by means of the feedback which

provides energy dissipation put forward in Chapter 3 of [1]. Their computability is explicitly provided by the Euclideanity of the functional metrics. These types of numbers are well-known under the name incommensurate numbers. However, if the frequency of the 3rd component is incommensurate, it would yield an inevitable resonance which in turn yields either destruction or adaptation. The same problem arises when a new line appears: it is also incommensurate and thus one faces the same conundrum.

It is worth noting that my previous result about self-sustained boundedness of logical and quantal error [5] is of no help here since it is derived for stable in an arbitrarily long run systems. Alongside, it is grounded on the fact the metrics of the functionality of a stable complex system are self-sustained to be Euclidean. Note that the latter property provides the means of computability since intervals obtained at different spatio-temporal locations are the same. In turn the latter provides grounds for comparing whether different numbers are equal or not. However, the appearance of a new line implies violation of the Euclideanity because of the reasons provided in [2].

Another strategy is the use of traditional algorithmic computing. However, as it will be demonstrated now, it also does not assist resolving the conundrum. Indeed, a great advantage of modern computers is that, by means of hardware engineering, the precision could be made arbitrarily large. This comes at the price of enlargement of computation time, but by means of clever engineering of the software, an appropriate balance could be achieved. Yet, however, this does not solve the major problem posed above since the ingenuity in mastering the match between software and the hardware holds only for stable solutions. For unstable solutions, a question arises whether truncation error at Taylor series is insensitive to round-off error? However, the latter holds for stable solutions only: around unstable solutions each and every term counts in a long run and on repetition. In turn, it implies that the consistency between logical and quantal error is violated and in result the logical error becomes ill-defined (it could vary from minus infinity to plus infinity) for each and every quantal error, no matter how small it is!

A notorious example for such behavior is the computing of periodic solutions which are neutral with respect to stability. Indeed, the computation of limit cycles as solutions of differential equations, is inevitably bound to degenerate into a motion on a spiral (ingoing or outgoing depending on any current realization of computing) which produces qualitatively different result in a long run: instead of bounded cycling motion, it approaches either steady point or infinity. The inevitability of this behavior lies in the fact that each and every term in the corresponding Taylor series has equal contribution in a long run despite of its current value. The latter, however, just confirms the conundrum, since it turns out that the number of significant terms is infinite while the precision comprises always only bounded number of digits.

Outlining, the conclusion is that modern day computing is unable to decide

with certainty whether a solution subject to resonance yields adaptation or destruction.

It is worth noting that the self-sustaining of Euclideanity of the functional metrics renders negligible error between the semantic computing (grounded of the use of Ramanujan-Fourier transform) and the traditional Fourier transform (grounded on the expansion in truncated Taylor series).

Yet, in practice a lot could be done: by means of monitoring and/or by means of appropriate intervention after skillful complementary investigations, the resonance could be postponed or even avoided. Yet, our intervention could be a double-blade razor: on the hand, we could postpone a resonance at a given hierarchical level but this could invoke sooner a resonance on other hierarchical levels. Thus everything is in the hands and abilities of our human mind to decide about our own future.

An immediate consequence of the fact that our human imagination is able to distinguish between incommensurate and irrational numbers prompts to suggest that the matter about what is intelligence is still far from resolution.

4. Conclusions

A general criterion for autonomous discrimination of causal and provisional correlations is established. It is grounded on a completely novel general theorem, proven by the author and called by her decomposition theorem, which is fundamentally different from the Central Limit Theorem. It also allows autonomous discrimination of the correlations commencing from the individual peculiarities of current individual; let alone the latter belongs to the same kind. The criterion holds in an unspecified environment and is conclusive about stable complex systems of all variety of their origin: meteorological, ecological, social networks, archaeological etc. Its power is spread over systems where the information about the targeted behavior is uncertain, missing and/or hazardous to be obtained.

Yet, the power of the criterion is limited to stable systems only because of the general impossibility for computing with certainty whether a given new line(s) yield destruction or adaptation. The flaw confirms once again after turning the fundamental difference between our human intelligence and all attempt to construct an artificial one. Yet, the considerations presented in the present paper once again confirm the decisive role of the human mind and its ingenuity for solving problems ranging from diseases, to climate changes and ultimately to our knowledge about the Universe. And all this comes out from the simple question what is a stable system and how it fits an unspecified environment.

Conflicts of Interest

The author declares no conflicts of interest regarding the publication of this paper.

References

[1] Koleva, M.K. (2012) Boundedeness and Self-Organized Semantics: Theory and Ap-

plications. IGI-Global, Hershey, PA. https://doi.org/10.4018/978-1-4666-2202-9

[2] Koleva, M.K. (2019) *Journal of Modern Physics*, **10**, 43-58. https://doi.org/10.4236/jmp.2019.101005

[3] Koleva, M.K., Elyias, A.E. and Petrov, L.A. (2000) Fractal Power Spectrum at Catalytic Oxidation of HCOOH over Supported Pd Catalyst. In*:* Russo, N. and Salahub, D.R., Eds., *Metal-Ligand Interactions in Chemistry*, *Physics and Biology*, NATO ASI Series C Vol. 546, Kluwer Academic Publishers, Dordrecht, 353-369. https://doi.org/10.1007/978-94-011-4245-8_15

[4] Koleva, M.K. (2018) *Journal of Modern Physics*, **9**, 335-348. https://doi.org/10.4236/jmp.2018.93024

[5] Koleva, M.K. (2020) *Journal of Modern Physics*, **11**, 157-167.

Journal of Modern Physics, 2020, 11, 779-787
https://www.scirp.org/journal/jmp
ISSN Online: 2153-120X
ISSN Print: 2153-1196

Solving the Mystery of the Tunguska Explosion

Jian'an Wang

Department of Physics, Shenzhen University, Shenzhen, China
Email: wja@szu.edu.cn

How to cite this paper: Wang, J.A. (2020) Solving the Mystery of the Tunguska Explosion. *Journal of Modern Physics*, **11**, 779-787.
https://doi.org/10.4236/jmp.2020.116050

Received: April 14, 2020
Accepted: May 25, 2020
Published: May 28, 2020

Abstract

In this paper, the asteroid "rockburst plus nuclear explosion" model of Tunguska explosion is proposed for the first time, and it is believed that the Tunguska explosion is a thermonuclear explosion in the air triggered by a "rockburst" after the asteroid entered the atmosphere, and all the abnormal phenomena produced by the Tunguska explosion are explained by using this model. The "rockburst" is the sudden release of the stress potential energy formed by the expansion of atoms in solid objects caused by the cosmic expansion. According to the "rockburst plus nuclear explosion" model, the "rockburst" was firstly triggered by the heat produced by the friction between the asteroid and the atmosphere after it entered the atmosphere, and then the high temperature and high pressure generated by the "rockburst" ignited the fusion fuel inside the asteroid, resulting in a thermonuclear explosion.

Keywords

Tunguska Explosion, Rockburst, Meteorite Explosion, Thermonuclear Explosion

1. Introduction

The Tunguska explosion [1] [2] is an explosion event that occurred at 7:17 a.m. on June 30, 1908, over what is now Siberia's evinci region in Russia. The explosion occurred 800 kilometers northwest of Lake Baikal near the Tunguska river. The estimated explosive power is equivalent to 20 million tons of TNT, or the equivalent of 1000 Hiroshima atomic bombs! More than 80 million trees burned over 2150 square kilometers. In the morning, locals in the northwest of Lake Baikal reportedly observed a huge fireball as bright as the sun streak across the sky, which was illuminated a few minutes later by a bright flash of light. Later, shockwaves from the explosion shattered windows in the vicinity of 650 kilometers, and the mushroom cloud was observed. The explosion was recorded by seismic monitoring sites across Europe and Asia, and the resulting atmospheric

instability was even detected by the barometrograph, which had just been developed by famous scientists in Britain at the time. In the days after the explosion, the sky over Tunguska, 9000 miles away, was shrouded in a grim orange; the phenomenon of white nights continued in large areas and the night sky was dark red in Asia and Europe. A decrease in atmospheric transparency was also observed at the Smithsonian Astrophysics Station and Mount Wilson Observatory in the United States for at least a few months. At the time of the explosion many lights went out in London, England, and the city was in darkness. The soil in the explosion area was magnetized. Trees in the explosion area grew faster; the width of the ring increased from 0.4 - 2 mm to more than 5 mm; genetic variation occurred in some animals; reindeer had a strange skin disease, jujube leper skin disease and so on. No impact crater was found. But Italian nuclear physicists found by heavy isotopes test that the fir trees destroyed in 1908 had higher levels of trace elements than in other years, and those trace elements could not come from earth. There was no sign of a radiation anomaly, indicating that it was not a natural nuclear fission explosion.

A series of unknowns and doubts have given rise to various hypotheses over the past 100 years [3] [4], which can be summarized as the "meteorite impact hypothesis", the "nuclear explosion hypothesis", the "alien spacecraft explosion hypothesis", the "antimatter hypothesis" and the "comet impact hypothesis". Each hypothesis has a certain truth, and each hypothesis can't stand up to scrutiny. So far, no very reasonable explanation has been found.

The purpose of this study is to solve the mystery of the Tungus explosion and to give reasonable explanations for the various abnormal phenomena produced by the Tungus explosion.

2. The Mechanism of Rock Burst

1) What is rock burst?

Rock burst is a phenomenon in which the elastic deformation potential energy accumulated in a rock mass is suddenly and violently released under certain conditions, causing the rock to burst and eject. Rock burst [5] [6] is one of the main safety hazards in deep well mines. A slight rock burst has only flaky rock, no ejection phenomenon, a severe rock burst can produce an earthquake with a magnitude of 4.6 and an intensity of 7 - 8 degrees, causing damage to ground buildings and accompanied by loud noises. Rockburst can occur instantly or for days to months.

At present, the scientific community cannot give a reasonable explanation of the source of rock burst energy, which has become the bottleneck of rock burst mechanism research. In the process of studying the geodynamics, the author found that the cosmic expansion is the power source of the earth's geological tectonic movement [7], and further found that rock burst is also a kind of planetary geological tectonic movement, which is a universal natural phenomenon.

2) The relationship between "rock burst" and cosmic expansion

From Formula (5.31) [8], it can be seen that the orbital radius of the electrons around the nucleus of the atoms or ions that make up the of the object increases with the decrease of the speed of the object moving in the ether. It can be seen that the atoms and ions (ions containing orbital electrons) that make up the objects become larger as the universe expansion slows down or the speed of the objects decreases relative to the cosmic ether system.

The effects of cosmic expansion on planets composed of solid crust (lithosphere) and liquid magma are very rich, including orogeny, epeirogenic movement, plate formation, earth expansion, sea floor spreading, continental drift, earthquake and volcanic eruption [7]. If we focus on the effect of cosmic expansion on solid objects, it is not difficult to find that the so-called "rock burst" is the sudden release of elastic potential energy formed by the long-term influence of cosmic expansion on solid objects. This release of elastic potential energy can be either spontaneous or artificially induced.

We can approximate the shape of the solid to the sphere for easy study. If the surface of a solid sphere remains unbroken (keeping the atoms next to each other), the surface area of the solid sphere is proportional to the square of the radius of the atoms forming the sphere, and the volume of the solid sphere is proportional to the cube of the atomic radius. So, as the atoms expand, the volume of the solid ball increases faster than the surface area increases, the stress in the solid ball gets bigger and bigger, and the deeper in the ball, the bigger the stress.

Since some naturally forming solid objects in the universe, such as meteors or asteroids, have been formed for billions or even over 10 billion of years, the stress that accumulates in these solid objects after billions or 10 billion of years of expansion in the universe is very large and the solid object will explode when the stress is greater than the structural force of the solid object. This is why there are so many irregularly shaped meteors (meteorites) in the universe. Because the small planets completely solidified so early, as the universe expanded, the stresses inside the solid planets outweighed their structural forces and exploded (rock burst), resulting in the formation of large numbers of irregularly shaped rocks (meteorites or meteors). So we can predict that if the universe continues to expand, the moon and all the planets will eventually become solid and explode into rubble (this could be the last violent scene of the tectonic movement).

As the atoms expand, the expanding force inside the rock increases and so does the surface tension of the rock. Once the surface tension exceeds the structural force, the surface of the rock will crack into powder or brittle pieces and fall off layer by layer. This is the process of desert formation.

It's not hard to explain why some meteorites explode when they enter the atmosphere. Because of the extremely fast running speed, when the meteorite falls into the atmosphere, it is heated by intense friction with the atmosphere, and when the temperature of the meteorite reaches the temperature that can release the stress potential energy inside the meteorite, these stress potential energy will be released in the form of explosion. Therefore, all naturally formed solid objects

in the universe contain stress internal energy, and the older a solid is formed, the higher the stress internal energy it contains. All the Earth's crustal rocks contain stress, the longer the rock formation, the higher the stress. These stresses will not be released when the rock bed is not destroyed because of the protection of the surrounding rock mass, and will suddenly be released when the surrounding rock mass is destroyed (such as tunnel construction), which is the mechanism of the artificial "rock burst".

3. The "Rock Burst plus Nuclear Explosion" Model of the Tunguska Explosion

Because of the enormous energy released by the Tunguska explosion (equivalent to 20 million tons TNT explosive, or 1000 Hiroshima nuclear bombs), the authors suspect that the Tunguska explosion is a thermonuclear explosion triggered by a "rock burst" triggered by the asteroid's entry into the atmosphere.

1) The "Rock burst plus nuclear explosion" model of the Tunguska explosion

a) The principle and structure of the hydrogen bomb:

A hydrogen bomb is a nuclear reactor that uses the nuclear fusion of hydrogen isotopes (deuterium and tritium) to release a large amount of energy instantly. Since light nuclei that produce fusion reactions all carry positive charges, a significant fusion reaction can occur only when they move very fast to overcome the electrostatic repulsion between positive charges. If the temperature of the thermonuclear loading is very high (only at temperatures above 14 million degrees ˚C, the reaction speed is large enough to achieve self-sustaining fusion reaction), the nuclei that make up the loading have a very high velocity (and thus a high kinetic energy). The fusion reaction that takes place using this method is called thermonuclear fusion reaction, or thermonuclear reaction. Because the hydrogen isotopes deuterium and tritium in light nuclei have the least repulsion between nuclei. Therefore, it is often chosen as the charge for hydrogen bombs. The main reaction mode between deuterium and tritium nuclei is as follows:

$$D + T \rightarrow 4He + n + 17.6MeT$$

where, *D*, *T*, 4He and n represent the deuteron, tritium, helium and neutron respectively.

The general structure of the hydrogen bomb is shown in **Figure 1**. The shell of the hydrogen bomb contains deuterium and tritium or solid lithium deuteride 6 (the nuclear material of hydrogen bombs), multiple atomic bombs, and detonators made from ordinary explosives. The hydrogen bomb uses the high temperature and high pressure generated during the explosion of the atomic bombs to ignite its thermonuclear material for nuclear fusion reaction (or thermonuclear reaction). When the detonator causes a conventional explosive to explode, it quickly compacts the separate blocks of nuclear material, creating fission reactions known as the atomic bomb explosion. The explosion of the atomic bombs immediately produced the ultra-high temperature and pressure needed to fuse

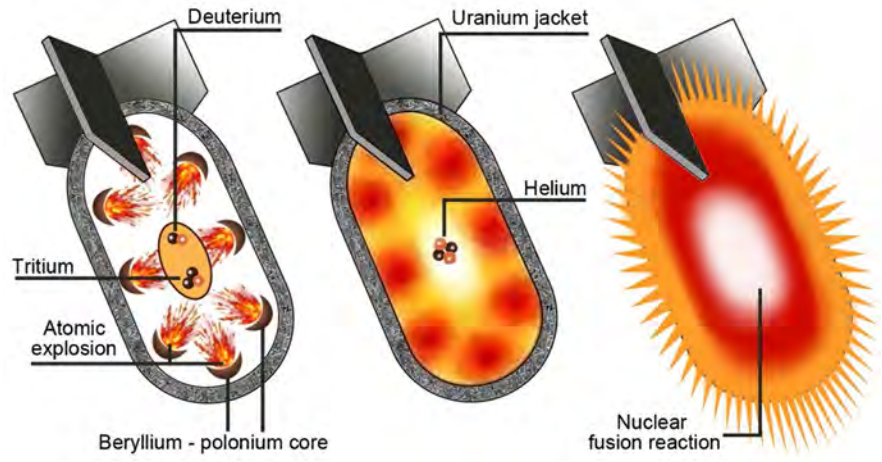

Figure 1. The principle and structure of the hydrogen bomb.

deuterium and tritium. Deuterium and tritium collide with each other at a speed of several hundred kilometers per second, and react quickly and violently to synthesize helium, releasing a lot of fusion energy, thus completing the whole explosion process of the hydrogen bomb. Since thermonuclear material loads have no critical mass limit, the hydrogen bomb can be made very large, with the average explosive power ranging from hundreds of thousands of tons to millions of tons, or even tens of millions of tons of TNT equivalent.

b) How does an asteroid produce a nuclear explosion?

The author suspects that the Tunguska explosion is a nuclear explosion in the air caused by an asteroid formed billions or ten billion of years ago with enough solid deuterium and tritium in its center, as shown in **Figure 2**. When the asteroid enters the atmosphere, it heats up because of friction with the atmosphere, which leads to the sudden release of the stress potential energy gathered inside the asteroid, or the occurrence of rock burst. The rock burst causes the pressure and temperature at the center of the asteroid to rise dramatically, causing deuterium and tritium at the center of the asteroid to explode in thermonuclear fusion reactions. The process of the asteroid entering the atmosphere is equivalent to the detonation of the atomic bomb in the hydrogen bomb, and the rock burst of the asteroid is equivalent to the explosion of the atomic bomb in the hydrogen bomb. Both ended up with deuterium and tritium fusing at high temperature and high pressure to produce a nuclear explosion. The debris created after the asteroid hydrogen bomb exploded continues to produce rockburst until it is completely turned into charged dust.

Since all elements with a smaller atomic weight than iron can release energy in fusion reactions at high temperatures and pressures, the possibility that the asteroid's nuclear explosion was caused by fusion reactions of other elements, except deuterium and tritium, cannot be ruled out.

Because hydrogen is the most abundant element in the universe and accounts for about 75% of its mass, asteroids or meteorites containing deuterium and tritium should be ubiquitous in the universe.

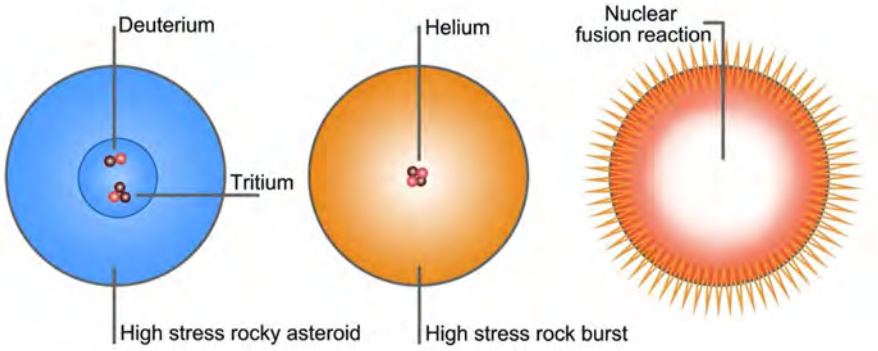

Figure 2. How does an asteroid produce a nuclear explosion?

A high-stress asteroid that is massive enough, and old enough to form, can produce a "rockburst" with the power comparable to that of an atomic bomb, so it can detonate a thermonuclear explosion.

2) Using the model of "rock burst plus nuclear explosion" of the Tungus explosion to explain the abnormal phenomena produced by the Tungus explosion

a) The energy released is huge: the estimated explosive power is equivalent to 20 million tons TNT explosive, equivalent to 1000 Hiroshima atomic bombs!

Answer: since there is no critical mass limit on the amount of thermonuclear material a thermonuclear bomb can contain, an asteroid thermonuclear bomb can be very large, with an explosive yield of tens of millions of tons of TNT or more.

b) The sky was unusual: the 9000-mile-wide sky of the Tunguska region was shrouded in a gloomy orange color in the days following the explosion, with white nights appearing in large areas and dark red in the skies of Asia and Europe. A decrease in atmospheric transparency was also observed at the Smithsonian Astrophysical Station in the United States and the Mount Wilson Observatory for at least a few months.

Answer: because the asteroid was blasted into the atmosphere as electrically charged dust, the sky over the explosion area was covered in this dark orange color. Because the dust that pervades the atmosphere reflects the sunlight, the white night phenomenon appeared, and because the red light is the most penetrating, the night sky appeared dark red. Because the dust in the air is very small so it falls slowly, and because the dust fills a lot of space and reaches a high altitude, it takes a long time for the dust to spread out, so the transparency of the atmosphere was reduced for several months.

c) At the time of the explosion, many lights in London, England, suddenly went out and the city was dark; the soil in the explosion area was magnetized; trees in the explosion area grew faster; ring width increased from 0.4 - 2 mm to more than 5 mm; some animals developed genetic mutations, and reindeer developed a strange skin disease, such as date toadiness.

Answer: the asteroid was blasted into electrically charged dust, which, along

with the rapid fluctuations of the blast wave, produced a powerful electromagnetic pulse that caused the electrical system in London, England, to trip, causing many lights to suddenly go out. It is this electromagnetic pulse, or the high-energy microwaves in it, that have caused the magnetization of the soil in the explosive area, the accelerated growth of the trees (the width of the rings has increased from 0.4 - 2 mm to more than 5 mm), and genetic variations in certain animals (e.g. strange skin disease of reindeer, jujube leper, etc.)

d) No impact crater was found; but using heavy isotopes, Italian nuclear physicists measured that the amount of trace elements of fir destroyed in 1908 is higher than in other years, and these trace elements can't come from earth, obviously, the explosion is related to meteorites. Survey teams in the 1950s and 1960s found tiny glass balls sprinkled on the ground in the area. Chemical analysis showed that the spheres contained large amounts of nickel and iridium—metals commonly found in meteorites—and determined that they came from beyond earth.

Answer: because each point of the asteroid contains stress, under the heat of the main "rock burst" and "nuclear explosion", the asteroid was blown into dust through a series of secondary" rock burst", so there was no crater left. Because asteroids contain these trace elements, dust containing these trace elements at the time of the big explosion entered the destroyed fir under the action of the explosion shock wave. In the blast zone, the heat melted particles of glass in the soil, mixing them with the dust particles that formed in the explosion. After the explosion, the melted glass particles cooled and solidified to form tiny glass spheres containing nickel and iridium, the metallic elements commonly found in meteorites.

e) There was no sign of a radiation anomaly, indicating that it was not a natural nuclear fission explosion.

Answer: Because the nuclear fusion reaction in the asteroid is caused by "rock burst", not by atomic bomb explosion, there is no nuclear fuel (radioactive element) that produces nuclear fission reaction, so there is no radioactive pollution.

4. Conclusions

1) The Tunguska explosion may have been a thermonuclear explosion in the air after the asteroid entered the atmosphere, and the nuclear explosion may have been triggered by the high temperature and high pressure caused by a rock burst of the asteroid; the rock burst is triggered by the high temperature caused by the friction between the asteroid and the atmosphere.

2) Since all elements with less atomic weight than iron can release energy in fusion reactions at high temperatures and pressures; the asteroid's nuclear explosion may have been caused by fusion reactions involving elements other than deuterium and tritium.

3) "Rockburst" is a physical phenomenon of sudden release of the stress potential energy formed in a solid body under the long-term action of cosmic expansion. "Rock burst" is the inevitable (final) process in the evolution of solid

planets.

4) As the universe expands, the atoms and ions (ions containing orbital electrons) of everything in the universe keep getting bigger. Since the surface area of a solid is proportional to the square of the radius of the atoms that make up the solid, and the volume of the solid is proportional to the cubic of the radius of the atoms that make up the solid, the stress in the solid becomes larger as the atom expands, and the "rock burst" occurs when the stress in the solid is greater than the sum of the structural force of the solid and the external environmental pressure.

The Main Contributions and Key Novelties in the Paper

1) This paper proposes for the first time that the Tunguska Explosion is a thermonuclear explosion caused by the high temperature and high pressure generated by the asteroid's "rock burst".

2) In this paper, it is pointed out for the first time that "rockburst" is a physical phenomenon of sudden release of the stress potential energy formed in a solid body under the long-term action of cosmic expansion, and that "rockburst" is the inevitable (final) process in the evolution of solid planets.

3) This paper presents for the first time the mechanism of "rockburst" formation: As the universe expands, the atoms and ions (ions containing orbital electrons) of everything in the universe keep getting bigger. Since the surface area of a solid is proportional to the square of the radius of the atoms that make up the solid, and the volume of the solid is proportional to the cubic of the radius of the atoms that make up the solid, the stress in the solid becomes larger as the atom expands, and the "rock burst" occurs when the stress in the solid is greater than the sum of the structural force of the solid and the external environmental pressure.

Future Works

1) Because any naturally formed solid object contains stress, and the older the solid object is formed, the greater the stress it contains, it is possible to see if an explosion will occur and measure the energy generated by the explosion by heating natural diamond or other relatively old solids, thereby experimentally verifying that the stress energy of "rock burst" is formed by the expansion of atoms caused by the expansion of the universe.

2) Because asteroids like or more powerful than the asteroid that caused the Tunguska explosion should be widespread in the universe，monitoring asteroids that could meet the earth and detonating them artificially by laser or other means is an important task for humans to protect the earth from devastating disasters like the Tunguska explosion.

Conflicts of Interest

The author declares no conflicts of interest regarding the publication of this paper.

References

[1] Chyba, C.F., Thomas, P.J. and Zahnle, K.J. (1993) *Nature*, **361**, 40-44. https://doi.org/10.1038/361040a0

[2] Xu, D.Y. (1986) *Journal of Catastrophology*, No. 1, 115-117.

[3] Yi, M. (2011) *Science & Technology Vision*, No. 15, 25.

[4] Perkins, S. (2008) *Science News*, **173**, 5-6. https://doi.org/10.1002/scin.2008.5591731904

[5] Ortlepp, W.D. and Stacey, T.R. (1994) *Tunnelling and Underground Space Technology*, **9**, 59-65. https://doi.org/10.1016/0886-7798(94)90010-8

[6] Zhang, J. and Fu, B. (2008) *Chinese Journal of Rock Mechanics and Engineering*, **27**, 2034-2042.

[7] Wang, J.A. (2020) *Journal of Modern Physics*, **11**, 407-431. https://doi.org/10.4236/jmp.2020.113026

[8] Wang, J.A. (2019) *Journal of Modern Physics*, **10**, 1615-1644. https://doi.org/10.4236/jmp.2019.1014107

Journal of Modern Physics, 2020, 11, 788-802
https://www.scirp.org/journal/jmp
ISSN Online: 2153-120X
ISSN Print: 2153-1196

Quasi-Relativistic Description of Hydrogen-Like Atoms

Luis Grave de Peralta

Department of Physics and Astronomy, Texas Tech University, Lubbock, TX, USA
Email: luis.grave-de-peralta@ttu.edu

How to cite this paper: de Peralta, L.G. (2020) Quasi-Relativistic Description of Hydrogen-Like Atoms. *Journal of Modern Physics*, **11**, 788-802.
https://doi.org/10.4236/jmp.2020.116051

Received: May 7, 2020
Accepted: May 30, 2020
Published: June 2, 2020

Abstract

Using a novel wave equation, which is Galileo invariant but can give precise results up to energies as high as mc^2, exact quasi-relativistic quantum mechanical solutions are found for the Hydrogen atom. It is shown that the exact solutions of the Grave de Peralta equation include the relativistic correction to the non-relativistic kinetic energies calculated using the Schrödinger equation.

Keywords

Quantum Mechanics, Schrödinger Equation, Relativistic Quantum Mechanics, Klein-Gordon Equation, Hydrogen Atom

1. Introduction

Quantum mechanics triumphed when physicists learned to describe the quantum states of the electrons in the atoms by solving the Schrödinger equation [1] [2] [3] [4] [5]. However, the Schrödinger equation is not Lorentz invariant but Galilean invariant [6] [7]; therefore, a relativistic quantum mechanics cannot be based on the Schrödinger equation. A fully relativistic quantum theory requires to be funded on equations that are valid for any two observers moving respect to each other at constant velocity [8] [9]. In contrast, the Galilean invariance of the Schrödinger equation means that two such observers will only agree in the adequacy of the Schrödinger equation for describing the movement of a massive free quantum particle when the relative speed between the observers is much smaller than the speed of the light in the vacuum (c). In practice, this is not a terrible limitation of the Schrödinger equation because up to today humans have been only able to travel at speeds much smaller than c. This is one of the principal reasons why the Schrödinger equation is still relevant almost 100 years after

its discovery. Moreover, there is another important limitation of the Schrödinger equation: it describes a particle in which linear momentum (p) and kinetic energy (K) are related by a classical relation that is not valid at relativistic speeds [6] [7] [8] [9] [10]. Nevertheless, wave mechanics triumphed when Schrödinger, using his equation, was able to reproduce the results previously obtained by Bohr for the energies of the bound states of the electron in the Hydrogen atom. This was possible because the electron in the Hydrogen atom moves at non-relativistic energies [1] [2] [3] [4] [5]. Rigorously, the number of particles may be not constant in a fully relativistic quantum theory [7] [8] [9]. This is because when the sum of the kinetic and the potential (U) energy of a particle with mass m equals the energy associate to the mass of the particle, *i.e.* $E_t = K + U = mc^2$, then a second particle with the same mass could be created from E_t. Consequently, the number of particles is constant when $E_t = K + U < mc^2$. This is what happens in atoms and molecules; thus, this explains why the results obtained using the Schrödinger equation are a good first approximation in chemistry applications [5]. In between the Galilean invariant Schrödinger equation and the fully relativistic quantum mechanics, there is a quasi-relativistic region where $E_t < mc^2$ but E_t is so large that it is necessary to use an equation that describes a particle having a relativistic relation between p and K. In this work, the use of the Grave de Peralta equation is explored [7] [11], which is a quasi-relativistic wave equation, for describing the bounded states of an electron in a Hydrogen-like atom with atomic number Z. It is shown that the energies calculated using the Grave de Peralta equation are in excellent correspondence with the sum of the energies calculated using the Schrödinger equation plus the relativistic Thomas correction [12]. This demonstrates both the correctness and the usefulness of the proposed approach at quasi-relativistic energies. In what follows, first, a brief summary of the Grave de Peralta equation and its basic properties is presented; then solutions of this equation are obtained for a central potential in general and for the Coulomb potential. Finally, the conclusions of this work are given in the last section.

2. The Grave de Peralta Equation

Formally, the one-dimensional (1D) Schrödinger equation for a free quantum particle with mass m can be obtained from the classical relation between K and p for a free particle when its speed (V) is much smaller than the c [1] [2] [3] [4] [5]:

$$K = \frac{p^2}{2m}, \quad p = mV. \tag{1}$$

Then, substituting K and p by the following energy and momentum quantum operators [1] [2] [3] [4]:

$$\hat{E} = \hat{K} = i\hbar\frac{\partial}{\partial t}, \quad \hat{p} = -i\hbar\frac{\partial}{\partial x}. \tag{2}$$

In Equation (2), $\hbar$ is the Plank constant (h) divided by 2π, results [1] [2] [3] [4] [5]:

$$i\hbar\frac{\partial}{\partial t}\psi_{Sch}(x,t)=-\frac{\hbar^2}{2m}\frac{\partial^2}{\partial x^2}\psi_{Sch}(x,t). \tag{3}$$

However, Equation (1) does not give the correct relation between K and p when the particle moves at faster speeds. Correspondingly, the Schrödinger equation (Equation (3)) is not Lorentz invariant but Galileo invariant [6] [7]; thus, only should be used for particles moving slowly. At larger particle's speed, one should use the following well-known relativistic relations [10]:

$$E^2-m^2c^4=p^2c^2 \Leftrightarrow \left(E+mc^2\right)\left(E-mc^2\right)=p^2c^2. \tag{4}$$

And:

$$E=\gamma_V mc^2,\quad p=\gamma_V mV. \tag{5}$$

Here, $E=K+mc^2$ is the total relativistic energy of the free particle, and [10]:

$$\gamma_V=\frac{1}{\sqrt{1-\frac{V^2}{c^2}}}. \tag{6}$$

One can then formally proceed as it is done for obtaining the 1D Schrödinger equation, and use Equation (2) for assigning the temporal partial derivative operator to E in the first expression of Equation (4) [7] [8] [9]. In this way, one can formally obtain the 1D Klein-Gordon equation [8] [9]:

$$\frac{1}{c^2}\frac{\partial^2}{\partial t^2}\psi_{KG}(x,t)=\frac{\partial^2}{\partial x^2}\psi_{KG}(x,t)-\frac{m^2c^2}{\hbar^2}\psi_{KG}(x,t). \tag{7}$$

The Klein-Gordon equation is Lorentz invariant and describes a free quantum particle with mass m and spin-0 [8] [9]. In contrast to the Schrödinger equation, a second-order temporal derivative is present in Equation (7). This determines that Equation (7) has solutions with positive and negative energy values while Equation (3) has only solutions with positive energies, which is in correspondence with K having only positive values in Equation (1) but E having positive and negative values in Equation (4). The factor ($E+mc^2$) is always different than 0 for $E>0$; consequently, Equation (4) and the following algebraic equation are equivalents for $E>0$:

$$\left(E-mc^2\right)=\frac{p^2}{\left(\gamma_V+1\right)m} \tag{8}$$

Each member of Equation (8) is just a different expression of the relativistic kinetic energy of the particle [7]. Assigning the temporal partial derivative operator in Equation (2) to E in Equation (8) results in the following differential equation [11]:

$$i\hbar\frac{\partial}{\partial t}\psi_{KG+}(x,t)=-\frac{\hbar^2}{\left(\gamma_V+1\right)m}\frac{\partial^2}{\partial x^2}\psi_{KG+}(x,t)+mc^2\psi_{KG+}(x,t). \tag{9}$$

A simple substitution in Equation (7) and Equation (9) shows that the follow-

ing plane wave is a solution of both equations for $E > 0$:

$$\psi_{KG+}(x,t) = \mathrm{e}^{\frac{i}{\hbar}(px-Et)}. \tag{10}$$

The plane wave ψ_{KG+} has an unphysical phase velocity equal to $c^2/V > c$ [7] [11]. However, one can look for a solution of Equation (9) of the following form:

$$\psi(x,t) = \psi_{KG+}\mathrm{e}^{iw_m t}, \quad w_m = \frac{mc^2}{\hbar}. \tag{11}$$

Such that ψ has a phase velocity smaller than c [7] [11]; thus:

$$\psi(x,t) = \mathrm{e}^{\frac{i}{\hbar}(px-Kt)}. \tag{12}$$

Substituting ψ given by Equation (11) in Equation (9) results in the 1D Grave de Peralta equation [7] [11]:

$$i\hbar\frac{\partial}{\partial t}\psi(x,t) = -\frac{\hbar^2}{(\gamma_V+1)m}\frac{\partial^2}{\partial x^2}\psi(x,t). \tag{13}$$

Equation (13) clearly coincides with the Schrödinger equation at low particle's speeds. Moreover, a positive probability density can be defined for the solutions of Equation (13) by analogy of how it is defined for the solutions of the Schrödinger equation and, like the Schrödinger equation, Equation (13) is Galilean invariant for observers traveling at low speeds respect to each other [7]. Despite this, Equation (13) can be used for obtaining precise solutions of very interesting quantum problems at quasi-relativistic energies [7] [11], where a particle moves at so large speeds that it is necessary to use the correct relativistic relation between p and K, but where the particle should not be moving too fast so that the number of particles remains constant. When the particle moves through a 1D piecewise constant potential $U(x)$, Equation (13) should be generalized in the following way [11]:

$$i\hbar\frac{\partial}{\partial t}\psi(x,t) = -\frac{\hbar^2}{\left[\gamma_V(x)+1\right]m}\frac{\partial^2}{\partial x^2}\psi(x,t) + U(x)\psi(x,t). \tag{14}$$

Often, one looks for solutions of Equation (14) corresponding to a constant value of the energy $E_\xi = K + U$, where E_ξ is not the total relativistic energy of the particle (E) but $E_\xi = E - mc^2$. At quasi-relativistic energies, the number of particles is constant; therefore, E_ξ is constant whenever E is constant. For a 1D piecewise constant potential E_ξ, K, γ_V, and V^2 are constants in each x-region where U is constant. In contrast to E_ξ, however, K, γ_V and V^2 have a discontinuity wherever $U(x)$ has one. Consequently, in Equation (14) γ_V is a function of x because, in general, the square of the particle's speed (V^2) depends on the position [11]. Nevertheless, for 1D piecewise constant potentials, one can look for a solution of Equation (14) with the following form in each of the regions where K, γ_V, and V^2 are constants [1] [2] [3] [4] [11]:

$$\psi(x,t) = X_K(x)\mathrm{e}^{-\frac{i}{\hbar}E_\xi t}, \quad E_\xi = K + U \tag{15}$$

X_K is a solution of the following equation [1] [2] [3] [4] [11]:

$$\frac{\mathrm{d}^2}{\mathrm{d}x^2}X_K(x)+\kappa^2 X_K(x)=0,\ \ \kappa=\frac{p}{\hbar}. \tag{16}$$

And [11]:

$$\kappa=\frac{p}{\hbar}=\frac{1}{\hbar}\sqrt{(\gamma_V+1)mK}=\frac{1}{\hbar}\sqrt{(\gamma_V+1)m(E-U)}. \tag{17}$$

Consequently, κ and X_K are not determined by the values of E but by the values of $K = E - U$. Once the allowed values of κ are determined from Equation (16) and the boundary conditions, the allowed values of the relativistic kinetic energy of the particle $K = E - U$ are given by:

$$K=\frac{\hbar^2\kappa^2}{(\gamma_V+1)m}. \tag{18}$$

As expected, when $\gamma_V \sim 1$, Equation (18) gives the non-relativistic values of the particle's energies at low speeds, $K \sim \hbar^2\kappa^2/(2m)$ [1] [2] [3] [4]. Moreover, from Equation (18) and the relativistic equation, $K=(\gamma_V-1)mc^2$, follows that [11]:

$$\gamma_V^2=1+\left(\frac{\lambda_C}{\lambda}\right)^2,\ \ \lambda_C=\frac{h}{mc},\ \ \lambda=\frac{2\pi}{\kappa}. \tag{19}$$

In Equation (19), λ_C is the Compton wavelength associate to the mass of the particle [8] [10], and λ is the De Broglie wavelength of the wavefunction given by Equation (7) and Equation (10) [1] [2] [3] [4]. Substituting Equation (19) in Equation (18) allows obtaining an analytical expression of the precise quasi-relativistic kinetic energy of the particle:

$$K=\frac{\hbar^2\kappa^2}{\left[1+\sqrt{1+\left(\frac{\lambda_C}{\lambda}\right)^2}\right]m}. \tag{20}$$

As expected, Equation (20) match the non-relativistic expression of the particle's kinetic energy when $p = h/\lambda$ is very small because $\lambda \gg \lambda_C$. However, in each region where the value of U is constant, the values of K and then $E = K + U$ calculated using Equation (20) are smaller than the ones calculated using the Schrödinger equation.

3. Movement in a Central Potential

A quantum state of a particle with mass m moving at quasi-relativistic energies in a central potential, $U(r)$, is a solution of the following 3D Grave de Peralta equation [7]:

$$i\hbar\frac{\partial}{\partial t}\psi(\mathbf{r},t)=-\frac{\hbar^2}{[\gamma_V(r)+1]m}\nabla^2\psi(\mathbf{r},t)+U(r)\psi(\mathbf{r},t). \tag{21}$$

In Equation (21), γ_V and V^2 depend only on the radial variable (r) because the

potential is a central potential. In spherical coordinates, the Laplacian operator in Equation (21) is given by the following expression [1]:

$$\nabla^2\psi = \frac{1}{r}\frac{\partial^2}{\partial r^2}(r\psi) + \frac{1}{r^2}\nabla^2_{\theta,\varphi}\psi. \tag{22}$$

In Equation (22):

$$\nabla^2_{\theta,\varphi} = \frac{1}{\sin\theta}\frac{\partial}{\partial\theta}\left(\sin\theta\frac{\partial}{\partial\theta}\right) + \frac{1}{\sin^2\theta}\frac{\partial^2}{\partial\varphi^2}. \tag{23}$$

Using Equation (22) and Equation (23) allows for rewriting Equation (21) in the following way [7]:

$$i\hbar\frac{\partial}{\partial t}\psi = -\frac{\hbar^2}{\left[\gamma_V(r)+1\right]mr}\frac{\partial^2}{\partial r^2}(r\psi) - \frac{\hbar^2}{\left[\gamma_V(r)+1\right]mr^2}\nabla^2_{\theta,\varphi}\psi + U(r)\psi. \tag{24}$$

The second term of the right size of Equation (24) corresponds to the rotational energy of the particle. For a quantum rotor, which describes a particle moving in a sphere, r is constant [2] [5]. This allows for simplifying Equation (24) in the following way [7]:

$$i\hbar\frac{\partial}{\partial t}\psi(\theta,\varphi) = -\frac{\hbar^2}{(\gamma_V+1)mr^2}\nabla^2_{\theta,\varphi}\psi(\theta,\varphi). \tag{25}$$

The explicit absence of a potential in Equation (25) determines that it has solutions with constant values of E, K, γ_V and V^2 [7]. However, one should expect to have solution of Equation (24) with constant values of E, but all K, γ_V and V^2 depending on r. Looking for a solution of Equation (24) as in Ref. [1]:

$$\psi(r,\theta,\varphi,t) = R(r)\Omega(\theta,\varphi)\mathrm{e}^{\frac{i}{\hbar}Et}. \tag{26}$$

Results:

$$\nabla^2_{\theta,\varphi}\Omega(\theta,\varphi) = \eta\Omega(\theta,\varphi). \tag{27}$$

And:

$$\frac{1}{r}\frac{\mathrm{d}^2}{\mathrm{d}r^2}(rR) + \frac{\left[\gamma_V(r)+1\right]mr^2}{\hbar^2}\left[E - U(r)\right]R = -\eta\frac{R}{r^2}. \tag{28}$$

Equation (27) is the well-known equation for the spherical harmonic functions [1] [2] [3] [4] [5], which solutions are:

$$\Omega_{l,m}(\theta,\varphi) = Y_l^{(m)}(\theta,\varphi);\ \eta = l(l+1);\ l = 0,1,2,\cdots;\ m = -l,-l+1,\cdots,0,1,\cdots,l. \tag{29}$$

Here, $Y_l^{(m)}$ are the spherical harmonic functions [1] [2] [3] [4] [5]. Substituting η given by Equation (29) in Equation (28) and looking for a solution of the form $R(r) = \chi(r)/r$ as in Ref. [4], then results the following equation:

$$\frac{\mathrm{d}^2}{\mathrm{d}r^2}\chi(r) + \frac{\left[\gamma_V(r)+1\right]m}{\hbar^2}\left[E - W(r)\right]\chi(r) = 0. \tag{30}$$

In Equation (30):

$$W(r) = \left[U(r) + \frac{\hbar^2}{\left[\gamma_V(r)+1\right]m}\frac{l(l+1)}{r^2}\right]. \tag{31}$$

The radial equation, Equation (30), is then formally identical to Equation (16) with:

$$\kappa(r)=\frac{p(r)}{\hbar}=\frac{1}{\hbar}\sqrt{\left[\gamma_V(r)+1\right]mK(r)}=\frac{1}{\hbar}\sqrt{\left[\gamma_V(r)+1\right]m\left[E-W(r)\right]}. \quad (32)$$

At low particle speeds, $\gamma_V(r) \sim 1$, thus Equation (30) coincide with the radial equation that can be obtained when solving the same problem using the Schrödinger equation [1] [2] [3] [4] [5]. However, at quasi-relativistic energies, γ_V depends on r; therefore, in general, the solutions of Equation (30) are different than the solutions of the radial equation for the Schrödinger equation. A notable exception is the infinite spherical well problem for $l = 0$ where $U(r)$ is given by the following expression [4]:

$$U(r)=\begin{cases}0, & r<r_o\\ U_o\to+\infty, & r\geq r_o\end{cases} \quad (33)$$

In this case $W(r)\equiv 0$; thus K, γ_V, and V^2 are constant inside the well. Equation (30) can then be solved as it is done for the Schrödinger equation. Consequently [4]:

$$E_n=K_n=n^2\frac{h^2}{\left(\gamma_V+1\right)mD_o^2}. \quad (34)$$

In Equation (34), $D_o = 2r_o$ and n is a positive integer number. From Equation (34) and the relativistic equation $K=\left(\gamma_V-1\right)mc^2$ follows that:

$$\gamma_V^2=1+n^2\left(\frac{\lambda_C}{D_o}\right)^2,\ \lambda_C=\frac{h}{mc}. \quad (35)$$

Substituting γ_V given by Equation (35) in Equation (34) results:

$$E_n=\frac{n^2}{\left[1+\sqrt{1+\left(\frac{n\lambda_C}{D_o}\right)^2}\right]}\left(\frac{\lambda_C}{D_o}\right)^2 mc^2. \quad (36)$$

As expected, $\gamma_V \sim 1$ when $n = 1$ and $D_o \gg \lambda_C$; thus, Equation (36) coincides with the energies of the infinite spherical well calculated using the Schrödinger equation [4]. In contrast, when the diameter of the well is close to λ_C, the minimum particle energy is quasi-relativistic; therefore, Equation (36) must be used. For instance, $\gamma_V^2=2$, $V \sim 0.7c$, and $K \sim 0.4mc^2$ when Equation (35) is evaluated for $n = 1$ and $D_o = \lambda_C$. However, $\gamma_V^2=5$ and $K \sim 1.2mc^2$ when $n = 1$ and $D_o = \lambda_C/2$. The number of particles may not be constant at these energies. Consequently, the Grave de Peralta equation establishes a fundamental connection between quantum mechanics and especial theory of relativity: no single particle with mass can be confined in a volume much smaller than $1/8\,\lambda_C^3$ because when this occurs, $K > mc^2$ and the number of particles may not be constant anymore; therefore, a single point-particle with mass cannot exist. Point-particles with mass can only exist in fully relativistic quantum field theories where the number of particles is not constant. This is true for an electron, a quark, and probably

may also be true for a black hole and the whole universe at the beginning of the Big Bang. This is consistent, for instance, with the confinement of an electron in the Hydrogen atom because for an electron $\lambda_C \sim 2.4 \times 10^{-3}$ nm, which is ~ 20 times smaller than the Bohr radius of the Hydrogen atom, $r_B \sim 5.3 \times 10^{-2}$ nm [1] [2] [3] [4] [5]. It should be noted that strictly speaking, the problem corresponding to the potential defined by Equation (33) is a relativistic problem because $|\Delta U| = U_o \gg mc^2$ and thus the number of particles may not be constant. Nevertheless, the non-relativistic and quasi-relativistic infinite well problems could be considered approximations to the problem of a quantum particle absolutely trapped in a finite region. This is because for obtaining Equation (34) and Equation (36) the infinitude of the potential is only used for arguing that $\chi(r)$ should be null everywhere except inside of the well, thus assigning null boundary conditions to Equation (30).

4. Hydrogen-Like Atoms

In the Hydrogen atom or in highly ionized atoms with a single electron, $U(r)$ is the Coulomb potential [1] [2] [3] [4] [5]:

$$U(r) = U_C(r) = -\frac{e^2}{4\pi\varepsilon_o}\frac{Z}{r}. \tag{37}$$

Here, e is the electron charge, Z is the atomic number, and ε_o is the electric permittivity of vacuum. Therefore, the radial equation corresponding to the quasi-relativistic states of the electron in a hydrogen-like atom with a nucleus of mass m_n is given by the Equation (30) with the electron mass, m_e, substituted by the reduced mass of the electron, $\mu = (m_e m_n)/(m_e + m_n)$, *i.e.*:

$$\frac{\mathrm{d}^2}{\mathrm{d}r^2}\chi(r) + \frac{[\gamma_V(r)+1]\mu}{\hbar^2}[E_r - W_C(r)]\chi(r) = 0. \tag{38}$$

In Equation (38):

$$W_C(r) = \left[U_C(r) + \frac{\hbar^2}{[\gamma_V(r)+1]\mu}\frac{l(l+1)}{r^2}\right]. \tag{39}$$

As expected, when the electron moves slowly ($V \ll c$) then $\gamma_V \sim 1$; therefore, Equation (38) reduces to the radial equation of a hydrogen-like atom obtained using the Schrödinger equation [4]. Using Equation (5), it is possible to eliminate γ_V from Equation (38) and Equation (39) by making:

$$\frac{[\gamma_V(r)+1]\mu}{\hbar^2} = \frac{K + 2\mu c^2}{c^2\hbar^2} = \frac{[E_r - U_C(r)] + 2\mu c^2}{c^2\hbar^2}. \tag{40}$$

Using Equation (40) then allows for rewriting Equation (38) in the following way:

$$\begin{aligned}&\left\{-\frac{\hbar^2}{2\mu}\frac{\mathrm{d}^2}{\mathrm{d}r^2}\chi(r) - [E_r - U_C(r)]\chi(r) + \frac{\hbar^2}{2\mu}\frac{l(l+1)}{r^2}\chi(r)\right\}\\ &-\frac{1}{2\mu c^2}[E_r - U_C(r)]^2\chi(r) = 0.\end{aligned} \tag{41}$$

The term between braces in Equation (41) coincides with the radial equation that should be solved when using the Schrödinger equation [4]. The last term of Equation (41) can be disregarded when $K \ll \mu c^2$; therefore, the last term is a quasi-relativistic correction to the non-relativistic radial equation. Proceeding like it is done when solving the non-relativistic radial equation, one can introduce [4]:

$$\zeta = \frac{1}{\hbar}\sqrt{-2\mu E_\zeta}. \tag{42}$$

For bound states, $E_\zeta < 0$; therefore, ζ is real. Using Equation (42) allows for rewriting Equation (41) in the following way:

$$\begin{aligned}\frac{1}{\zeta^2}\frac{\mathrm{d}^2}{\mathrm{d}r^2}\chi(r) = \Bigg\{&\left[1-\frac{\mu e^2}{2\pi\varepsilon_o\hbar^2\zeta}\frac{Z}{(\zeta r)}+\frac{l(l+1)}{(\zeta r)^2}\right]\\ &-\left[\frac{\alpha^2Z^2}{(\zeta r)^2}-\frac{\hbar\zeta}{\mu c}\frac{\alpha Z}{(\zeta r)}+\left(\frac{\hbar}{2\mu c}\right)^2\zeta^2\right]\Bigg\}\chi(r).\end{aligned} \tag{43}$$

where α is the fine-structure constant [8] [9] [12]:

$$\alpha = \frac{1}{4\pi\varepsilon_o}\frac{e^2}{\hbar c} \sim 1/137. \tag{44}$$

It is convenient to rewrite Equation (43) as:

$$\begin{aligned}\frac{1}{\zeta^2}\frac{\mathrm{d}^2}{\mathrm{d}r^2}\chi(r) = \Bigg\{&\left[1-\left(\frac{\hbar\zeta}{2\mu c}\right)^2\right]-\left[\left(\frac{\mu e^2}{2\pi\varepsilon_o\hbar^2\zeta}-\alpha\frac{\hbar\zeta}{\mu c}\right)\frac{Z}{(\zeta r)}\right]\\ &+\frac{l(l+1)-\alpha^2Z^2}{(\zeta r)^2}\Bigg\}\chi(r).\end{aligned} \tag{45}$$

So that introducing the new variables:

$$\rho \equiv \zeta r, \quad \rho_o \equiv \left(\frac{\mu e^2}{2\pi\varepsilon_o\hbar^2\zeta}-\alpha\frac{\hbar\zeta}{\mu c}\right)Z, \quad \rho_1 \equiv \left[1-\left(\frac{\hbar\zeta}{2\mu c}\right)^2\right]. \tag{46}$$

Allows for rewriting Equation (45) in the following way:

$$\frac{\mathrm{d}^2}{\mathrm{d}\rho^2}\chi(\rho) = \left[\rho_1-\frac{\rho_o}{\rho}+\frac{l(l+1)-\alpha^2Z^2}{\rho^2}\right]\chi(\rho). \tag{47}$$

If the electron was free and moving slowly with kinetic energy $K = E_\zeta$, then its linear momentum would be $\hbar\zeta \ll \mu c$. In this limit, one can approximate Equation (46) in the following way [3] [4]:

$$\rho \equiv \zeta r, \quad \rho_o \sim \frac{\mu e^2 Z}{2\pi\varepsilon_o\hbar^2\zeta}, \quad \rho_1 \sim 1. \tag{48}$$

Using Equation (48), and considering that for the Hydrogen atom $\alpha^2Z^2 \ll 1$, allows for approximating Equation (47) in the following way [3] [4]:

$$\frac{\mathrm{d}^2}{\mathrm{d}\rho^2}\chi(\rho) = \left[1-\frac{\rho_o}{\rho}+\frac{l(l+1)}{\rho^2}\right]\chi(\rho). \tag{49}$$

which is the equation that is solved for the Hydrogen atom when using the Schrödinger equation [4]. Consequently, when solving the Schrödinger equation can be found that [4]:

$$\rho_o = 2n, \quad n = 1, 2, 3, \cdots \tag{50}$$

From Equation (50), Equation (48), and Equation (42) then follows for $Z = 1$ the following well-known result [2] [3] [4]:

$$E_{n,Sch} = -\left[\frac{\mu}{2\hbar^2}\left(\frac{e^2}{4\pi\varepsilon_o}\right)^2\right]\frac{1}{n^2}. \tag{51}$$

However, each of the three terms in the right side of Equation (47) contains a different quasi-relativistic correction to the radial equation of hydrogen-like atoms. Nevertheless, one can try to solve the quasi-relativistic Equation (47) as Equation (49) is solved [4]. When $\rho \to \infty$, the constant term in the brackets in Equation (47) dominates, so (approximately):

$$\frac{\mathrm{d}^2}{\mathrm{d}\rho^2}\chi(\rho) = \rho_1\chi(\rho). \tag{52}$$

which general solution is:

$$\chi(\rho) = A\mathrm{e}^{-\sqrt{\rho_1}\rho} + B\mathrm{e}^{\sqrt{\rho_1}\rho}. \tag{53}$$

But $\rho_1 > 0$; therefore, B must be null, so for large ρ:

$$\chi(\rho) \sim A\mathrm{e}^{-\sqrt{\rho_1}\rho}. \tag{54}$$

On the other hand, when $\rho \to 0$ the centrifugal term dominates; approximately, then:

$$\frac{\mathrm{d}^2}{\mathrm{d}\rho^2}\chi(\rho) = \frac{l(l+1)-\alpha^2Z^2}{\rho^2}\chi(\rho). \tag{55}$$

Which general solution is:

$$\chi(\rho) = C\rho^{\frac{1}{2}\left[1+\sqrt{(1+2l)^2-4\alpha^2Z^2}\right]} + D\rho^{\frac{1}{2}\left[1-\sqrt{(1+2l)^2-4\alpha^2Z^2}\right]}. \tag{56}$$

Therefore, D must be null, so for small ρ:

$$\chi(\rho) \sim C\rho^{\frac{1}{2}\left[1+\sqrt{(1+2l)^2-4\alpha^2Z^2}\right]}. \tag{57}$$

As expected, if the quasi-relativistic corrections are very small, then Equation (54) and Equation (57) reduces to the ones obtained when using the Schrödinger equation [4]. After knowing the asymptotic behavior of $\chi(\rho)$, one can look for a solution of Equation (47) as [4]:

$$\chi(\rho) \equiv \tau(\rho)\rho^{\frac{1}{2}\left[1+\sqrt{(1+2l)^2-4\alpha^2Z^2}\right]}\mathrm{e}^{-\sqrt{\rho_1}\rho}. \tag{58}$$

From Equation (58) and Equation (47) then follow that $\tau(\rho)$ is a solution of the following equation:

$$\rho\frac{\mathrm{d}^2}{\mathrm{d}\rho^2}\tau(\rho)+\left[1-\left(2\sqrt{\rho_1}\right)\rho+\sqrt{(1+2l)^2-4\alpha^2Z^2}\right]\frac{\mathrm{d}}{\mathrm{d}\rho}\tau(\rho)$$
$$+\left[\rho_o-\sqrt{\rho_1}\left(1+\sqrt{(1+2l)^2-4\alpha^2Z^2}\right)\right]\tau(\rho)=0. \tag{59}$$

Again, as expected, if the quasi-relativistic corrections are very small, then Equation (59) reduces to the one obtained when using the Schrödinger equation [4]. Finally, assuming that $\tau(\rho)$ can expressed as a finite power series in ρ [4]:

$$\tau(\rho)=\sum_{j=0}^{j_{\max}}a_j\rho^j. \tag{60}$$

And substituting Equation (60) in Equation (59) results:

$$a_{j+1}=\frac{\sqrt{\rho_1}\left[2j+\left(1+\sqrt{(1+2l)^2-4\alpha^2Z^2}\right)\right]-\rho_o}{(j+1)\left[j+\left(1+\sqrt{(1+2l)^2-4\alpha^2Z^2}\right)\right]}a_j. \tag{61}$$

Evaluating Equation (61) for $j=j_{\max}$ and making $a_{j_{\max}+1}=0$, results:

$$\frac{\rho_o}{\sqrt{\rho_1}}=\left[2j+\left(1+\sqrt{(1+2l)^2-4\alpha^2Z^2}\right)\right]. \tag{62}$$

As expected, if the quasi-relativistic corrections are very small, then Equation (62) reduces to Equation (50) with $n=j+l+1$ [4]. Nevertheless, one can re-write Equation (62) in the following way:

$$\rho_o=\left[2n+\Delta(l,Z)\right]\sqrt{\rho_1}. \tag{63}$$

In Equation (63):

$$\Delta(l,Z)=\left[\left(1+\sqrt{(1+2l)^2-4\alpha^2Z^2}\right)-2(l+1)\right]. \tag{64}$$

Substituting ρ_o and ρ_1 given by Equation (46) in Equation (63), solving the resulting equation for ζ, and using Equation (42) allows for obtaining an exact analytical expression for E_ζ, which now depends not only on the principal quantum number n, but also on the angular quantum number l, and Z. For instance, assuming that the quasi-relativistic corrections included in ρ_o and ρ_1 do not need to be accounting for because they are too small, the effect of the quasi-relativistic correction included in the centrifugal term in Equation (63) is quantified by the following equation:

$$E_{\zeta n,l}=-\left[\frac{\mu}{2\hbar^2}\left(\frac{e^2}{2\pi\varepsilon_o}\right)^2\right]\frac{Z^2}{\left[2n+\Delta(l,Z)\right]^2}. \tag{65}$$

As expected, if α was null and $Z=1$, then Equation (65) would be identical to Equation (51). However, $\Delta(l,Z)<0$ and $\left|\Delta(l,Z)\right|$ increases when Z increases. Therefore, for $n>1$ and $l>0$, the degeneration of $E_{\zeta n}$ given by Equation (51) is broken by the quasi-relativistic correction $\Delta(l,Z)$. This effect is more pronounced for heavy elements. In addition, as shown in **Figure 1**, $\left|\Delta(l,Z)\right|$ decreases when l increases; therefore, $E_{\zeta n,l}\to E_{\zeta n}$ when l is large. **Figure 1** shows a

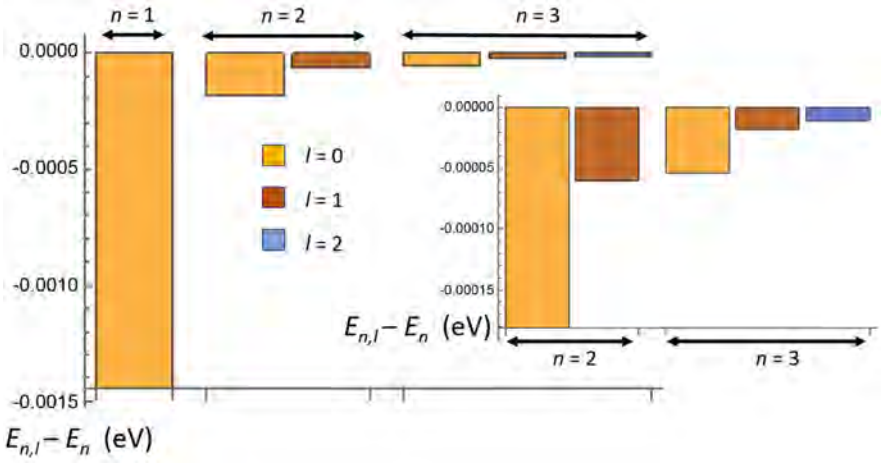

Figure 1. Schematic of the values of $E_{n,l}$ - E_n (in eV), which are calculated for $Z = 1$ and $n = 1, 2, 3$ using Equation (65) and Equation (51), respectively. The inset at the right permits to appreciate the details corresponding to the energy levels $n = 2$ and 3.

schematic of the calculated values of $E_{n,l} - E_n$ in eV, where $E_{n,l}$ and E_n were evaluated using Equation (65) with $Z = 1$ and Equation (51), respectively. In all cases, stabilizing negative quasi-relativistic corrections to the non-relativistic energies were obtained. This is because the negative contribution of $-\alpha^2 Z^2$ in the numerator of the centrifugal term in Equation (47).

In columns 2 and 3 in Table 1 are reported the calculated values of $E_{n,l}$ (in eV) that were calculated using Equation (65) and Equation (63), respectively. The difference between the approximated values (Equation (65)) and the exact values (Equation (63)) of $E_{n,l}$ are ~0.01 meV; thus smaller than the exact values of $E_{n,l=0} - E_n$ reported in the third column of Table 1. Therefore, Figure 1 also represents a good schematic of the exact values of $E_{n,l} - E_n$; *i.e.* calculated using Equation (63) and Equation (51). There is an excellent correspondence between the exact values of $E_{n,l} - E_n$ reported in the third column of Table 1, and previously reported values of the relativistic correction to E_n [4] [12]. This suggests that the solutions of Equation (63) are approximately equal to [4] [12]:

$$E_{n,l} \sim E_{n,Sch} Z^2 \left\{ 1 - \frac{\alpha^2}{n^2} \left[\frac{3}{4} - \frac{n}{l + \frac{1}{2}} \right] \right\}. \tag{66}$$

where $E_{n,l,Sch}$ given by Equation (51) correspond to the Hydrogen energies calculated using the Schrödinger equation. In correspondence with this, one can show that the values of $E_{n,l}$ calculated using Equation (65) are approximately equal to:

$$E_{n,l} \sim E_{n,Sch} Z^2 \left(1 + \frac{2\alpha^2}{n(2l+1)} \right). \tag{67}$$

Indeed, Equation (65) can be rewritten as:

$$E_{n,l} = -\mu c^2 \alpha^2 Z^2 \frac{1}{\left[2n + \Delta(l, Z) \right]^2}. \tag{68}$$

Table 1. First four columns: Calculated values of $E_{n,l}$ (in eV) and $E_{n,l}$ - E_n (in meV). The last three columns report the calculated values of the energies (in eV) and wavelengths (in nm) corresponding to the Hydrogen's Lyman (second row) and average Balmer α-line (sixth row), which were calculated using the exact quasi-relativistic values of $E_{n,l}$ reported in the third column.

(n,l)	Equation (65)	Equation (63)	$E_{nl} - E_n$ (meV)	$(n',l') \to (n,l)$	$E_{n'l'} - E_{n,l}$	λ (nm)
(1,0)	−13.5997	−13.5992	−0.90526	(2,1) → (1,0)	10.1996	121.558
(2,0)	−3.39975	−3.39972	−0.147102	(3,1) → (2,0)	1.88879	656.422
(2,1)	−3.39963	−3.3996	−0.0264008	(3,0) → (2,1)	1.88863	656.477
(3,0)	−1.51097	−1.51097	−0.046938	(3,2) → (2,1)	1.88867	656.462
(3,1)	−1.51094	−1.51093	−0.0111749	(3) → (2,1)	1.88863	656.4695
(3,2)	−1.51093	1.51092	−0.00402301			

Then Equation (67) can be obtained from Equation (68) using the following approximated relations:

$$\frac{1}{\left[2n+\Delta(l,Z)\right]^2} \sim \frac{1}{(2n)^2}\left[1-\frac{\Delta(l,Z)}{n}\right], \quad \Delta(l,Z) \sim -\frac{2\alpha^2}{2l+1}. \tag{69}$$

This is an important result: the quasi-relativist energies calculated using the Grave de Peralta equation corresponds to the sum of the non-relativistic energies calculated using the Schrödinger equation plus the relativistic corrections to the kinetic energy. Consequently, these energies do not include the Darwin energy term [12]. In addition, like the Schrödinger equation, Equation (21) and Equation (38) describe a charged particle with spin-0 moving in a Coulomb potential; therefore, no spin-orbit interaction is included in Equation (63) and Equation (65). It is well-known that both the Darwin and spin-orbit corrections are needed for a successful description of the Hydrogen spectrum [8] [9] [12]. Nevertheless, it is good to emphasize the improvement that can be obtained by using the Grave de Peralta equation in comparison to using the Schrödinger equation. The quasi-relativistic approximation to the Hydrogen spectral lines corresponding to the α-lines of the Lyman and Balmer series can be estimated using the values of $E_{n,l}$ reported in the third column of **Table 1** and the spectral rule $\Delta l = \pm 1$ [12]. The calculated values of $E_{n',l'} - E_{n,l}$ (in eV), which correspond to all possible transitions between the states (n, l) reported in the third column of **Table 1**, are reported in the sixth column of **Table 1**. The corresponding wavelength values (in nm) are reported in the last column of **Table 1**. **Table 2** allows for making a breve comparison between the calculated values reported in the last two columns of **Table 1** and previously reported experimental data [13] [14]. The doublet structure of the α-Lyman Hydrogen line cannot be explained without the spin-orbit interaction because only the transition (2,1) to (1,0) satisfices the spectral rule $\Delta l = \pm 1$. However, the existence of the doublet fine-structure of the Balmer's α-line could be calculated as corresponding to the λ_1 = 656.422 nm spectral line produced by the (3,1) to (2,0) atomic transition and the λ_2 = 656.4695 nm spectral line, which was estimated as in the middle of the spectral

Table 2. Experimental (second column) and calculated (third column) wavelengths corresponding to the doublet structure of the Hydrogen's Lyman (first two rows) and Balmer α-lines (last two rows).

(In nm)	Experimental	Calculated
α-Lyman (λ in nm)	121.567	121.558
α-Lyman ($\Delta\lambda$ in nm)	0.006	No
α-Balmer (λ in nm)	656.279	656.422
α-Lyman ($\Delta\lambda$ in meV)	0.04	0.16

lines corresponding to the atomic transitions (3,0) to (2,1) and (3,2) to (2,1). This corresponds to a Balmer's α-doublet separation of $\Delta\lambda \sim 0.048$ nm or $\Delta E \sim 0.16$ meV. Nevertheless, as shown in Table 2, this value is four times larger than the experimental value [14], which demonstrates the need for including in the calculation both the Darwin and the spin-orbit contributions.

5. Conclusion

It has been shown how to solve the Grave de Peralta equation for a charged quantum particle with mass and spin-0, which is moving in a Coulomb potential or contained in a spherical infinite well. The solutions were found following the same procedures and with no more difficulty than the corresponding to solving the same problems using the Schrödinger equation. Nevertheless, the solutions found in this work are also valid when the particle is moving with quasi-relativistic energies. For instance, it was shown that the energies of the electron in a Hydrogen atom, which were calculated by solving the Grave de Peralta equation, includes the relativistic Thomas correction. Moreover, the relativistic correction to the kinetic energy is just an approximation found using a perturbative approach while Equation (63) was exactly solved. In addition, it should be noted that Equation (41) is different than the radial equation obtained using the Schrödinger equation. The author is currently working on solving Equation (41). This will allow to obtain more precise expressions for the atomic orbitals currently used in numerous *ab initio* computer packages dedicated to computer calculations in physical-chemistry and atomic and solid-state physics.

Conflicts of Interest

The author declares no conflicts of interest regarding the publication of this paper.

References

[1] Bohm, D. (1964) Quantum Theory. 11th Edition, Prentice-Hall, USA.

[2] Davydov, A.S. (1965) Quantum Mechanics. Pergamon Press, Oxford.

[3] Merzbacher, E. (1970) Quantum Mechanics. 2nd Edition, John Wiley & Sons, New York.

[4] Griffiths, D.J. (1995) Introduction to Quantum Mechanics. Prentice Hall, USA.

[5] Levine, I.N. (2014) Quantum Chemistry. 7th Edition, Pearson Education, New York.

[6] Home, D. (1997) Conceptual Foundations of Quantum Physics: An Overview from Modern Perspectives. Plenum Press, New York.

[7] Grave de Peralta, L. (2020) *Journal of Modern Physics*, **11**, 196-213. https://doi.org/10.4236/jmp.2020.112012

[8] Strange, P. (1998) Relativistic Quantum Mechanics: With Applications in Condensed Matter and Atomic Physics. Cambridge University Press, New York. https://doi.org/10.1017/CBO9780511622755

[9] Greiner, W. (1990) Relativistic Quantum Mechanics: Wave Equations. Spring-Verlag, New York.

[10] Jackson, J.D. (1975) Classical Electrodynamics. 2nd Edition. John Wiley & Sons, New York.

[11] Grave de Peralta, L. (2020) *Results in Phys*ics, Under Review.

[12] Nanni, L. (2015) arXiv:1501.05894.

[13] Parthey, C.G. (2011) *Ludwig Maximilian University of Munich*. http://citeseerx.ist.psu.edu/viewdoc/summary?doi=10.1.1.232.5350

[14] Lewis, G.N. and Spedding, F.H. (1933) *Physical Review*, **43**, 964. https://doi.org/10.1103/PhysRev.43.964

Journal of Modern Physics, 2020, 11, 803-853
https://www.scirp.org/journal/jmp
ISSN Online: 2153-120X
ISSN Print: 2153-1196

New Properties of HM16 Ether, with Submicroparticles as Self-Functional Cells Interacting through Percussion Forces, Establishing Nature of Electrical Charges, including Gravitation

Ioan Has[1], Simona Miclaus[1], Aurelian Has[2]

[1]Land Forces Academy "Nicolae Balcescu", Sibiu, Romania
[2]Independent Researcher, Rm. Valcea, Romania
Email: hasavo@yahoo.com, simo.miclaus@gmail.com, hasaurelian@yahoo.com

How to cite this paper: Has, I., Miclaus, S. and Has, A. (2020) New Properties of HM16 Ether, with Submicroparticles as Self-Functional Cells Interacting through Percussion Forces, Establishing Nature of Electrical Charges, including Gravitation. *Journal of Modern Physics*, **11**, 803-853.
https://doi.org/10.4236/jmp.2020.116052

Received: April 27, 2020
Accepted: May 31, 2020
Published: June 3, 2020

Abstract

Article continues and complements our previous articles on the HM16 ether (ETH) model. Here, we describe the mechanism of occurrence of the submicroparticle (SMP). A general hypothesis, HFVI, is introduced for the modalities of interaction between two SMPs, based on periodic mechanical percussion forces, produced by fundamental vibrations FVs. A mechanism for describing the interaction between a SMPs and the ETH is presented. Positive and negative particles are defined by their membrane types of movement, such as $+,-u/+,-v$ vibrations, and rotations at speeds $+\Omega/-\Omega$. The process of creating a pair of SMPs is discussed. Applying HFVI to the interaction between pairs of SMPs immobile in ETH, and considering longitudinal FVL, was obtained the forces of attraction/repulsion $+F_{L21}/-F_{L21}$, which correspond to the completed Coulomb force F_{CC} including gravitation. The resultant F_{RL21} will form an oriented field of forces, which is a quasielectric field *QE*, equivalent to actual *E* electric field. Considering transversal FVT, was obtained the vibratory forces $+,-F_{T21}$, whose resultant forms an vibrating field of forces, *QHs*, a quasimagnetic special field, which may explain some of the quantum properties of SMPs. Considering a mobile SMP, two new γ strains in ETH appear. Strains γ_L are created by the displacement of SMP with velocity *V*, whose force $+,-F_{T12}$ is the support of a component of the magnetic field *H* (quasimagnetic field *QH*), giving the QH_L component. Strains γ_{R} are created by the rotation of SMP with speed Ω, whose force $+,-F_{\mathrm{R12}}$ constitutes physical support of the component QH_R of magnetic field *H* (*i.e. QH*). The crea-

tion of a photon PH is modelled as a special ESMP containing two zones of opposed rotations, and a mechanism is presented for its movement in the ETH with speed c based on the HS hypothesis of screwing in ETH, with frequency ν.

Keywords

Nature of Electrical Charges, Submicroparticle Constitution, Microparticle Interaction by Percussions, Ether Model HM16 with Fundamental Vibrations, Completed Coulomb's Law, Photon Constitution and Travel

1. Composition of Submicroparticles in the Form of Complex Self-Functional Cells

The HM16 ether model, originally proposed by the present authors in 2016 [1], will be used as the starting point in this article for development regarding the composition, behaviour and effects of the ETH in nature, and particular in physics. We will use the abbreviations used in [1], and these will be redefined and completed here.

We use the following terminology: MP: microparticle, SMP: submicroparticle, SMPP: positive submicroparticle (rather than SMP^+), SMPN: negative submicroparticle (rather than SMP^-), ESMP: elementary or special submicroparticle, PH: photon, RF: reference frame, EC: base cells of the ether, PC: constituent cell of an SMP, EP: ether constituents (etherons α, β), and MB: material body.

We will also refer to neutral SMPs as SMPNEs. These include neutrons, and consist of SMPP and SMPN types, in pairs (**Figure 1**).

We denote the ether as ETH, with its customisation, the HM16 model, which contains the fundamental vibrations FV of the EC cells of free ETH. PV is used to denote the vibrations of PC cells inside any type of microparticle (MP). F_{CC} indicates the corrected/completed Coulomb electrical force, while F_C represents the classical electrical Coulomb force; F_N means Newton's classical gravitation force, and F_{DC} denotes the corrected electrical force between two electrical dipoles that actually constitute gravity [2] [3]. We use ε and γ to represent the specific/unitary linear and angular/tangential deformations (strains), while σ and τ represent the normal and tangential unitary forces (stresses), respectively.

It should be noted that in HM16, all types of MPs, including SMPs and ESMPs, have the composition of an SMP autonomous cell (SMPAC) at the internal organisational level, as they are complex and self-functional in a similar way to live organism cells (LOCs).

Although we present SMPs as having a simple spherical shape, they may also take on more complex forms such as cylinders, ellipsoids, stars, neurons, etc., since SMPs form the most complex existing body, the universe, which requires interconnectable foundation bricks of similar complexity (**Figure 1**).

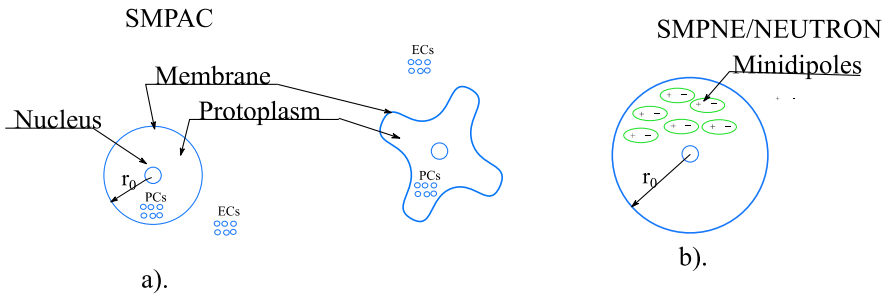

Figure 1. SMPAC shape model of SMPs. (a) SMPS spherical and neuronal types; (b) Neutron type.

This composition of the particles of all known existing matter mainly involves the make-up of all SMPs in nature, in the form of SMPACs, and we call this the hypothesis of cellular organisation (HCO) of SMPs.

In the HCO, SMPAC cells have well-known LOC substructures, including a nucleus (NC), protoplasm (PP), and a membrane (MM) (**Figure 1**). The MM is primarily responsible for protecting the integrity of the SMP and preserving its number of substructures, all having an ethereal nature. The role of the MM is to preserve its own energy E, and thus to ensure the functional maintenance of the SMP. The MM also determines the possible interaction, contact and association of SMP with other surrounding SMPs or MPs, and ensures permanent contact with the first row of ECs from free ETH, or even with basic etherons (ETs), so constituting the S surface of SMP, noted S/MM.

The MM is also responsible for facilitating exchanges of the etheronic material of ECs, energy (E) or information (INF) (related to energy) between SMPs or between MPs.

In the HCO, the PP constitutes the basic matter of the SMP, and is made up of PCs. However, these PCs are formed of ETs, which make up the internal cells of the PC. PP ensures lossless storage of the energy E_p of the SMP, and consists of permanent vibrations/vortices with rotation speed ω, of the internal PCs ethereal cells. The PP therefore directly participates in any changes or exchanges of energy, and even of ECs cells with external ETH, or with other SMPs, thus ensuring the functionality of the SMP.

The PP also has the primary role of preserving the SMP's mass m through the PCs it contains; this mass will need to be defined in the future.

In this model, the NC core is responsible for recording and storing the footprint (FP) of the SMP in terms of the nature of the information recorded internally in the NC. The NC stores and processes information exchanged with the ether and with the SMPs in the external environment. It also determines by commands the actions/reactions of the SMP and creates the reactions of the SMP to INF received from the outside, including specific reactions of attraction or rejection, as part of the process of interaction between the SMPP and SMPN (Sections 3, 4).

To achieve this, the NC core has a DNA composition in the same way as in an

LC cell, due to the formation of the SMP, which allows it to perform these smart functions.

It follows from the HCO that MPs, including SMPs, have the same behaviour or manifestations as LC entities, and are in a permanent state of vibration and movement, and therefore should not be regarded as inert or "dead" particles.

2. HFVI Hypothesis: Interaction between SMPs via Percussive Forces, Given by FVLs and FVTs

In our original 2016 paper on the HM16 ether model [1], we discussed the ability of MPs and SMPs to transmit FVs to the ETH around them, thus justifying interactions between SMPs in principle. Today, these interactions are considered to be electrical or gravitational forces, although the actual physical nature of these two interactions and forces and the concrete mechanism of interaction via mechanical forces acting between SMPs have not yet been explained.

In this article, we present and discuss in detail a new complex hypothesis called HFVI, which involves the fundamental vibration interactions and the mechanism for interaction between SMPs via the percussive forces created by the FVs of the ETH, permanently acting in the ETH, and between all SMPs.

2.1. General Framework for the Implementation of HFVI

We first admit the mechanical interactions unity principle (MIUP), according to which an interaction force F (here, F, p, p_s, σ, τ, etc.) and the accompanying deformation δ (here, Δx, u, v, u_s, v_s ε, γ, etc.) are inseparable, as a moment t_i in time, and as the point M_i of the interaction in space (ether). The presence of one of these parts logically implies the presence of the other part.

In HFVI, these interactions between SMPs via FVs occur exclusively through mechanical actions of periodic percussion forces $+,-p_p$, which act discretely at the SMP level. We consider here that the percussion forces $+,-p_p$ are the only real actions that are physically possible, both in the case of interactions between MBs in nature and interactions between SMPs in physics, including electromagnetism, atomic physics and quantum physics. We assume that any force F in physics or nature that is considered to be continuous, in fact is based on periodic percussion forces $+,-p_p$. These periodic percussion forces form the actual physical basis of quantum mechanical interactions.

It should be noted that this mechanism of percussion forces $+,-p_p$ that in HFVI explains the behaviour of SMPs and their interactions via FVs has not been confirmed on an experimental basis at the SMP scale; only laboratory-scale experiments have been carried out, and we rely on these here. This is the reason for the development in this paper of a physical mechanism of interaction at SMP scale through percussion forces $+,-p_p$, in the form of the HFVI hypothesis.

However, our HFVI can be initially confirmed by ensuring the functionality of the HM16 ether model based on the results of analyses of detailed interactions between SMPs, as discussed later in this article.

It should be noted that HFVI is not consistent with currently accepted concepts in mainstream physics, as it does not allow for the existence of the ether and instead assumes the validity of the SRT and GR. However, as we have previously demonstrated theoretically [4] [5] [6] [7] [8], these two theories are beautiful mathematical inventions that correctly describe the behaviour of SMPs at the macro scale, but do not describe the interactions at SPMs scale in a mechanical sense. This is similar to the situation created by Ptolemy's geocentric theory, which for many centuries was able to explain the movements of the planets on a large scale via the geometric contrivance of epicycles, but which ultimately proved to be inconsistent with observable astronomical reality.

Our hypothesis (HFVI) for the action of FVs arises from the actual behaviour of continuous elastic crystalline bodies (ECBs), which we propose are similar to our model of the type A ether, called HM16 [1]. These ECBs are found in daily life on a human scale in many forms, for example in natural rocks, manufactured metals, man-made buildings, industrial materials, etc.

In our previous paper [1], we postulated that the ETH is also a real natural elastic body with a special nature or composition and somewhat ideal properties, which are as yet unknown from direct study. These properties are known only indirectly from observations of the interactions between ETH and ordinary matter (still noted with OM). It follows that the mechanical behaviours and properties of these two bodies, the ETH and the ECB, can and must be common and similar.

2.2. Similarities between the Properties of Elastic Body ECB and the ETH

It is known from mechanics that an ECB will undergo relative displacements of its component particles through deformations of its shape, if it is acted on at one of its points M at some time t by a local instantaneous force on a small area, called a percussion force or simply percussion, p.

We will assume that these percussions are always periodic forces $p = +,-p_p$, if they act for a finite period of time on the ECB.

As a general rule, we will consider that the sign of any force F, including the percussion $+,-p_p$, will be positive (+/P) if it produces tension on the surface on which it acts and vice versa, *i.e.* a force will be negative (–/N) if it causes compression at that surface.

It is known that the percussion forces acting on an ECB can be of two types: normal forces on the surface on which they act, denoted here as $+,-p_n$ (with the related unit force or stress $+,-\sigma$) and tangential forces at the surface, denoted as $+,-p_t$ (with the related unit force or stress τ). Depending on the significance of the force, we can also use other notations and indices.

The deformations in the ECB created by a periodic force $+,-p_p$ will have the general forms known from mechanics: linear deformations u, created by p_n forces, and shear angular deformations v, created by p_t forces. These u and v deformations will create in the ECB specific deformations or strains, that are linear

(ε) and angular (γ), respectively, and these are also periodic.

These two types of deformations in the ECB environment (linear u/ε and angular v/γ) may occur in any combination, *i.e.* separately (u/ε or v/γ), or together. We assume in HFVI that in the special physical body of the ETH, a third combination is also possible over time, at any point in space.

A real situation in mechanics and nature that is similar to an SMP within the ETH is the spatial deformation of a body/environment caused by an explosion or shock/percussion at a point M inside a massive ECB. In this context, we can mention the explosion caused by a bomb or shell in the air, water or earth, the explosion of dynamite in a mountain to create a tunnel, or the more well-known and well-studied case of the onset of an earthquake in the rock of the earth's crust.

The way in which waves are transmitted in an ECB environment is very well illustrated by seismic waves, which appear and are transmitted through the earth's crust in all directions in spatial/spherical form, starting from a point called the hypocentre at which the earthquake originated. In this case, u-type longitudinal waves are also called principal waves (P), and the v-type transversal waves are called secondary waves (S); these are known to spread independently and with different propagation speeds, V_P and V_S, respectively, within the rock of the earth's crust [9].

Obviously, the similarity with the ECB/ETH system is only partial, since the two cases involve different phenomena; in the case of explosions or earthquakes, the short duration does not allow the static equilibrium steady state described in Section 2.3.2 (**Figure 3**) to be achieved, and energy transport will be present in the ECB. However, the deformations of types u and v are similar.

2.3. Mode of Functioning of SMPs in the ETH in HFVI

2.3.1. SMP Behaviour Exposing Deformations u_s and v_s Creating FVs in the ETH

1) Case of deformations u_s:

In HFVI, we postulate that the ETH is made up internally of individual ECs with bonds between them that are elastic at small deformations to form a continuous and infinite body, whose overall behaviour can be represented by the HM16 [1] model.

We consider the situation where an SMP1 is present at a point $M = O_1$ in the ETH at time t_0, whose outer surface/membrane S/MM we assume to be near spherical; the surface S is represented by the cell membrane MM in HCO.

For the purpose of positioning the physical elements in space, any point M_i in space is represented in HFVI using a Cartesian coordinate system Oxyz (**Figure 2**), with the origin fixed at a point O attached to an object/SMP, whose velocity V relative to the ETH is considered to be known. The orientation of the x, y, z axes is chosen based on the directions of symmetry of the crystalline structure of the ether, which we assume are known.

We also assume in HFVI that the surface S/MM exhibits normal/radial vibra-

tions $+,-u_s$ with frequency f_n. As a result, we assume that *S*/*MM* is the source of periodic normal deformations $+,-u$ in surrounding ETH.

But *S*/*MM* also rotates around the O*z* axis with rotational speed Ω (frequency f_t) (Figure 2). As a result, we assume that *S*/*MM* is the source of periodic tangential deformations $+,-v$ in surrounding ETH after the subsequent mechanism.

The vibrational deformations of SMP1, denoted by $+,-u_s$ (Figure 2), are considered to be normal at *S*/*MM*. They are therefore radial, with alternate expansion and contraction, and have the same spherical symmetry as the SMP1.

The $+,-u_s$ deformations at the *S*/*MM* surface of SMP1 will act directly on the first layer r_1 of the ECs in the ETH that are in contact with *S*/*MM* (Figure 2), producing equivalent deformations $+,-u$ in the ECs from the first row r_1 of the ETH cells. Obviously, at *S*, we have:

$$+,-u = +,-u_s \tag{1a}$$

Due to the direct contact and links between all ECs in the ETH, deformations $+,-u$ in row r_2 of the ECs will also occur, and then deformations in row 3 of the cells, and so on ad infinitum (Figure 2). These deformations $+,-u$ will be transmitted in the ETH from *S*/*MM* to infinity, creating longitudinal fundamental vibrations FVL. We note that $+,-u$ are not influenced by the rotational speed Ω of SMP.

2) Case of deformations v_s:

The rotations with speed Ω of the *S*/*MM* surface of SMP1 are considered to be circular (*i.e.* continuously rotating) around an axis O*z*, after the parallel circles of *S*, and produce in combination with $+,-u_s$, the equivalent/reactive tangential deformations in *S*/*MM* denoted by $+,-v_s$ according to the mechanism described below (Figure 2).

Thus, at the contact points between *S*/*MM* and the outer ETH in crystalline form, which in HM16 is assumed to be immobile, a series of periodic attachments and detachments will occur between *S*/*MM*, and the 1st layer of crystalline

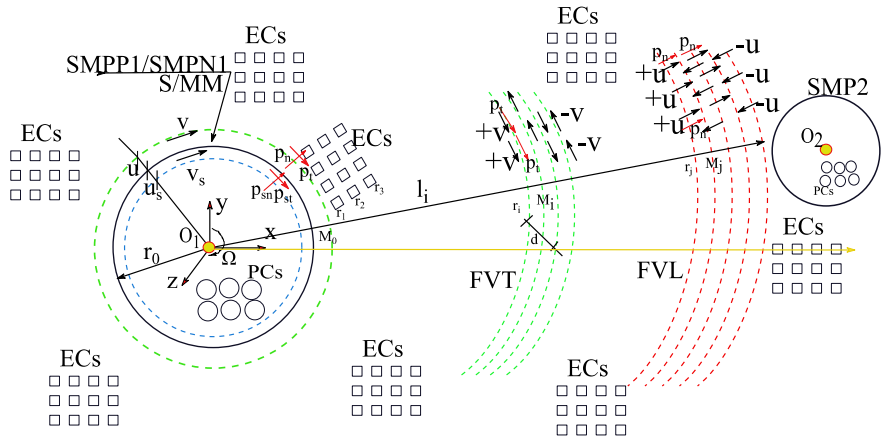

Figure 2. Simplified spherical model of an SMP showing the $+,-u_s$ and $+,-v_s$ vibrations at its surface and the $+,-u$ and $+,-v$ fundamental vibrations in the ether.

ECs, due to the periodic oscillatory of normal deformations $+,-u_s$ of *S*/*MM*; these have frequency f_n (T_n period) and are mechanically coupled with the rotation speed Ω of *S*/*MM* with frequency f_t (T_t period), will follow (Figure 2).

During the first time interval $\Delta t_a = T_n/2$, referred to here as the Active phase (PHA), viz. when SMP acts upon ETH, as long as the deformation by expansion $+u_s$ (of *S*/*MM*) lasts, an active attachment appears between SMP1 and ETH, and a tangential elastic clockwise deformation $+v$ is produced by SMP, in the first layers of the ECs in the ETH, due to the rotation of the SMPP with rotation speed +Ω. In PHA, the SMP is active and transmits an active tangential percussion p_{ta} to ETH together with a tangential deformation $+v$, involving mechanical active work:

$$L_1 = p_{ta} v \tag{1b}$$

As a reaction to the deformation $+v$, a tangential elastic deformation $-v_s$ will also appear counterclockwise in the first layers of the *S*/*MM*, where:

$$v_s = v \tag{1c}$$

In the following period $\Delta t_r = T_n/2$, referred to here as the Reactive phase (PHR), viz. when ETH acts upon SMP as long as the deformation by contraction $-u_s$ (of *S*/*MM*) lasts, a reactive deformation appears between SMP1 and ETH, and a tangential elastic counterclockwise deformation $-v$ is produced (as recovery of $+v$) in the first layers of the ECs in ETH, concomitant with the rotation of the SMPP with a period T_n (speed +Ω), (Figure 2). In PHR, the ETH is active, and transmits a reactive percussion p_{tr} to the SMP together with a deformation $-v$, involving mechanical active work:

$$L_2 = p_{tr} v \tag{1d}$$

Under stationary conditions of the couple SMP/ETH, the percussion forces will be equal, *i.e.* $p_{tr} = p_{ta}$, (Newton's 3rd law) and from (1b), (1c) and (1d), this results in a equality in the works done:

$$L_2 = L_1 \tag{2a}$$

Hence, no loss of energy occurs. The energy accumulated in ETH during PHA is entirely returned to the SMP in PHR.

We note that between PHA and PHR when manifests strong adherence between SMP/ETH, there may be a certain period of time Δt_s when adherence disappears, in which slipping occurs between them, without effort τ or deformation v, in order to allow for a free rotation speed +Ω of SMP.

The process of periodic transversal deformations $+,-v$ of ETH completed with Δt_s of slipping SMP/ETH, will be continuous, with normal T_n periods:

$$T_n = \Delta t_a + \Delta t_r + \Delta t_s \tag{2b}$$

According to Newton's third law and the MIUP principle from Section 2.1, any deformations $+,-v$ in the ECs from the first few rows (1, 2, 3, …) of the adjacent ETH will correspond to the pairs of deformations $+,-v_s$ from *S*/*MM* of the SMP (Figure 2(a)). But this $+,-v_s$ is only a partial deformation of *S*/*MM*, pro-

duced between slipping times Δt_s, when in a slipping time the rest of a complete rotation displacement v_{slip}, of S/MM sphere takes place by slipping.

We note that PHA/PHR phases in case of a SMPN are offset with $T_n/2$ compared to SMPP.

The frequency f_n of the PHA and PHR processes with period T_n from Equation (2a), and the size of the deformations $+,-v_s$ at the S/MM surface, must be a function of the nature of the contact surfaces, the speed of sliding between S/MM and the surrounding ECs, and of the rotation speed/frequency Ω (f_t) which are as yet unknown.

However, in the present analysis, it is not strictly necessary to know the sizes of these parameters, and it is sufficient to assume the existence of the deformations $+,-v$ in the ETH, which create FVTs. We will assume that $f_t/(\Omega)$ and f_n are correlated as whole multiples, depending of number of protuberances in the SMP (Figure 1), including the case where $f_n = f_t$, for a sphere. In the general case, the vibrations FVL and FVT will have a frequency of integer multiples between them, resulting in:

$$f_t = nf_n \quad \text{or} \quad T_n = nT_t \tag{3}$$

but in the following analyse we assume for simplicity $n = 1$, so $f_n = f_t$.

Hence, u_s and v_s type vibrations of SMP will result in periodic deformations $+,-u$ and $+,-v$ in the ETH. These deformations of longitudinal type u and transversal type v, will give rise to permanent vibrations of the ECs in ETH. These vibratory deformations $+,-u$ and $+,-v$, are referred to as FVs in HM16, since they are permanent in time and are uninterrupted by the vibratory deformations in the overall ETH, starting from each SMP1 and reaching or exceeding every existing SMP2 (Figure 2).

FVs may be of two types, corresponding to $+,-u$ and $+,-v$ deformations, and these are referred to as FVLs and FVTs, respectively. Also the lasts may be of two types, corresponding to P and N electric sign, as will follow.

2.3.2. Energy Equilibrium and Transmission

We now note that at any intermediate point M_i on the front surface of an FV wave (Figure 2), each active (initial, from PHA) percussion force p_p created by an active initial EC in the ETH will correspond a reactive (secondary, from PHR) force p'_p (Figure 3(a)).

These percussions p'_p will be created by the EC' located on the opposite side of the FV front of the vibratory wave, u and v and respectively, of FVL/FVT.

In a state of static equilibrium we have the equality:

$$p_p = p'_p \tag{4}$$

The situation for any string ST/l_i or line/path through the vibratory ECs in ETH with p_p/p'_p percussion pairs is shown in Figure 3(a).

A theoretical model of the ECs of the ETH is shown in Figure 3(b), in which these are represented by a string of harmonic oscillators of mass m, connected with elastic springs.

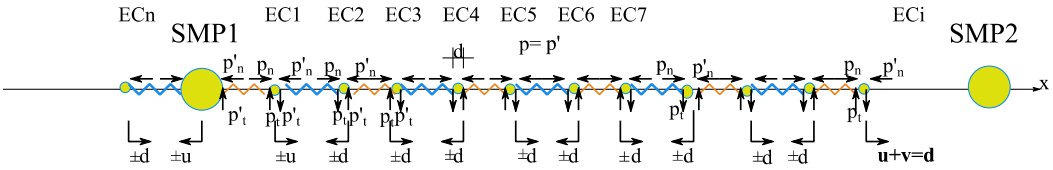

a). Situation of a series of ECs+SMP1 oscillators in ETH in permanent equilibrium of percutions p_n and p_t with **d** total deformation, without energy transport

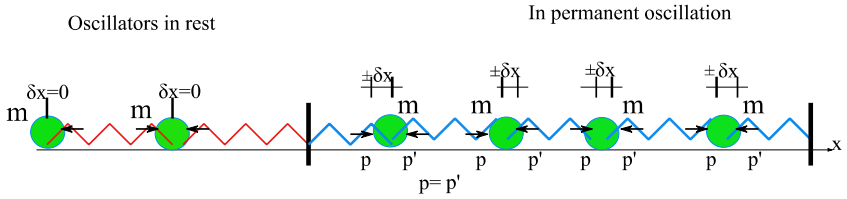

b). Situation of a series of harmonic oscillators from mechanics, in permanent equilibrium of force percutions p With δx deformation, without energy transport

Figure 3. Simplified mechanical model of FVs in a string of ECs in the ETH, without energy loss, as a series of harmonic oscillators.

We notice that the percussion force p_p can be transmitted between two SMPs, in a step-by-step manner via a direct string ST_0 of ECs arranged on a straight line O_1-O_2 between them, through the ETH (**Figure 2** and **Figure 3**), as well as via other less direct paths or strings, according to [8].

We admit in HFVI that at a time t_0 in the initial periods of the existence of SMP1, considered to be mobile with speed V_1, and of SMP2, which is mobile with a speed V_2, in the area/zone of influence (AI) of SMP1 (**Figure 2** and **Figure 3**), the p'_p reactive force will be less than the active force p_p when mechanical work L will be consumed during deformation with u or v (or with the resulting deformation d) of the ECs, due to the non-zero difference in forces $p_p - p'_p \neq 0$.

$$L = \left(p_p - p'_p\right) d = E \tag{5}$$

The mechanical work consumed, L, represents a transfer of energy E between the active cell EC and the reactive cell EC', and this process will eventually lead to an transfer of energy E between SMP1 and SMP2 along the l_i path or between SMP1 and the ETH ether in the AI, fulfilling the condition $p_p \neq p'_p$.

We note that this transfer of energy E can take place between SMP1 and SMP2 in any direction, along various indirect paths between them, l_i.

The energy E that corresponds to this mechanical work L will come from the potential energy U created by the percussion-type interaction forces p_p, which in fact represent the corrected Coulomb-type forces F_{CC} with which the SMP1 and SMP2 assembly (**Figure 2**) was originally endowed at the time t_0 of their creation or stabilization.

We will now consider the situation of the point M_i in the ETH at a later time $t_1 > t_0$, when a state of equilibrium between the active p_p percussion forces and the reactive p'_p force has been reached, thus fulfilling the condition $p'_p = p_p$ along the entire path l_i (**Figure 2** and **Figure 3**). As a result, at time t_1, no more mechanical work L will be consumed/developed at point M_i on the surface of FV' contact front, between p'_p and p_p. This is because the two values of the afferent mechanical work L and L' will be equal according to Equation (2a), due to the equality of the forces $p'_p = p_p$ and to the identical movements with u or v (or d) of their points of application.

This will occur when all ECs in the ETH in the area of any point M_i achieve a state of vibration with permanent FVs over time, via $+,-u$ and $+,-v$ deformations, the size of which has become permanent over time (**Figure 2** and **Figure 3**). This can occur when all SMPs in the area reach an immobile state, *i.e.* they have speed $V = 0$. In this way, the percussion forces will be stabilised at a constant value $p'_p = p_p$, shortly after they reach speed $V = 0$; however, the oscillation deformation $+,-u$ and $+,-v$ of the ECs remain non-zero and are preserved.

Since the ETH has ideal properties, without friction or other forms of energy loss, there will be no further remote transmission/transfer of energy E between SMP1 and SMP2 in the situation where $p'_p = p_p$ (**Figure 3**).

In the case of static and dynamic equilibrium between the specific percussion forces $+,-p_n$ and $+,-p_t$ (**Figure 2** and **Figure 3**), no energy transmission from SMP1 to SMP2 occurs via the ECs of ETH. The initial/stabilised energy of SMP1 will be preserved, although the particle will continue to transmit FVLs and FVTs continuously over time. However, these FVs will no longer absorb energy from SMP_0, meaning that they will no longer transmit energy through the ETH during operation under these conditions for SMPs that are immobile and have reached static and energy equilibrium.

This is because in the case of static equilibrium, the specific percussion forces $+,-p_n$ and $+,-p_t$, will act symmetrically both ways at their contact point M_i. As a result, an energy balance situation is reached in the ETH in the AI zone (**Figure 2** and **Figure 3**).

The majority of the ETH in nature is in this situation of energy equilibrium, in AI areas, free from SMPs or far from any SMP moving at a speed $V \neq 0$.

The physical matter in the universe, consisting of SMPs, is only in this state of energy balance and static equilibrium between percussion forces p_p, if these SMPs are in a motionless state so with $V = 0$, or at a finite time interval, after the creation of these SMPs (if created).

This results in the case discussed in this Section above, where an energy E/L balance can be achieved under certain conditions in the process of emission/reception of FVs by an SMP1. These FVs can be continuously emitted over an indefinite time by any SMP1 in equilibrium, without consuming the SMP1's own energy. We can therefore conclude the following:

1) We are justified in assuming in the HFVI that in the ETH, within an energy balance AI zone, due to the creation at a given point M on S/MM surface, of pe-

riodic spherical forces (balloon type) of normal $+/-p_{sn}$ percussions of tensile/compression $+/-\sigma$ type, a series of linear $+/-u/\varepsilon$ deformations, will be created throughout the surrounding ETH. And that these $+,-u$ are transmitted in the form of longitudinal spherical vibrations (FVLs) that are permanent over time, at energy equilibrium (Figure 2).

2) In the event of the appearance of periodic transversal/circular $+/-p_{st}$ percussion forces of the $+,-\tau_s$ shear type at point M on a spherical surface S/MM with vibration/rotation axis O_1z, periodic transversal/angular deformations $+,-v/\gamma$ will be created throughout the ETH, which shall be transmitted in the form of transversal spherical FVT vibrations, permanent over time, at energy equilibrium (Figure 2).

However, we admit that the vibratory deformations $+,-u$ and $+,-v$ in ETH can be transmitted by any SMP1 via periodic $+,-p_p$ percussion forces, from one EC to another in the form of a cell string (CS_i) (Figure 2 and Figure 3), and deformations occur in the form of FVL and FVT vibrations.

We do not currently have concrete data on the sizes of the propagation velocities c_{fL} and c_{fT} of the FVLs and FVTs, respectively, or on the sizes of their frequencies, f_{fL} and f_{fT}, however, these are not strictly necessary in our current analysis.

2.4. Physical Nature of electrical Charges Due to PVP/PVN Vibrations of SMPs in HFVI

Based on experience, we can assume in HFVI that SMPs must be differentiated firstly in terms of their electrical aspect, currently considered in physics to be given by an electrical charge $+q/-q$ that is intimately attached to an SMP, although this $+q/-q$ charge has not been defined physically, as substance.

This electrical aspect of SMPs is physically manifested in specific ways that can be distinguished in experiments, *i.e.* SMPP and SMPN (denoted in [1] as SMP^+ and SMP^-, respectively).

We also assume the existence of neutral SMPNEs, including neutrons, but we admit that these are also composed of particles of types SMPP and SMPN. Inside an SMPNE, these SMPPs and SMPNs are grouped into neutral minidipoles (MDs) with zero electrical charge (Figure 1(b)), resulting in a total electrical charge of zero.

We can verify this structure of the SMPNE neutron. For this, we assume that a neutron has a diameter 10 times as large as an electron/positron. It therefore comprises approximately 10^3 such MDs, consisting of electron/positron doublets (whose arm b is about 10 times smaller than for atomic dipoles) (Figure 1(b)). The mass of a neutron results about 2×10^3 times the mass of an electron m_e, as the currently accepted mass of the proton/neutron is close to $1840m_e$. Hence, electron/positron doublets within the neutron represent an organised accumulation of highly compacted MD doublets, which in the presence of an adequate energy input ΔE can release an electron or positron; when a single electron is released, the neutron becomes a proton. A proton has the same composition as a

neutron, but possesses an extra positron (or equivalently, lacks an electron).

This electrical differentiation of the observable, external manifestation of SMPPs and SMPNs, must originate in the specific internal modes of vibration of the internal PCs, from the PVs of the PR protoplasm, including the vibration/rotation mode with rotation speed ω of the PCs, which constitutes the external membrane MM. These PCs are also particles of an ethereal nature but have their own composition that is different from ECs; this is likely to incorporate a large number of ECs, actually constituting a series of quark-type SSMPs.

Thus, we postulate in HFVI that there will be a system of internal vibration/rotation PVs of PCs in the positive SMPP, denoted as PVP (particle vibration positive); an internal vibration system for SMPN PCs, denoted as PVN; and for SMPNEs, denoted as PVNE.

Next, we assume that the primary difference between vibration modes, PVP and PVN, of SMPs lies in the sense of the rotation of the S/MM surface/membrane with the rotation speed $+/-\Omega$ around the Oz axis (**Figure 2**).

We assign the clockwise sense ($+\Omega$) of rotation around the Oz axis to the rotation mode of the PC from the MM of the SMP denoted by PVP, and the anti-clockwise rotation direction ($-\Omega$) for the rotation mode of the PC cell from the MM of SMP, denoted by PVN.

The PVP and PVN modes arise on the outside S/MM rotations $+/-\Omega$, of the SMP superposed with the $+,-p_{sn}$ and $+,-p_{st}$ percussions, which are associated to the deformations $+,-u_s$ and $+,-v_s$ on the outer surface S of the SMP (*i.e.* the *MM*). And then PVP/PVN modes, manifest through the percussions $+,-p_n$ and $+,-p_t$ associated to deformations $+,-u$ and $+,-v$ of ETH cells ECs, as discussed in Sections 2.6 and 4.

The $+,-u$ and $+,-v$ deformations in ETH will give rise to the FVs of the ECs of the ETH external to SMP1. The two types of particle, SMPP and SMPN, will appear on the outside ETH, by their specific FVs, and are differentiated based on the effect that is referred to today as electric, but in reality arises from the specific FVs created in the ETH (**Figure 2**).

In the following, we will denote the FVLs/FVTs produced by the positive particles (+/P) SMPP as FVLP/FVTP, respectively; we will denote the FVLs/FVTs produced by negative particles (−/N) SMPN as FVLN/FVTN, and the vibrations of neutral particles as FVLNE/FVTNE.

2.5. Creation of a Pair of SMPs

In order to obtain information on how to differentiate between the vibrations produced by SMPPs and SMPNs, we can analyse the initial phase of creation of these SMPs according to HFVI.

We assume that the creation of SMPPs and SMPNs is a phenomenon similar to the creation of electron/positron pairs by hard electromagnetic (E-M) γ waves. We assume that the starting point for the creation of SMPs is at the origin O of a Cartesian RF Oxyz that is fixed in the ETH (**Figure 4**).

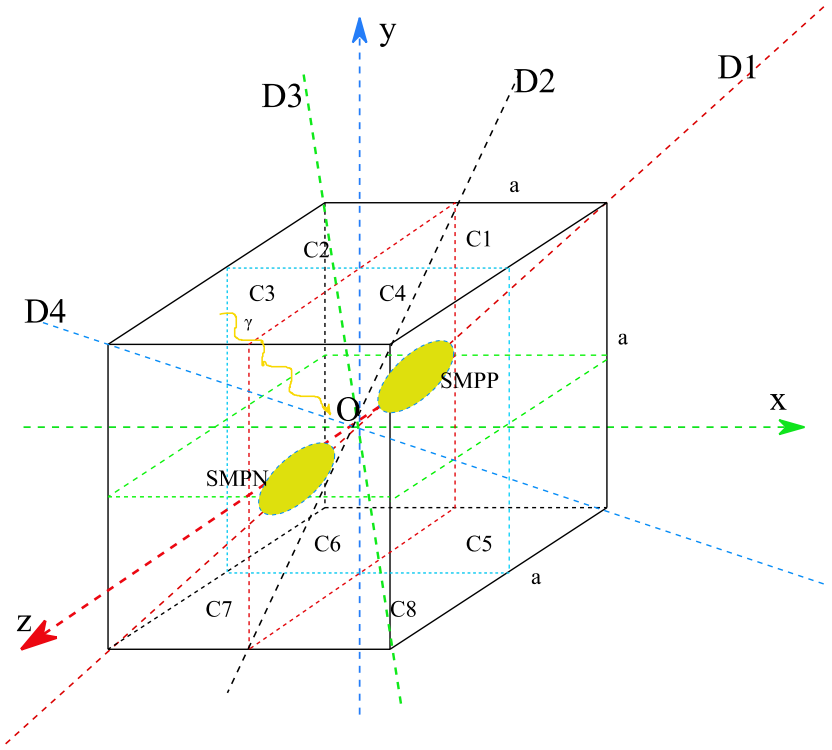

Figure 4. The Oxyz reference frame at the centre of a cube with sides a, diagonals D_1 - D_4, and quadrants C_1 - C_8 at the time of creation of an SMPP/SMPN pair.

Immediately after its creation, the SMPP will be located in the C_1 quadrant of RF, and the SMPN will simultaneously be located symmetrically from the origin O, along the D_1 diagonal of the RF, meaning that it is in quadrant C_7 (**Figure 4**). The SMPP and SMPN are shown here in a simplified form, immediately after their creation, by two ellipsoids aligned along diagonal D_1.

Let us now look at the likely deployment of the creation of the two particles, SMPP and SMPN, by a PH photon with total energy E_{ph} of the radiation γ order and with size smaller than an SMP, but of the same order of magnitude.

Initially, at point O, within an area close to an MPP/MPN pair of microparticles (not shown), the photon PH begins to develop spatially within the ETH. PH will release its E_{ph} energy into the ETH, and as a result, a series of vortices (VOs) will occur in ETH, comprising the first ECs within the surrounding ETH. These ECs cells will become groups of particle cells (GPCs), and will also take up an amount ΔE of the energy E_{ph}.

This group of VOs undergoes rapid expansion over the neighbouring ETH, initially creating an expanding bubble BU_0 around PH made up of all the newly formed VOs, grouped into new GPCs. However, within a short period, BU_0 will tend to divide to give two new SMPs. Thus, BU_0 becomes elongated in the direction of the diagonal D_i of the O*xyz* reference frame (**Figure 4**). In the opposite quadrants C_1 and C_7, two ellipsoids EL_1 and EL_2 emerge from BU_0; these are at first united by a thick common area that rapidly thins, and towards the end forms a connecting cord CO_0 (**Figure 4**). This cord rapidly thins, becoming a

single CS string of ECs, and finally breaks completely.

Thus, in the two quadrants I and VII, the two SMPP and SMPN are formed from EL_1 and EL_2, due to which we can admit that there is a differentiation in the shape of the two spherical/symmetrical surfaces *S*, given by the last stage of the CO_0 break. A flaring will arises in the SMPP remaining from CO_0, and in the SMPN, a deepening produced by CO_0 will arise; however, these differentiations are equivalent as volume of ether and these differentiations makes sense to exist.

These differentiations between the SMPP and SMPPN arise from the start of their formation as embryo ELs as new autonomous SMPAC cells (Section 1), when a nucleus NC structure was created for the positive (DNAP) and negative (DNAN) particle types. Due to their specific ADNs, these NCs are differentiated based on their future electrical charge-type behaviours, resulting in the positive SMPP and the negative SMPN, as described in Section 2.4.

We also postulate in HFVI that during the formation and growth of the original two ELs, an equilibrium is created between the volume of ECs cells embedded in any EL and the number of CEs taken from the ETH, meaning that there is no change in the volume of the ETH in the BU_0 zone from the creation of the SMPP and SMPN, and no change in the natural pressure of the ETH in the area.

We postulate in HFVI that at the time of breaking of the cord CO_0, it is in a state of tension ($+\sigma$) that opposes the break-up of the SMPP and SMPN. We also assume that within both the CO_0 cord and the ELs, and also in the new SMPP and SMPN, internal rotations/vortices PV of the particles, with rotation speed ω, arise to maintain the energy reserve E of PH, in similar way to other SMPs. This energy reserve E allows for the creation and distancing of the two particles, SMPP and SMPN, with a certain initial speed V_0. After reaching an equilibrium speed V_{eq}, or $V = 0$, the SMPP/SMPN system will possess a potential energy U that is equivalent to the kinetic energy E_{kin} at the initial time of expulsion of the particles; this energy ensures normal operating conditions for the system in the ETH.

At a later time, the two particles, SMPP and SMPN, will be able to approach again, and will tend to reunite to give the original form of the photon PH through the annihilation process (the inverse of the process described above in this Section). The proximity needed for this reunion can be achieved by an interaction force $+F_L$ from the attraction between the SMPP and SMPN, produced by periodic percussions $+,-p_p$ that are created by each particle in the ETH by FVLs (as discussed in Section 3).

The force $+F_L$ will also arise as described in Section 1, for SMPAC and HCO, through the specific attraction orders provided by the NCs of the SMPP and SMPN. In addition, $+,-p_p$ percussions are generated from the FVLs created by each type of SMP: FVLP or FVLN, depending on the electrical sign (+/P or −/N) of the SMP respectively.

When a SMPP and SMPN pair regroups (**Figure 4**), a new CO_0 cord will be created between them, representing an initial CO_0 reproduction; this will initial-

ly consist of a CS_0 string of ECs, and will regain its initial stretching effort $(+\sigma)$, created by permanent percussions $+,-p_p$, each of which exerts a reciprocal force of attraction $+F_L$ between SMPP and SMPN, as described in Section 3.

However, when grouping a pair of two identic signs SMPs, a new CO_0 cord will be created between the two particles. This will also now gain a compression effort created by permanent percussions $+,-p_p$ $(-\sigma)$, thereby exerting a mutual force of rejection $-F_L$ between the two particle, which both have the same electrical nature, as they have the same sign, as discussed in Section 2.4. This physical manifestation is confirmed by the presence of Coulomb-type forces, with the charges $+q$ and $+q$ from electrostatics.

A more detailed mechanism for the process of interaction between SMPs via forces F_L, based on percussion forces $+,-p_p$, will be presented in Section 3.

We note that this mode of interaction between two SMPs is also supported by the fact that it corresponds to a manifestation in the ETH of the dialectical principle of attraction of the opposites. This principle is also found in nature in the process of reproduction of living beings (and also in inanimate world in some situations), for example the attraction between different sexes; this is spontaneous and natural, since most animals can reproduce only by combining two types of DNA. The reverse of this principle, manifested by the natural revulsion between identical sexes, which have only one type of DNA, also holds true, and this is also manifested in the case of SMPs, as described above.

2.6. Specific Action Modes of SMPP/SMPN on ETH, for Creating the four Types of FVs

1) SMPP with FVLP:

We postulate in HFVI that an SMPP which produces FVLs, is in a permanent state of energy balance with the external ETH, as discussed in Section 2.3.2

Then, radial/linear deformations $+,-u_s$ at its S/MM surface, with spherical symmetry, starts at some time t_0, through a positive dilation $+u_s$ that corresponds to an increase in radius r_0, and this gives rise to an expulsion of a volume of ETH corresponding to $+u_s$ (mechanism is presented in Section 3.). This initial dilation $+u_s$ will be followed by a contraction $-u_s$ in S/MM, so that an absorption of the ETH corresponding to $-u_s$ is produced (**Figure 2**). A new cycle will follow over a period T_L of dilation/contraction of S/MM with $+,-u_s$ deformations with frequency f_L, etc.

Thus, the total variation in the radius r_0 of the SMPP over one complete vibration will be $+,-u_s$ of amplitude $1/2u_s$, which corresponds to an average expulsion of ETH of $+1/2u_s$. The maximum deformations $+,-u_s$ will be periodic, and thus vibratory, giving rise in ETH to FVLPs with frequency f_L or period T_L.

This is the specific manifestation of SMPP considering the creation in ETH of $+,-u$ deformations with spherical symmetry, which will produce FVLPs in whole ETH.

2) SMPN with FVLN:

We also postulate in HFVI that in the case of an SMPN, which produces FVLs, the phenomenon is symmetrical to the case described in point **1)** for the SMPP, including spherical symmetry of deformations, as shown in Figure 2. At the initial time t_0, there will be an initial contraction deformation of size $-u_s$, at the surface S/MM, corresponding to the negative direction of the radius vector r_0, and hence also an initial absorption of a volume of ETH corresponding to $-u_s$, thus offsetting the deformation $+u_s$ for the SMPP from point **1)**. This initial contraction will be followed by a dilation/growth of r_0 on S/MM with $+u_s$. A new cycle of contraction/dilation of r_0 on S will follow with $+,-u_s$ deformations etc. (Figure 2). Thus, the total variation in the radius r_0 of the SMPN in a complete vibration with frequency f_L will be $-u_s$, with amplitude $1/2u_s$, corresponding to an average absorption of $-1/2u_s$ of ETH and maximum deformation $-,+u_s$, giving rise in ETH to FVLNs with frequency f_L or period T_L.

This is the specific manifestation of SMPN considering the creation in ETH, of $+,-u$ deformations with spherical symmetry, which will produce FVLNs in whole ETH

But this contraction of $-u_s$ in r_0 in the SMPN, occurs exactly during the period of dilation by $+u_s$ from the corresponding SMPP (Figure 2). The two deformations $+u_s$ and $-u_s$ in the SMPP and SMPN are therefore in phase opposition, and the expulsion of ETH by the SMPP corresponds in time to the absorption of ETH by SMPN.

After each period T_L, because the directions of deformation $+,-u_s$ are opposed $-,+u_s$, thus preserving the volume of the ETH, by ensuring a null variation in its volume ($\Delta V_{ol} = 0$), thus maintaining constant the volume of ETH in the space around the SMPP and SMPN pair (Figure 2). This is similar to the phenomenon of liquid compensation between two interconnecting vessels, and can explain the observation in electrostatics of the cancellation of the total charge around two charges $+q$ and $-q$ that are close one to another. This is also the specific way in which an electric DI dipole is manifested through FVL.

3) SMPP with FVTP:

We also postulate in HFVI the case of an SMPP having the rotation speed $+\Omega$, which will be the source of FVTP produced by ETH deformations $+,-v$.

But deformations $+,-v$ will be created by equivalent tangential/transversal deformations $+,-v_s$ in its S/MM surface, with cylindrical symmetry around the Oz axis. These equivalent deformations $+,-v_s$, are special, being even those which, if there were real, would create in the ETH the vibrations deformations $+,-v$, with $v_s = v$.

These equivalent deformations $+,-v_s$ are due to rotation speed $+\Omega$ of SMPP, produced by successive adhesion and sliding between S/MM and the adjacent ECs in ETH, according to the mechanism mentioned in Section 2.4 and described in Section 4. More formally, the deformations $+,-v_s$ correspond to alternating partial rotations of S/MM around its own axis Oz, starting at a given time t_0 (Figure 2). These equivalent deformations in the SMPP are periodic with fre-

quency f_t (or rotation speed $+\Omega$) around the Oz axis of the SMP, or period T_t.

In the case of the SMPP, we assume that the initial equivalent tangential deformation at t_0 is $+v_s$, a clockwise rotation (denoted here as positive), followed by a counterclockwise rotation $-v_s$, then by a rotation $+v_s$, and so on (Figure 2). All rotation deformations $+,-v_s$, have the frequency f_t or period T_t and involve oscillating rotation of the radius r_0 of the SMPP around the Oz axis.

This is the specific manifestation of SMPP considering the creation in ETH of tangential $+,-v$ deformations with cylindrical symmetry around the Oz axis, which will produce FVTPs in whole ETH as at point 5).

4) SMPN with FVTN:

In the case of the SMPN, which produces FVTNs, we assume that the initial rotation equivalent deformation is $-v_s$ counterclockwise (negative), followed by a clockwise rotation $+v_s$, then by a rotation $-v_s$, and so on, with cylindrical symmetry around the Oz axis. All rotations have frequency f_t and involve deformations $-v_s$ corresponding to a counterclockwise rotation of the radius r_0 of the SMPN around the Oz axis, giving rise to vibrations (Figure 2). These deformations $-,+v_s$ are actually periodic grips/slips between S/MM and the ETH (similar to the fault slippages that create transversal waves in earthquakes).

This is the specific manifestation of SMPN considering the creation in ETH of $-,+v$ deformations with cylindrical symmetry around the Oz axis, which will produce FVTNs in whole ETH, as at point 5).

Therefore here we postulate in HFVI that these tangential equivalent deformations at time t_0 (*i.e.* the first $+v_s$ in the SMPP and the first $-v_s$ in the SMPN) are in opposition (*i.e.* out of phase) in terms of the sense of rotation (Figure 2). This opposition between the senses of rotation $+v_s$ and $-v_s$ creates compensation (constancy) between the kinetic moments J of the SMPP and SMPN pair, starting at the moment t_0 of their creation. There is then no need to transfer the kinetic moment J, according to Newton's third law, to the ETH external from the SMPP and SMPN pair, as the mechanism described above and in Sec. 4 is in effect. At the same time, the change in volume of the ETH due to $+,-\gamma$ will be compensated.

5) Consequences of ETH deformations produced by SMPs:

We also postulate in HFVI that these periodic deformations $+,-u_s$ and $+,-v_s$, which produce at frequencies f_L, f_T, on the surface S/MM of the SMP, will be immediately transmitted to the surrounding ETH in the form of periodic external deformations $+,-u$ and $+,-v$ (Figure 2). These produce FVLs and FVTs in the ETH, respectively, due to the mechanism discussed above, and in Sections 2.4, 3 and 4, respectively.

We also assume in HFVI that these periodic deformations $+,-u_s$ and $+,-v_s$ in the surface of an SMP, as well as the deformations $+,-u$ and $+,-v$ in the ETH, are deformations/displacements with minimum intrinsic/predetermined size in both SMPs and ECs, and represent the minimum steps or displacements Δx in quantum mechanics.

3. Application of HFVI to the Interaction between Immovable SMPs in the Case of FVLs

3.1. Interaction between Two Positive Immovable SMPPs through FVLs

1) General conditions of SMPPs:

In some SMPPs, vibrational deformations $+,-u_s$ will appear on the surface S, and physically on the membrane MM, as explained in Section 2.6.(a) (**Figure 2**). These radial deformations $+,-u_s$ are spherically distributed on S/MM, and are completely symmetrical to a point.

Figure 5(a) shows a section through a pair of particles SMPP1 and SMPP2 that are fixed in the O_1xyz reference frame attached to SMPP1, which is considered immovable in the ETH.

Figure 5(a) also shows the vibratory deformation vectors $+,-u_s$ (radial) for SMPP1 and the S/MM surface/membrane of SMPP2 (the first with size $+u_s$ and the remainder with size $-,+u_s$) and the vibratory deformation vectors $+,-u$ (radial) of the first row of ECs r_1 in the ETH adjacent to the surfaces of the SMPPs. The vibratory deformations FVLs are created by $+,-u_s$ acting on the surface S/MM of the SMPP through percussion forces $+,-p_s$ from SMPP on the ECs adjacent to the surface S/MM in the ETH, as described in Sections 2.3.1, 2.4, 2.6, and illustrated in **Figure 2**.

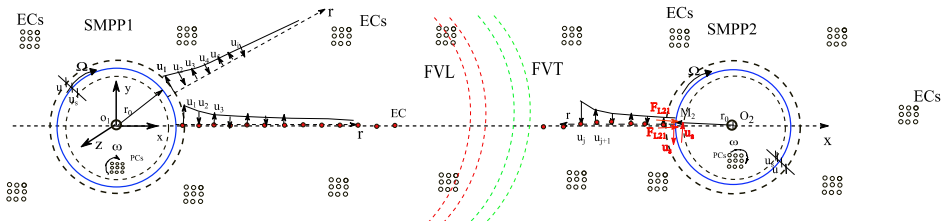

a). Situation of SMPP1/SMPP2 with deformation u, u_s and normal forces F_{L21}

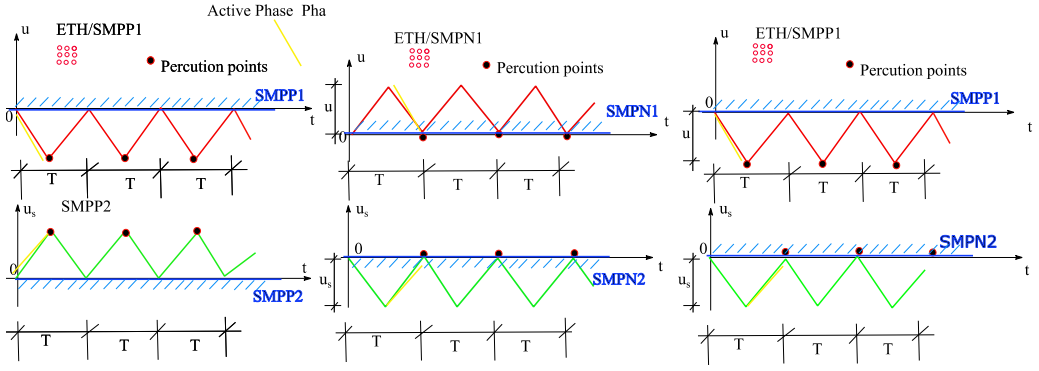

b). Grafic of u deformations in time t and percution points upon SMPP2 from SMPP1 giving F repulsion forces

c). Grafic of u deformations in time t and percution points upon SMPN2 from SMPN1 giving F repulsion forces

d). Grafic of u deformations in time t and percution points upon SMPN2 from SMPP1 giving F attraction forces

Figure 5. Physical mechanism of the interaction via percussions $+,-p_p$, and the evolution of attached deformations u over time, between pairs of SMPs through their FVLs in the ETH.

The deformations $+,-u$ in the ETH are spherically propagated, since they are completely symmetrical to a point, in all space. The vibratory deformations $+,-u$ induced in the rest of the ETH will be permanently accompanied by related periodic percussions $-,+p_p$ (on a single EC) arising from SMPP. We consider that the dilation deformations $+u_s$ correspond to the percussion forces $-p_p$ in the ETH, since compression is denoted as negative, and vice versa: the deformations $-u_s$ correspond to $+p_p$, *i.e.* tensile forces.

The first deformations $+,-u$ are then transmitted, starting from each SMP, step by step via adjacency/contact, in the form of continuous strings (STs) of ECs, and will reach through the other ECs via the surrounding ETH, including from SMPP1 to SMPP2. However, the sizes of these deformations $+,-u$ will be reduced with increasing distance r (**Figure 5(a)**) corresponding to a variation $1/r^2$ in a similar way to Coulomb's law (as described in Section 6 of [8]).

For clarity, the vibratory deformations $+,-u$ in the rest of the ETH at various distances r are represented by 90˚ folds perpendicular to the direction of the ray r by tangent arrows of appropriate size, starting from the surface S of SMPP1 and SMPP2 (**Figure 5(a)**)

Figure 5(a) shows several fronts of action of the vibratory deformations u, which are represented as portions of large dotted circles (red for FVLs from an SMPP), as fundamental spherical FVL waves, in the ether ETH, (symbolically represented by rare squares/circles groups, although ECs must in fact be adjacent). Here, we analyse only the direct interaction between SMPPs through a single linear, direct string ST_0 (the central one) of ECs cells of radius r_{00} (**Figure 5(a)**).

The indirect interaction between two SMPPs via multiple strings ST_i, in the form of a series of progressive curves, and the effect of these strings/paths that create the corrected Coulomb force F_{CC} as a result, were analysed in [1].

2) Action on SMPP2:

We will first analyse the case in which the forces produced by SMPP1 in M_2, the central point on the surface/membrane S/MM of SMPP2, are oriented towards SMPP1 (**Figure 5(a)**). Periodic linear/longitudinal (here, radial) deformations $+,-u$, the first with size $+u$, and the remainder with size $-,+u$ (associated with $-,+p_n$ from SMPP1) near SMPP2, as well as the deformations $+,-u_s$ in SMPP2 (associated with $-,+p_n$ from SMPP2) permanently act on the surface S/MM of SMPP2, and are shown as dependent on the time t in the detail in **Figure 5(b)** by a periodic zigzag line (ZL), with a regular period of variation $T = T_L$, starting from $t_0 = 0$.

Although the correct real ZL allure may be different from that shown in **Figure 5(b)** (for example a periodically interrupted curve, lines with different slopes, or even a sinusoid), this detail is not significant in the current analysis.

When the vibratory deformations $+,-u$ from SMPP1 reach point M_2 on SMPP2 at time t_0 (**Figure 5(a)**), we postulate that the phase of the vibration $+u$ from FVLP from SMPP1 is the same phase as the vibration $+u_s$ of PVP from SMPP2. In fact, the FVLPs arrive with the same phase at all SMPPs in the ETH,

due to the theoretically ideal properties of the HM16 ETH, while also respecting the situation of the phases, since the moment of creation of the two SMPs described in Sections 2.4, 2. 5.

We will analyse the action of SMPP1 on SMPP2 through FVLs, under the general conditions for the behaviour of SMPs in HFVI, described in Sections 2.3.1., 2.6.

At the central point M_2 on the surface S/MM of SMPP2 facing SMPP1 (**Figure 5(a)** and **Figure 5(b)**) we observe that at time $t_0 = 0$, the first deformations $+u$ of the ECs in the adjacent ETH, originating in SMPP1 become $-u$ (due to the reversal of the direction of the $+u$ axis) when applied to SMPP2.

It follows that the deformations $+,-u$ in ETH, which have become $-,+u$ (**Figure 5(b)**), now have the opposite orientation to the $+,-u_s$ deformations in the PC cells in SMPP2, although they have the same phase. The peak points P_i of the ZL curve of the periodic $-,+u$ deformations in ETH at various time intervals T, where the percussion forces $-p_n$ are focused, (on a single EC, as part of PHA active phase, from Sections 2.3.1., 2.4), will be directly opposite to the peak points P_i of the ZL curve of the $+,-u_s$ deformations in SMPP2 (**Figure 5(b)**). The compressive/active percussion forces $-p_n$ are concentrated at these contact points P_i having opposed senses, so giving repulsion force (**Figure 5(b)**).

In this case, in point M_2 on the surface of SMPP2, in the area of a single EC, normal/linear compression percussion forces $-p_n$ (negative $-\sigma$ compression effort), will occur, *i.e.* the repulsion of SMPP2 from SMPP1.

Hence, on the elementary surface S_s (a circle with radius r_{00}) corresponding to the central string ST_0 of ECs, at point M_2 located on the surface S/MM of SMPP2, a continuous $-\underline{p_n}$ (underlined) repulsive force will appear as an average over a time T of the periodic percussion forces $-p_n$. This periodic force of repulsion upon SMPP2 due to SMPP1, denoted as $-F_{L21}$, is created by periodic percussions $-p_n$, based on their average effort $-\sigma$, on the elementary surface S_s of an EC:

$$-F_{L21} = -p_n = S_s(-\sigma) \tag{6}$$

This repelling force $-F_{L21}$ corresponds to the direction/line O_1-O_2 of direct interaction between SMPP1 and SMPP2 through ST_0 of line l_0 (**Figure 5(a)**).

From **Figure 5(a)** and **Figure 5(b)**, the nature of $-F_{21}$ (on a single EC) is obvious; this is a mechanical force derived from the compressive percussion forces $-p_n$ through their average $-\sigma$ compression efforts, over the area S_s of an EC, according to the mechanism discussed above and illustrated in **Figure 5(b)**. At the same time, it can be seen from **Figure 5(a)** that the force $-F_{L21}$ corresponds to the Coulomb force of repulsion F_C between two positive charges, $+q/+q$, and that the force $-F_{L21}$ must vary as $1/r^2$ in the same way as F_C at relatively short distances.

$$-F_{L21} = f\left(r_0, r_{00}, p_n, \frac{1}{r^2}\right) \tag{7}$$

The full form of the function f in Equation (7) can be established in future on

an experimental basis depending on the geometry of the SMPs (radius r_0) and the ECs (radius r_{00}).

Note 3.1: This correlation between the periodic deformations $-,+u$ of SMPP2 and SMPP1 giving repulsion force $-F_{L21}$, (on a single EC) is also ensured according to the mechanism described in Section 1 for SMPAC and HCO, through the specific rejection commands provided by the NCs of SMPP1 and SMPP2

Note 3.2: This correlation between the periodic deformations $-,+u$ of SMPP2 and $+,-u$ of SMPP1 giving repulsion force, is also ensured according to the mechanism described in Section 2.3.1., where the percussion forces $-p_n$ are focused, as part of superposition of two PHA active phases, having opposed senses, so giving repulsion force.

Note 3.3: We postulate in HFVI that the action at the level of an EC cell of the percussions $-p_n$ and the equivalent force $-F_{L21}$ (on a single EC) in Equation (7) represent forces of intrinsic minimum/predetermined size for the SMPs and ETH, which are exactly same as the minimum forces of action ΔF in quantum mechanics.

Summary 3.1: We postulate in HFVI that the vibratory deformations $+,-u_s$ at the surface S/MM of SMPP1 create VFL vibrations in the ETH with deformations $+,-u$ and associated periodic percussion forces $+,-p_n$, (on a single EC) which act upon SMPP2 over the area S_s of ST_0, the central string (**Figure 5(a)**). These deformations $+,-u$ overlap at the maximum points of contact P_i with the deformations $+,-u_s$ at the surface S of SMPP2. The deformations $+,-u$ and $+,-u_s$ have opposite phases in terms of their physical direction, belonging to PHA of Section 3.2 (**Figure 5(b)**). Hence, at the overlapping points, percussion forces $-p_n$ will be created with the same sign, where $-p_n$ represents compression forces, and thus SMPP2 is repelled by SMPP1 (**Figure 5(b)**). As a result, periodic percussion forces $-p_n$ on SMPP2 will create periodic $-\sigma$ efforts at the surface S_s of an EC of radius r_{00}, which give an average resultant force $-F_{L21}$ (average effort $-\sigma$). The force $-F_{L21}$ can be considered continuous over time along the direction O_1-O_2, and thus acts in a similar way to the Coulomb force F_C (but it is F_{CC} in fact) between two electric charges with the same sign.

3) Action on SMPP1

We now look at the situation with percussions $-p_n$ that act on the surface S/MM of SMPP1 under the influence of SMPP2, and find that the position of the $-,+u$ deformations in the ETH in the area of SMPP1 is completely symmetrical with regard to the situation of $-,+u$ arising from SMPP2, as described in **2)** (**Figure 5(a)** and **Figure 5(b)**). Symmetry is also maintained in the case of the deformations $+,-u_s$. As a result, the normal/orthogonal $-p_n$ percussion forces exerted on SMPP1 will be symmetrical to those acting on SMPP2, and will result in a force $-F_{L12}$ (on single EC) (of $-\sigma$ nature):

$$-F_{L12} \cong -F_{L21} \tag{8}$$

This force $-F_{L12}$ will also be a Coulomb-type force F_C of repulsion of SMPP1 by SMPP2 (but F_{CC} in fact).

3.2. Interaction between Two Negative Immovable SMPNs through FVLs

1) General conditions of SMPNs:

In this case, Figure 5(a) must be adapted to reflect the new situation: here, we have SMPN1 and SMPN2 (rather than SMPP1 and SMPP2), and the angles of the internal vortices and external rotations $+\omega/+\Omega$ must be reversed to become $-\omega/-\Omega$, while the directions of the arrows representing the sizes of the deformations $+,-u$ will be inverted to give $-,+u$, as explained in Section 2.4.

2) Action on SMPN2:

Here, we analyse the situation of the percussion forces produced by SMPN1 at point M_2 on the surface/membrane S/MM of SMPN2, facing SMPN1 (Figure 5(a)-adapted).

The vibratory linear/longitudinal deformations (here, radial) both those in the ETH, $-,+u$, with the first $-u$, and the rest $+,-u$, as well as $-,+u_s$ at the S/MM surface of the SMPN2 particle, are represented in the inset to Figure 5(c) by a periodic zigzag line (ZL) with period T, depending on t.

Hence, the order of occurrence of the phases of the deformations $+,-u$ will be reversed twice: once due to the reversal of the direction of the $+u$ axis, and once from reporting to SMPN2, as described in Section 3.1. These then become the first positive $+,-u$ deformations in ETH around SMPN1, and the deformations at the surface S/MM of SMPN2 will become the first negative ones $-,+u_s$ (Figure 5(c)).

At point M_2 on SMPN2 facing SMPN1 (Figure 5(a)-adapted, Figure 5(c)), we find that at time $t_0 = 0$, the deformations in the ETH will be positive deformations $+,-u$ in the ECs of the adjacent ETH, originating in SMPN1. In the case of the PC cells at the surface S/MM of SMPN2 (Figure 5(c)), their first deformations are negative $-,+u_s$ and these appear in the opposite direction to the deformations $+,-u$, in the ETH, but with the same phase.

The peak points P_i of the ZL curve of the periodic deformations $+,-u$ in the ETH coming from SMPN1 at various timeframes T, will be directly opposite to the peak points P_i of the ZL curve for the $-,+u_s$ deformations in SMPN2. The compressive percussion forces $-p_n$ from ETH are focused in these contact points P_i where the percussion forces $-p_n$ from SMPP2 are focused, (as part of PHA active phase from Section 2.3.), having opposed senses, so giving repulsion forces (Figure 5(c)).

In this case, normal/linear compression percussion forces $-p_n$ (negative compression effort $-\sigma$) will occur at point M_2 on the near half of the surface S/MM of SMPN2, over the area S_s of a single EC (circle radius r_{00}), *i.e.* repulsion of SMPN2 from SMPN1. Hence, at the elementary surface S_s corresponding to the central string ST_0 of ECs at point M_2, a continuous rejection force $-\underline{p}_n$ will appear as an average over a period T of periodic percussion forces $-p_n$. This force $-p_n$ will be continuous over time, repelling SMPN2 due to SMPN1, and is denoted as $-F_{L21}$; it is created by periodic percussion forces $-p_{n1}$, through their av-

erage effort $-\sigma$ over the elementary surface S_s of an EC.

This repulsion force $-F_{L21}$ (on a single EC) will be created by p_n percussions through their average $-\sigma$ effort on the elementary S_s surface of the EC, according to Figure 5(a)-adapted, Equation (6) being valid here also.

$$-F_{L21} = -p_n = S_s\left(-\sigma\right) \tag{9a}$$

Note 3.1, **Note 3.2**, **Note 3.3** adjusted, and the adjusted **Summary 3.1** from Section 3.1, final of point **2)** are also valid here.

3) Action on SMPN1:

If we look at the case of SMPN1 under the influence of SMPN2, we find that the position of the deformations $+,-u$ within the area of SMPN1 are completely symmetrical to the those of $+,-u$ in the area of SMPN2, as explained in point **2)** above (Figure 5(a)-adapted, Figure 5(c)). Symmetry is also maintained in the case of deformations $-,+u_s$.

As a result, the percussion forces $-p_n$ (of $-\sigma$ nature) exerted on SMPN1 will be symmetrical to those acting on SMPN2. A resulting repulsion force $-F_{L12}$ will also be exerted on SMPN1; this will also be a Coulomb-type force F_C, (but it is F_{CC} in fact) which constitutes a repulsive force on SMPN1 by SMPN2. Equation (9a) is also valid here:

$$-F_{L12} \cong -F_{L21} \tag{9b}$$

3.3. Interaction between Immovable SMPP and SMPN through FVLs

1) General conditions of SMPP/SMPN:

Figure 5(a) must be adapted to reflect this situation, in which SMPP1 is preserved and SMPP2 is replaced by SMPN2 (Figure 5(a)-adapted). Here, the angles of the internal vortices and external rotations $+\omega/+\Omega$ for SMPP1 must be reversed to become $-\omega/-\Omega$ for SMPN2, and the directions of the arrows representing the sizes of the deformations $+,-u$ will be adapted to each SMP, as described in Section 2.4.

2) Action on SMPN2: We will analyse the case of the forces created at point M_2 on the surface/membrane S/MM of SMPN2 (Figure 5(a)-adapted). The linear/longitudinal vibratory deformations (radial in this case), both those in the ETH, $+,-u$ (in which the first has size $+u$, and the rest $-,+u$) and those at the surface of particle SMPN2, $-,+u_s$ (in which the first has size $-u_s$, and the rest $+,-u_s$) are represented in the inset of Figure 5(d) by a periodic zigzag line with period T, as function of t.

The order of the phases of the particle deformations will therefore be reversed at SMPN2, becoming $-,+u_s$ at the surface S/MM (Figure 5(d)). At point M_2 (Figure 5(a)-adapted, Figure 5(d)) we find that at time $t_0 = 0$, the deformations of the ECs in the adjacent ETH will be with the first negative, $-,+u$, after reversing $+,-u$ directions of the deformations coming from SMPP1. And the longitudinal/radial deformations of PCs cells from the surface S/MM of SMPN2 will be with the first $-,+u_s$ negative and the rest, $+,-u_s$. They will have the same direc-

tion as the longitudinal/radial deformations $-,+u$ in ETH and will have the same phase, according to the HVFA hypothesis presented in Sections 2.3.1, 2.4.

Hence, at point M_2, the peak points P_i (at which the percussion forces $-,+p_n$ are focused) of the broken line ZL of deformations $-,+u$ in the ETH coming from SMPP1 will occur at various timeframes T in positions identical to the P_i peaks in the ZL of the deformations $-,+u_s$ of SMPN2, thus twisting/penetrating themselves, having identical senses, so giving attraction forces (**Figure 5(d)**).

In this case, at the peak points P_i in the ETH/SMPN2 surface S/MM where the percussion forces $-p_n$ are focused, (as part of inversed PHA active phase from Section 2.3.1), positive percussion forces $+p_n$ (*i.e.* tensile forces) will be created in the ETH with regard to SMPN2. When applied to the surface of SMPN2, these positive percussion forces $+p_n$ will create an attraction force $+F_{L21}$ on SMPN2, as shown in **Figure 5(d)**.

On the elementary surface S_s (circle with r_{00}) of an EC belonging to the central string ST_0 of ECs, at point M_2, an average attractive percussion force $+p_n$ (over $+p_n$) will appear as an average over a time period T of the percussions $+,-p_n$.

This average force will be continuous over time, due to the attraction of SMPN2 by SMPN1, denoted here as $+F_{L21}$. This is created by percussion forces $+p_n$, by their average effort $+\sigma$ on the elementary surface S_s of an EC:

$$+F_{L21} = +p_n = S_s\left(+\sigma\right) \tag{10}$$

This force $+F_{L21}$ (on a single EC) corresponds to the O_1-O_2 direction of the connection r between SMPP1 and SMPN2 (**Figure 5(a)**-adapted).

In **Figure 5(a)**-adapted, it is obvious that $+F_{L21}$ is a mechanical force of attraction arising from periodic percussion forces $+p_n$ and from their average tensile stresses $+\sigma$, based on the mechanism described above and illustrated in **Figure 5(d)**; these forces vary as $1/r^2$ over short distances, in the same way as F_C:

$$+F_{L21} = f\left(r_0, r_{00}, p_n, \frac{1}{r^2}\right) \tag{11}$$

The full form of function f from Equation (11) can be determined in a similar way to that in Equation (8).

Here, we assume that $-,+u$ of the VFLs in the ETH within the area of SMPN2 have the same phase and same direction/sign as $-,+u_s$ from SMPN2; as a result, these percussion forces $+,-p_n$ (on a single EC) will give tensile stresses $+\sigma$, and periodic forces $+F_{L21}$ of attraction to SMPN2 with period T. The force $+F_{L21}$ is permanent over time in the direction of SMPN2; this force of attraction therefore acts in a similar way to the Coulomb force F_C (but it is F_{CC} in fact) between two electrical charges $+q/-q$ with opposite signs, although it is different in nature.

Here is also the case of the **Note 3.1**-adapted, of **Note 3.3**-adapted and of **Summary 3.1**-adapted from Section 3.1., final of point **2)**.

Note 3.2-adapted: This correlation between the periodic deformations $-,+u$ and $-,+u_s$ of SMPP2 and SMPP1 giving attraction force, is also ensured according to the mechanism described in Section 2.3.1, where the percussion forces $-p_n$

are focused, as part of superposition of a PHA active phase and of a PHR reactive phase.

3) Action on SMPP1: If we analyse the case of SMPP1 under the influence of SMPN2, we find that the position of the deformations $-,+u$ in the area of SMPP1 is similar to the case of $-,+u$ in the area of SMPN2, as described in point **2)** above (Figure 5(a)-adapted, Figure 5(d)). Symmetry is also maintained in the case of deformations $-,+u_s$.

As a result, percussion forces $+p_n$ (of nature $+\sigma$) exerted on SMPP1 will be symmetrical with those exerted on SMPN2. The attraction force $+F_{L12}$ (on a single EC) will also then appear on SMPP1, as attraction from the part of SMPN2.

$$+F_{L12} = +p_n = S_s\left(+\sigma\right) \tag{12}$$

It should be noted that the force $+F_{L12}$ also corresponds to the Coulomb attraction force F_C between a positive and a negative charge. Equation (7) obviously applies here, in the same way as in Section. 3.1:

$$F_{L12} \cong F_{L21} \tag{13}$$

4. Application of HFVI to the Interaction between Immovable SMPs in Ether via FVTs

4.1. Interaction of Two Immovable SMPPs in the Ether via FVTs

1) General conditions of SMPPs: We consider here in HFVI, how the FVTs in the ETH are produced by the global rotations of SMPPs with rotation speed $+\Omega$, according to the mechanism basically described in Sections 2.3.1, 2.4 and 2.6.

Figure 6(a) shows a plane section perpendicular to the central axes of rotation, O_1z and O_2z, of SMPP1 and SMPP2, which are parallel to each other, and perpendicular to the plane of Figure 6(a). The reference frame O_1xyz is attached to SMPP1, which is immovable in the ETH, with distance D between them.

In the case of SMPPs we will admit through HVFI, that the deformations $+,-v_s$ of the S/MM surface, are the result of the superposition of the effects of vibratory deformations u_s, with the general rotational movement with $+\Omega$ of the SMPP around the Oz axis, according to the mechanism in Section 2.3., 2.4.

These deformations $+,-v_s$ are in fact equivalent/special deformations, which would create in the ETH the transversal vibrations/deformations $+,-v$, with $v_s = v$, according to Section 2.6. These deformations $+,-v_s$ develops in two phases: active phase (PHA), when SMP acts upon ETH transmitting energy (only which counts), and passive phase (PHP), when ETH acts upon SMP, retransmitting energy.

The deformations $+,-v$ in the ETH are initially, cylindrically propagated, since they have cylindrical symmetry around Oz axis of rotation, but at great distances, they are spherical propagated.

In the case of SMPP, we will assume that the initial deformation v_s are the result of a clockwise rotation of S/MM with $+v_s$, (corresponding to the sense $+\Omega$,

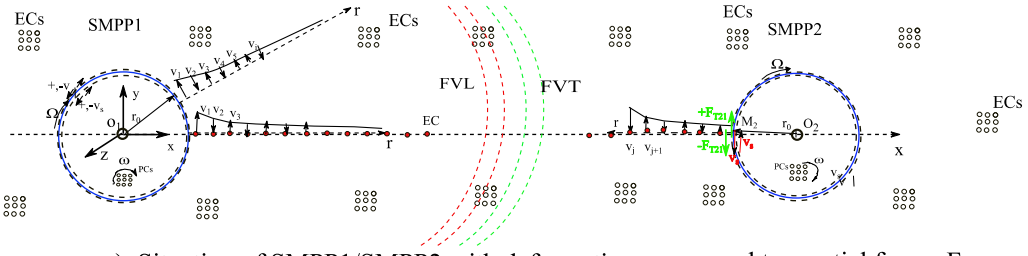

a). Situation of SMPP1/SMPP2 with deformation v, v_s and tangential forces F_{L21}

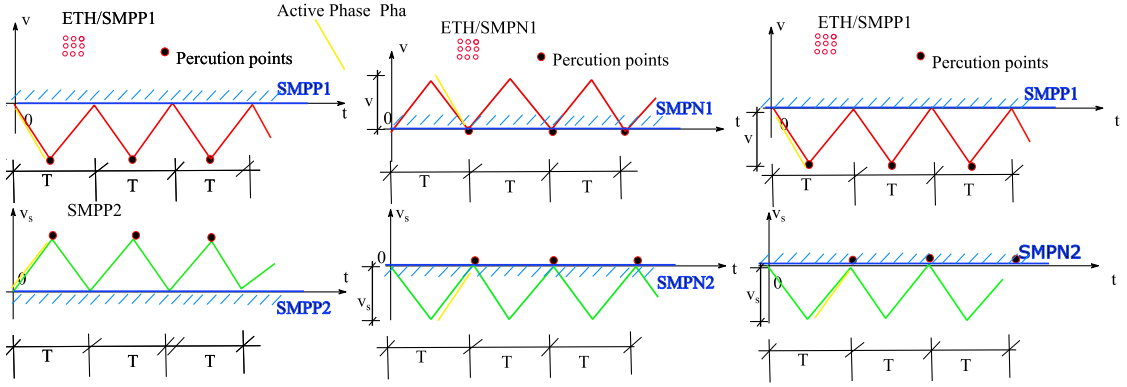

b). Grafic of v deformations in time and percution points upon SMPP2 from SMPP1 as counterclockwise first F force

c). Grafic of v deformations in time and percution points upon SMPN2 from SMPN1 as counterclockwise first F force

d). Grafic of v deformations in time and percutions points upon SMPN2 from SMPP1 as clockwise first F force

Figure 6. Physical mechanism of interaction between pairs of SMPs through their FVT vibrations in the ether, via percussions p_p, through the evolution in time of attached deformations v.

in PHA), that is denoted as positive here, followed by a counterclockwise rotation $-v_s$, in PHR and then followed by pairs of oscillations $+,-v_s$, and so on, with frequency f_t and period T_t.

The deformation $+v_s$ corresponds to the rotation of the radius r_0 (of the point M situated on the parallel circle of the sphere of SMPP), clockwise around the Oz axis through an angle $+,-\delta$ of vibrations, with size appropriate to the displacement $+,-v_s$. And the point M has the position angle λ, of the parallel circle (**Figure 2** and **Figure 6(a)**).

Deformations from $+,-v_s$, will occur tangentially to the surface S/MM, as the alternating/vibratory displacements $+,-v_s$ of the M point on the S/MM surface (**Figure 6(a)**). The displacements $+v_s$ will correspond to the specific angular deformations $\gamma_r = v_s/r_0$, with frequency ν_t.

For the SMPP, the initial displacement is considered to be $+v_s$, in PHA while for the SMPN the initial displacement will be $-v_s$, in PHR corresponding to the two types of effects from the quasielectrical charges $+q,-q$, of SMPP and SMPN respectively, as defined in Section 2.5.

Once the deformations $+,-v_s$ appear, tangential percussion forces $+,-p_t$ will arise at the surface of the SMP upon ETH, through the MM membrane at the surface S of the SMP. These periodic percussion forces $+,-p_t$ (on a single EC)

will then be exerted on ECs in the adjacent external ETH, and thus deformations $+,-v$ are produced in ETH. And being associated to deformations $+,-v$, the fundamental vibrations FVTs will also arise in ETH (**Figure 2**, **Figure 6(a)**).

This mode of occurrence of FVT, when the PCs cells or GPCs/quarks inside the SMP may continuously rotate individually with rotation speed $+,-\omega$, allowing concomitantly the general rotation of the SMP with rotation speed $+/-\Omega$ of the membrane MM on the surface S/MM of the SMP.

This model of FVT, is well correlated with other observed physical phenomena, such as the storage of energy E_0 in a GPC, with rotation speed ω, and with the spin of SMPs, due to SMP general rotation with speed $+/-\Omega$ (**Figure 2**, **Figure 6(a)**).

Thus, the spin arises from the effect of the rotations Ω of PCs at the outer surface of the SMP, since the rotations $+/-\omega$ of the inner PCs/quarks will be cancelled in pairs at the tangent points of the PCs, where the directions of the rotations $+/-\omega$ are opposite.

This is similar to the occurrence of Ampere currents in magnetism, although the energy E is present in the rotations $+/-\omega$ of all inner PCs/quarks, and will be accumulated and preserved.

Figure 6(a) indicates the direction of the transversal vibrational deformations $+,-v$ of the ECs in ETH, at circumferences of different rays r_p, related to the FVTs of SMPP1's with period T_T. The transversal deformations $+,-v_s$ of the surfaces S/MM of the SMPs are also shown.

These circular, pulsating deformations $+,-v$ of the ETH are imprinted by circular pulsating $+,-v_s$ deformations in the surface S/MM of SMPP1 in PHA, in the first layer of the adjacent EC cells in ETH, as described in Section 2.3.1, 2.4, 2.6.

These vibrational deformations $+,-v$ are then transmitted/imprinted in a step-by-step way to all the external ECs layers within the ETH through the mechanism of periodic transversal percussion forces $+,-p_t$ which produce FVTs, starting from SMPP1. The values of these deformations $+,-v_i$ will decrease as $v_0 > v_1 > v_2 > v_3 > \cdots > v_n$, (**Figure 6(a)**) corresponding to a variation of $1/r^2$, in a similar way to Coulomb's law, as described in [1] [8].

The deformations $+,-v$ will create in ETH, associated specific angular deformations or strains $+,-\gamma$, and this is possible in the case of HM16 crystalline variant A.

We assume that the FVTs of an SMP start from S/MM as a set of cylinders around the Oz axis of rotation, which then expand to the whole ETH, becoming spherical at large distances.

We must consider that the $+,-v$ deformations, are local, discrete, on a single EC, as a quantum effect.

2) Action on SMPP2:

We will first analyse the action of SMPP1 on SMPP2 via FVTs under the general conditions of the behaviour of SMPs in HFVI, as described in Sections 2.3.1,

2.4., 2.6. and above.

Here, we examine the case where the Oz axes of both SMPs are parallel, to simplify the analysis. We analyse a direct interaction between two SMPs, given by percussions $+,-p_t$ that are associated with vibrational deformations $+,-v$ via a single string ST_0 of ECs, and which is central, linear and direct between O_1 and O_2 (**Figure 6(a)**).

The total forces, including the indirect interaction forces between two SMPs via multiple STs as series of curved paths l_i and their effect through $+,-v$ of the FVTs upon SMPP2, can be analysed separately in the same way as for the vibrations $+,-u$ of FVLs; these act as a corrected Coulomb force F_{CC} as described in [2] [8], although here these $-,+v$ originate in the FVTs.

Figure 6(b) shows how the first deformations $+v$ of the ECs in the adjacent ETH, derived from SMPP1, become $-v$ (due to the reversal of the direction of the axis $+v$) when applied to SMPP2.

In this simple case, at point M_2 on SMPP2, a series of tangential percussion forces $+,-p_t$ during PHR will be transmitted from SMPP1 via the ETH, with the first being the negative $-p_t$ due to a reversal of the sense of $+v$ when switching from SMPP1 to SMPP2 (**Figure 6(a)**, **Figure 6(b)**).

At point M_2, we therefore find that at time $t_0 = 0$, the first deformations of the ECs will be $-v$, during PHA of SMPP1 *i.e.* in the opposite direction to the first deformations $+v_s$ in the PCs within SMPP2, although these deformations have the same phase, and during PHA of SMPs.

The peaks in the zigzag line ZL at the points P_i (where the percussion forces $-,+p_t$ are focused, as effects of PHA, **Figure 6(b)**), *i.e.* periodic deformations $-,+v$ of the ETH at various timeframes $T/2$, will therefore be directly opposite to the direction of movement of the peaks P'_i of the deformations $+,-v_s$ in SMPP2 having opposed senses, so giving repulsion forces. (**Figure 6(b)**). It follows that the percussions $-,+p_t$ will constitute forces that oppose the direction of the deformations $+,-v_s$ in the surface of SMPP2, and are thus also opposite to the corresponding forces $+,-p_{st}$ afferent to the SMPP2 surface S/MM, as effects of PHA superposition from Section 3.2.1, indicating rejection of SMPP2 from SMPP1, which finally will be reciprocal.

In this way, at point M_2 on the elementary surface S_s of a single EC (a circle with radius r_{00}) of the central string ST_0 of ECs, tangential periodic percussions $-,+p_t$ with period $T/2$ will arise.

The percussion forces $+,-p_t$ from ETH (**Figure 6(b)**), will be opposed to the deformations $+,-v_s$ in SMPN2, and hence form tangential efforts $-,+\tau$ restraining the deformations in SMPN2 and mitigating its rotation, giving:

$$-,+\tau = -,+p_t/S_s \tag{14}$$

This will result in an average percussion force $-,+p_t$ (over $-,+p_t$, and thus $-,+p_t = -,+p_t/2$), as an average force over a semi-period $T/2$, noted with $-,+F_{T21}$, derived from percussion forces $-,+p_t$ (on a single EC) via the average periodic effort $-,+\tau$ and this will have the form:

$$-,+F_{T21} = -,+p_t = S_s\left(-,+\tau\right) \tag{15}$$

The force $-,+F_{T21}$ will therefore be a periodic tangential force that produces a alternating rotation in SMPP2 by SMPP1, while creating a braking/attenuating effect on the periodic vibration $+,-v_{st}$ or on rotation $+,-\Omega$, of SMPP2, as shown in **Figure 6(a)**.

This tangential force $+,-F_{T21}$ will be continuous over $T/2$, due to SMPP1, and is created by the percussion forces $-,+p_t$, through their average $-,+\tau$ effort on the elementary surface S_s of an single EC.

This force $-,+F_{T21}$ corresponds to the direction/line O_1-O_2 of direct connection l_0 through ST_0 between SMPP1 and SMPP2 (**Figure 6(a)**).

From **Figure 6(a)**, it can be seen that the force $-,+F_{T21}$ also corresponds to a special tangential force of Coulomb type F_C between two positive charges $+q/+q$, although with a different nature. The nature of $-,+F_{T21}$ is obvious; it is a tangential mechanical force derived from the tangential percussion forces $+,-p_t$, and from their average efforts $-,+\tau$, according to the mechanism described above and illustrated in **Figure 6(b)**. This force varies as $1/r^2$ over short distances, in the same way as F_C:

$$F_{T21} = f\left(r_0, r_{00}, p_t, \frac{1}{r^2}\right) \tag{16}$$

The full form of the function f in Equation (16) can be established on an experimental basis depending on the geometry of the SMPs (radius r_0) and on the ECs (radius r_{00}), and also on the positions of the axes Oz.

As a result, from the percussions $-,+p_t$ arising from SMPP1, and hence also from the force $-,+F_{T21}$, acting tangentially on SMPP2 (with radius r_0), a moment $-,+M_{T21}$ of rotation (periodic in the same way as $-,+v$) will result:

$$-,+M_{T21} = -,+F_{T21}r_0 \tag{17}$$

Since the deformations $-,+v$ at the extreme points P_i on the lines of variation ZL over time t for ETH and near SMPP2 have signs/directions that are opposite to those of the deformations $+,-v_s$ (**Figure 6(a)** and **Figure 6(b)**), then the percussions $-,+p_t$ (including the forces $-,+F_{T21}$ and their efforts $-,+\tau$) will be opposed to $+,-v_s$, so representing a decrease in the $+,-\gamma_0$ rotational trend of SMPP2 due to SMPP1.

As a result, the moment $-,+M_{21}$ will also be a periodic/vibrational rotation moment on SMPP2 with a braking effect on its oscillations/rotations due to the influence of SMPP1, which is unknown at present and may have a quantum interpretation.

Note 4.1: This correlation in the periodic deformations $-,+v_s$ and $-,+v$ between SMPP2 and SMPP1 giving repulsion forces $-,+F_{T21}$ also arises as described in Section 1 for SMPAC and HCO, through the suitable commands for reversing the direction $-,+v$ provided by the NCs of SMPP1 and SMPP2.

Note 4.2: This correlation between the periodic deformations $-,+v_s$ and $-,+v$ of SMPP2 and SMPP1 giving repulsion forces $-,+F_{T21}$, is also ensured according

to the mechanism described in Section 2.3.1., where the percussion forces $-p_t$ are focused, as part of superposition of two PHA active phases, having opposed senses, so giving repulsion force $-,+F_{T21}$ and braking moment M_{T21}.

Note 4.3: We admit in HFVI that the above forces action is at the single EC area of the $+,-p_t$ and the equivalent force $+,-F_{T21}$ in Equation (16) and also the moment $-,+M_{T21}$ in Equation (17). So $+,-F_{T21}$ and $-,+M_{T21}$ represents the forces/moments with minimum intrinsic/predetermined sizes for the SMPs and the ETH, which constitute the minimum forces/moments $\Delta F/\Delta M$ in quantum mechanics. Hence, these forces F_{T21} may constitute a kind of special magnetic field QH_s whose nature needs to be researched in future.

3) Action on SMPP1:

In the case of the action of the force from SMPP2 on SMPP1, due to the symmetry of the situation (Figure 6(a)), the same result as in point **2)** will be obtained and the periodic $+,-F_{T12}$ force will result :

$$-,+F_{T12} = -,+p_t = S_s\left(-,+\tau\right) \cong -,+F_{T21} \tag{18}$$

The periodic rotation moment $-,+M_{T12}$ will also arise:

$$-,+M_{T12} = -,+F_{T12}r_0 \cong -,+M_{T21} \tag{19}$$

where $-,+M_{T12}$ is a periodic/vibrational moment of rotation on SMPP1 with a braking effect on its oscillation due to SMPP2.

4.2. Interaction of Two SMPNs that are Immovable in the Ether, through FVTs

1) General conditions of SMPNs:

In this case, Figure 6(a) must be adapted to represent SMPN1 and SMPN2 with the internal rotations ω and external rotations Ω that are reversed, becoming $-\omega$ and $-\Omega$, respectively. The senses of the arrows representing the deformations $+,-v$ will also be inverted (Figure 6(a)).

Thus, the order of occurrence of the phases of the deformations $+,-v$ will be reversed on both sides, becoming $-,+v$, in the ETH around the SMPN and $-,+v_s$ (with the first of size $-v_s$, and the rest of size $+,-v_s$) at the surface S/MM of the SMPN.

In the case of interaction between two negative SMPs, SMPN1 and SMPN2, by means of FVTs, the situation is similar to that discussed in Section 4.1 above, with Figure 6(a)-adapted, showing the changed directions of ω, Ω angles and of $+,-v$ senses.

This is because the difference between an SMPN and an SMPP in respect of FVTs consists only of the senses of transversal deformation $+,-v$ and the related $+,-\gamma$ angle, as illustrated in HFVI in Section 2. This means that for an SMPN, the initial rotation is $-v$, and $-\gamma$, *i.e.* counterclockwise. This reversed direction of the initial deformation/vibration has no influence on the size of the forces F_T or the moment M_T, but only on their directions in Equation (18), Equation (19).

2) Action on SMPN2:

The transversal/pulsating deformation $-,+v_s$ (initially with size $-v_s$, and then $+,-v_s$) at point M_2 on the surface S/MM of SMPN2, and deformations/vibrations $+,-v$ in the adjacent ETH, is represented in the inset in **Figure 6(c)**, and depends on the time t over a period T. This results in a periodic zigzag line ZL, due to the pulsating and periodic character of $+,-v$ and $+,-v_s$ with time step $T/2$.

The first deformations $-v$ of the ECs in the ETH adjacent to SMPP1 become $+v$ in **Figure 6(c)** near SMPN2 (due to the change in direction of the axis $+v$).

At the central point M_2 on the face of SMPN2 facing SMPN1 (**Figure 6(a)**-adapted, **Figure 6(c)**), we find that at time $t_0 = 0$, the deformations $+,-v$ in the ECs caused by SMPN1 in the adjacent ETH are opposite in direction/sense to the deformations $-,+v_s$ of the PCs of MM within SMPN2, although they have the same phase.

Hence, the peaks at points P_i where the percussion forces $+,-p_t$ are focused (as part of PHA active phases superposition, from Section 2.3.1.), having opposed senses, so giving repulsion forces (**Figure 6(c)**). So on the line ZL of periodic deformations $+,-v$ in the ETH at various timeframes $T/2$, deformations $+,-v$ will be directly opposite to the peaks of the deformations $-,+v_s$ in SMPN2 with period $T/2$ indicating rejection of SMPN2 which finally will be reciprocal (**Figure 6(c)**).

The transversal vibratory deformations $+,-v$ of the ECs in the ETH adjacent to SMPN2 will be accompanied by periodic transversal/tangential percussion forces $+,-p_t$ at point M_2 (initially positive, on a single EC) on the nearby half-surface S/MM, of the nature of some tangential $+,-\tau$ efforts, and these are also vibrational. The average of these efforts $+,-\tau$ at point M_2 on the area S_s of an single EC projection (with radius r_{00}) on the half-surface S close to SMPN2, will give the force $+,-F_{T21}$. The first impulse of $+,-F_{T21}$ is counterclockwise, starting from SMPN1, and this is reversed to the clockwise sense on SMPN2, as explained in Section 2 (**Figure 6(a)**-adapted, **Figure 6(c)**).

In this way, an average percussion force $+,-p_t$ (over $+,-p_p$, thus $+,-p_t = +,-p_t/2$) will appear at point M_2 as an average force over a half-period $T/2$, denoted as $+,-F_{T21}$ (on a single EC), arising from percussion forces $+,-p_t$ through their average periodic effort $+,-\tau$, and will have the form:

$$+,-F_{T21} = +,-p_t = S_s\left(+,-\tau\right) \tag{20}$$

Thus, the force $+,-F_{T21}$ (on a single EC) will be a periodic tangential force on S/MM that produces a rotation in SMPN2 due to SMPN1, but creates a braking/attenuating effect on its own periodic rotations $-,+v_s$ as shown in **Figure 6(a)**-adapted.

This tangential force $+,-F_{T21}$ corresponds to the direction/line O_1-O_2 of direct connection l_0 through ST_0, between SMPN1 and SMPN2 (**Figure 6(a)**-adapted).

As a result of the percussion forces $+,-p_t$ and hence the forces $+,-F_{T21}$ (on a single EC) acting tangentially on SMPN2 (radius r_0), a rotation moment $+,-M_{T21}$ (periodic in the same way as $+,-v$) will emerge:

$$+,-M_{T21} = +,-F_{T21}r_0 \tag{21}$$

As explained in Sec. 4.1, also here, since the deformations $-,+v$ at the extreme points of the lines ZL of variation during t for ETH and for SMPN2, have signs/senses that are opposite to the deformations $+,-v_s$ (Figure 6(a)-adapted, Figure 6(c)), the percussions $-,+p_t$ (including the forces $-,+F_{T21}$ and their efforts $-,+\tau$) will be opposite to $+,-v_s$, representing an attenuation in the rotation of SMPN2 $+,-\gamma_0$ due to SMPN1.

The moment $+,-M_{T21}$ will therefore be an alternating rotation moment on SMPN2 due to the influence of SMPN1, which will tend to oppose the own moment $-,+M_{T21}$ of SMPN2 by braking.

Here, **Note 4.1.**-adapted**, Note 4.2.**-adapted and **Note 4.3.**-adapted from Section 4.1 point **2)** are also valid here.

3) Action on SMPN1:

In the case of the action of SMPN2 on SMPN1, due to the symmetry of the deformations v, and hence also of the percussion forces p_t (Figure 6-adapted), the same result as in point **2)** will be obtained for the force $+,-F_{T12}$ and the moment $+,-M_{12}$ given in Equation (20) and Equation (21):

$$+,-F_{T12} = +,-p_t = S_s\left(+,-\tau\right) \cong +,-F_{T21} \tag{22}$$

$$+,-M_{T12} = +,-F_{T12} r_0 \cong +,-M_{T21} \tag{23}$$

The moment $+,-M_{T12}$ will be a periodic/oscillating rotational moment on SMPN1 with a braking effect on the own oscillation/rotation $-,+M_{sT1}$ of SMPN1.

4.3. Interaction between Immovable SMPP and SMPN, in the Ether, via FVTs

1) General conditions of SMPP/SMPN:

In this situation, Figure 6(a) must be adapted to represent SMPP1 and SMPN2, with internal rotation ω and external rotation Ω, which are reversed for SMPN2 to give $-\omega$ and $-\Omega$, respectively, and the senses of the arrows of the deformations $+,-v$, will be inverted for SMPN2 (Figure 6(a)) as discussed in Section 2.

Thus, the order of occurrence of the phases of deformations $+,-v$ will be reversed, becoming $-,+v$, in the ETH around SMPN2 and remaining $+,-v_s$ (with initial size $+v_s$ and then $-,+v_s$ pairs) at the surface S/MM of SMPP1.

2) Action on SMPN2:

The transversal/circular deformations $-,+v_s$, as vibrations at the point M_2 on the surface S/MM of SMPN2, and the FVT deformations/vibrations $-,+v$ in the adjacent ETH, are represented in detail in Figure 6(d), and depend on time t, over periods T.

The first deformations $+v$ of the ECs in the ETH adjacent to SMPP1 become $-v$ in Figure 6(d) near SMPN2 (due to the change in direction of the $+v$ axis) when applied to SMPN2.

At the central point M_2 on the face of SMPN2, the zigzag lines ZL of the deformations $-,+v$ and $-,+v_s$ (Figure 6(d)) will result with the same sign (where the first deformation in ETH will be $-/+v$) with time step $T/2$. These deformations have the same phase.

The extreme peaks at points P_i where the percussion forces $-p_t$ are focused as part of PHA active phases superposition, from Section 2.3.1., having identical senses, so giving attraction forces (**Figure 6(d)**). So on the ZL line of the periodic deformations $-,+v$ in the ETH at various timeframes $T/2$, the deformations $-,+v$, will therefore match the peaks in the deformations $-,+v_s$ in SMPN2, and since they have the same direction/senses, these lines will twist/penetrate themselves indicating attraction of SMPN2 which finally will be reciprocal attraction (**Figure 6(d)**).

The transversal vibratory deformations $-,+v$ of the ECs in the ETH adjacent to SMPN2 will be accompanied by periodic transversal/tangential percussion forces $-,+p_t$ at point M_2 (initially negative) at the S/MM half-surface, of the nature of some tangential $-,+\tau$ efforts, which are also vibrational. The average of these efforts $-,+\tau$ at point M_2 on the area S_s of an single EC projection (radius r_{00}), on the surface S/MM close to SMPN2 will give the force $-,+F_{T21}$ (where the initial impulse of $-F_{T21}$ is clockwise, starting from SMPN1, but is reversed to counterclockwise for SMPN2) as discussed in Section 2.3.1. (**Figure 6(a)**-adapted, **Figure 6(d)**).

In this way, an average percussion force $-,+p_t$ (over $-,+p_t$) will appear at point M_2 as an average force over time with period $T/2$, denoted as $-,+F_{T21}$, (on a single EC) arising from the percussion forces $-,+p_t$ through the average periodic effort $-,+\tau$, and will have the form:

$$-,+F_{T21} = -,+p_t = S_s\left(-,+\tau\right) \tag{24}$$

Thus, the force $-,+F_{T21}$ will be a periodic tangential force that produces a oscillatory rotation in SMPN2 due to SMPN1, and creates a boosting effect for its own periodic rotation $-,+v_s$ or $-,+\Omega$, (**Figure 6(a)**-adapted, **Figure 6(d)**).

This tangential force $-,+F_{T21}$ corresponds to the line O_1-O_2 of direct interaction line l_0 through ST_0, between SMPN1 and SMPN2 (**Figure 6(a)**-adapted). Here, the force $-,+F_{T21}$ is a Coulomb-type force but with a different nature, arising from VFTs.

As a result of the percussion forces $-,+p_t$, and hence the forces $-,+F_{T21}$ due to SMPN1 tangentially acting on SMPN2 (radius r_0), a special rotational moment $-,+M_{T21}$ (periodic in the same way as $-,+v$) will emerge:

$$-,+M_{T21} = -,+F_{T21}r_0 \tag{25}$$

The alternating rotation moment $-,+M_{T21}$ (on a single EC) will act on SMPN2 due to the influence of SMPN1, tending to boost SMPN2's own moment $-,+M_{s21}$.

It can also be seen from **Figure 6(a)**-adapted that the $-,+F_{T21}$ force also corresponds to a Coulomb force F_C between two different charges $+q/-q$, although it has a different nature.

Note 4.1.-adapted, **Note 4.2.**-adapted and **Note 4.3.**-adapted, from Section 4.1 point **2**) are also valid here.

3) Action on SMPP1:

In the case of the action of SMPN2 on SMPP1, due to the anti-symmetry of the situation (Figure 6(a)-adapted, Figure 6(d)), the result described in point **2)** will also be obtained for the force $-,+F_{T12}$ and the moment $-,+M_{T12}$, as given in Equation (26a) and Equation (26b):

$$-,+F_{T12} = -,+p_t = S_s\left(-,+\tau\right) \cong -,+F_{T21} \tag{26a}$$

$$-,+M_{T12} = -,+F_{T12}r_0 \cong -,+M_{T21} \tag{26b}$$

The resulting force $-,+F_{T12}$ and the moment $-,+M_{T12}$ on the elementary surface S_s (on a single EC) will produce a boost in its own rotation $-,+v_s$ and its own moment $-,+M_{s21}$.

5. Effect Produced by FVs in ETH, Created by the Ordered Orientation of SMPs from an Immobile GSMP, Creating *QE* and *QH* Fields

5.1. FVL Vibrations Creating *QE*

We now consider the situation of a group of SMPs, GSMP1, that are homogeneous in electrical nature (P or N), and ordered in terms of their orientation on the O*z* axis (Figure 7). These SMPs will each transmit FVL waves in an AI-zone of the ETH near SMP2, in the presence of which vibrational deformations of type $+,-u$ and strains $+,-\varepsilon$ respectively will occur within the EC network of the ETH (Figure 7). These vibrations of the linear strains $+,-\varepsilon$ will be oriented in one direction and will have the same sense, and thus will accumulate from all the SMPs in the group within the AI. As a result, a sum of oscillatory percussions $\Sigma+,-p_n$ (on a single EC) will appear, which will act on SMP2 as explained in Section 3. Then, the sum of oscillatory forces $\Sigma+,-F_{L21}$ from Equation (9a) will be developed, with attraction/repulsion effect on SMP2 depending on the type (P or N) of the SMP2 and GSMP1 pair, as discussed in Section 3.

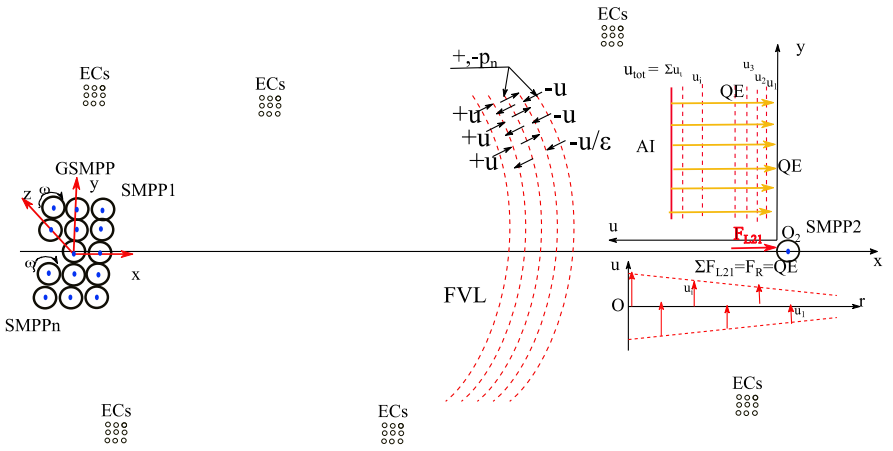

Figure 7. Mechanism of interaction of percussion forces between immobile GSMP and a SMPP, via FVLs and deformations $+,-u$, creating a quasielectric field *QE* in the ETH.

Thus, the effect of $+,-F_{L21}$ from the GSMP1 group of ordered particles accumulates, giving a resulting force F_R acting on SMP2 that is equivalent to the presence of a stronger quasielectric field QE (Figure 7).

Here, QE has a clear physical explanation, as it is produced by the normal percussion forces $+,-p_n$ (on a single EC, only in PHA) created by the FVLs from GSMP.

This QE field will produce the same physical effects as the E field; the nature of QE is clear here, as it is an effect of the percussion forces p_i created by the strains $+,-\varepsilon$ produced by the FVLs from the GSMP.

5.2. FVT Vibrations Creating a Special QH_s

The FVTs of a stationary group of SMPs, GSMP1, can create in a certain AI near SMP2, from space/ETH, a special state of ordering of the vibrational deformations $+,-v$ and the associated angles $+,-\gamma$ from the EC network of the ETH (Figure 8).

This situation can only occur if GSMP1 has component SMPs that are homogeneous in nature (P or N) and are ordered in terms of their orientation and the directions of their Oz axes. Then the positions and orientations of the angles $+,-\gamma$ in the AI zone of ETH produced by all SMPs, will have the same direction and sense, cumulating from all SMPs in the GSMP (Figure 8).

As a result, pulsating tangential percussion forces $+,-p_t$ will arise as a sum, $\Sigma+,-p_t$, (on a single EC) and will act tangentially on the surface S/MM of SMP2 as described in Section 4. At the same time, the associated forces accumulate as $\Sigma+,-F_{T21} = +,-F_{RT21}$, and this resultant tangent force will create the vibrational/special moment of torsion $+,-M_{SR}$ (on a single EC) that acts on SMP2. The moment $+,-M_{SR}$ will have a damping or boosting effect on the rotations/vibrations of SMP2, based on the types of SMP2 and GSMP (P or N), as explained in Section 4.

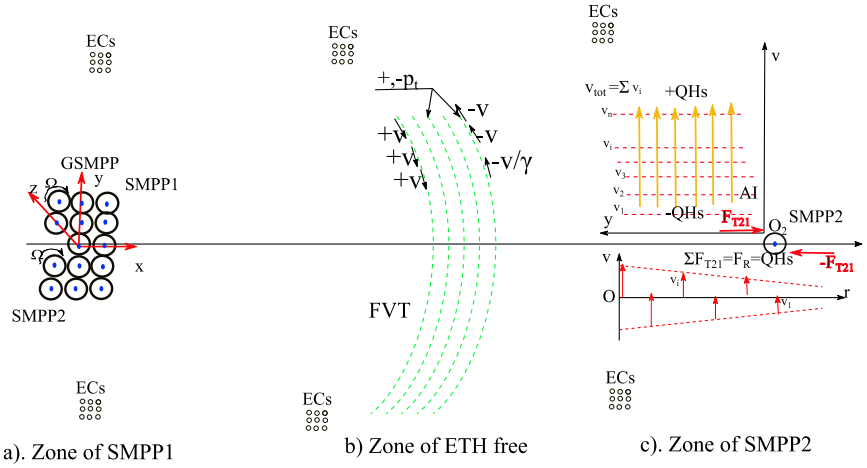

Figure 8. Mechanism of interaction of percussion forces between an immobile GSMP and a SMPP, via FVTs and deformations $+,-v$, creating a quasimagnetic special field QH_s in the ETH.

This damping or boosting action depends on the relative position of the axes Oz of SMP2 and of GSMP; a parallel direction gives the best result, due to the highest interference of the associated strains γ.

The creation of a vibrational moment $+,-M_{SR}$ (on a single EC, only in PHA) acting on the surface S/MM of an SMP2 is equivalent to the presence in the AI of a more powerful vibrating quasimagnetic special field $+,-QH_s$; although this has no actual equivalent field in physics, it may explain some of the quantum properties of SMPs (**Figure 6**).

6. Effect of FVs in the ETH Created by a Mobile SMP with Velocity V

6.1. FVLs of a Mobile SMP

For a dynamic state of the SMP1/SMP2 pair, when SMP2 moves with velocity V along the Ox axis through the ETH (**Figure 9**), an additional effect will appear, namely a dynamic component of the deformation $+,-u$ with size Δu, oriented in the x direction.

This dynamic component $+\Delta u$ represents the displacement of SMP2 in the direction of V for a half-period $T/2$, during which the deformation $+,-u$ of the surface S/MM of SMP2 occurs.

The deformation $+\Delta u$ in the area of SMP2 will then be transmitted in a radial/spherical way throughout the rest of ETH, and will reach SMP1, but with values $+\Delta u'$ decreasing as $1/r^2$ according to Coulomb's law (in the same way as $+,-u$, described in Section 3).

The new effect $+\Delta u$ or the associated $+\Delta\varepsilon$, will cause a change of $\Delta\varepsilon$ in $+,-\varepsilon$, including in the AI of SMP1, and will therefore create a modification of the force $+,-F_{L12}$ on SMP1, as described in Section 3, but only when the direction of V coincides with the direction O_1-O_2 (**Figure 9**).

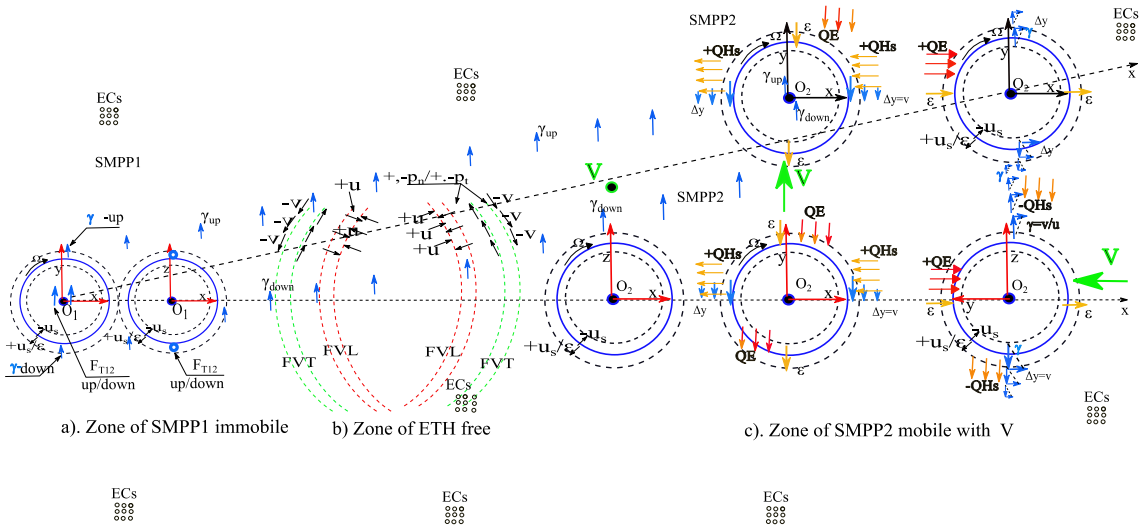

Figure 9. Deformations u and v in the interaction between mobile SMP2 and the EYH resulting quasielectric (QE) and quasimagnetic (QH) fields in the ETH.

We also note that the deformation $+\Delta u$ is discrete and vibrating, due to the vibrating nature of $+,-u$ with which it is associated, and this vibration will be transmitted to $+\Delta\varepsilon$ and $+\Delta F_{L12}$.

The new effect $+\Delta u$ will produce a change in the base force $+F_{L12}$, (on a single EC, only in PHA) as explained in Section 3, by a new force $+\Delta F_{L12}$ of repulsion/attraction type, of SMP1 by SMP2 due to velocity V.

From the reciprocity of the interaction discussed in Section 3, a similar modification of the force $+\Delta F_{L21}$ on SMP2 due to SMP1 will be created, with size $+\Delta F_{L21} = +\Delta F_{L12}$. This force $+\Delta F_{L21}$ is the reaction of the ETH acting on SMP2, opposing to its movement with speed V.

We note here that Δx is the displacement of SMP2 during the period Δt of the expansion of SMP2, where $2u/2 = u$, during a semiperiod $T/2$. We can therefore write:

$$\Delta x = \Delta t \cdot V \tag{27}$$

As a result, the total deformation u_t of the point M_2 located on the surface S/MM of SMP2 within a semi-period $T/2 = \Delta t$ will be:

$$u_t = u + \Delta x = u + \Delta t \cdot V \tag{28}$$

The time Δt over which the deformation u takes place, with its own velocity of deformation c_u of the surface S/MM, during a single vibration $T/2$ within the FVL, will be:

$$\Delta t = \frac{u}{c_u} \tag{29}$$

We introduce Equation (29) into Equation (28), and obtain for the total deformation:

$$u_t = u + \frac{u}{c_u} \cdot V \tag{30}$$

For the total final specific deformation/strain ε, from Equation (30), we obtain:

$$\varepsilon_t = \frac{u_t}{r_0} = \frac{u + \frac{u}{c_u} V}{r_0} = \frac{u}{r_0} + \frac{u}{c_u} \cdot \frac{V}{r_0} = \varepsilon_0 + \varepsilon_0 \cdot \frac{V}{c_u} \tag{31}$$

The variation in the specific deformation, $\Delta\varepsilon$, from Equation (31) is then:

$$\Delta\varepsilon = \varepsilon_t - \varepsilon_0 = \varepsilon_0 \cdot \frac{V}{c_u} \tag{32a}$$

In the case of an SMP2 moving with velocity V in a direction different from O_1-O_2 (**Figure 9**), the influence on $\Delta\varepsilon$ will arise only from the component of V in the direction Ox, meaning that this will be smaller than in the case in Equation (32a). So the dynamic effect $+\Delta F_{L12}$ created by $\Delta\varepsilon$ will modify the basic force $+F_{L12}$ by a second factor V/c_u as follows:

$$+\Delta F_{L12} = +F_{L12} \cdot \frac{V}{c_u} \tag{32b}$$

Since the force F_{L12} is modified as shown in Equation (32b), the force F_{CC} will also be modified, and hence the intensity of the quasielectric field QE will be modified by ΔQE.

This modification will normally be negligible, due to the negligible value of V compared to the velocity of deformation c_u of S/MM from Equation (32a), based on the results from Sections 2 and 3.

It follows that the final size of $+\varepsilon$, and hence also the sizes of the resulting forces $+,-F_{L12}$ and $+,-F_{L21}$, cannot be significantly influenced, in the case of movement with normal velocity V in the ETH, or between SMP2 and SMP1. However, for high speeds V, this influence ΔF_{L12} cannot be neglected, as it results in important consequences at both the microscale and the macroscale. It affects the electric interaction forces F_{CC} and the gravitational forces F_{DC} according to [1] [2].

6.2. FVTs of Mobile SMPs

In this case, we consider the special situation of a mobile SMP with velocity V, which produces FVTs by means of rotation with speed $+\Omega$ around the axis Oz.

We take into consideration the fact consider that an immobile SMP will produce only simple, tangential circular deformations $+,-v$, but with an asymmetrical variation in the period T associated with the FVs, as described in Sections 2 and 3.

In the case of a mobile SMP with velocity V will result the superposition of two effects:

- basic tangential/circular deformations $+,-v$ as described in Section 3 for an immobile SMP;
- new tangential/longitudinal deformations $+\Delta v$ for a mobile SMP, which will be analysed below.

In an analysis of $+\Delta v$, we need to consider two phenomena that arise in conjunction with it:

1) The linear displacement of SMP with velocity V.

2) The concomitant rotation with speed $+\Omega$ for an SMPP or speed $-\Omega$ for an SMPN.

These two important phenomena are analysed below.

1) Linear displacement of SMPs with velocity V:

The new deformation $+\Delta v$ appears as an result of the mobile/dynamic state of SMP2 moving with velocity V in the direction of the axis Oy, normal to the direction O_1-O_2, relative to SMP1, which is considered to be immobile.

The velocity V must be considered against the ETH, and in this case, the velocities V of both parts of the analysed interaction need to be considered (**Figure 9**). This is because SMP1 will show the same effect if it moves with speed V_1.

First, we analyse the dynamic component $+\Delta v$ representing the change in the velocity V of the surface S/MM of SMP2 in the direction Oy, over a semiperiod $T/2$, during which the normal/radial deformation $+,-u$ of the surface S/MM of

SMP2 develops, as described in Section 3. During $T/2$ time, SMP2 travels a distance $+\Delta y = +\Delta v$.

The deformation $+\Delta v$ in the area of mobile SMP2, will be transmitted further, not spherically as FVLs but cylindrically/radially as special FVTs, throughout the rest of the ETH. The deformation $+\Delta v$ will also reach SMP1, but with values $+\Delta v'$ that decrease as $1/r^2$, according to Coulomb's law (as explained for $+,-u$ in Section 3).

The deformations $+\Delta v$ will develop longitudinally on the surface of a cylinder CL, with its axis oriented in the direction of Oy, where CL is circumscribed to the sphere of SMP2 (**Figure 9**). The deformations $+\Delta v$ will be radially transmitted from this cylinder throughout the ETH, as described above.

We also note that the deformation $+\Delta v$ has a discrete, oscillating asymmetrical character in an period T, due to the vibrating nature of $+,-u$ with which it is associated, and this oscillating character of $+\Delta v$ will be transmitted to $\Delta\gamma$ and to associated $+\Delta F_{T12}$.

The new effect $+\Delta v$ will created a change $+\Delta\gamma$ in the strains $+,-\gamma$ in ETH, including within the area AI of SMP1, and hence will produce a modification $+\Delta F_{T21}$ in the force $+,-F_{T12}$ acting on SMP1 (on a single EC), as discussed in Section 4 (**Figure 9**).

However, the specific deformations $+\Delta\gamma$ in the ETH resulting from the displacement of SMP2 with velocity V will be simple as sense, but will oscillate in the direction of the velocity, $+V$. A change in the strain $+\Delta\gamma$ will be created by $+\Delta v$, produced by the mobile SMP2, and will be accompanied by the efforts variation $+\Delta\tau$, and by the resulting variation $+\Delta F_{T21}$ of the forces $+,-F_{T12}$.

For simplicity, we will refer to the modification $+\Delta\gamma$ that is due exclusively to the speed V, which we will denote simply as $+\gamma$.

In fact, by the deformations $+\Delta v$ and $+\gamma$, respectively, created by mobile SMP2, whose *S*/*MM* will create a new dredging/training force $+F_{ST21}$ on the ETH, as discussed in Sections 4 and 6.1. According to Newton's third law of the reciprocity of forces, and as explained in Section 4, a similar change $+\Delta F_{T21}$ in the force on SMP2 due to ETH will be created, where $+\Delta F_{T21} = +\Delta F_{T12}$. This force, $+\Delta F_{T21}$, is the reaction force of the ETH on the mobile particle SMP2, in a direction opposed to its movement with velocity V.

The forces $+F_{T21}$ vary in size with distance r according to Coulomb's law, within the AI of the ETH, close to SMP1 (**Figure 9**).

In the case where SMP2 is in a dynamic/mobile state, travelling through the ETH with velocity V directed tangentially to the SMP1 direction O_1-O_2, the above dredging/training effect of the ETH will appear. This new effect consists of a component $\Delta y = +\Delta v$, oriented orthogonally to the end of the representation segment of the deformation u, but acting in the y direction, forming an angle $+\Delta\gamma$ (denoted as γ) with u or with z (**Figure 9**). Δy represents the displacement along y of the mobile particle SMP2 over the period $\Delta t = T/2$, which corresponds to the expansion of *S*/*MM* of SMP2, with $2u/2 = u$. We can therefore write:

$$\Delta v = \Delta t \cdot V \tag{33}$$

As a result, the 90˚ angle between the deformation u and the axis Oy will become 90˚ + γ (Figure 9), where $+\gamma$ represents the angle of deformation of the rectangular crystal lattice of the ETH. We can then write, using Equation (33):

$$\gamma = \frac{\Delta v}{u} = \Delta t \cdot \frac{V}{u} \tag{34}$$

The time Δt during which the deformation u is produced, with a velocity c_u of deformation of the S/MM surface of SMP2, will be:

$$\Delta t = \frac{u}{c_u} \tag{35a}$$

We introduce Equation (35a) into Equation (34) and obtain:

$$\gamma = \Delta t \cdot \frac{V}{\Delta t \cdot c_u} = \frac{V}{c_u} \tag{35b}$$

Thus, the angle $+\gamma$ of deformation of the crystalline network of the ETH (Figure 9) is proportional to the velocity V and inversely proportional to c_u. The velocity c_u can be considered to be a constant, and this will be evaluated in the future.

Hence, the new effect of V, resulting in a strain $+\gamma$, will lead to a modification of the basic force $+,-F_{T21}$, as described in Section 3, by a new force $+\Delta F_{T21}$ with dredging effect between SMP2 and ETH, corresponding to the speed V of SMP2 with respect to ETH. Assuming an elastic ETH, we can write:

$$+\Delta F_{T21} = K_{ET} \cdot \gamma \tag{36a}$$

where K_{ET} is an elastic constant to be determined in future works.

Here, we assume that SMP2 has constant velocity V over a long continuous period t_{con}, so that SMP2 in this movement can be considered a DC current.

The additional tangential force $+\Delta F_{T12} = +\Delta F_{T21}$ acting on SMP1, or on any other SMP in the ETH, will constitute the longitudinal component H_L of the field H which is generally referred to as magnetic but which in HM16 model we call the quasimagnetic field QH. The component QH_L is caused by the movement of the SMP with longitudinal velocity V via FVLs.

The presence of QH in an area AI can be associated with the presence in the AI of the specific strains $+\gamma$ of the ETH network (Figure 9).

2) Rotation of SMPs at speed +/−Ω:

This phenomenon of rotation of an SMPP/SMPN must be given the same importance as the velocity V in point **1)** to enable a correct understanding of the phenomenon of interaction between two SMPs.

We mention that for this mechanism of rotation with +/−Ω on the SMP scale, we do not have detailed information, but only the general knowledge of current physics, a multitude of phenomena involved in practically all chapters of physics.

The following paragraphs complements the discussion of HFVI in Section 2, and aims to ensure the compatibility of +/−Ω rotation phenomenon, with the

rest of the interaction mechanisms of SMPs in HFVI, previously set out in [1] and in this paper as HFVI hypothesys. HFVI provides a logical explanation of the interaction process between the SMPs in the microcosm based on the mechanism of percussion forces, which form the basis of all phenomena in physics and nature.

For this purpose, we assume that the SMPP and SMPN are mainly characterised by their direction of rotation around the Oz axis with speeds $+\Omega$ and $-\Omega$, respectively.

We also assume that the two SMPs analysed previously, *i.e.* SMP1 and SMP2, have parallel Oz axes (**Figure 9**). Regarding the senses of the two Oz axes, we can admit the existence of both orientations of the analysed pair, but we will have to admit that the results of the interactions, as percussion forces, will differ in the two cases, but similar as a mode of interaction.

Based on these general considerations, we admit that the deformations $+,-v$ in the ETH produced by the two SMPs will arise from the surface S/MM according to the mechanism described in Section 2.3.1., 2.6.

The deformations $+,-v_s$ is considered during the rotation $+,-\Omega$ of an SMP, and will form a tangent to an intermediate circle parallel to the equatorial plane of the SMP, with radius r_0. We therefore consider that $+,-v_s$ has an average value corresponding to a circle of radius r_0 at 45˚ (**Figure 9**). These deformations $+,-v_s$ of S/MM will also be transmitted to ETH in the form of deformations $+,-v$, which form the fundamental vibrations FVPP and FVPN, respectively.

For a SMPP, we assume that the deformation v_s at time t_0 constitutes an initial deformation $+v_s$, that is clockwise and positive in the active phase, PHA. This will be followed by a counterclockwise deformation, $-v_s$, in the reactive phase, PHR, followed by another deformation $+v_s$, and so on, following the mechanism presented in Sec. 2.3.1., 2.6.

3) Superposition of phenomena from 1) and 2) for SMPs:

According to the mechanism proposed in Section 2.3.1., 2.6, deformations $+,-v_s$ in the surface S/MM and their counterparts $+,-v$ in ETH develop in two phases, *i.e.* an active and a reactive phase, without impeding the continuous rotations $+,-\Omega$ of the SMP. Only the active deformation v will be transmitted by SMP to the ETH, giving a series of deformations $+v$, $+v$, $+v$, … acting on the ETH.

All of these deformations have frequency $f_T/+\Omega$, or period T, and the deformations $+v_s$ correspond to the clockwise rotation of the radius r_0 of the SMP around the axis Oz. These properties will be transmitted to the ETH as deformations $+,-v$ of the ETH with $v_s = v$ (**Figure 9**).

In the case of an SMPN, the phenomenon is similar to that for an SMPP, but with a reversal of the rotation sense, $-\Omega$.

Hence, the rotation of the SMP will give rise to a series of deformations $+v$, $+v$, $+v$, … with frequency $f_T/+\Omega$, as in point **2)**.

As a result, a two deformations vector summation will occur: one of the new

deformations $+\Delta v$ from V in period T from point **1)**, and ones on the base from rotations from **2)** $(+v)$. Thus, a series of cumulated deformations $+\Delta v_c$ will result, referred to here, as cumulative deformations:

$$\Delta v_c = v + \Delta v \quad (36b),$$

Or their associate γ strains:

$$\Delta \gamma_c = \gamma_R + \Delta \gamma_V \quad (36c)$$

These cumulative deformations $+\Delta v_c$ will have as their starting points the surface of a cylinder CL resulting from the translation of the largest circle of the sphere of SMP2, which is moving with velocity V along the Oy axis.

In this way, the trajectories of the deformations $+\Delta v_c$ will appear as spirals that evolve in time after their departure from the surface of the cylinder CL. These deformations will be transmitted to the overall ETH (**Figure 9**).

The sense of rotation of the spirals will depend on whether the particle is an SMPP or an SMPN. The mechanical effect of these deformations $+\Delta v_c$ or of associated strains $+\gamma$ will be the percussion forces $+\Delta \boldsymbol{F}_{C12}$ acting on SMP1. These are also cumulative vectorial forces, $\boldsymbol{F}_{C12}$, as are vectorial also deformations γ of their origin (36c):

$$+\Delta \boldsymbol{F}_{C12} = +,-\boldsymbol{F}_{R12} + \Delta \boldsymbol{F}_{V12} \quad (36d)$$

The force $+\Delta \boldsymbol{F}_{C12}$ will form a field in ETH called the H field, which in mainstream physics is referred to as magnetic but which in the HM16 model we call the quasimagnetic field $\boldsymbol{QH}$. As can be seen from Equation (36c), the field has two components: rotational $\boldsymbol{QH}_R$ and velocity $\boldsymbol{QH}_V$ components:

$$\boldsymbol{QH} = \boldsymbol{QH}_R + \boldsymbol{QH}_V \quad (36e)$$

The presence of $\boldsymbol{QH}$ in an area AI can be associated with the presence in the AI of the specific cumulative strains $+\gamma_c$ from (36c) of the ETH network (**Figure 9**).

The force $+\Delta F_{C12}$ will have the same effect as the Lorenz force F_L, of transverse thrust/dredging of SMP2, created by a field H on an electric charge $+,-q$ that is in transverse motion with velocity V (**Figure 9**).

The force $+\Delta F_{C12}$ is tangential and spiral (based on the two components shown in Equation (36d)), and will also produce a cumulative rotational moment $+\Delta M_{C12}$, which acts on SMP1 as explained in Section 4. This moment $+\Delta M_{C12}$ will contain the dredging effect of the force $+\Delta F_{V12}$, thus creating an additional quantum effect on SMP1.

Note that these forces will act simultaneously on SMP1, *i.e.* both the dredging force $+\Delta F_{V12}$ arising from the velocity difference V between the two components, and the forces $+,-\boldsymbol{F}_{R12}$ due to the rotations from FVTs produced by moving SMP2, as shown in Equation (36d) and described in Section 4.

In the case of a group GSMP2, the individual force $+\Delta F_{C12}$ will have a considerable size, since it is proportional to the number n of SMPs in GSMP2.

Here, we consider the contribution to the forces $+\Delta F_{C12}$ from the central string

ST_0 in the direction O_1-O_2 of the ECs, as discussed in Section 2 (**Figure 9**). The total resultant will be a tangential force F_{TCC} which is calculated by considering the set of paths l_p as set out in [8].

The orientation of the QH field will depend on the direction and sense of the velocity V of the SMP2, and also on the sense of rotation +/−Ω of SMP2, as follows: it will create cumulative, oscillating strains +,$-\gamma_c$ in ETH, inclined in the direction and sense of the velocity V, containing also rotating strains $+\gamma_R$ in the sense of +/−Ω in the AI area of SMP1 (**Figure 9**). The cumulative effect will result in a complex $+\Delta\gamma_c$ in the overall ETH.

At the same time, the QH field represents the classical properties of the magnetic field $+H$, for the inclination/orientation angles $+\gamma_c$, and rotation +,−Ω in the Oxyz reference frame, according to Fleming's rule of magnetic induction, and depending on the type of particle (SMPP or SMPN). Thus, the oscillating force $+\Delta F_{C21}$ will be of the Lorenz type, and will be exerted on SMP1 due to the velocity V and rotation +/−Ω of SMP2, and due to the effect of the oscillating moment $+\Delta M_{C21}$. The force $+\Delta F_{C21}$ and the moment $+\Delta M_{C21}$ will be imprinted to SMP1, over its own rotation vibrations +,$-u/v$ and rotations +/−Ω, resulting a complex effect containing forces/percussions F/p_p associated to displacements u/v, all of a quantum nature, because forces/percussions/displacements, act on a single EC.

But the dredging effect $+\Delta F_{CT21}$ of mobile SMP2 will be transmitted to SMP1 upon his γ_c, with a decreased effect, with r as a Coulomb type effect (**Figure 9**).

If we assume that SMP2 has a constant velocity V over a long period t_{con}, it can be considered a linear DC current, given by a string of SMP2 of P or N type, having the same orientation of Oz axes, but only considering the concomitant phenomenon of the rotation of SMP2 with speed +,−Ω (**Figure 9**).

In the case of a moving SMP2 with velocity V describing a circle as part of a spiral, with a constant radius R over a long period t_{con}, the SMP2 can be considered a solenoid containing a DC current, with a specific strong QH field at the inner part of the radius R (**Figure 9**). This strong QH field is caused by the concentration within a limited zone of radius R of all the paths of the deformations u/v, from the half of the linear current case, but only considering the phenomenon of rotation of SMP2 with speed +,−Ω. This results in a complex effect upon SMP1, involving forces F and displacements u/v of a quantum nature.

6.3. Energetic Aspects

As set out in Sections 6.1 and 6.2, the energy ΔE_U is related to the percussions +,$-p_n$ and +,$-p_t$, including the related forces +,$-F_{L21}$ and +,$-F_{T21}$, respectively, which change their point of application and produce mechanical work L, which will come from the potential energy U of the SMP2−GSMP1 system, energy left since its creation. Such energy will be released by the movement of SMP2 at speed V (**Figure 9**). This situation also corresponds also to the proper application of the general law of Lorenz force [10] [11]:

$$F = qE + qv \times B \tag{37}$$

The potential U energy of the SMP2-GSMP system is stored in the $QE + QH$ fields.

In this case, the energy $+\Delta E$ taken from the potential energy U is associated with the SMP2-GSMP1 system of MPs disposed in the neighbouring AI of SMP2, from ETH. The transfer will take place through the QE or QH fields. These quasielectric and quasimagnetic fields create the percussion forces $+,-p_n$ and $+,-p_t$ and the associated forces $+,-F_{L21}$ and $+,-F_{T21}$, to give the associated moments $+M_{L21}$ and $+M_{T21}$, fields, which will imprint to SMP2 the speed V, or the speed increase $+\Delta V$ and the rotation increase $\Delta\Omega$ respectively (**Figure 9**).

It should be noted that the specific deformations $+,-\varepsilon$ and $+,-\gamma$ corresponding to deformations $+,-u$ and $+,-v$ may vary in space. The deformations $+,-u$ and $+,-v$ appear in the ETH due to the change in the reference distance r, through V between two SMPs, which are initially immobile in the ETH (also considered immobile). These deformations will be produced by one of the SMPs, which moves at velocity V through the ETH.

The initiation of the displacement with velocity V through the ETH of SMP2, occurs under the influence of the field $QE + QH$. SMP2 also gains rotational movement with a change of speed $\Delta\Omega$, as a subtle quantum effect (**Figure 9**).

7. Mechanism of PH Emission and Movement with Speed *c* in the ETH

Here, we discuss a possible approach to compiling and operating a PH that travels freely into space, and therefore within the ETH, at speed c.

We assume that the PH can be considered an ESMP, *i.e.* that the basic composition consists of ECs of PCs (including quarks). Simple etherons (ETs) inside any SMP are likely to be grouped into PCs. We assumed in [1] that the composition of ECs and their grouping within ETH is based on a crystal type body, according to the HM16 ether model, Type A. An EC cell comprises a small number (maybe two to eight) of ETs, while a PC comprises a larger number of ETs.

We assume that the PH comprises a large number of etheronic cells PCs of particle type, that are assembled in the form of a PH compact body, constituting an autonomous PAC as described in Section 1 (**Figure 10**).

In HFVI, we admit that PH moves through the ETH at a specific speed c, without training in its displacement, the ECs cells encountered, which remain in place as ECs at the same fixed point M, like initial ECs, at the same M point, after PH's passage through point M. The PH behaves like a vortex that entrains ECs only in its vortex movement only within its own volume V, along its path.

This mode of movement of a PH in the ETH without transporting ECs has also been considered in regard to the MH16 model [1], a hypothesis that became useful only here for the best functioning of the PH.

We admit in HFVI that the PH can be created by a pair of particles SMP1/SMP2 or a GMP that is organised in a certain stable form for a while.

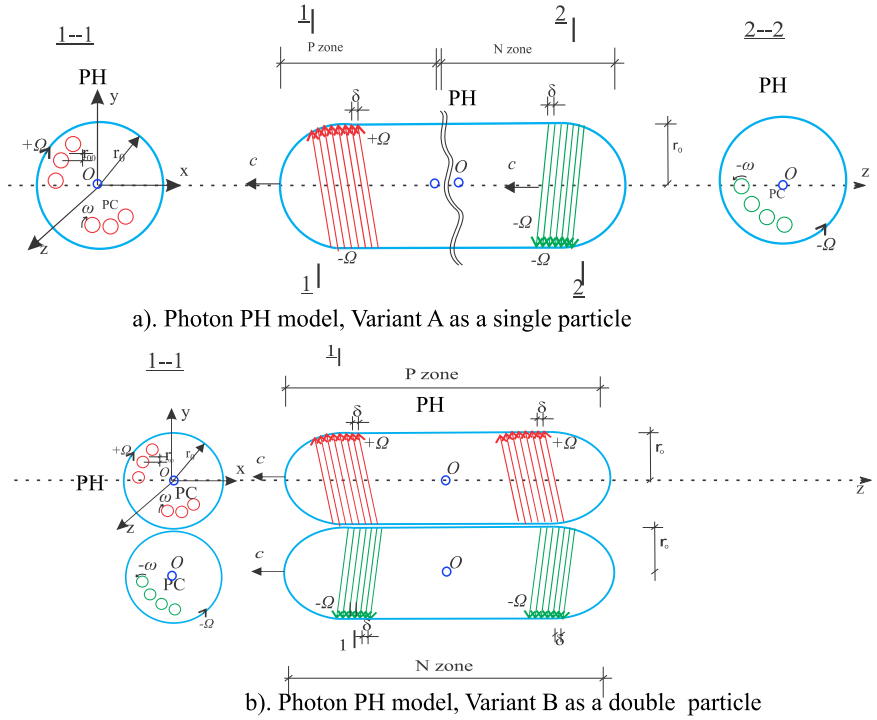

a). Photon PH model, Variant A as a single particle

b). Photon PH model, Variant B as a double particle

Figure 10. Physical mechanism of movement of a PH in the ETH with velocity c based on the hypothesis of scrubbing.

A PH is created when the energy level E of an MP or GMP decreases by $-\Delta E$ for some reason, usually after a prior energy increase of $+\Delta E$. The creation of a PH consists of the expulsion at the speed of light c of a PH by a pair of MPs, and this PH will take the equivalent energy E_{ph} from the MPs or GMP, where $E_{ph} = \Delta E$. In the HM16 ether model, we assume that the received energy ΔE is stored in the PH within the PP, permanently in a vibrational state with vortices of rotation speed ω, either individually or grouped into certain PC/quark-type.

In the case of the creation of a PH with energy E_{ph}, the mass m of the MPs will also have to be reduced by $\Delta m = E_{ph}/c^2$, corresponding to a certain number of PC cells. This is Variant 1 for the transformation of the mass m of some PCs into the energy transmitted to PH, since the PCs are also the carriers of the mass Δm of the MP/SMP.

The energy difference $-\Delta E$ will be entirely found in the PH photon, as vortices/vibrations of ECs/PCs, temporarily contained in the PH's volume that moves at speed c and, likewise, the mass difference Δm must also be found in PH.

Since at least one SMPP and one SMPN are involved when the PH is created by annihilating pairs of particles, the resulting PH will have to comprise two areas with characteristics specific to these SMPs. Additional support for this mechanism also arises from the phenomenon of the creation of pairs (Section 2.5), when a PH turns into an SMPP and an SMPN.

We admit in HFVI that the PH will have an ellipsoid shape, including a positive zone (PZ) in which its own sense of rotation will be clockwise (considered

positive), and a negative zone (NZ), in which the sense of rotation will be counter clockwise (**Figure 10**).

These two areas can be coupled either in series or in parallel (**Figure 10(a)** and **Figure 10(b)**).

In photon Variant VPH 1, we assume that the two zones (PZ and NZ) are coupled in series, forming a single ellipsoid (**Figure 10(a)**), while in Variant VPH 2, we assume that they are coupled in parallel to form a double ellipsoid (**Figure 10(b)**).

In photon Variant VPH 3, we assume that the two zones (PZ and NZ) are complete separated, forming two simple ellipsoids (**Figure 10(a)**-adapted), which are moving separately, which correspond to simultaneous emission of two PHs.

The energy ΔE will be transmitted over a short period of time to the PH by two types of kinetic: kinetic energy of displacement E_{dis} at speed V, and rotation energy E_{rot} at rotation speed Ω.

These two movements, one involving linear advance, and the other involving the rotation of the PH in the ETH, will be produced by periodic percussion forces p_{sn}-normal and p_{st}-tangential applied to the PH by the S/MM of the two MPs. Percussions will be applied via associated vibrations $+,-u$ and $+,-v$ of the PC$S/MM$ in final contact with PH at the time of its detachment from the two MPs (**Figure 10**).

After the detachment of the PH from the SMPs, it will produce in ETH its own percussions p_s in the same way as an ESMP, which will simultaneously create own FVLs and FVTs of the ECs of the surrounding ETH.

The movement of the PH at speed c starts with the two SMPs imprinting of the τ-type efforts on its lateral surface S/MM, creating a sudden rotation of the PH with the speed $+,-\Omega(\nu)$, which will be applied differently to the two zones, PZ and NZ of the PH (**Figure 10**).

This correlation will also be guided by the nuclei NUs, considering the role of those NUs of the SMPs, involved in the creation of the PH, according to the SMPAC hypothesis presented in Section 1. Thus, the speed c resulting from the advancement process by its double screwing in ether will be imprinted to PH (**Figure 10**).

Simultaneously, the efforts of type σ from the percussions p acting on the back surface S/MM of the PH may contribute to the launch/creation of the PH by imprinting speed c.

We put forward here the hypothesis of scrubbing (HS) as a valid and feasible in the physical reality in which the PH starts and moves through the ETH due to a screwing process in the ETH. We assume here that the PH has a hydrodynamic ellipsoid shape, and to simplify the calculations we will approximate this ellipsoid by an elongated cylinder of equivalent volume (**Figure 10**).

This process of displacement at speed c occurs due to the rotation of this ellipsoid /cylinder around its longitudinal axis with rotation speed/frequency Ω/f. We assume that the surface/membrane S/MM of the PH's ellipsoid, has certain regular striations or protrusions, which may play the role of a spiral helical thread

arranged around and along the ellipsoid, differentiated by the directions of rotation in the two zones (PZ and NZ) of the PH, with step size δ specific to each PH (**Figure 10**).

The HS is based on a simple process that facilitates the advance of a certain body into a compact, penetrating environment, by scrubbing. The validity of the HS can be initially confirmed by the theoretical results it provides, as shown below.

In the HS, for a PH with frequency ν (here we use the Greek ν rather than f) and a spiral step δ, moving through the ETH at speed c, we have the equation:

$$c = \delta\nu \tag{38}$$

We will denote the initial mass of the PH as m_P and apply to it the equation of total energy E_{ph}:

$$E_P = m_{ph}c^2 \tag{39}$$

If we also take into account Planck's law [11], we can write:

$$h\nu = E_{ph} \tag{40}$$

Combining (39) with (40) gives:

$$h\nu = m_{ph}c^2 \tag{41a}$$

$$m_{ph} = \frac{h\nu}{c^2} \tag{41b}$$

If we multiply by c in Equation (41a) we get:

$$m_{ph}c = \frac{h\nu}{c} = \frac{h}{\lambda} \tag{42}$$

We introduce c from Equation (38) into Equation (41b) to give:

$$m_{ph}\delta\nu = \frac{h\nu}{c} \tag{43}$$

Simplification with ν in Equation (32a) gives:

$$m_{ph}\delta = \frac{h}{c} \tag{44}$$

From Equation (44), given that the product $c.m_{ph}$ represents the pulse p_{ph} of the PH, we obtain:

$$\delta = \frac{h}{m_{ph}c} = \frac{h}{p_{ph}} \tag{45}$$

Equation (45) can be generalised using de Broglie's theory to any MP of mass m, pulse p and speed $v < c$ moving through the ether, also through the phenomenon of scrubbing with its own step δ, giving:

$$\delta = \frac{h}{mv} = \frac{h}{p} \tag{46}$$

We now apply Equation (45) to the case of a photon with any frequency ν, for which the resting mass is m_{ph} in Equation (41b):

$$\delta = \frac{h}{\frac{h\nu}{c^2}c} = \frac{c}{\nu} = \lambda \tag{47}$$

So for a PH of frequency ν moving through the ether by scrubbing, the thread step δ is equal to the wavelength λ, equivalent to the frequency ν. This result confirms the well-known physical phenomenon of advancing a drill by rotation into a compact environment, and hence the HS is theoretically confirmed.

8. Conclusions and Consequences

In this article, we have presented a new way of constructing SMPs as complex cells such as LCs, with their own MM, PP, and NC.

A complex hypothesis called HFVI for the interaction between SMPs was developed based on periodic percussion forces $+,-p_p$ created by the FVs produced by any SMP in the ETH upon a single EC. We have shown that these percussions $+,-p_p$ are the smallest forces occurring in the interactions between any two SMPs, and are periodic with associated deformations $+,-u/+,-v$, at a frequency f, with energy of $+,-p_p$ upon a single EC, representing Planck's constant h as a physical phenomenon related to quantum actions between particles.

Based on the FVs of SMPs, which create periodic linear $+,-u$ and transversal $+,-v$ deformations in the ETH, and which vibrate and act simultaneously, it was possible to establish the physical nature of the electrical charges $+,-q$, given by the specific rotation $+/-\Omega$ and vibration of an SMPP and of a SMPN, *i.e.* positively and negatively charged SMPs, respectively, starting from the moment of creation of this the pair, due to a PH photon.

Based on this knowledge of the physical nature of the electrical charges $+,-q$ generated by SMPs producing specific FVs, it was possible to confirm the manner of interaction between two SMPs through $+,-F_{L21}$ forces as completed Coulomb's type attraction/repulsion forces F_{CC} between two SMPs, via normal $+,-p_n$ percussion forces upon a single EC generated by specific longitudinal FVL vibrations.

The nature of magnetic interaction could also be confirmed in the case of movements with velocity V between two SMPs, via tangential percussion forces $+,-p_t$, upon a single EC generated by specific FVTs created by the particles.

So a mechanism for interactions between SMPs was proposed based on the velocity V and the rotation speed Ω of the SMPs. This results in explaining the properties of the quasielectric field QE, given by specific ordered/oriented strains $+\varepsilon$, and the properties of the quasimagnetic field QM, given by specific ordered/oriented strains $+\gamma$ created by a GSMP of the same type of particle (+/P or −/N) that are ordered and moving together. This mechanism also considers the associated forces $+F_{L21}$ and $+F_{T21}$, of the $+,-p_n$ and $+,-p_t$ percussions, for an SMP in the ETH.

Based on the periodic percussions $+,-p_p$, a scrubbing mechanism was postulated for the start and movement at speed c in the ETH of a photon PH, which

can be considered as being made up of two zones with opposite rotations traveling without transporting matter, only energy.

Based on these new results, the validity of our complex hypothesis HFVI is theoretically confirmed.

As a general consequence, it follows that there is a need for the HM19 model of the ether and the above HFVI hypothesis to be accepted into mainstream physics. Concomitantly it must renounce at classical SRT, GR, gravity, electromagnetism theories.

Therefore will resulting in a new NPHM19 physics, based on the ether ETH, starting from the HM16 model, which will be able to provide a physical explanation of quantum mechanics as true classical mechanics phenomena in microcosm based on periodic percussion forces p_p upon a single EC NPHM19 can be developed on these new basis by a broad community of open-minded physicists released by SRT, who will be necessary to guide the main theoretical concerns and experimental research on NPHM19 towards new areas.

It will obviously be necessary to correct certain assumptions, reasoning or calculations in our previous works, that may prove to be incorrect in future. In this way, NPHM19 will be able to give correct new answers to some of the many unresolved questions and problems in physics, astronomy, chemistry, biology and other fields. However, some unanswered questions will still remain and new questions will also constantly arise.

We believe that the human mind is able to encompass, understand and resolve situations in nature at increasingly profound levels, both at the microcosmic and macrocosmic levels, but only in a step-by-step way; a definitive ultimate truth is probably too far away to be touched.

Acknowledgements

The first author gratefully acknowledges initial advice on the subject and encouragement from his late professor N. Barbulescu, a Sommerfeld follower. He is also sincerely grateful to late Prof. P. Mazilu from TUCB Bucharest, for his rigorous lessons on rationality, and is indebted to Gen. Prof. G. Barsan, Col. Prof. Al. Babos from LFA Sibiu, Prof. D. Stoicescu from ULBS Sibiu, Prof. D. Siposan from MTA Bucharest, and Ms Veronica Has from Bucharest, for their support.

Conflicts of Interest

The authors declare no conflicts of interest regarding the publication of this paper.

References

[1] Has, I. and Miclaus, S. (2017) *Physics Essays*, **30**, 45-56. https://doi.org/10.4006/0836-1398-30.1.45

[2] Has, I., Miclaus, S. and Has, A. (2017) *Physics Essays*, **21**, 303-312. https://doi.org/10.4006/1.3038751

[3] Has, I., Miclaus, S. and Has, A. (2015) *American Journal of Modern Physics*, **4**,

97-108. https://doi.org/10.11648/j.ajmp.20150403.11

[4] Has, I., Miclaus, S. and Has, A. (2014) *Optics*, **3**, 24-32. https://doi.org/10.11648/j.optics.20140304.11

[5] Has, I., Miclaus, S. and Has A. (2018) *Journal of Applied Mathematics and Physics*, **6**, 1886-1895. https://doi.org/10.4236/jamp.2018.69160

[6] Has, I., Miclaus, S. and Has, A. (2019) *Journal of Physics*: *Conference Series*, **1251**, 1-24. https://doi.org/10.1088/1742-6596/1251/1/012020

[7] Has, I., Miclaus, S. and Has, A. (2018) *Journal of Applied Mathematics and Physics*, **6**, 1507-1521. https://doi.org/10.4236/jamp.2018.67127

[8] Has, I., Miclaus, S. and Has, A. (2019) *Journal of Modern Physics*, **10**, 1090-1124. https://doi.org/10.4236/jmp.2019.109071

[9] Constantinescu, L., Tanasescu, P., Radulescu, M., Doicin, D., Rosca, V., Enescu, D., Candea, I., Constantinescu, P. and Barbu, M. (1965) Geophysical Prospecting Vol. II. Editura Tehnica, Bucharest, 215-286. (In Romanian)

[10] Barbulescu, N. (1962) Elements of General Physics. Editura Didactica & Pedagogica, Bucharest, 283-344. (In Romanian)

[11] Spolski, E.V. (1954) Atomic Physics I. Editura Tehnica, Bucharest, 234-240. (In Romanian)

Journal of Modern Physics, 2020, 11, 854-885
https://www.scirp.org/journal/jmp
ISSN Online: 2153-120X
ISSN Print: 2153-1196

Galactic Haloes from Self-Interacting Neutrinos

Richard B. Holmes

The Boeing Company, Chicago, USA
Email: rholmes001@aol.com

How to cite this paper: Holmes, R.B. (2020) Galactic Haloes from Self-Interacting Neutrinos. *Journal of Modern Physics*, **11**, 854-885.
https://doi.org/10.4236/jmp.2020.116053

Received: May 10, 2020
Accepted: June 1, 2020
Published: June 4, 2020

Abstract

The objective of this research is to provide an explanation of galactic haloes using established particles and forces using recent theoretical developments. Light fermions, with masses on the order of 1 eV/c^2, are not a leading candidate for dark matter because of their large free-streaming scale length and their violation of the Tremaine-Gunn bound. With a self-interaction of fermions, the free-streaming scaling length is reduced, and the tenets of the Tremaine-Gunn bound are not applicable. Binding of neutrinos via a feeble SU(3) force is considered as a model for such interactions. The assumed sum of masses of the three neutrino flavors is 0.07 eV/c^2. The resulting form of matter for such bound neutrinos is found to be a degenerate Fermi fluid. Pressure-equilibrium approaches applied to this fluid provide cuspy solutions and match observationally-inferred profiles for galactic haloes. Such approaches also match the observed total enclosed mass for galaxies similar to the Milky Way. The computed structures are found to be stable. The hypothesis is considered in view of observationally-inferred halo-halo interactions and gives results that are consistent with the observed Bullet cluster halo interaction. The theory gives agreement with observationally-inferred properties of dark matter near earth. Questions related to interaction rates, consistency with SN1987a data, the cosmic microwave background, the issue of SU(3) interactions between neutrinos and quarks, free-streaming after neutrino decoupling, and dark-matter abundance are addressed in a companion paper.

Keywords

Galactic Haloes, Dark Matter, Halo-Halo Interactions

1. Introduction

Dark matter (DM) has been postulated to take many forms, including hot dark matter [1] [2], warm dark matter [3] [4], massive compact halo objects [5] [6]

[7], weakly interacting massive particles [3], and cold dark matter (CDM) [8] [9]. The conventional picture of neutrinos as dark matter was ruled out early [10]. The best current model for CDM is the Λ-CDM model [11], which assumes a certain fraction of the matter in the universe is cold (non-relativistic), non-interacting, and stable [12]. However, the model has a number of open issues [13] [14]. In particular, there is no explanation for dark matter. Massive neutrinos as inserted in the Standard Model have been postulated for dark matter [1] but rejected because in the conventional view neutrinos are almost always relativistic particles so any structure would diffuse away quickly and could not lead to the structures observed in the universe today. There are currently many hypothetical explanations for dark matter. Extensions to the Standard Model have been proposed to explain dark matter, dark energy, and other aspects of cosmology, e.g. [15] [16] [17] [18] [19]. QCD-like and nuclear like forces have recently been suggested for self-interacting dark matter, e.g. [20] [21]. In this paper, an SU(3) force applied to neutrinos is hypothesized as an explanation for galactic haloes, and by extension, DM.

The standard view posits that DM was in thermal contact with visible matter in the early universe when the temperature was much greater than the DM mass. In those eras, the DM number density would be comparable to photon number density. If the DM number density was still comparable to the photon number density when it froze out, it would overproduce the observed amount of DM mass when the DM particle mass is more than about 1 eV/c^2 [22]. Thus, there is a need to deplete the abundance of any massive dark matter that is sufficiently cold at recombination. This is the path that leads to DM particles that are required to be largely annihilated in the early universe. An interaction energy of 100 GeV ~ kT leads to a weak interaction cross section that when multiplied by the density and velocity at that time leads to a decay rate comparable to the expansion rate. Here k is Boltzmann's constant and T is the temperature. This would result in freeze-out at that early time in the primordial universe for the corresponding particle mass. Hence DM masses of order 100 GeV would be candidates for DM under these standard assumptions. These would become extremely cold (non-relativistic) over the eons as the universe expanded.

Thus, the most anticipated masses of cold dark matter are associated with weakly interacting massive particles (WIMPs), with masses in the range of 10 to 100 GeV. However, in the absence of significant evidence of massive DM, the community is looking to lighter alternatives. To avoid the free-streaming issue with lighter DM, one approach is for DM to bind and/or cool early in the history of the universe. One might look for particles and/or forces for which such cooling and binding occurs. Such behavior might be analogous to the binding via SU(3) of quarks into hadrons in the early universe.

In the past 4 decades, computationally-intensive approaches have investigated the consistency of lighter DM with astronomical observations. Such investigations began with [10] regarding the possibility of neutrinos for dark matter. Reference [23] investigated consistency of dark matter with Lyman-α lines. Early

modeling on light DM and self-interacting DM (SIDM) include [24] with elastic collisions and [25] on gravothermal collapse. Reference [26] simulated subhaloes and [27] considered the impact of fermions. More recently, [28] [29] performed extensive modeling of galaxy formation within larger structures in the Universe, [30] investigated an effective theory for small scale structure, [20] [31] considered SIDM and halo interactions, [32] considered the impact of SIDM on structure and self-assembly history, and [33] modeled SIDM that includes inelastic scattering. There have been recent reviews of SIDM by [21] and of the larger topic of dark matter haloes and subhaloes by [34]. Most of the more recent papers consider particles with masses of the order of a keV/c^2, as is consistent with observationally inferred values from the latest Lyman-α forest absorption measurements [35] and gravitational lensing measurements [36]. However, both these observationally-inferred mass bounds and the other aforementioned papers rely on assumptions that are not consistent with relativistic fermions with a mass of order 0.1 eV that bind into a number of species of heavier particles in the primordial era, which then further bind into macroscopic structures later.

Section 2 considers the basic application of the SU(3) hypothesis to neutrinos in the early universe. Section 3 compares the predictions of the hypothesis to the observed small- and large-scale structure of the universe. Section 4 discusses the hypothesis in the context of the Tremaine-Gunn bound. Section 5 computes the properties of the proposed bound neutrinos near earth. Section 6 discusses the self-interacting properties of the proposed DM in haloes and between haloes. Section 7 summarizes the overall findings of this effort.

2. The Feeble SU(3) Hypothesis and Neutrinos

The hypothesis of a feeble form of SU(3) for the neutrino family is not immediately obvious from the standard model. From the standard model one might expect an interaction energy of the order of the QCD energy scale, ~200 MeV [37]. However, motivation can be found for a feeble SU(3) interaction between neutrinos in a modest extension of the standard model [38]. In this extension, SU(3) is not precluded for the neutrino family. In this theory, neutrino oscillations are direct evidence that neutrinos form bound states via SU(3). As shown in **Appendix A**, this extension also provides a means for estimating the neutrino interaction strength by scaling the quark interaction strength by $\left(m_\nu/m_q\right)^2$, where m_ν is the mass of the highest-mass neutrino and m_q is the mass of the highest-mass quark of the up or down families. This scaling applies when the interaction involves relativistic neutrinos. Using m_ν of about 0.055 eV/c^2 for the tau neutrino for minimal neutrino masses and the normal hierarchy [39] one finds a reduction in the SU(3) strength for relativistic neutrinos by a factor of 1.73×10^{-22} to 1.01×10^{-25} using the bottom quark or top quark, respectively, for m_q. This theory also has the property that in addition to the 8 massless gluons, there are 15 massive Goldstone bosons (massive gluons) for each family with gluon energies of the order of $m_\nu c^2$. These massive gluons satisfy most of the cri-

teria proposed by [17] for a correction to the observed effective number of neutrinos. This extended form of SU(3) will be denoted $SU(3)_{ve}$ and the standard form of SU(3) applied to the neutrino family will be denoted $SU(3)_{vs}$. It will be seen that both forms of SU(3) are consistent with galactic halo data, but the former provides estimates of binding energies and particle masses whereas the standard SU(3) does not.

What are the consequences of a feeble analogue of quark confinement with neutrinos? Neutrinos typically start out as ultra-relativistic isolated particles near infinite redshift. In the early universe, the neutrinos would have formed a neutrino/neutrino-gluon plasma, much as would have occurred with quarks and gluons. By analogy with quarks, neutrinos would be bound into "mesonic" or "baryonic" neutrinos, and they would then remain confined to the present day. When excited with sufficient energy, perhaps by hot stellar neutrinos, such bound states might "hadronize" to form additional bound neutrinos while remaining confined, analogous to the behavior of quarks we see today.

Table 1 shows that the partition of energy using the standard approach, e.g. [40], applied to the hypothesis. It is seen that both forms of SU(3) can supply a fraction of the mass-energy that corresponds to the modern estimate of the fraction of mass-energy in the dark matter sector, about 84% [41]. The confined baryonic neutrinos would hold the vast reservoir of the mass-energy of SU(3) neutrino gluons shown in Table 1.

When would the above interactions terminate? Such neutrinos should "hadronize" when their total center-of-mass (CM) collision energy exceeds about $4m_{v\mu}c^2$, where $m_{v\mu}$ is the mass of the muon neutrino, by analogy with the quark families, assuming the normal hierarchy. Hence this limits the maximum kinetic energy to about $m_{v\mu}c^2$ for each particle. Also, there is no interaction pathway to hadronize when the total CM energy of any neutrino state is less than $4m_{ve}c^2$. Here m_{ve} is the mass of the lowest-mass neutrino, the electron neutrino in the normal hierarchy. This gives a range of kinetic energies from $m_{ve}c^2$ to $m_{v\mu}c^2$ in the CM frame, and about a factor of 2 more in the local rest frame in the early universe. From our current knowledge of neutrino masses in the normal hierarchy,

Table 1. Energy density degrees of freedom in the early universe with kT at ~1 MeV assuming standard SU(3) for neutrinos, $SU(3)_{ns}$, and an extended version, $SU(3)_{ne}$.

Particle	Degrees of Freedom, $SU(3)_{vs}$	Degrees of Freedom, $SU(3)_{ve}$
Electron family	(1)(4) = 4 (×7/8)	(1)(4) = 4 (×7/8)
Photons	2	2
Neutrino family	(3)(2)(3) = 18 (×7/8)	(3)(2)(3) = 18 (×7/8)
Neutrino family gluons	(8)(2) = 16	(15)(3) + (8)(2) = 61
Total degrees of freedom	37.25	82.25
Total degrees of freedom in neutrino sector	31.75	76.75
% Degrees of freedom in neutrino sector	83.9%	93.3%

$m_{ve}c^2$ ~ 0.005 eV and $m_{v\mu}c^2$ ~ 0.01 eV [39]. The implied approximate range of steady-state mean thermal kinetic energy is (3/2)kT = 0.01 to 0.02 eV, *i.e.* kT = 0.007 to 0.014 eV. For the inverted hierarchy, the range of kT is 0.007 to 0.07 eV assuming appropriate adjustments of the above masses. These estimates for kinetic energies would apply at the end of the hypothesized period of neutrino binding into baryonic neutrinos; further evolution would be expected as the universe expands.

3. Consistency of the Hypothesis with the Size and Shape of Galactic Haloes

3.1. Equations and Inputs for Spatial Structure of DM

The spatial density profile derived from the hypothesis of bound neutrinos is compared to observationally-inferred galactic halo structures. The characteristic scales sizes of galaxies for ordinary radiant matter (OM) are 1 - 200 kpc depending on the galaxy and somewhat larger for the associated haloes [42].

To analyze the spatial distribution of low-energy neutrinos or other weakly interacting particles, an N-body simulation [20] [31] or the Vlasov equation is typically preferred [43]. Herein, two simplified governing equations are considered for DM density profiles. The first is the standard equation for hydrostatic equilibrium in a spherically-symmetric geometry. This equation is known to be inadequate for dark matter haloes, as further shown below. This equation is given by

$$\left(1/\rho\right)\left(\mathrm{d}P/\mathrm{d}r\right) = -m_{bv}M_{enc}\left(r\right)G/r^2 \ . \tag{1}$$

Here ρ is the number density of DM, P is the pressure, r is the radius, m_{bv} is the mass of a DM particle, $M_{enc}\left(r\right)$ is the enclosed mass, and G is the gravitational constant. This equation can be solved using the well-known Lane-Emden formulation [44] if pressure is a function of density only:

$$P = c_\gamma \rho^\gamma \ , \tag{2}$$

where c_γ is a constant for a given polytropic exponent γ. An inhomogeneous form of the Lane-Emden equation can be used when OM is present. As shown later in this section, initial calculations using Equation (1) with a galaxy similar to the Milky Way for OM do not match key published results from simulations or inferences from observations for DM. In particular, the solutions have no cusp at the origin, and are a poor match to the standard de-projected Sersic or Einasto profiles based on observations [42] [45]-[51]. This is found to be true for any polytropic exponent between 4/3 and 2.

To address this, a generalization of Equation (1) is used. The derivation and the properties of the resulting equation are given in [52]. The basic result is

$$\begin{aligned}&\left(1/\rho\right)\mathrm{d}P/\mathrm{d}r + \left(1/\rho\right)\left(\mathrm{d}\rho/\mathrm{d}r\right)\left[m_{bv}M_{enc}\left(r\right)G/r\right]\\ &= -m_{bv}M_{enc}\left(r\right)G/r^2 - \left(\mathrm{d}P/\mathrm{d}\rho\right)/r\end{aligned} \tag{3}$$

when pressure is assumed to be a function of density only. It can be seen that

this equation reduces to Equation (1) when the second terms of both sides of the equation are negligible. When all terms are included, Equation (3) is seen to give a $1/r$ dependence for the density. Equation (3) with a total mass constraint and a density constraint is the most justifiable based on theoretical considerations, comparisons with data, and comparisons with others' calculations and simulations. This best-justified result is given by

$$\rho(r)=\begin{cases}\rho_0 \text{ in a spherical region about the origin of radius } r_0, \text{ or}\\ \rho(r) \text{ satisfies } \dfrac{\mathrm{d}\ln\rho}{\mathrm{d}\ln r}=-1-2\left(\dfrac{r}{r_c}\right)\left(\dfrac{\rho_c}{\rho}\right)\end{cases} \tag{4}$$

In this equation, r_c is the cutoff radius and ρ_c is the cutoff number density where the density drops due to the mass constraint. The last key equation used for calculations of haloes is the Fermi-Dirac equation for the number density given temperature T and particle mass m_{bv}:

$$\rho=n_s\Big/\left(2\pi^2\hbar^3\right)\int p^2\mathrm{d}p\Big/\left[\exp\left(\left\{\left[(pc)^2+\left(m_vc^2\right)^2\right]^{1/2}-m_vc^2-\mu_v\right\}\Big/kT\right)+1\right], \tag{5}$$

where n_s is the number of spin states and p is the fermion momentum. Note that the general form is used, applicable to both relativistic and non-relativistic states. The chemical potential is denoted by μ_v and will be estimated later. Note that for trapped neutrinos the chemical potential may be non-zero, as with ordinary bound matter. Equation (5) yields the result $P=\left(1.914\hbar^2/m_{bv}\right)\rho^{5/3}$ for non-relativistic fermions with two spin states. This equation is used to set the density at the origin, and then Equation (1) and Equation (2) or Equation (4) are used to generate a spatial profile. The resulting solution of Equation (4) for number density $\rho(r)$ can be expressed as a function of its inputs, $\rho(r)=\rho(r,\rho_0,r_0,\rho_c,r_c)$. Using Equation (5), $\rho(r)$ can also be expressed as a function of temperatures and mass, $\rho(r)=\rho(r,T_0,r_0,T_c,r_c,m_{bv},\mu_v)$, where T_0 is the temperature at the origin, T_c is the temperature corresponding to the cutoff density ρ_c, and the other variables are defined above. This notation will be used below.

To solve Equation (1) and Equation (2), an equation of state that relates pressure to density and temperature must be chosen. In many treatments in astronomy and astrophysics, the pressure is a function of density only as in Equation (2), yielding an implicit relationship between temperature and density. One natural choice that relates temperature and density is Equation (5). The relativistic and non-relativistic versions have been used to derive the equation for the density in dwarf stars [53] [54]. The relativistic and non-relativistic versions give polytropic exponents of 4/3 and 5/3, respectively. The latter choice might be expected to be a good one for a cool fermionic gas.

As another option for the polytropic exponent, one may look for physical models in the literature for chargeless baryonic particles in a gravitational field. Such a model can be found in treatments of neutron stars. Treatments of neutron stars typically use a polytropic exponent ranging from 3/2 to 2, with near 2 as the most common and most likely choice [55] [56] [57]. Such an exponent is

also present in the van der Waals equation of state. Thus, a choice $\gamma = 2 - \varepsilon$ with $0 < \varepsilon \ll 1$ is also considered below for galactic haloes.

To complete the initial conditions, the density at $r = 0$ must be known or assumed. Given the discussions at the end of Section 2, one expects kT to be in the range of 0.007 to 0.07 eV near galactic centers at the time of halo formation. This range of temperatures corresponds to a range of densities given by Equation (5).

Such a range of mean kinetic energies is considered in combination with the possible range of masses of baryonic neutrinos. As given in **Appendix A**, the range of masses considered for baryonic neutrinos is 0.025 to 0.6 eV/c^2. A possible range of key properties of a fermion gas is shown in Table 2. In particular, the table assumes a temperature of 0.0134 eV/k = 155 K, which is found to give good agreement with density profiles of galactic haloes inferred from data, as will be shown in the next section. From Equation (5) one then obtains a number density, shown in the second column (with the chemical potential initially set to zero). The third column shows the root-mean-square (RMS) velocity, v_{rms}, which is obtained from the well-known relation between relativistic velocity and kinetic energy. The fourth column shows the energy density computed using $\rho m_{bv} c^2 \Big/ \left[1 - \left(v_{rms}/c\right)^2\right]^{1/2}$.

From this table, one sees a range of mildly relativistic velocities. These velocities are not consistent with gaseous dark matter that is bound in galactic haloes solely by gravitational attraction, since the escape velocity for a galaxy is typically of the order of 500 km·sec^{-1} [41]. To address this issue, one may recall the analogous states of baryonic quarks, which form atomic nuclei or neutron stars, as mentioned above. In the absence of electrostatic repulsion, nuclei can be of unbounded size, according to the Weizsacker model [58]. Hence, one might surmise that baryonic neutrinos form a similar macroscopic state in which very weak binding occurs (but not binding with other forms of matter).

Such a binding energy between neutrinos in baryonic states would need to be at least the mean kinetic energy, *i.e.* the value of about 0.02 eV in order to avoid the free-streaming issue. To estimate such a binding energy, one might consider the nuclear binding energy of about 15 MeV per nucleon and use the ratio of the

Table 2. Tentative range of key properties of a baryonic neutrino medium near a galactic center[a].

Mass (eV/c^2)	Number Density, $\rho_{0,mv}$ ($\times 10^{15}$ m^{-3})	RMS velocity/c	Energy Density (GeV·cm^{-3})
0.025	0.185	0.83	0.0083
0.05	0.36	0.70	0.0250
0.10	0.81	0.55	0.0966
0.2	2.01	0.42	0.441
0.3	3.55	0.35	1.13
0.4	5.34	0.30	2.23
0.6	9.58	0.25	5.91

[a]Assumes a mean kinetic energy of 0.02 eV, corresponding to a temperature of 155 K as described in text.

mass of a baryonic neutrino to that of a neutron. Such a scaling gives a binding energy of about (15 MeV) × (0.4 eV)/(939 MeV) = 0.0064 eV between neutrino-based baryons. This linear scaling of baryonic binding with particle mass is partially justified by **Appendix A**. One might also envision a binding between up to six neighboring baryonic neutrinos (divided by two since bonds are shared), leading to a total binding energy up to about 0.0192 eV, which is comparable to the mean kinetic energy of 0.02 eV given above. A more detailed ab initio calculation is beyond the scope of this paper. However, these estimates of binding energy and thermal kinetic energy are roughly consistent with what is required from the virial theorem for a medium in equilibrium ($\langle K.E.\rangle = n\langle V\rangle$ with $n=-1$ for massless gluons or gravity and $n\sim 1$ for a *br* inter-particle potential, where "$\langle K.E.\rangle$" denotes a time average of the total kinetic energy and "$\langle V\rangle$" denotes the time average of the total potential energy).

With estimates for a binding energy and a range of densities, one may then estimate a chemical potential to use in Equation (5). The standard formula from the free electron model for the chemical potential for non-relativistic particles is given by

$$\mu_{\nu 0} = \varepsilon_F = \left[(\hbar c)^2 / 2m_{b\nu}c^2\right]\left(3\pi^2\rho\right)^{2/3}, \tag{6}$$

and relevant values are shown in Table 3.

One may set the chemical potential equal to the Fermi energy and use Equation (5) with these chemical potentials and with the associated upper limit $(2m\varepsilon_F)^{1/2}$. The resulting densities at $T = 155$ K range from 72% to 60% of the results of Table 2 for the masses shown. The computed densities are not equal to the input densities because the integral does not converge with the aforementioned upper limit. For masses above 0.1 eV/c^2, if the upper limit of the integral is extended until it converges, the resulting densities are consistent with the input densities from Table 2. This state of matter corresponds to Fermi temperatures varying from 162 to 172 K, and to thermodynamic temperatures (T in Equation (5)) of 2 to 15 K, with little variation in that range of T. The lower thermodynamic temperatures are expected from the theory of metals. For masses at or below 0.1 eV/c^2, the particles are sufficiently relativistic that the Fermi temperatures need to be adjusted to maintain consistency with Table 2. For these

Table 3. Fermi energy and Fermi temperature versus baryonic neutrino mass. Numbers in parenthesis are adjusted values to account for relativistic effects at lower masses, to match densities of Table 2.

	Mass (eV/c^2)						
	0.025	0.05	0.1	0.2	0.3	0.4	0.6
Fermi Energy ε_F (eV)	0.0241 (0.018)	0.0188 (0.016)	0.0161 (0.015)	0.0148	0.0144	0.0142	0.140
Fermi Temperature T_F (K)	279 (206)	218 (187)	187 (174)	172	167	164	162

lower masses, the Fermi temperature is set to 206, 187, and 174 K for masses of 0.025, 0.05, and 0.1 eV/c^2, respectively. The result is that a thermodynamic temperature of 2 to15 K still gives the densities of **Table 2** for all masses shown. Hence T will be set to 2 K in what follows, roughly consistent with the expected temperature of free neutrinos in the modern universe [12], p. 154. Given that the baryonic neutrinos were bound early in the history of universe when the mean kinetic energy was approximately 0.02 eV, the haloes comprising such matter should remain relatively stable after formation, much as bound ordinary matter. This expectation for halo evolution is justified in detail in Section 6.

It is also possible that multiple species of baryonic neutrinos could result in lower average temperatures and lower RMS velocities that further reduce diffusion of the hypothesized matter away from galactic centers. There are 3 basic types of neutrinos, so there are expected to be at most $3^3 = 27$ possible types of a colorless baryonic triplet, just as with the discrete SU(3) symmetry for (u, d, s) states in the quark sector. Accounting for antiparticles there may be as many as 54 species. To achieve the same total number density, one then requires a temperature of 12 K with 54 species rather than 155 K, assuming a Fermi-Dirac distribution and a mass of 0.4 eV/c^2. The RMS velocity in such cases is about 0.09c, which is still sufficient to overcome a galactic escape velocity if there is no other form of binding. One might expect that all such species would be present in the hot early universe. Then, as the universe cools only a few species that are most stable would remain, matching the known behavior of the quark sector. With this in mind the analyses related to the modern era will assume one or two stable baryonic neutrino species. It is possible that a few mesonic neutrino states may be present. The net effect of two baryonic neutrino states would change the Fermi temperature from 155 K, for example, to about 99 K to achieve the same total density (at a mass of 0.4 eV/c^2).

The mid and upper range of energy densities in **Table 2** is somewhat greater than the current nominal estimate of 0.3 GeV·cm^{-3} for the dark matter mass-energy near earth [41] [59] [60], which is a desirable property for dark matter near a galactic center.

Next, the distribution of ordinary matter must be specified. In recent years, the model of choice [47] for describing the projected density of elliptical galaxies is due to Sérsic [48]. An approximate de-projected form is given by [61]. A similar form for the density versus radius was developed by Einasto [49]. The center bulge of the Milky Way has a cluster with a Sersic exponent of $n = 3$ [50] for OM. As is well known, for spiral galaxies the overall Sersic exponent n is a measure of the balance between the disk and the bulge, two clearly distinct components. A typical Sersic exponent for a spiral galaxy might be 4 or more, but for the central bulge 2 is a common number [51]. For elliptical galaxies, 2 - 4 is a common number [42] for OM. With these various results in mind, a Sersic exponent of 2 is initially chosen for ordinary matter. The projected form of the Sersic equation is

$$\rho_{rad} = \rho_{rad0} \exp\left(-Ar^{a}\right) \tag{7}$$

where ρ_{rad0}, A, and α are constants. The de-projected Sersic (dpS) density distri-

bution for radiant matter is approximated by [42] [61]:

$$\rho_{rad} = \rho_{rad0}\left(r/R_e\right)^{-p_n} \exp\left[-b_n\left(r/R_e\right)^{1/n}\right]. \quad (8)$$

The parameter ρ_{rad0} is obtained by setting the volume integral of Equation (8) equal to the measured or inferred ordinary mass of the galaxy. The variable R_e denotes the radius which encloses 1/2 the total light of the galaxy. The other two parameters in Equation (8) are given conveniently and approximately from Equation (19) and Equation (27) of [42],

$$p_n = 1.0 - 0.6097/n + 0.05463/n^2, \quad (9a)$$

and

$$b_n = 2n - 1/3 + 0.009876/n. \quad (9b)$$

Figure 1 shows the $n = 2$ dpS radial profile and also a profile with $n = 4$. The assumed total OM mass of the galaxy is assumed to be $M_{gal} = 9 \times 10^{10}$ solar masses, approximating that of the Milky Way [60] [62]. It is assumed to have a black hole of 4×10^6 solar masses at its center.

The dpS profile is also used with some success for characterization of the DM density profile versus radius. Another density distribution used for characterization of DM is the Einasto distribution, which for the purposes of this paper is given by

$$\rho_{Ein} = \rho_0 \exp\left[-d_n\left(r/R_{e,\mathrm{DM}}\right)^{1/n}\right], \quad (10a)$$

where $R_{e,\mathrm{DM}}$ is the radius of the volume enclosing 1/2 the total of the galaxy, and d_n is given approximately by Equation (24) of [42]:

$$d_n \approx 3n - 1/3 + 0.0079/n, \text{ for } n > 0.5. \quad (10b)$$

Both the dpS and Einasto distributions will be compared against the DM density profiles computed using Equation (1) through (5).

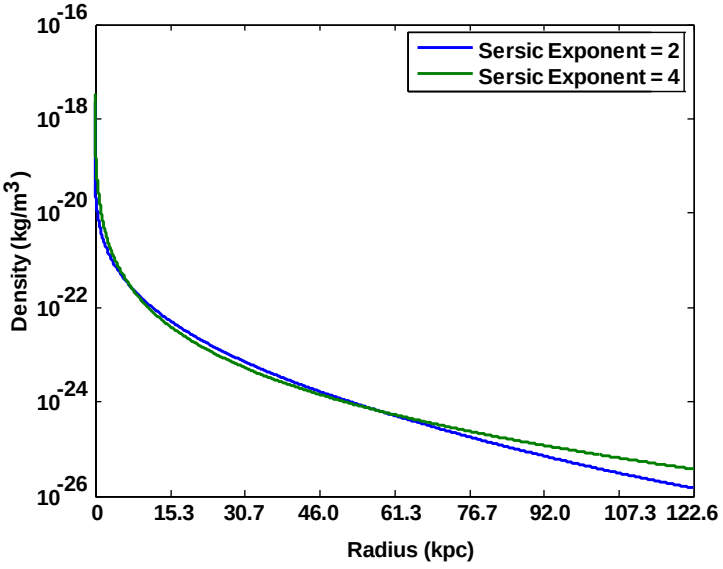

Figure 1. Profiles for a de-projected Sersic model with Sersic index of 2 (blue) and 4 (green). Radius parameter = 15.3 kpc.

The radiant matter distribution is the source term for Equation (1) and Equation (2). To use these equations to compute a profile, a polytropic exponent must be chosen. Based on the discussions above, two polytropic exponents are considered, $\gamma = 5/3$ and $\gamma = 2 - \varepsilon$, with ε a positive number much less than 1. The polytropic relation for $\gamma = 5/3$ is given above. For the case of $\gamma = 2 - \varepsilon$, one can use the polytropic relation $P = c_{2-\varepsilon}\rho^{2-\varepsilon}$ with $c_{2-\varepsilon}$ given by [55]

$$c_{2-\varepsilon} = (2/\pi) G m_{b\upsilon}^2 R_{gh}^2 \rho_0^{\varepsilon} \equiv P_0 / \rho_0^{2-\varepsilon} . \quad (11)$$

Here R_{gh} is the nominal radius of the galactic halo, chosen to be 92 kpc for the purposes of this paper. It will be checked for consistency in the following solutions. The pressure P_0 at the center of a galactic halo is defined by Equation (10). So, for example, with a baryonic neutrino mass m_{bv} of 0.4 eV/c^2 and Equation (11) one obtains c_2 = 2.08 × 10^{-40} J·m^3. In this case, P_0 = 1.53 × 10^{-9} J·m^{-3}. For ρ in units of m^{-3} one obtains the correct units in Equation (11). Other approaches are available to estimate the value of $c_{2-\varepsilon}$, for example as given in [52]. Such an approach gives a value within 1.5 orders of magnitude of that given here.

This section provided the equations and the input parameters needed to compute solutions for DM density. Variations about these input assumptions are also considered.

3.2. Galactic-Scale Solutions

Moving on to full numerical solutions of Equations (1)-(5), consider conditions corresponding to a galaxy similar to the Milky Way as mentioned above. To obtain a solution, a density at the origin must be specified. These are given in the second column of **Table 2** for the respective masses. For example, for a baryonic neutrino mass of 0.4 eV/c^2, the number density is ρ_0 = 5.34 × 10^{15} m^{-3}.

Table 4 summarizes the inputs used for the results of this section. Note that the quoted temperature is the thermodynamic temperature used in Equation (5), with chemical potentials μ_v given in **Table 3**.

Table 4. Inputs for calculations of this section.

Input Parameter	Values	Comment
Thermodynamic Temperature, T	2 K	T of Equation (5)
Fermi Temperature T_0 at origin	160 - 210 K	From **Table 3**
Masses of baryonic neutrinos, m_{bv}	0.025 - 0.6 eV/c^2	Upper limit of mass is from **Appendix A**
Galactic halo radius, r_c	92 kpc	r_c in Equation (4)
Polytropic exponents	5/3 to 2	As discussed above
Ordinary matter profile	dpS profile	Exponent = 2, radius = 15.3 kpc
Total ordinary matter mass, M_{gal}	9 × 10^{10}	Solar masses
Fermi Temperature T_{out} at radius r_c, with chemical potential $\mu_{vc} \equiv kT_{out}$	5 - 16 K	Sets density ρ_c at outer radius in Equation (4) using Equation (5)
Inner scale r_0	1 kpc	Sets radius of constant density region in Equation (4), approximate size of bulge of Milky Way

The numerical integration of Equation (1) and Equation (4) for the density uses 4000 steps at 30.7 pc each. A simple finite-difference numerical approach proves adequate with the quoted step size. If the density is reduced below 10^9 m^{-3}, then the density is set to that value for display purposes.

The results of the calculations are shown in Figure 2 and Figure 3 for the standard and generalized equations of hydrostatic equilibrium, respectively. The horizontal axes in these figures are the dimensionless ratio radius/R_{gh}, where R_{gh} = 92 kpc as discussed above. A comprehensive (but not exhaustive) search was performed over fermionic mass, polytropic exponent, and mean kinetic energy within the ranges shown in Table 4. The search attempted to find the best match to the following properties of dark matter reported in the literature: 1) outer radius

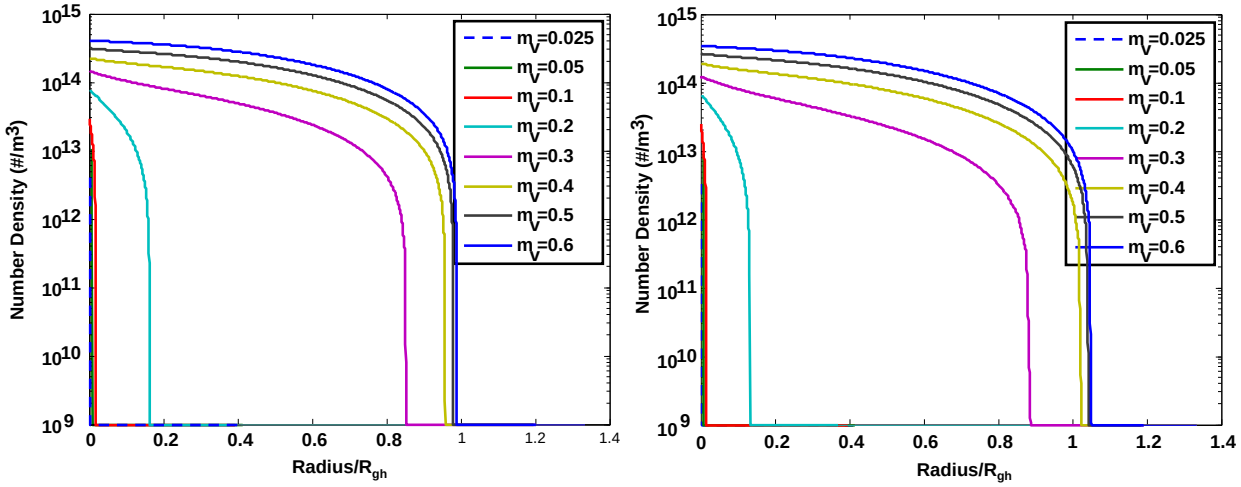

Figure 2. Calculated dark-matter profiles versus radius for various masses of a baryonic neutrino for a galaxy similar to the Milky Way with a Sersic index of 2. Standard hydrostatic equation assumed. Legend shows masses ranging from 0.025 to 0.6 eV/c^2. Left: $\gamma = 1.995$, T_0 = 19 to 20 K. Right: $\gamma = 1.90$, T_0 = 17 K.

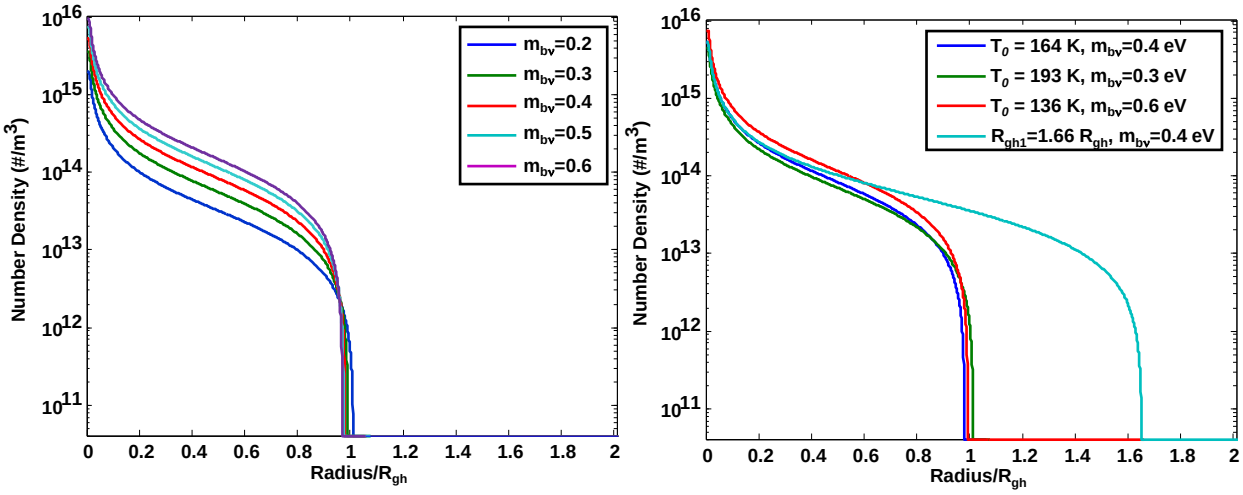

Figure 3. Calculated dark-matter profiles versus normalized radius for various masses of baryonic neutrino for a galaxy similar to the Milky Way. Generalized hydrostatic equation assumed. Left: varying mass, T_0 as shown in Table 4, r_0 = 1 kpc, T_{out} = 8 K. Right: T_0 varied as given in the legend to overlay curves for different masses. Also shown is a case with galactic halo radius set to 1.66 R_{gh} = 153 kpc = r_c, with m_{bv} = 0.4 eV/c^2, T_0 = 155 K, r_0 = 1 kpc, and T_{out} = 5 K.

consistent with the assumed radius of DM of 92 kpc; 2) cusp near the origin; 3) mass-energy density at radius of Sol; 4) ratio of DM in galactic halo to OM in galaxy; 5) quantitative shape consistent with published simulations and inferences from observations, and 6) consistency of temperature at outer radius with standard cosmology. The best or near-best fits considering all these criteria are shown in the figures.

Results for the standard hydrostatic equation, Equation (1), are shown in Figure 2 for varying masses of baryonic neutrino and for two different polytropic exponents near 2. The results for the cutoff radius shown here are a good match to the assumed radius of DM, R_{gh} = 92 kpc, for particle masses ranging from 0.3 to 0.6 eV/c^2. However, as expected, it is seen that the results using the standard hydrostatic equation are not a good match to a dpS profile, by comparison to Figure 1. No cusp is present. The quantitative shape is also not a match to any accepted dpS profiles. The shapes shown in Figure 2 are typically close to the expected result for the Lane-Emden equation, $\sin(\pi r/R)/(\pi r/R)$ for some R, assuming the standard hydrostatic equation with a polytropic exponent near 2. The shapes are expected to differ somewhat from this standard form because (a) the exponents are not exactly 2, and (b) the solutions shown are for the inhomogeneous form of the equation with a strong concentration of OM at and near the origin.

It should also be noted that with a polytropic exponent near 2 and using Equation (11), the lower masses have less pressure and so result in smaller half-max radii. This differs from the case of a polytropic exponent of 5/3, which yields larger half-max radii for lower masses in view of the expression for fermions given after Equation (5). With smaller exponents such as 5/3, dramatically larger galactic haloes are computed using the standard hydrostatic equation, and so are not shown.

Several other metrics are worth discussion for Figure 2. First, the total enclosed mass is in the range of 4 to 60 times the ordinary matter for particle masses ranging from 0.3 to 0.5 eV/c^2 for the plots shown. For 0.4 eV/c^2, the total enclosed mass is within 15% of 15 times ordinary matter. Second, the mass-energy density (as computed in Table 2) at the radius of Sol is 0.06 to 0.2 GeV·cm^{-3} for particle masses ranging from 0.4 to 0.6 eV/c^2 for Figure 2. Values of T_0 much larger or smaller than the range shown in Figure 2 do not show a radius consistent with the assumed halo radius for γ near 2. Overall, the results of Figure 2 are a match to the assumed halo radius and enclosed mass for some particle masses. However, such solutions have a relatively low energy density at earth compared to observational inferences and also do not have the cusp deduced from data.

Sample results for the generalized hydrostatic equation, Equation (4), are shown in Figure 3. In this case, as in Figure 2, the plots with the specified inputs also show a radius that is in the neighborhood of R_{gh} = 92 kpc, consistent with the assumed radius. However, it is seen that the results using the generalized hydrostatic equation are a qualitative match to a dpS profile. A cusp is present out-

side of a radius of 1 kpc with a logarithmic slope of about −1.

The left plot of Figure 3 shows the sensitivity of the result to the mass of the hypothesized baryonic neutrino. It is seen that the range of masses that are consistent within 10% of R_{gh} is from 0.2 to 0.6 eV/c^2 for the chosen inputs. Lower masses did not show such agreement. The right plot shows sensitivity to T_0 in the vicinity of the nominal 155 K, showing the masses required to obtain a similar density profile. The right plot also shows a sample case for the galactic radius set to $1.66R_{gh}$ = 153 kpc with a baryonic neutrino mass of 0.4 eV/c^2 with appropriate choice of temperatures. The point of this plot is that other (self-consistent) galactic halo radii can be achieved with similar input parameters.

Further calculations, not shown, give consistent results for R_{gh} with particle masses up to about 5.0 eV/c^2 for smaller values of r_0, r_0 as low as 0.1 kpc. These typically require lower values of T_0 and T_{out}. For larger particle masses, the temperature needed for T_{out} is 0.1 K or less to match both galactic halo size (R_{gh}) and enclosed DM mass. For larger values of particle mass, above 5.0 eV/c^2, consistency with both observationally-inferred galactic halo size and mass cannot be met simultaneously; either the computed radius matches R_{gh} but the total enclosed DM mass is too large, or the total mass matches expectations but the radius is too small. Dwarf galaxies with masses of 10^7 to 10^{10} solar masses can be obtained with this approach for particle masses of 0.2 eV/c^2 to 0.6 eV/c^2. The required input values for dwarf galaxies are T_0 the same as in Table 4, with r_0 in the same range (0.1 to 1 kpc), R_{gh} = 1 to 2.5 kpc, and T_{out} = 30 to 95 K.

Figure 4 shows plots of two relevant metrics. The curve on the left of Figure 4 shows the ratio of the enclosed DM mass to OM mass for the curves on the left of Figure 3. A dotted line shows the estimated universal average ratio of 6:1. This ratio is believed to be of the order of 15:1 for the galactic halo of the Milky Way [60]. The values of baryonic masses consistent with ratios of 6:1 to 30:1 are about 0.25 to 0.50 eV/c^2.

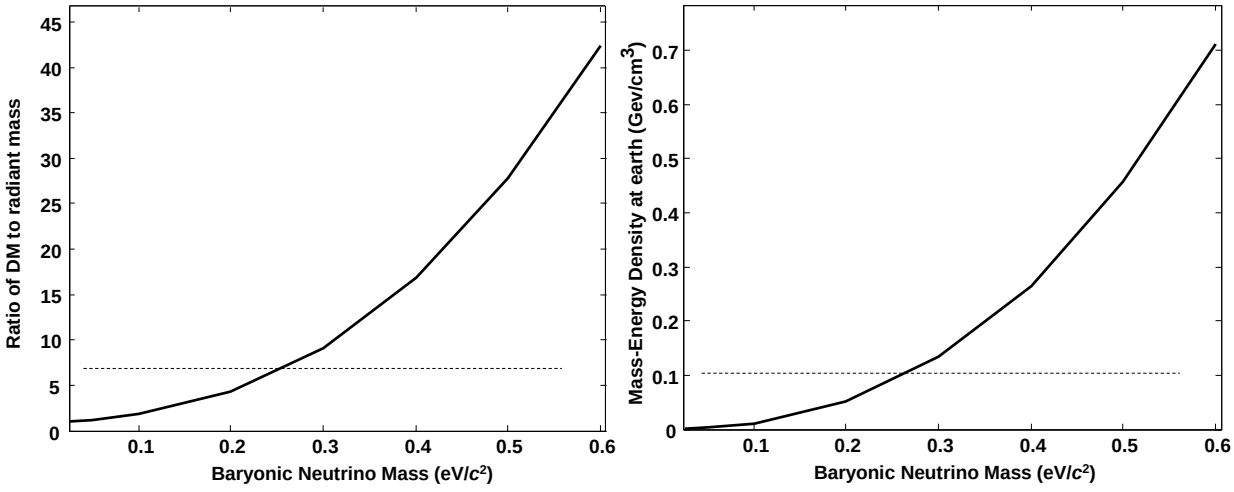

Figure 4. Left: Computed ratio of DM to OM versus mass of the baryonic neutrino (eV/c^2) for conditions corresponding to the left plot of Figure 3. Right: Computed mass-energy density of DM at the radius of earth for conditions corresponding to the left plot of Figure 3.

The plot on the right of Figure 4 shows the computed mass-energy density of DM at a radius of 7.9 kpc for plots on the left of Figure 3. 7.9 kpc corresponds to the distance of earth from the galactic center. As discussed above, the mass-energy density is given by $\rho m_{bv} c^2 \Big/ \left[1-\left(v_{rms}/c\right)^2\right]^{1/2}$. As mentioned earlier, the estimated mass-energy density at earth is 0.3 GeV·cm^{-3}, "within a factor of 2 - 3," as stated in the Astrophysical Constants section of the most recent PDG document [41]. The resulting lower bound is 0.1 GeV·cm^{-3}, and this lower bound is shown in the right plot as a dotted line. The particle masses consistent with these estimates from data are about 0.25 to 0.65 eV/c^2.

The nominal computed density profile from Figure 3 with a baryonic neutrino mass of 0.40 eV/c^2 is fit to various model profiles as shown in Figure 5. In addition to this single-species computation, a two-species computation is also shown, and will be discussed below. The densities of Figure 5 are all limited from above to the value of $m_{bv}\rho_0 = 3.76 \times 10^{-21}$ kg·m^{-3} within 1 kpc of the origin, consistent with the nominal computed profile for a baryonic neutrino mass of 0.40 eV/c^2. The vertical axis is normalized by this density. This limit at the origin is used and shown because it is in better accord with most measured data [63] [64] [65] than the model profiles and also because such a limit is in better accord with a density that is limited by Fermi-Dirac statistics. Just outside this core, all densities of all profiles of Figure 5 have an approximate $1/r$ dependence, including the dpS and Einasto model profiles. However, at larger radii, the nominal density profile has a slower decline than the dpS and Einasto model profiles up to a radius of about $0.9R_{gh}$.

The chosen parameters for the model profiles are given in Table 5. The parameters for the dpS and Einasto models are within the accepted range for the exponent and the radius, by comparison with the values shown at the bottom of

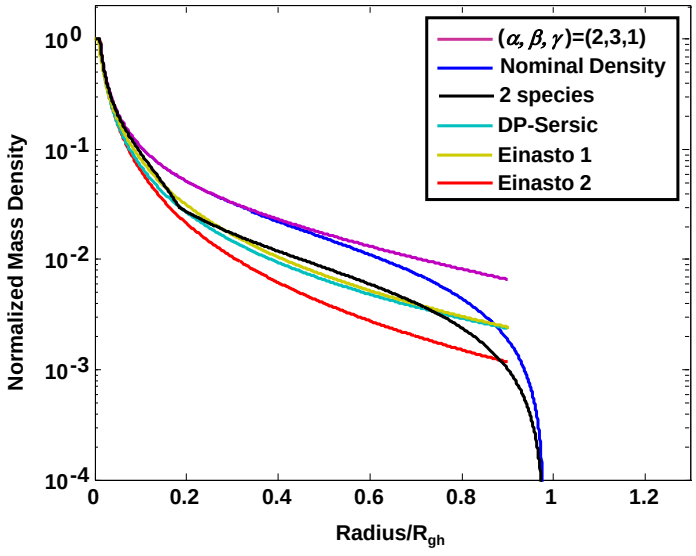

Figure 5. Nominal computed density profile of Figure 3 with a baryonic neutrino mass of 0.40 eV/c^2, a 2-species computed profile, and various model profiles. Model inputs and fit metrics are given in Table 5.

Table 5. Model parameters and fit metrics of model profiles versus computed profiles for **Figure 5**[a].

Input Parameters and Metrics:	n	$R_{e,\mathrm{DM}}$ (kpc)	$\rho_0/\rho_{0,mv}$	Metric 1	Metric 2	M/M_{gal}
(2, 3, 1), fit to nominal	-	r_{02} = 92	1	0.20	0.91	19.6
dpS, fit to nominal	3.3	700	0.011	0.47	0.45	7.8
Einasto-2, fit to nominal	5.5	400	220	0.61	0.68	4.9
dpS, fit to 2-species	3.3	700	0.011	0.033	0.18	7.8
Einasto-1, fit to 2-species	5.5	800	110	0.011	0.20	8.6
Einasto-2, fit to 2-species	5.5	400	220	0.18	0.18	4.9
Galaxy-sized haloes, dpS	3.1 - 4.6	110 - 230	-	-	-	-
Galaxy-sized haloes, Einasto	5.3 - 7.8	190 - 400	-	-	-	-
Cluster-sized haloes, dpS	2.2 - 3.5	700 - 4700	-	-	-	-
Cluster-sized haloes, Einasto	3.9 - 7.4	1200 - 6000	-	-	-	-

[a]Bottom four rows are from [42].

the table, which are from [42]. However, as expected, the central density parameters are quite different. This is expected because of the large derivatives of the model profiles at the origin, as discussed in [52], which do not match measured values [63].

Table 5 also shows two metrics for the quality of the fits. These metrics are

$$\text{Metric 1} = \left\{\Sigma_r U(r)\left[\rho_M(r)-\rho_C(r)\right]^2 r^2\right\}^{1/2} \Big/ \left\{\Sigma_r U(r)\left[\rho_C(r)\right]^2 r^2\right\}^{1/2}, \quad (12a)$$

and

$$\text{Metric 2} = \left\{\Sigma_r U(r)\left[\rho_M(r)/\rho_C(r)-1\right]^2 r^2\right\}^{1/2} \Big/ \left\{\Sigma_r U(r) r^2\right\}^{1/2}, \quad (12b)$$

where $\rho_C(r)$ is the numerically-computed profile and $\rho_M(r)$ is the model profile. Three classes of model profiles are considered: (α, β, γ), dpS, and Einasto. The metrics are computed over the range of radii for which the densities are appreciable ($U(r) = 1$ for $r < 0.9\ R_{gh}$, 0 otherwise). The metrics for these model fits to the nominal curve vary from 20% to 91%, which is not particularly good, but are expected from visual inspection of **Figure 5**. It should be noted that both metrics 1 and 2 weight the agreement at the outer radii quite heavily, and this is a significant contributor, especially for the (α, β, γ) model.

Table 5 additionally shows the total enclosed mass within a radius of 0.9 R_{gh}. For reference, the nominal density profile, the blue curve of **Figure 5** has a total enclosed mass of $15.2M_{gal}$ within this radius. The (α, β, γ) model has an enclosed mass close to expectations, about $19M_{gal}$. The profiles labelled dpS and Einasto have a total enclosed mass ratio (DM/OM) that is low compared to expected values of 15 or more. Also considered but not shown are dpS and Einasto profiles with an inner core that is about 2 kpc in radius, matching the mean radius of the bulge in the Milky Way. These had higher enclosed masses, of the order of 10 to $15M_{gal}$, but the fit metrics were no better than shown in the table.

Overall, the differences between the best-fit dpS and Einasto models and the nominal computed solution are not negligible. This difference can be addressed via several physically reasonable approaches. Such approaches include (a) inclusion of angular momentum in the computation, (b) an allowance for non-equilibrium profiles at larger radii, or (c) inclusion of multiple particle species. These three approaches are discussed briefly in the following three paragraphs. As shown in **Figure 5**, approach (c) was found to readily provide a good match to observationally-inferred profiles.

Angular momentum profiles in CDM haloes have undergone considerable study using N-body simulations of particles that interact by gravity alone. Such studies include [66] [67] [68] [69] [70]. However, the parametric relationship between the density profile and the angular momentum profile has not been considered at length. Further, such studies are of limited relevance because they focus on non-interacting particles rather than the Fermi fluid posited in this paper. Such studies find typical estimated velocities of the order of 300 km·sec^{-1} associated with angular momentum for the Milky Way [71]. For a DM particle mass of 0.4 eV/c^2, such velocities correspond to kinetic energies of about 2×10^{-7} eV, which is much less than the estimated inter-particle binding energy of ~0.02 eV of the posited Fermi fluid. Hence, by analogy with other well-understood liquid or semi-solid celestial bodies, the primary impact of angular momentum would be distortion of the halo, with a limited impact on the density profile.

Approach (b) involves appeal to density profiles that do not strictly adhere to the $1/r$ equilibrium profile at larger radii. Such non-equilibrium profiles are discussed in [34] and [52] and are attributed to the ongoing process of halo accretion and mergers. These profiles were considered in this effort but were found to differ from the model profiles even more than the nominal $1/r$ profile. This is because if the model profile and the $1/r$ profile agree at small radii and the computed non-equilibrium profiles are even flatter at intermediate radii then they are always above the $1/r$ profile. From **Figure 5**, one can see that such a profile would offer worse agreement at larger radii However, with a larger particle mass, e.g. about 0.6 eV/c^2, a sharper decline near the center could support a flatter profile at larger radii, as shown in the 2-species profile of **Figure 5**.

Approach (c) was also considered and the result is shown in the black curve of **Figure 5**. It can be seen that this 2-species model is a particularly good match to the dpS and Einasto-1 models. Both model curves have a radius in the range of 700 to 800 kpc, corresponding to small galactic clusters. This 2-species approach can be described succinctly using the notation developed for Equation (4) and Equation (5). The mass density profile involving two species is denoted by $\rho_{m,\text{2-species}}(r)$ and can be written

$$\rho_{m,\text{2-species}}(r) = m_1\rho(r, T_{01}, r_{01}, T_{c1}, r_{c1}, m_1, \mu_{v1}) + m_2\rho(r, T_{02}, r_{02}, T_{c2}, r_{c2}, m_2, \mu_{v2}) \quad (13)$$

Clearly, there are more parameters in Equation (13) that permit a better fit a model profile. Experimentation with the parameters indicated that values of m_1 of 0.3 to 0.5 eV/c^2 led to a good fit at larger radii. Larger masses, m_2 = 0.6 to 0.8

eV/c^2, lead to a better fit at smaller radii with a steeper mass-density slope, while still matching the total enclosed mass. Larger masses led to excessive total enclosed mass, and smaller masses led to insufficient total enclosed mass given the range of values for the chemical potentials and temperatures shown above. Note also that both species of masses lie within the range of values expected from **Appendix A**. Table 6 shows the inputs used to obtain the 2-species curve shown in Figure 5.

In summary, assuming the generalized hydrostatic Equation (4) and the posited baryonic neutrinos with masses of 0.4 eV/c^2 ± 50%, the results are roughly consistent with the following observationally-inferred and simulated properties of galactic-scale or cluster-scale DM structure reported in the literature: 1) halo width consistent with the assumed radius of 92 kpc for a galaxy similar to the Milky Way; 2) relatively flat density profiles within a core radius of ~1 kpc; 3) cusp in the region outside of this core; 4) mass-energy density at radius of Sol; 5) ratio of DM in galactic halo to OM in a galaxy similar to the Milky Way; 6) qualitative shape; and with multiple species, 7) quantitative shape. Further, the temperature at the edge of the galactic halo is consistent with expectations from standard cosmology, with a temperature of 2 K (Fermi temperatures of 5 to 16 K).

The above represents a summary of a search over multiple parameters, including baryonic-neutrino mass, particle temperature, polytropic exponents, and core radius. The standard and generalized hydrostatic equations are both considered. The generalized hydrostatic equation gives a better overall match for metrics derived from fits to representative models and data than does the standard equation for these ranges of values, when all 7 of the criteria mentioned in the previous paragraph are considered. However, the generalized hydrostatic equation of equilibrium does not fully trace to DM material properties. Only four of the six inputs to the solution are traceable to material properties: the particle mass and Fermi temperature of the constituent particle, both at the origin and outer radius. The other two inputs, the inner radius r_0 and the outer radius r_c, are not traceable to fundamental physical properties and make it too easy to fit some of the measured parameters. Nonetheless, selection of these two parameters allows a simultaneous fit to multiple criteria, which seems more than fortuitous.

4. The Hypothesis and the Tremaine-Gunn Bound

Reference [72] identified a bound that assumes (a) that the subject particles are fermions, (b) that such particles are non-relativistic, and (c) that such particles

Table 6. Parameters used for 2-species plot of Figure 5.

Input Parameters	m (eV/c^2)	$T_0 = T_c$ (K)	r_0 (kpc)	r_c (kpc)	μ_{v0}/k (K)	μ_{vc}/k (K)
Species 1	0.4	2	1	92	104	8
Species 2	0.6	2	1	9.2	51	16

are non-interacting. In this paper, (a) is true, (b) is approximately true, but (c) is not true near a galactic center. Regarding (a), neutrinos should form baryonic neutrinos with odd multiples of half-integer spin, as expected by analogy with quark-based baryons. Regarding (b), the estimated speed of baryonic neutrinos for a temperature of 2 K is about $0.03c$ to $0.05c$ depending on mass, and possibly less if there are multiple species. Regarding (*c*), the hypothesized baryonic neutrinos are weakly bound near a galactic center, based on the findings of Sections 3.1 and 3.2, and therefore interact. Hence (c) is not true. In the depths of space, far from any ordinary matter clusters, one might expect that neutrinos or the bound neutrino states considered herein are likely non-relativistic and not interacting and the Tremaine-Gunn bound is indeed expected to apply.

5. The Hypothesis and Observation of DM near Earth

One might question whether such baryonic neutrinos might be observed at earth. As seen in **Figure 4**, one finds consistency of the hypothesis for the mass-energy density near earth with accepted values [41] [59] for baryonic neutrino masses of 0.25 to 0.6 eV/c^2. This basic comparison supports the hypothesis. Somewhat larger masses are possible as well.

It is estimated that the flux of solar neutrinos from the sun at earth is about 7×10^{10} cm^{-2}·sec^{-1}, see, e.g. [73]. Given that solar neutrinos travel at nearly the speed of light, the corresponding density is about 2.3 cm^{-3}. From the previous two sections, with the 2018 PDG mass-energy density of DM at the earth of ~0.3 GeV·cm^{-3} one obtains a baryonic neutrino density of about 10^9 cm^{-3}, assuming a baryonic neutrino mass of 0.3 eV/c^2. Based on a simple scaling of the electroweak force which goes as the square of the CM energy, DM baryonic neutrinos should interact much more weakly than solar neutrinos via the electroweak force by a factor of about $1/(3 \times 10^5)^2$ or less, because they have much lower energy than solar neutrinos in the earth reference frame (<1 eV for the former versus ~0.3 MeV for the latter). Hence, direct observation of such baryonic neutrinos seems challenging.

Further, solar neutrinos should interact in a very limited way with such DM via $SU(3)_{ve}$, because solar neutrinos are predominately electron neutrino states, which are mono-color based on the theory of [38]. It should be noted that this property would not follow from a simple application of SU(3) to neutrinos. Specifically, they are color green using the conventions of that work. DM consists of baryonic states which are already colorless. Hence solar neutrinos cannot be absorbed or bound by DM in any significant way. Further, solar neutrinos cannot bind with each other to form baryonic or mesonic neutrinos to form colorless states since they are the same color (with no anti-color contribution). Thus, the interaction of solar neutrinos with themselves or DM should be limited to elastic (Rutherford) or quasielastic (Mott) scattering via $SU(3)_{\nu}$. The latter would have similarities to high-energy electron scattering in bulk material. It will be seen in the companion paper that such elastic or quasielastic scattering should not sig-

nificantly alter the composition, energy spectrum, or the flux of solar neutrinos as seen at earth, and this is consistent with observations to date. Note that solar neutrinos are not initially bound to other neutrinos partly because of the way they are created, but also partly because they are ultra-relativistic, just as quarks were not initially bound in the hot early universe. It should be re-stated that the experimental fact of neutrino oscillations is direct evidence that neutrinos will form bound states via $SU(3)_{ve}$ within the context of the extended-color theory.

Possible observations for DM near earth also include an annual variation of the order of 1% of the time-average of scintillation in sodium iodide detectors at specific energies [74]. The observed energies of ~6 keV are not obviously related to the form of DM proposed herein. Measured values of the relative annual variation range from 0.0026 to 0.025 from **Table 1** of that reference. The peak-to-valley velocity difference of earth relative to DM is about $v_{\text{Sol}} = 250$ km·sec^{-1}, *i.e.* $\sim 10^{-3}c$, assuming that DM is not rotating and the earth's orbital plane around the sun is oriented at 60˚ relative to the sun's velocity vector around the galactic center [41]. The RMS velocity v_{rms} of the proposed DM is $0.03c$ to $0.05c$ with $T = 2$ K. This gives an estimate of the relative annual variation of the flux of DM of $v_{\text{Sol}}/v_{rms} = 10^{-3}/0.03$ to $10^{-3}/0.05$. Thus, the estimated range of relative flux variation is a factor of 0.8 to 1.33 times the maximum measured relative variation of 0.025 quoted above.

The standard cosmological theory of neutrinos [12] [75] indicates that cold relic neutrinos are also present. The presence of bound neutrino states is not inconsistent with neutrinos interspersed with ordinary and DM matter. It is thus expected that there is a substantial fraction of free neutrino states near earth. Because of their low relative velocity, the helicity of such neutrinos of mass 0.005 to 0.055 eV/c^2 would differ from those of high-energy free neutrinos observed in typical experiments, assuming that such neutrinos have mass and have Dirac wavefunctions. This would result in a relatively large fraction of right-handed neutrinos. Such neutrinos would be difficult to detect, however, because of the known inability to induce right-handed neutrinos to interact with normal matter [76]. Such relic neutrinos with a temperature of about 2 K would have electroweak cross sections comparable to those of bound neutrino states, and so would also be difficult to detect.

6. The Hypothesis, Halo Stability, and Halo-Halo Interactions

The hypothesis of $SU(3)_{\nu}$ leads to an investigation of other self-interacting dark matter (SIDM) proposals. Recent papers [20] [21] [30] [31] discuss related phenomenologies. In the taxonomy of [21], this proposal is one of composite DM in which the mediators are both SU(3) massless gluons and/or lightly-broken SU(3) with massive mediators. In this case, the latter have mass of the order of the mass of the most massive constituent neutrino, and their effective binding energy is 4 to 12 times that of the highest-mass neutrino based on **Appendix A**.

With the self-interaction discussed here, DM is a dense form of matter that

maintains its volume due to fermion degeneracy pressure of baryonic neutrinos. This dense form of matter is justified with the core assumption that the constituent baryonic neutrinos interact and are bound via $SU(3)_v$ and obey non-relativistic Fermi-Dirac statistics. The SU(3) interaction with its approximate $1/E^2$ dependence on CM energy E [77] gives a large cross-section and a vanishing mean free path as temperatures tend to zero. Further, the computed Fermi temperature of Table 3 is typically much greater than the thermodynamic temperature of 2 K, much as occurs with ordinary condensed matter. These considerations justify the simplest calculation for the mean free path, ℓ:

$$\ell = \left(2^{1/2}\pi\rho d^2\right)^{-1}, \tag{14}$$

where ρ is the density appropriate to the specific location in the halo and d is the "size" of the particle. The values of ρ are given by the densities of Table 2 assuming a macroscopic bound state with the given Fermi temperatures. The value of d should be approximately $\hbar/p_F$, where p_F is the Fermi momentum of the particle. The value of mean free path is shown in Table 7, along with the RMS velocity, v_{rms}, which is $0.036c$ based on a temperature of 2 K and a particle mass of 0.4 eV/c^2, in accord with the discussions following Table 3. The table also shows the Fermi temperature, T_F, the diffusion constant, $\kappa = \ell v_{rms}$, the mean free time between collisions, $\tau = \ell / v_{rms}$, and the time to diffuse 1 kpc, $t_{1\,\mathrm{kpc}} = (1\,\mathrm{kpc})^2 / \kappa$. Also shown is the medium pressure, assuming a polytropic exponent of 2 and assuming c_2 equals 2.08×10^{-40} J·m^3, as in the discussion surrounding Equation (11).

The table shows a diffusion constant varying from about 200 to 2000 m^2·sec^{-1}, which is quite high compared to conventional matter. However, this diffusivity leads to negligible mass or heat transfer over scale sizes of the order of 1 kpc over the age of the universe, as can be seen by the second-to-last column. This implies that the density and temperature distributions are expected to be relatively stable from the time of creation up to the present day, so that there is little evolution other than modest gravitational and SU(3)-based contraction and subhalo aggregation over most of the universe's lifetime. There are alternative formulations for the mean free path that differ from Equation (14), in which the cross section is calculated based on an interaction strength rather than the hard-sphere approximation. These estimates also lead to very long mass-transfer time constants, of the order of the age of the universe for haloes of 100 kpc in size.

Table 7. Fluid properties of proposed DM versus density, assuming m_{bv} = 0.4 eV/c^2 and temperature T = 2 K.

Density ρ (m^{-3})	T_F (K)	$p_F/m_{bv}c$	l (μm)	κ (m^2·sec^{-1})	τ (psec)	$t_{1\mathrm{kpc}}$ (yrs)	P (J·m^{-3})
5×10^{15}	157	0.323	19.3	209	1.80	1.5×10^{29}	4.4×10^{-9}
5×10^{14}	34	0.148	40.9	442	3.79	6.9×10^{28}	4.4×10^{-11}
5×10^{13}	7.3	0.069	87.8	948	8.14	3.2×10^{28}	4.4×10^{-13}
5×10^{12}	1.6	0.032	189	2040	17.5	1.5×10^{28}	4.4×10^{-15}

The above shows that the DM derived in this paper has some degree of self-consistency for a single halo. What does the above imply for halo-halo interactions? This is a very complex subject [34], involving baryonic feedback, dynamical friction, tidal stripping, and more. However, some calculations can be performed for the hypothesis under consideration. First, consider the kinetic energy of halo-halo interactions, which involve relative velocities v_{rel} of 30 to 3000 m/sec, see e.g. [21]. The corresponding kinetic energy per particle $m_{b\upsilon} v_{rel}^2 /2$ ranges from 2×10^{-9} to 2×10^{-5} eV. Note that these values are less than both the estimated inter-baryonic-neutrino binding energy, 6.4×10^{-3} eV, as well as the estimated intra-baryonic neutrino binding energy, 0.4 eV. Hence the medium is not expected to dissociate, but rather to maintain its form.

Given that the medium is a fluid, the interaction should be characterizable in terms of dimensionless parameters such as Reynolds number, *Re*, and Mach number, *Ma*. These are shown in **Table 8** for three interaction velocities and for the same 4 densities shown in **Table 7**. The Reynolds number is computed assuming the value of κ in **Table 7**, the velocities shown, and a scale size of 1 kpc, which is assumed to be the typical diameter scale of a subhalo. The acoustic velocity is computed in the standard way assuming a polytropic exponent of 2 as in the discussion surrounding Equation (11).

From **Table 8**, it is evident that most of the Reynolds numbers are astronomical in comparison to typical values of terrestrial interest, and that the corresponding solutions are mathematically similar to those with very small viscosity. This, combined with the essentially incompressible properties of a quantum fluid satisfying Fermi-Dirac statistics, suggests that the fluid might approximate potential flow, which is known to have very low drag [78].

With such large Reynolds numbers, the accepted drag coefficient is about 0.2 for a sphere, as can be found in any textbook in fluid mechanics, neglecting possible quantum fluid effects. A drag coefficient as low as 0.1 occurs for an ellipsoid with a 2:1 aspect ratio, as may be found for subhaloes like the dwarf Sagittarius galaxy. With the above information, the drag-induced slowing of a subhalo in a larger medium can be computed using the simple differential relation

$$\rho_{sh} \, \mathrm{d}|\mathbf{v}|/\mathrm{d}t \, V = (C_d/2) \rho_{gal} |\mathbf{v}|^2 A . \tag{15}$$

Here ρ_{sh} is the DM density of the subhalo, set equal to 5×10^{15} m^{-3}, ρ_{gal} is the DM

Table 8. Reynolds number and Mach number, respectively, for halo-halo interactions. Scale size for *Re* is 1 kpc, particle mass is 0.4 eV/c^2.

Density ρ (m^{-3})	v_{rel} = 30 km·sec^{-1}	v_{rel} = 300 km·sec^{-1}	v_{rel} = 3000 km·sec^{-1}
5×10^{15}	4.4×10^{21}, 0.019	4.4×10^{22}, 0.19	4.4×10^{23}, 1.9
5×10^{14}	2.1×10^{21}, 0.061	2.1×10^{22}, 0.61	2.1×10^{23}, 6.1
5×10^{13}	9.8×10^{20}, 0.19	9.8×10^{21}, 1.9	9.8×10^{22}, 19.1
5×10^{12}	4.6×10^{20}, 0.61	4.6×10^{21}, 6.1	4.6×10^{22}, 60.6

density of the galaxy in the vicinity of the subhalo, and v is the velocity of the subhalo relative to the galaxy. V is the volume of the subhalo, set equal to $4\pi r_{sh}^3/3$, and r_{sh} is the subhalo radius, set equal to 0.5 kpc. C_d is the drag coefficient, and A is the cross-sectional area of the subhalo presented to the flow, set equal to πr_{sh}^2. Equation (15) is readily solvable assuming the densities are constant over time (as a first approximation). Sample results are shown in **Table 9** versus initial relative velocity v_{rel0} and local galaxy density, for times corresponding to 50% and 90% reductions in velocity.

The table shows, for example, that the 50% and 90% times are about 22 and about 197 Myr, respectively, for a subhalo diameter of 1 kpc located at the outer edges of a galaxy where v_{rel0} = 300 km·sec^{-1}. For haloes of order 1 kpc in diameter and v_{rel0} = 30 km·sec^{-1}, the orbit decay times range from about 0.2 Gyr to 2 Gyr based on the lower left values of **Table 9**. The lower end of this range, 0.2 Gyr, is definitely smaller than expected [34], for which typical subhalo decay times are predicted to lie in the range of 2 to 4 Gyr. This is a potential inconsistency which could be investigated via observations and simulations to test this theory as well as to inform the theory of the possibility of lower drag for this form of matter.

Referring to Equation (15), one sees that these numbers can be interpreted as the decay time per kpc diameter. So, for example, for a 10 kpc subhalo such as the Sagittarius dwarf spheroid, the predicted velocity decay time constant is about 1970 Myr for the 90% decay time with an initial velocity of 300 km·sec^{-1}, referring to the bottom of the middle column of **Table 9**. If the shape of the subhalo is elliptical with major axis in the flow direction, as is the case for Sagittarius, the drag coefficient might be a factor of 2 lower, resulting a time constant of about 4 Gyr. These numbers are within a factor of 2 of those inferred from observations [79] [80]. It is not clear that this result is consistent with such observations, due to the neglect of many other effects such as the type of orbit and dynamical friction.

Another well-known constraint on self-interacting dark matter is the observation of the Bullet Cluster halo collision. In this collision the r_{200} radius (the radius at which the galactic density is 200 times that of background) is about 2140 kpc for the main cluster and about 995 kpc for the smaller Bullet Cluster. The final observationally-estimated lag of DM behind stellar matter is 25 ± 29 kpc [31] [81]. The drag-induced lag of the Bullet cluster halo relative to its associated ordinary stellar matter can be computed using Equation (15). Hernquist density

Table 9. Time (Myr) for velocity to decay by 50% and 90% for halo-subhalo interactions using Equation (15) and inputs described in text.

Density ρ_{gal} (m^{-3})	v_{rel0} = 30 km·sec^{-1}	v_{rel0} = 300 km·sec^{-1}	v_{rel0} = 3000 km·sec^{-1}
5×10^{15}	0.22, 1.97	0.022, 0.197	0.002, 0.020
5×10^{14}	2.2, 19.7	0.22, 1.97	0.22, 0.197
5×10^{13}	21.8, 197	2.2, 19.7	0.22, 1.97
5×10^{12}	218, 1970	21.8, 197	2.2, 19.7

profiles are assumed as in [31] with the same initial velocity of 3000 km/sec and same initial separation of 4 Mpc. Nominal motion is in a straight line. Values of closest approach of 10 to 100 kpc of the cluster centers are used. A central number density of 5×10^{15} m^{-3} at a radius of 1 kpc is used for the main cluster, and number densities of 5×10^{15} to 5×10^{14} m^{-3} are used for central portion of the Bullet cluster, in accord with Section 3. The Bullet cluster radius is chosen to equal the Hernquist α-parameter, 279 kpc, as in [31]. Using the r_{200} radius of 995 kpc results in smaller lags due to the larger mass and therefore lower acceleration. A drag coefficient of 0.2 is used. The resulting computed lags range from 0.35 to 7.7 kpc, when 700 kpc past closest approach, which is within error bars of that measured (25 kpc).

Using a strict $1/r$ density profile for the main cluster rather than the Hernquist profile gives a lag of as much as 15 kpc, because of the greater column density traversed by the Bullet Cluster. Also, a larger drag coefficient of 1.0 gives about 1.75 to 37 kpc of lag instead of 0.35 to 7.7 kpc. If these larger numbers are combined with a $1/r$ density profile, the result is about 73 kpc of lag as an extreme worst case, which is outside the error bars. Convergence of these calculations was checked; the computed lags are accurate to within 0.01% using up to 10^4 steps in time. The lags are relatively small because of the large size of the Bullet cluster halo, as noted in the previous paragraph, so its large mass decelerates less. Evidently, this form of self-interacting dark matter is consistent with the measured lag of the Bullet cluster collision, based on the simplest relevant drag calculation for this state of matter.

The net effect of the above calculations is decay of subhaloes into a larger halo, with associated erosion and assimilation. Scaling the results of **Table 9**, the slowing is most significant for the smaller haloes. From this, one sees a partial explanation for the unexplained dearth and diversity of smaller satellite haloes mentioned by other authors [21] [34]. Note that the decay rates for such haloes are significantly shorter than the time scales involving dynamical friction, so this offers observational means for assessing or informing this theory. Further, this picture of halo interaction is quantitatively consistent with the observed Bullet cluster halo interaction, provided the halo centers do not pass closer than about 10 kpc of each other, using the simplest relevant calculation. The basic picture for halo-halo interactions is that a smaller dense halo moves through the less-dense perimeter of the larger halo in a manner similar to that of a mercury ball as it moves through water under the influence of gravity, with additional mass stripping due to friction and diffusion. Much more could be said about halo-halo interactions as it relates to the self-interacting form of DM that derives from the hypothesis of this paper; hopefully the above is sufficient for an initial treatment.

7. Summary

Straightforward calculations of galactic haloes are performed for DM assuming an SU(3) interaction applies to neutrinos. Both $SU(3)_{ve}$ and $SU(3)_{vs}$ are largely

consistent with observations if one allows $SU(3)_{vs}$ to have a different strength than that of SU(3) for quarks. The key attributes of this force can be and are chosen consistent with $SU(3)_{ve}$ given by [38], whereas the standard SU(3) provides no guidance on key parameters such as the bound state mass or the coupling parameter, as discussed in Section 2.

As shown in Section 3, such baryonic neutrinos in haloes need a relatively high temperature to maintain the density and the associated total mass observed for haloes. Since the corresponding velocity exceeds the galactic gravitational escape velocity, some sort of additional binding is inferred. It is found that an $SU(3)_{v}$ binding that is similar to the SU(3) binding of neutrons in neutron stars will produce sufficient binding. Because the resulting state of matter is similar to that for neutron stars, such haloes might be viewed as a form of "neutrino star". Such binding near galactic centers implies that the Tremaine-Gunn bound is not expected to apply as discussed in Section 4. The coupling constant g_s of the feeble $SU(3)_{v}$ is deduced to be as low as $[(137)^2 \times 10^{-25}]^{1/4} = 6.58 \times 10^{-6}$ of that of the electric force (e) from theoretical estimates. This coupling strength applies for relativistic neutrinos and is greater at lower energies due to the running of the coupling parameter as well as the interaction probability as discussed in **Appendix A**.

As shown in Section 3, a generalized form of the equation for hydrostatic equilibrium provides a better match than the standard equation for the observationally-inferred cuspy behavior for DM near galactic centers. Such calculations provide a good match to the inferred total galactic-halo mass and to the DM mass-energy density near earth. Solutions to the generalized hydrostatic equation are found to have long spatial "tails" that are cut off based on a galactic-halo mass constraint. Other explanations for the details of a halo density profile are explored. These include (a) multiple species, (b) angular momentum, and (c) a transition to a condition in which the standard hydrostatic equation applies. An approach using 2 species provides a particularly good fit to sample Einasto and de-projected Sersic model profiles. Further, the generalized solution offers a resolution to the "core-cusp" problem in dwarf galaxies. The solutions must have a core due to the density-limiting Fermi-Dirac statistics of baryonic neutrinos, in the absence of a gravitational singularity. Dwarf galaxies are found to have the "core" portion of the solution in Section 3.2, but either lose the cusp portion of their DM or never accumulate it.

Section 5 discusses the prospects for observation of such DM near earth. Solar neutrinos are not expected to interact significantly with each other or with such dark matter because they are created mono-color (all solar neutrinos are "green" in the conventions of [38]). Hence, they would not bind with each other or the colorless states of the hypothesized form of DM. However, elastic or quasi-elastic scattering might occur. Also, some contact is made with earth-based DM detection experiments, for which the measured amplitude of annual modulation is a fair match with what might be expected from this form of DM.

Halo solutions are stable and self-consistent, having low thermal and mass

diffusivity as discussed in Section 6. Also shown in Section 6 is that the fluid hypothesis is consistent with observed galactic halo interactions (particularly the Bullet Cluster interaction) via arguments put forth here and by other authors, e.g. [82]. The issue of SIDM cross-section is apparently not relevant for the same reasons. Also considered is the motion of smaller haloes, less than 1 kpc in diameter in a larger halo. It is found that the orbital decay is a factor of 1 to 10 times faster than expected from the standard DM model. Further observations of haloes and their interactions would provide helpful tests of the theory presented here. It remains to be seen if the hypothesis proposed herein has full consistency with the preponderance of observational evidence. Further work definitely remains.

A key issue for this form of dark matter is the free-streaming scale in the early universe. This issue is relegated to a companion paper. However, the calculations here show stability of haloes because of the relatively short mean free path of the hypothesized form of dark matter. This short mean free path applied to the early universe results in diffusive rather ballistic transport, vastly shortening the associated "free-streaming scale length" of such matter. Also covered in the companion paper is a discussion of the interaction strength of this form of DM with ordinary matter, dark-matter fraction of total matter, consistency with cosmic microwave background measurements, SN1987a data, neutrino accelerator anomalies, and the issue of SU(3) interactions between neutrinos and quarks

Acknowledgements

Portions of this work were presented in Paper APR19-000356 at the 2019 April Meeting of the American Physical Society. The material of this paper represents significant improvements over that of the conference paper. The author also wishes to thank T. Slatyer, and A. Nelson (deceased) for helpful discussions and E. Vishniac for critical comments on earlier versions of this paper.

Conflicts of Interest

The author declares no conflicts of interest regarding the publication of this paper.

References

[1] Doroshkevich, A.G., Khlopov, M.Yu., Sunyaev, R.A., Szalay, A.S. and Zeldovich, B.Ya. (1981) *Annals of the New York Academy of Sciences* **375**, 32-42. https://doi.org/10.1111/j.1749-6632.1981.tb33688.x

[2] Bond, J.R., Centrella, J., Szalay, A.S. and Wilson, J.R. (1984) *NATO Advanced Study Institute* (*ASI*) *Series C*, **117**, 87-99. https://doi.org/10.1007/978-94-009-7245-2_5

[3] Blumenthal, G.R., Pagels, H. and Primack, J.R. (1982) *Nature*, **299**, 37-38. https://doi.org/10.1038/299037a0

[4] Bond, J.R., Szalay, A.S. and Turner, M.S. (1982) *Physical Review Letters*, **48**, 1636-1639. https://doi.org/10.1103/PhysRevLett.48.1636

[5] Paczynski, B. (1986) *The Astrophysical Journal*, **304**, 1-5.

https://doi.org/10.1086/164140

[6] Griest, K. (1991) *The Astrophysical Journal*, **366**, 412-421. https://doi.org/10.1086/169575

[7] Alcock, C., Allsman, R.A., Alves, D.R., Axelrod, T.S., Becker, A.C., *et al.* (2000) *The Astrophysical Journal*, **542**, 281-307. https://doi.org/10.1086/309512

[8] Lee, B.W. and Weinberg S. (1977) *Physical Review Letters*, *39*, 165-168. https://doi.org/10.1103/PhysRevLett.39.165

[9] Blumenthal, G.R., Faber, S.M., Primack, J.R. and Rees, M.J. (1984) *Nature*, **311**, 517-525. https://doi.org/10.1038/311517a0

[10] White, S.D.M., Frenk, C.S. and Davis, M. (1983) *The Astrophysical Journal*, **274**, L1-L5. https://doi.org/10.1086/184139

[11] Davis, M., Efstathiou, G., Frenk, C.S. and White, S.D.M. (1985) *The Astrophysical Journal*, **292**, 371-394. https://doi.org/10.1086/163168

[12] Weinberg, S. (2008) Cosmology. Oxford University Press, Oxford.

[13] Liddle, A.R. (2004) *Monthly Notices of the Royal Astronomical Society*, **351**, L49-L53. https://doi.org/10.1111/j.1365-2966.2004.08033.x

[14] Del Popolo, A. and Le Delliou, M. (2017) *Galaxies*, **5**, Paper 17. https://doi.org/10.3390/galaxies5010017

[15] Pagels, H. and Primack, J.R. (1982) *Physical Review Letters*, **48**, 224-227. https://doi.org/10.1103/PhysRevLett.48.223

[16] Covi, L., Kim, J.E. and Roszkowski, L. (1999) *Physical Review Letters*, **82**, 4180-4183. https://doi.org/10.1103/PhysRevLett.82.4180

[17] Weinberg, S. (2013) *Physical Review Letters*, **110**, Article ID: 241301. https://doi.org/10.1103/PhysRevLett.110.241301

[18] Dey, U.K., Ray, T.S. and Sarkar, U. (2018) *Nuclear Physics B*, **928**, 258-267. https://doi.org/10.1016/j.nuclphysb.2017.12.005

[19] Allahverdi, R., Dutta, K. and Maharana, A. (2018) *Journal of Cosmology and Astroparticle Physics*, **18**, 038. https://doi.org/10.1088/1475-7516/2018/10/038

[20] Robertson, A., Massey, R. and Eke, V. (2017) *Monthly Notices of the Royal Astronomical Society*, **467**, 4719-4730. https://doi.org/10.1093/mnras/stx463

[21] Tulin, S. and Yu, H.-B. (2017) *Physics Reports*, **730**, 1-58. https://doi.org/10.1016/j.physrep.2017.11.004

[22] Slatyer, T. (2018) Dark Matter: Where and What? SLAC Summer Institute Lecture, Stanford, August 2018.

[23] Hernquist, L., Katz, N., Weinberg, D.H. and Miralda-Escudé, J. (1996) *The Astrophysical Journal*, **457**, L51-L55. https://doi.org/10.1086/309899

[24] Yoshida, N., Springel, V., White, S.D.M. and Tormen, G. (2000) *The Astrophysical Journal*, **544**, L87-L90. https://doi.org/10.1086/317306

[25] Balberg, S., Shapiro, S.L. and Inagaki, S. (2002) *The Astrophysical Journal*, **568**, 475-487. https://doi.org/10.1086/339038

[26] Vogelsberger, M., Zavala, J. and Loeb, A. (2012) *Monthly Notices of the Royal Astronomical Society*, **423**, 3740-3754. https://doi.org/10.1111/j.1365-2966.2012.21182.x

[27] Shao, S., Gao, L., Theuns, T. and Frenk, C.S. (2013) *Monthly Notices of the Royal Astronomical Society*, **430**, 2346-2358. https://doi.org/10.1093/mnras/stt053

[28] Vogelsberger, M., Genel, S., Sijacki, D., Torrey, P., Springel, V., *et al.* (2013)

Monthly Notices of the Royal Astronomical Society, **436**, 3031-3067. https://doi.org/10.1093/mnras/stt1789

[29] Vogelsberger, M., Genel, S., Springel, V., Torrey, P., Sijacki, D., *et al.* (2014) *Nature*, **509**, 7499-7531. https://doi.org/10.1038/nature13316

[30] Cyr-Racine, F.-Y., Sigurdson, K., Zavala, J., Bringmann, T., Vogelsberger, M., *et al.* (2016) *Physical Review D*, **93**, Article ID: 123527. https://doi.org/10.1103/PhysRevD.93.123527

[31] Robertson, A., Massey, R. and Eke, V. (2017) *Monthly Notices of the Royal Astronomical Society*, **465**, 569-587. https://doi.org/10.1093/mnras/stw2670

[32] Brinckmann, T., Zavala, J., Rapetti, D., Hansen, S.H. and Vogelsberger, M. (2018) *Monthly Notices of the Royal Astronomical Society*, **474**, 746-759. https://doi.org/10.1093/mnras/stx2782

[33] Vogelsberger, M., Zavala, J., Schutz, K. and Slatyer, T.R. (2019) *Monthly Notices of the Royal Astronomical Society*, **484**, 5437-5453. https://doi.org/10.1093/mnras/stz340

[34] Zavala, J. and Frenk, C.S. (2019) *Galaxies*, **7**, 81-135. https://doi.org/10.3390/galaxies7040081

[35] Iršič, V., Viel, M., Haehnelt, M.G., Bolton, J.S., Cristiani, S., *et al.* (2017) *Physical Review D*, **96**, Article ID: 023522.

[36] Hsueh, J.-W., Enzi, W., Vegetti, S., Auger, M.W., Fassnacht, C.D., *et al.* (2019) *Monthly Notices of the Royal Astronomical Society*, **492**, 3047-3059.

[37] Tanabashi, M., Hagiwara, K., Hikasa, K., Nakamura, K., Sumino, Y., *et al.* (2018) *Physical Review D*, **98**, Article ID: 030001, Section 9.

[38] Holmes, R. (2018) A Quantum Field Theory with Permutational Symmetry. Lambert Academic Press, Riga.

[39] Tanabashi, M., Hagiwara, K., Hikasa, K., Nakamura, K., Sumino, Y., *et al.* (2018) *Physical Review D*, **98**, Article ID: 030001, Section 14.

[40] Husdal, L. (2016) *Galaxies*, **4**, 78-107. https://doi.org/10.3390/galaxies4040078

[41] Tanabashi, M., Hagiwara, K., Hikasa, K., Nakamura, K., Sumino, Y., *et al.* (2018) *Physical Review D*, **98**, Article ID: 030001, Section 2.

[42] Merritt, D., Graham, A.W., Moore, B., Diemand, J. and Terzic, B. (2006) *The Astronomical Journal*, **132**, 2685-2700. https://doi.org/10.1086/508988

[43] Ringwald, A. and Wong, Y.Y.Y. (2004) *Journal of Cosmology and Astroparticle Physics*, **12**, Paper 005. https://doi.org/10.1088/1475-7516/2004/12/005

[44] Lane, J.H. (1870) *American Journal of Science*, **2**, 57-74. https://doi.org/10.2475/ajs.s2-50.148.57

[45] Hernquist, L. (1990) *The Astrophysical Journal*, **356**, 359-364. https://doi.org/10.1086/168845

[46] Navarro, J.F., Frenk, C.S. and White, S.D.M. (1996) *The Astrophysical Journal*, **462**, 563-575. https://doi.org/10.1086/177173

[47] Graham, A.W. and Driver, S.P. (2005) *Publications of the Astronomical Society of Australia*, **22**, 118-127. https://doi.org/10.1071/AS05001

[48] Sérsic, J.L. (1963) *Boletín de la Asociación Argentina de Astronomía*, **6**, 41-43.

[49] Einasto, J. (1965) Kinematics and Dynamics of Stellar Systems. Trudy Institute Astrofizica Alma-Ata, Vol. 5, 87-xx.

[50] Graham, A.W. and Spitler, L. (2009) *Monthly Notices of the Royal Astronomical*

Society, **397**, 2148-2162. https://doi.org/10.1111/j.1365-2966.2009.15118.x

[51] Weinzirl, T., Jogee, S., Khochfar, S., Burkert, A. and Kormendy, J. (2009) *The Astrophysical Journal*, **696**, 411-447. https://doi.org/10.1088/0004-637X/696/1/411

[52] Holmes, R.B. (2020) *Journal of Modern Physics*, **11**, 648-667. https://doi.org/10.4236/jmp.2020.115042

[53] Chandrasekhar, S. (1931) *The London, Edinburgh, and Dublin Philosophical Magazine and Journal of Science*, **48**, 592-596. https://doi.org/10.1080/14786443109461710

[54] Koester, D. and Chanmugam, G. (1990) *Reports on Progress in Physics*, **53**, 837-915. https://doi.org/10.1088/0034-4885/53/7/001

[55] Ruffert, M. and Janka, H.-T. (2010) *Astronomy and Astrophysics*, **514**, A66. https://doi.org/10.1051/0004-6361/200912738

[56] Cho, H.S. and Lee, C.H. (2010) *Publications of the Astronomical Society of Japan*, **62**, 315-321. https://doi.org/10.1093/pasj/62.2.315

[57] Ozel, F. and Freire, P. (2016) *Annual Reviews of Astronomy and Astrophysics*, **54**, 401-440. https://doi.org/10.1146/annurev-astro-081915-023322

[58] von Weizsäcker, C.F. (1935) *Zeitschrift für Physik*, **96**, 431-458. https://doi.org/10.1007/BF01337700

[59] Read, J. (2014) *Journal of Physics G: Nuclear Particle Physics*, **41**, Article ID: 063101. https://doi.org/10.1088/0954-3899/41/6/063101

[60] Kafle, P.R., Sharma, S., Lewis, G.F. and Bland-Hawthorn, J. (2014) *The Astrophysical Journal*, **794**, 59. https://doi.org/10.1088/0004-637X/794/1/59

[61] Prugniel, P. and Simien, F. (1997) *Astronomy and Astrophysics*, **321**, 111-122.

[62] McMillan, P.J. (2011) *Monthly Notices of the Royal Astronomical Society*, **414**, 2446-2457. https://doi.org/10.1111/j.1365-2966.2011.18564.x

[63] de Blok, W.J.G. (2010) *Advances in Astronomy*, **2010**, Article ID: 789293. https://doi.org/10.1155/2010/789293

[64] Oh, S.-H., Hunter, D.A., Brinks, E., Elmegreen, B.G., Schruba, A., *et al.* (2015) *The Astronomical Journal*, **149**, 180-276. https://doi.org/10.1088/0004-6256/149/6/180

[65] Graham, A., Merritt, D., Moore, B., Diemand, J. and Terzic, B. (2006) *The Astronomical Journal*, **132**, 2701-2710. https://doi.org/10.1086/508990

[66] Vitvitska, M., Klypin, A.A., Kravtsov, A.V., Wechsler, R.H., Primack, J., *et al.* (2002) *The Astrophysical Journal*, **581**, 799-809. https://doi.org/10.1086/344361

[67] Maccio, A.V., Dutton, A.A., van der Bosch, F.C., Moore, B., Potter, D., *et al.* (2007) *Monthly Notices of the Royal Astronomical Society*, **378**, 55-71. https://doi.org/10.1111/j.1365-2966.2007.11720.x

[68] Book, L.G., Brooks, A., Peter, A.H.G., Benson, A.J. and Governato, F. (2011) *Monthly Notices of the Royal Astronomical Society*, **411**, 1963-1979. https://doi.org/10.1111/j.1365-2966.2010.17824.x

[69] Bett, P., Eke, V., Frenk, C.S., Jenkins, A. and Okamoto, T. (2010) *Monthly Notices of the Royal Astronomical Society*, **404**, 1137-1156.

[70] Liao, S., Chen, J. and Chu, M.-C. (2017) *The Astrophysical Journal*, **844**, 86-96. https://doi.org/10.3847/1538-4357/aa79fb

[71] Vogelsberger, M., Helmi, A., Springel, V., White, S.D.M., Wang, J., *et al.* (2009) *Monthly Notices of the Royal Astronomical Society*, **395**, 797-811. https://doi.org/10.1111/j.1365-2966.2009.14630.x

[72] Tremaine, S. and Gunn, J.E. (1979) *Physical Review Letters*, **42**, 407-410. https://doi.org/10.1103/PhysRevLett.42.407

[73] Grupen, C. (2005) Astroparticle Physics. Springer, Berlin.

[74] Kelso, C., Savage, C., Sandick, P., Freese, K. and Gondolo, P. (2018) *European Journal of Physics C*, **78**, Paper 223. https://doi.org/10.1140/epjc/s10052-018-5685-4

[75] Perkins, D.H. (2000) Introduction to High Energy Physics. 4th Edition, Cambridge University Press, Cambridge.

[76] Patrignani, C., Agashe, K., Aielli, G., Amsler, C., Antonelli, M., *et al.* (2016) *Chinese Physics C*, **40**, Article ID: 100001, Section 14. https://doi.org/10.1088/1674-1137/40/10/100001

[77] Sterman, G. and Weinberg, S. (1977) *Physical Review Letters*, **39**, 1436-1439. https://doi.org/10.1103/PhysRevLett.39.1436

[78] White, F.M. (1986) Fluid Mechanics. McGraw-Hill, New York.

[79] Johnston, K.V., Majewski, S.R., Siegel, M.H., Reid, I.N. and Kunkel, W.E. (1999) *Astronomical Journal*, **118**, 1719-1726. https://doi.org/10.1086/301037

[80] Law, D.R. and Majewski, S.R. (2010) *The Astrophysical Journal*, **714**, 229-254. https://doi.org/10.1088/0004-637X/714/1/229

[81] Randall, S.W., Markevitch, M., Clowe, D., Gonzalez, A.H. and Bradac, M. (2008) *The Astrophysical Journal*, **679**, 1173-1180. https://doi.org/10.1086/587859

[82] Agrawal, P., Cyr-Racine, F.-Y., Randall, L. and Scholtz, J. (2017) *Journal of Cosmology and Astroparticle Physics*, **17**, Paper 022. https://doi.org/10.1088/1475-7516/2017/05/022

Appendix A: Estimate of Binding Energy of Hadronic Neutrinos and SU(3)$_{ve}$ Interaction Strength

This Appendix estimates the binding energy of baryonic and mesonic neutrinos as well as the SU(3)$_{ve}$ interaction strength for relativistic neutrinos. Because the SU(3) binding energy is a large fraction of the mass-energy of bound quarks, one might expect that this would be the case for SU(3)-bound neutrinos as well (should they exist). This fact is utilized for estimation of the mass-energy of bound neutrino states.

The binding energy of baryonic neutrinos is estimated first. From equation (10.27a) of [38], the binding energy E_b of a baryonic neutrino can be approximated by

$$E_b = \beta_{\upsilon\tau}^2 \left(\hbar c/4\right)\left\{4\pi\alpha_3 \left(m_{\upsilon e}^2 + m_{\upsilon\mu}^2 + m_{\upsilon\tau}^2\right)^{1/2} c^2/\left(\hbar c\right)\right\}^2 \left|\Delta x\right|, \tag{A1}$$

where $\beta_{\upsilon\tau}^2$ is the probability of an upper-mass tau neutrino state (assuming the normal hierarchy), and α_3 is the dimensionless coupling parameter for the strong force, $g_s^2/\left(4\pi\hbar c\right)$. The neutrino flavor masses are $m_{\nu e}$, $m_{\nu\mu}$, and $m_{\nu\tau}$. $|\Delta x|$ is the characteristic size of an SU(3)-bound neutrino. The value of α_3 is chosen to equal 1 in this calculation because for bound SU(3) states the coupling parameter is close to 1 for bound quark-quark interactions, and that should apply here as well. The probability of an upper-mass neutrino state from the same reference for a marginally relativistic bound state is given by

$$\beta_{\upsilon\tau}^2 = m_{\upsilon e}/\left(m_{\upsilon e} + m_{\upsilon\tau}\right). \tag{A2}$$

This probability is approximately 0.1 for $m_{\nu e}$ ~ 0.005 eV/c^2 and $m_{\nu\tau}$~ 0.05 eV/c^2, assuming the normal hierarchy for neutrino masses, the known mass-squared differences, and the least possible mass for the tau neutrino. Under the same assumptions, the muon neutrino mass is about 0.01 eV/c^2. The last input to Equation (A1) is the characteristic size of SU(3)-bound neutrinos. For this, use an estimate based on the Heisenberg uncertainty principle:

$$\left|\Delta x\right| \geq \hbar c/\left(pc\right) \approx \hbar c/\left(m_{\upsilon\tau}c^2\right). \tag{A3}$$

Using the nominal value of $m_{\nu\tau}$ given above, one obtains $|\Delta x|$ ~ 3.3 microns. One might also use $m_{\nu e}$ or $m_{\nu\mu}$ in Equation (A3), but the basis of Equation (A1) suggests that $m_{\nu\tau}$ should be used. Substituting the above into Equation (A1), one obtains an estimate of the binding energy of baryonic neutrinos.

$$E_b \geq 4\pi^2 m_{\upsilon e}c^2 = 0.2 \text{ eV}. \tag{A4}$$

One can see that with these approximations and assumptions, the binding energy is roughly independent of the upper neutrino mass value. In Equation (A3), one might also use $\left(m_{\upsilon\tau}m_{\upsilon e}\right)^{1/2}c^2$ for the denominator based on Ch. 10 of [38]. With this assumption, one obtains

$$E_b \geq 4\pi^2 m_{\upsilon e}c^2 \left(m_{\upsilon\tau}/m_{\upsilon e}\right)^{1/2} = 4\pi^2 \left(m_{\upsilon\tau}m_{\upsilon e}\right)^{1/2} c^2 = 0.62 \text{ eV}. \tag{A5}$$

To this range of binding energies, one must add the masses of the constituent

neutrinos, which might range from $3m_{ve}$ to $3m_{v\tau}$. This then leads to a range of baryonic neutrino masses from about 0.22 eV/c^2 to about 0.8 eV/c^2. Assuming the baryonic neutrinos comprise the lower-mass neutrino states as in quarks, a tighter range would be 0.22 to 0.64 eV/c^2. On the other hand, a baryonic neutrino mass as high as 0.8 eV/c^2 should not immediately be ruled out. Equation (10.27b) of [38] gives a similar equation for mesonic neutrino states, and the corresponding range of masses is 0.08 to 0.35 eV/c^2.

The above mass-scaling analysis can also be applied to relativistic particles using Equation (10.13b) rather than (10.13a) of [38]. In this limit, $\beta_{v\tau}^2 \sim 0.5$, independent of the interacting masses. Referring to Equation (A1) and removing the $|\Delta x|$ to obtain the interaction force coupling parameter, one finds that the interaction scales as $m_{v\tau}^2$ in this case. One then has a scaling factor of $\left(m_{\upsilon\tau}/m_b\right)^2$ to $\left(m_{\upsilon\tau}/m_t\right)^2$ of the quark interaction strength to the neutrino family interaction strength, scaling from the down family or the up family, respectively. Here m_b is the bottom quark mass and m_t is the top quark mass. Note that the scaling factor between the down-quark family and up-quark family should be of order 1 because all hadrons bound by a strong quark interaction have sufficient energy for the presence of both $u-\overline{u}$ and $d-\overline{d}$ sea quarks. There is also the running of the coupling parameter that should be included; the standard calculation indicates that the correction is negligible when applied to neutrinos.

Journal of Modern Physics, 2020, 11, 886-906
https://www.scirp.org/journal/jmp
ISSN Online: 2153-120X
ISSN Print: 2153-1196

Relating Some Nonlinear Systems to a Cold Plasma Magnetoacoustic System

Jennie D'Ambroise[1], Floyd L. Williams[2]

[1]Department of Mathematics/CIS, SUNY Old Westbury, Old Westbury, NY, USA
[2]Department of Mathematics and Statistics, University of Massachusetts, Amherst, MA, USA
Email: dambroisej@oldwestbury.edu, williams@math.umass.edu

How to cite this paper: D'Ambroise, J. and Williams, F.L. (2020) Relating Some Nonlinear Systems to a Cold Plasma Magnetoacoustic System. *Journal of Modern Physics*, **11**, 886-906.
https://doi.org/10.4236/jmp.2020.116054

Received: March 20, 2020
Accepted: June 2, 2020
Published: June 5, 2020

Abstract

Using a Gurevich-Krylov solution that describes the propagation of nonlinear magnetoacoustic waves in a cold plasma, we construct solutions of various other nonlinear systems. These include, for example, Madelung fluid, reaction diffusion, Broer-Kaup, Boussinesq, and Hamilton-Jacobi-Bellman systems. We also construct dilaton field solutions for a Jackiw-Teitelboim black hole with a negative cosmological constant. The black hole metric corresponds to a cold plasma metric by way of a change of variables, and the plasma dilatons and cosmological constant also have an expression in terms of parameters occurring in the Gurevich-Krylov solution. A dispersion relation, moreover, links the magnetoacoustic system and a resonance nonlinear Schrödinger equation.

Keywords

Cold Plasma, Magnetoacoustic Waves, Resonance Nonlinear Schrödinger Equation, Reaction Diffusion System, Jackiw-Teitelboim Black Hole, Dilaton Field, Ricci Scalar Curvature, Jacobi Elliptic Function

1. Introduction

Over the past years, points of connection of plasma physics to various nonlinear equations of significant importance have been explored. An initial connection can be traced back to H. Washimi and T. Taniuti [1], for example, who showed that the one-dimensional asymptotic behavior (as $t \to \infty$) of small amplitude ion-acoustic waves was described by the Korteweg-deVries equation—following on a parallel track work of C. S. Gardner and G. K. Morikawa [2]. The paper of A. Jeffrey [3] provides for some systematic details on this particular connection, and it includes remarks, for example, on the work of Y. A. Berezin and V. I.

Karpman [4].

In the 2007 paper [5] of J.-H. Lee, O. K. Pashaev, C. Rogers, and W. K. Schief the *resonance* nonlinear Schrödinger (RNLS) equation

$$i\psi_t + \psi_{xx} + \gamma|\psi|^2\psi = \delta\frac{|\psi|_{xx}}{|\psi|}\psi \tag{1}$$

appears in connection with a discussion of one-dimensional, long magnetoacoustic waves in a cold plasma subject to a transverse magnetic field $\vec{\boldsymbol{B}}$. Here $\gamma,\delta\in\mathbb{R}=$ the field of real numbers with $\delta>1$, and $|\psi|_{xx}/|\psi|$ is a de Broglie quantum potential. For $\gamma=-1/2$, a complex-valued wave function solution ψ of the form

$$\psi(x,t)=\sqrt{\rho(x,t)}\mathrm{e}^{-iS(x,t)} \tag{2}$$

was obtained, where $\rho>0$ is the plasma density and S is a real-valued velocity potential. That is, the velocity field u of the plasma is given by $u=-2S_x$. In the present paper we consider for an arbitrary $\gamma<0$ solutions of Equation (1) of the form

$$\psi=\mathrm{e}^{R-iS} \tag{3}$$

for real-valued functions $R(x,t),S(x,t)$. Such a function ψ is a solution if and only if the pair (R,S) is a solution of the Madelung fluid system

$$\begin{aligned} &R_t - S_{xx} - 2R_xS_x = 0\\ &S_t + (1-\delta)\left[R_{xx}+R_x^2\right] - S_x^2 + \gamma\mathrm{e}^{2R} = 0 \end{aligned} \tag{4}$$

independently of the assumption $\gamma<0$.

The system of main interest for us is the nonlinear magnetoacoustic system (MAS)

$$\begin{aligned} &\rho_t + (\rho u)_x = 0\\ &u_t + uu_x + \rho_x + \beta^2\left[\frac{\rho_{xx}}{\rho} - \frac{1}{2}\left(\frac{\rho_x}{\rho}\right)^2\right]_x = 0 \end{aligned} \tag{5}$$

which describes the propagation of the aforementioned magnetoacoustic waves in the cold plasma, under some simplifying assumptions that include the uni-axial propagation assumption

$$\vec{\boldsymbol{B}}(x,t)=B(x,t)\vec{k},\ \vec{u}(x,t)=u(x,t)\vec{i}. \tag{6}$$

Here $\beta>0$ and $\vec{i},\vec{k}$ are unit vectors along the x and z axes. The system (5) is derived by way of a shallow water type approximation of the system

$$\begin{aligned} &\rho_t + (\rho u)_x = 0\\ &u_t + uu_x + \frac{B}{\rho}B_x = 0\\ &B = \rho + \left(\frac{1}{\rho}B_x\right)_x \end{aligned} \tag{7}$$

where a change of variables $(x,t)\to(\beta x,\beta t)$ is employed (under which the first

two equations in (7) are invariant and third one becomes $B=\rho+\beta^2\left(B_x/\rho\right)_x$), and where an expansion of B of the form

$$B=\rho+\beta^2\left(\frac{\rho_x}{\rho}\right)_x+\mathcal{O}\left(\beta^4\right) \tag{8}$$

is inserted into the second equation [5] [6] [7].

We will work with the following explicit traveling wave solution $\left(\rho>0,u\right)$ of the MAS (5) given by A. Gurevich and A. Krylov (G-K) in [8]. For a choice $u_0>0$, $\alpha_3>\alpha_2\geq\alpha_1\geq 0$, define

$$\begin{aligned} &v\overset{\text{def}}{=}u_0/\beta>0,\ a\overset{\text{def}}{=}+\left(\alpha_3-\alpha_1\right)^{\frac{1}{2}}\Big/2\beta>0,\ \kappa\overset{\text{def}}{=}\left(\frac{\alpha_3-\alpha_2}{\alpha_3-\alpha_1}\right)^{\frac{1}{2}}\in(0,1),\\ &C\overset{\text{def}}{=}+\left(\alpha_1\alpha_2\alpha_3\right)^{\frac{1}{2}}=\left(\alpha_1\left[4a^2\beta^2\left(1-\kappa^2\right)+\alpha_1\right]\left[4a^2\beta^2+\alpha_1\right]\right)^{1/2}\end{aligned} \tag{9}$$

where the second expression for C in (9) follows as $1-\kappa^2\overset{\text{def}}{=}\left(\alpha_2-\alpha_1\right)/\left(\alpha_3-\alpha_1\right)$ and $4a^2\beta^2\overset{\text{def}}{=}\alpha_3-\alpha_1\Rightarrow\left[4a^2\beta^2\left(1-\kappa^2\right)+\alpha_1\right]\left[4a^2\beta^2+\alpha_1\right]=\alpha_2\alpha_3$. Then for the standard Jacobi elliptic function $dn\left(x,\kappa\right)$ with elliptic modulus κ [9]

$$\begin{aligned} &\rho\left(x,t\right)=\alpha_1+4a^2\beta^2dn^2\left(a\left(x-\beta vt\right),\kappa\right),\\ &u\left(x,t\right)=u_0+C/\rho\left(x,t\right).\end{aligned} \tag{10}$$

The choice for $\delta>1$ in (1) will be $\delta\overset{\text{def}}{=}\beta^2+1$. As shown in [10] (also compare [5] [7]), given a solution $\left(\rho>0,u\right)$ of the MAS (5) and the assumption $\gamma<0$, one can construct a corresponding solution $\left(R,S\right)$ of the Madelung fluid system (4) where

$$R\overset{\text{def}}{=}\frac{1}{2}\log\left(\frac{\rho}{-2\gamma}\right),\ S_x\overset{\text{def}}{=}-\frac{u}{2} \tag{11}$$

and, moreover, a corresponding solution $\left(r,s\right)$ of the reaction diffusion system (RDS)

$$\begin{aligned} &r_t-r_{xx}+Br^2s=0\\ &s_t+s_{xx}-Brs^2=0\end{aligned} \tag{12}$$

where

$$\begin{aligned} &r\left(x,t\right)\overset{\text{def}}{=}\mathrm{e}^{R\left(x,t/\beta\right)}\mathrm{e}^{\phi\left(x,t\right)},\\ &s\left(x,t\right)\overset{\text{def}}{=}-\mathrm{e}^{R\left(x,t/\beta\right)}\mathrm{e}^{-\phi\left(x,t\right)},\\ &\phi\left(x,t\right)\overset{\text{def}}{=}S\left(x,t/\beta\right)/\beta,\\ &B\overset{\text{def}}{=}-\gamma/\beta^2=-\gamma/\left(\delta-1\right)>0.\end{aligned} \tag{13}$$

In the present case of (10) therefore

$$\begin{aligned} r\left(x,t\right)&=\left[\rho\left(x,t/\beta\right)/\left(-2\gamma\right)\right]^{\frac{1}{2}}\mathrm{e}^{\phi\left(x,t\right)}\\ &=\left[\frac{\alpha_1+4a^2\beta^2dn^2\left(a\left(x-vt\right),\kappa\right)}{-2\gamma}\right]^{1/2}\mathrm{e}^{\phi\left(x,t\right)},\end{aligned}$$

$$s(x,t) = -\left[\rho(x,t/\beta)/(-2\gamma)\right]^{\frac{1}{2}} e^{-\phi(x,t)} = -\left[\frac{\alpha_1 + 4a^2\beta^2 dn^2\left(a(x-vt),\kappa\right)}{-2\gamma}\right]^{1/2} e^{-\phi(x,t)}. \tag{14}$$

As before, we see in (11) that S is a potential function for the velocity field u. Note also that by (3) and (11) we obtain the solution

$$\psi(x,t) = \left[\rho(x,t)/(-2\gamma)\right]^{\frac{1}{2}} e^{-iS(x,t)} = \left[\frac{\alpha_1 + 4a^2\beta^2 dn^2\left(a(x-\beta vt),\kappa\right)}{-2\gamma}\right]^{1/2} e^{-iS(x,t)}, \tag{15}$$

of the RNLS equation (1).

The formulas (11), (14), (15) relate the nonlinear systems (4), (12) and the resonance nonlinear Schrödinger Equation (1) to the cold plasma system (5) with solution (10). In Section 2 we relate the solution (10) also to nonlinear systems of Broer-Kaup, Boussinesq, and Hamilton-Jacobi-Bellman and their anti-systems given by the time reversal $t \to -t$. Here we find solutions of these systems that generalized in a non-trivial way those found in [11], for example. By choosing $\kappa = 1$ so that $dn(x,\kappa) \overset{\text{def}}{=} \operatorname{sech}(x)$, and choosing $\alpha_1 = 0$ so that $C = 0$ by (9) and $u = u_0$ is a constant function in (10), in particular, our r in (14) and v^+ in (34) of section 2 reduce to the dissipaton e^+ and shock soliton v^+ in Sections 2 and 4 of [11].

Attention in Section 4 is turned to further remarks on the cold plasma-2d black hole connection set up in [10]. The main result of that section is the computation of two more plasma dilaton fields such that these combined with the one computed in [10] form a linearly independent set. This too generalizes in a non-trivial way (namely the case $\alpha_1 \neq 0$) a result found in [12].

Finally, in Section 5, we switch from the traveling wave solution (ρ, u) to a plane wave solution of the system (5). Remarkably, its dispersion relation coincides with the dispersion relation obtained from the linearization of the RNLS Equation (1) about a suitably normalized ground state solution ψ_0.

Throughout, an attempt is made to maintain an expository style in the presentation of the material, for the sake of completeness.

2. Elliptic Function Solutions of Broer-Kaup, Boussinesq, and Hamilton-Jacobi-Bellman Systems

In addition to the solutions (11), (14) of the Madelung fluid and RD systems (4), (12), and the RNLS solution (15) of (1), all of which were constructed by way of the G-K solution (10), we consider now solutions of nonlinear systems of Broer-Kaup (B-K), Boussinesq, and Hamilton-Jacobi-Bellman (H-J-B), and of their time reversal ($t \to -t$) systems. Here, again, the G-K solution (10) of the MAS (5) plays an underlying, subtextual role.

2.1. Conservation Laws and the B-K System

From the RDS (12), conservation laws can be deduced by which, in turn, one can

derive the B-K system. We provide a sketch of this derivation, for the sake of completeness, and we present a general elliptic function solution.

The continuity equation $\rho_t + (\rho u)_x = 0$, or conservation law, in (5) is one of many such laws. The RDS (12) gives rise to the conservation law

$$(rs)_t - (r_x s - r s_x)_x = 0, \tag{16}$$

for example, for which the particular value $B = -\gamma/\beta^2$ there does not matter. To check (16), start with the equation $-(r_x s - r s_x)_x \overset{(i)}{=} r s_{xx} - s r_{xx}$. Multiply the first RD equation in (12) by s and the second one by r. Addition of these two multiplied equations eliminates B and gives the equation $0 = r_t s + s_t r - r_{xx} s + s_{xx} r = (rs)_t - (r_x s - r s_x)_x$, by (i), which is the assertion in (16).

In addition to (16), we also need the conservation law

$$\left[r_x s_x + \frac{B}{2}(rs)^2 \right]_t = \left[r_x s_t + s_x r_t \right]_x, \tag{17}$$

which also follows from (12). Namely, the l.h.s. in (17) is $r_x s_{xt} + r_{xt} s_x + Brs\left[r s_t + r_t s \right]$, where the third term here is $\left(Br^2 s\right) s_t + \left(Brs^2\right) r_t \overset{\because}{=} \left(-r_t + r_{xx}\right) s_t + \left(s_t + s_{xx}\right) r_t$ (by (12)) $= r_{xx} s_t + s_{xx} r_t$. Thus the l.h.s. in (17) is $r_x s_{xt} + r_{xt} s_x + r_{xx} s_t + s_{xx} r_t = (r_x s_t)_x + (s_x r_t)_x$, by the equality of mixed partials: $r_{tx} = r_{xt}$ and $s_{tx} = s_{xt}$. Equation (17) is now established.

Define

$$\sigma \overset{\text{def}}{=} -rs. \tag{18}$$

For $r > 0$ and $s < 0$, we see that $\sigma(\log r)_x \overset{\text{def}}{=} -\frac{rsr_x}{r} \overset{(ii)}{=} -sr_x$ and similarly $\sigma(\log -s)_x = -rss_x/s \overset{(iii)}{=} -rs_x$, which says that the conservation law (16) can be written as

$$\sigma_t \left(\overset{\text{def}}{=} -(rs)_t \right) = \left[\sigma(\log r)_x - \sigma(\log -s)_x \right]_x. \tag{19}$$

Also by (ii), (iii), $\sigma_x = \sigma(\log r)_x + \sigma(\log -s)_x \Rightarrow$

$$\sigma_{xx} = \left[\sigma(\log r)_x + \sigma(\log -s)_x \right]_x, \tag{20}$$

so that (19) and (20) together give the equations

$$\sigma_t + \sigma_{xx} = \left[2\sigma(\log r)_x \right]_x, \quad \sigma_t - \sigma_{xx} = \left[-2\sigma(\log -s)_x \right]_x, \tag{21}$$

which suggests that one defines

$$v^+ \overset{\text{def}}{=} (\log r)_x = \frac{r_x}{r}, \quad v^- \overset{\text{def}}{=} (\log -s)_x = \frac{s_x}{s}: \tag{22}$$

$$\sigma_t + \sigma_{xx} = \left(2\sigma v^+ \right)_x, \quad \sigma_t - \sigma_{xx} = \left(-2\sigma v^- \right)_x. \tag{23}$$

Then

$$\left(v^+\right)_x + \left(v^+\right)^2 = (r_x/r)_x + r_x^2/r^2 = \left(r r_{xx} - r_x^2\right)/r^2 + r_x^2/r^2 = r_{xx}/r = \left(r_t + Br^2 s\right)/r$$

(by (12)) $\overset{\text{def}}{=} r_t/r - B\sigma$ (by (18)) $= (\log r)_t - B\sigma$. That is,

$$\left[v_x^+ + \left(v^+\right)^2 + B\sigma\right]_x = \left(\log r\right)_{tx} = \left(\log r\right)_{xt} \overset{\text{def}}{=} \left(v^+\right)_t. \tag{24}$$

Similarly, by (12) and (18) again,

$$\left(v^-\right)_x + \left(v^-\right)^2 = s_{xx}/s = \left(-s_t + Brs^2\right)/s = -\left(\log -s\right)_t - B\sigma \Rightarrow$$

$$\left[\left(v^-\right)_x + \left(v^-\right)^2 + B\sigma\right]_x = -\left(\log -s\right)_{tx} = -\left(\log -s\right)_{xt} \overset{\text{def}}{=} -\left(v^-\right)_t. \tag{25}$$

Putting the pieces together, (Equations (23)-(25)), we have derived from the RDS (12), for $r>0, s<0$, and B arbitrary (not necessarily the specific value $B=-\gamma/\beta^2$ there) the Broer-Kaup systems

$$\begin{aligned} &\sigma_t + \sigma_{xx} = \left(2\sigma v^+\right)_x,\ \left(v^+\right)_t = \left[\left(v^+\right)_x + \left(v^+\right)^2 + B\sigma\right]_x \\ &\sigma_t - \sigma_{xx} = -\left(2\sigma v^-\right)_x,\ \left(v^-\right)_t = -\left[\left(v^-\right)_x + \left(v^-\right)^2 + B\sigma\right]_x \end{aligned} \tag{26}$$

for σ and $v^{\pm}$ defined in (18) and (22). The second system in (26) (with the minus signs) corresponds to the time reversal $t \to -t$.

We can obtain elliptic function solutions of the systems in (26) immediately, by way of the solutions r, s in (14). Note first that by (10), (14), (18)

$$\begin{aligned} \sigma(x,t) &\overset{\text{def}}{=} -r(x,t)s(x,t) = \rho(x,t/\beta)/(-2\gamma) \\ &= \left[\alpha_1 + 4a^2\beta^2 dn^2\left(a(x-vt),\kappa\right)\right]/(-2\gamma) \end{aligned} \tag{27}$$

Also by (14)

$$\begin{aligned} \log r(x,t) &= \frac{1}{2}\left[\log\rho(x,t/\beta) - \log(-2\gamma)\right] + \phi(x,t) \\ \log -s(x,t) &= \frac{1}{2}\left[\log\rho(x,t/\beta) - \log(-2\gamma)\right] - \phi(x,t). \end{aligned} \tag{28}$$

From [9], the identities and differentiation formulas

$$\begin{aligned} &sn^2(x,\kappa) + cn^2(x,\kappa) = 1,\ \ dn^2(x,\kappa) + \kappa^2 sn^2(x,\kappa) = 1, \\ &sn(x,1) = \tanh(x),\ \ cn(x,1) = dn(x,1) = \operatorname{sech}(x), \\ &\frac{\mathrm{d}}{\mathrm{d}x} sn(x,\kappa) = cn(x,\kappa)dn(x,\kappa),\ \ \frac{\mathrm{d}}{\mathrm{d}x} cn(x,\kappa) = -sn(x,\kappa)dn(x,\kappa), \\ &\frac{\mathrm{d}}{\mathrm{d}x} dn(x,\kappa) = -\kappa^2 sn(x,\kappa)cn(x,\kappa) \end{aligned} \tag{29}$$

hold for the standard Jacobi elliptic functions $sn(x,\kappa), cn(x,\kappa), dn(x,\kappa)$. The following is a useful inequality:

$$\frac{sn^2(x,\kappa)cn^2(x,\kappa)}{dn^2(x,\kappa)} \le 1. \tag{30}$$

By definitions (13), (11), (10), (9), respectively

$$\begin{aligned} \phi_x(x,t) &= \frac{S_x(x,t/\beta)}{\beta} = -\frac{u(x,t/\beta)}{2\beta} = -\frac{u_0}{2\beta} - \frac{C}{2\beta\rho(x,t/\beta)} \\ &= -\frac{v}{2} - \frac{C}{2\beta\rho(x,t/\beta)}. \end{aligned} \tag{31}$$

By (10) (again)

$$\rho(x,t/\beta)=\alpha_1+4a^2\beta^2 dn^2\left(a(x-vt),\kappa\right) \tag{32}$$

so that the last differentiation formula in (29) gives

$$\rho_x(x,t/\beta)=-8a^3\beta^2\kappa^2\left(sncndn\right)\left(a(x-vt),\kappa\right), \tag{33}$$

which with (22), (28), (31) and (32) gives

$$\begin{aligned} v^+(x,t)&\overset{\text{def}}{=}(\log r)_x(x,t)=\frac{-4a^3\beta^2\kappa^2\left(sncndn\right)\left(a(x-vt),\kappa\right)-C/2\beta}{\rho(x,t/\beta)=\alpha_1+4a^2\beta^2 dn^2\left(a(x-vt),\kappa\right)}-\frac{v}{2},\\ v^-(x,t)&\overset{\text{def}}{=}(\log -s)_x(x,t)=\frac{-4a^3\beta^2\kappa^2\left(sncndn\right)\left(a(x-vt),\kappa\right)+C/2\beta}{\rho(x,t/\beta)=\alpha_1+4a^2\beta^2 dn^2\left(a(x-vt),\kappa\right)}+\frac{v}{2}, \end{aligned} \tag{34}$$

for C given in (9).

The formulas (27) and (34) therefore provide for a solution (σ,v^+,v^-) of the Broer-Kaup systems in (26). There we take $B=-\gamma/\beta^2$, since we used the specific solution (r,s) in (14) of the RDS (12).

The solution (σ,v^+) of the first system in (26) vastly generalizes the one (ρ,v^+) found in [11], where the notation ρ there corresponds to σ here, and where a solution of the second system in (26) is not addressed.

The generalization here is not simply that of elliptic functions over hyperbolic function, but it is in large part due to the freedom to allow α_1 to be non-zero: $\alpha_1>0$. Indeed for $\alpha_1=0$, all results of this paper, and those of [10], simplify greatly—mainly because then $C=0$, by (9). For $\alpha_1=0$, the formulas in (27) and (34), for example, reduce to

$$\begin{aligned} \sigma(x,t)&=4a^2\beta^2 dn^2\left(a(x-vt),\kappa\right)/(-2\gamma),\\ v^\pm(x,t)&=-a\kappa^2\frac{sncn}{dn}\left(a(x-vt),\kappa\right)\mp\frac{v}{2}, \end{aligned} \tag{35}$$

which, moreover, for $\kappa=1$ reduce further to

$$\begin{aligned} \sigma(x,t)&=4a^2\beta^2\operatorname{sech}^2\left(a(x-vt)\right)/(-2\gamma),\\ v^\pm(x,t)&=-a\tanh\left(a(x-vt)\right)\mp\frac{v}{2}, \end{aligned} \tag{36}$$

which apart from v^- are the results that appear in [11], with a different choice of constants—the v^+ in (36) being the shock soliton mentioned in the introduction. We shall see in Section 3 that in case $\alpha_1=0$, there is also a nice choice for the potential function $S(x,t)$ in (11), and thus a nice expression for $\phi(x,t)$ in (13), (14), and for $\psi(x,t)$ in (15) exists in this case.

2.2. Boussinesq Systems

Given the bulk of details and formulas in Section 2.1, we can glide more easily through this section. A good number of equations for various mathematical models are referred to as Boussinesq equations. It is perhaps best then to consider the systems discussed here more properly as Boussinesq type systems. This prolific French researcher, Joseph Valentin Boussinesq (1842-1929) made numerous high level contributions to fluid mechanics that involved the theory of

solitary waves and the KdV equation, for example, and contributions to several other fields including the propagation of light and the theory of linear elasticity.

Define the "pressure" functions $p^{\pm}(x,t)$ by

$$p^{\pm} \overset{\text{def}}{=} B\sigma + \left(v^{\pm}\right)_x. \tag{37}$$

As before we will choose $B \overset{\text{def}}{=} -\gamma/\beta^2$. By (26),

$$\left(v^{\pm}\right)_t = \pm\left[\left(v^{\pm}\right)_x + \left(v^{\pm}\right)^2 + B\sigma\right]_x = \pm\left[\left(v^{\pm}\right)_{xx} + 2v^{\pm}\left(v^{\pm}\right)_x + B\sigma_x\right] \tag{38}$$

so that

$$\left(v^{\pm}\right)_t \mp 2v^{\pm}\left(v^{\pm}\right)_x = \pm\left(v^{\pm}\right)_{xx} \pm B\sigma_x \overset{\text{def}}{=} \pm\left(p^{\pm}\right)_x. \tag{39}$$

One can compute $\left(p^{\pm}\right)_t$ also, and in the end, with (39), derive the Boussinesq type systems

$$\begin{aligned} &\left(p^{+}\right)_x = \left(v^{+}\right)_t - 2v^{+}\left(v^{+}\right)_x,\ \left(p^{+}\right)_t = \left(v^{+}\right)_{xxx} + \left(2p^{+}v^{+}\right)_x \\ &-\left(p^{-}\right)_x = \left(v^{-}\right)_t + 2v^{-}\left(v^{-}\right)_x,\ \left(p^{-}\right)_t = -\left(v^{-}\right)_{xxx} - \left(2p^{-}v^{-}\right)_x \end{aligned} \tag{40}$$

The second system in (40) (with the minus signs) corresponds to the time reversal $t \to -t$.

As with the B-K systems in (26), one can obtain explicit elliptic function solutions of the systems in (40), or simpler hyperbolic function solutions as in (36), by taking $\kappa = 1$. For this one simply applies the formulas for σ and $v^{\pm}$ in (27) and (34) to compute $p^{\pm}$ in definition (37)—perhaps with the help of Maple. Generality in an alternate direction of importance is provided by Professor Pashaev in [11] who considers kink-soliton and two-soliton solutions of the Broer-Kaup and Boussinesq systems (26) and (40). These latter systems trace back to the analysis of water waves propagating in a long narrow channel [13] [14].

2.3. A Hamilton-Jacobi-Bellman System

Given two functions $f_1(x,t), f_2(x,t)$, consider the Lagrangian density

$$\mathcal{L} \overset{\text{def}}{=} \frac{f_2}{2}\left[\frac{\partial f_1}{\partial t} - \frac{\partial^2 f_1}{\partial x^2}\right] - \frac{f_2}{4}\left(\frac{\partial f_1}{\partial x}\right)^2 - \frac{B}{2}f_2^2. \tag{41}$$

The corresponding Euler-Lagrange equations of motion are

$$\frac{\partial}{\partial t}\left(\frac{\partial \mathcal{L}}{\partial f_{jt}}\right) + \frac{\partial}{\partial x}\left(\frac{\partial \mathcal{L}}{\partial f_{jx}}\right) - \frac{\partial^2}{\partial x^2}\left(\frac{\partial \mathcal{L}}{\partial f_{jxx}}\right) = \frac{\partial \mathcal{L}}{\partial f_j} \tag{42}$$

for $j = 1,2$, which are immediately computed:

$$\begin{aligned} &\frac{\partial \mathcal{L}}{\partial f_{1t}} = \frac{f_2}{2},\ \frac{\partial \mathcal{L}}{\partial f_{2t}} = 0,\ \frac{\partial \mathcal{L}}{\partial f_{1x}} = -\frac{f_2}{2}\frac{\partial f_1}{\partial x}, \\ &\frac{\partial \mathcal{L}}{\partial f_{2x}} = 0,\ \frac{\partial \mathcal{L}}{\partial f_{1xx}} = -\frac{f_2}{2},\ \frac{\partial \mathcal{L}}{\partial f_{2xx}} = 0,\ \frac{\partial \mathcal{L}}{\partial f_1} = 0, \\ &\frac{\partial \mathcal{L}}{\partial f_2} = \frac{1}{2}\left[\frac{\partial f_1}{\partial t} - \frac{\partial^2 f_1}{\partial x^2}\right] - \frac{1}{4}\left(\frac{\partial f_1}{\partial x}\right)^2 - Bf_2 \end{aligned} \tag{43}$$

so that the equations of motion are

$$\begin{aligned}&\frac{\partial f_2}{\partial t}-\left(f_2\frac{\partial f_1}{\partial x}\right)_x+\frac{\partial^2 f_2}{\partial x^2}=0,\\&\frac{\partial f_1}{\partial t}-\frac{\partial^2 f_1}{\partial x^2}-\frac{1}{2}\left(\frac{\partial f_1}{\partial x}\right)^2-2Bf_2=0.\end{aligned}\tag{44}$$

Now going back to the first B-K equation

$$\sigma_t-\left(\sigma 2v^+\right)_x+\sigma_{xx}=0\tag{45}$$

in (26), which we compare with the first equation in (44), we are obviously motivated to think of f_2 as σ and to take

$$\frac{\partial f_1}{\partial x}=2v^+\overset{\text{def}}{=}\left(2\log r\right)_x.\tag{46}$$

That is, we choose

$$f_1=A^+\overset{\text{def}}{=}2\log r.\tag{47}$$

Then (44) is the system

$$\begin{aligned}&\sigma_t-\left[\sigma\left(A^+\right)_x\right]_x+\sigma_{xx}=0\\&\left(A^+\right)_t-\left(A^+\right)_{xx}-\frac{1}{2}\left[\left(A^+\right)_x\right]^2-2B\sigma=0\end{aligned}\tag{48}$$

where the second equation in (48) is a Hamilton-Jacobi-Bellman (H-J-B) equation, which as remarked in [11] is well-known in the theory of optimal stochastic control for continuous Markov processes [15]. Although this equation was derived by way of a suitable action functional, defined by the integration of $\mathcal{L}$ in (41) for choices $f_1=2\log r\left(\overset{\text{def}}{=}A^+\right)$, $f_2=\sigma$, another path to it is by way of the first RD equation in (12) divided by r;

$$\begin{aligned}0&=\frac{r_t}{r}-\frac{r_{xx}}{r}+Brs\overset{\text{def}}{=}\left(\log r\right)_t-\frac{r_{xx}}{r}-B\sigma\\&=\left(\frac{A^+}{2}\right)_t-\left[\left(v^+\right)_x+\left(v^+\right)^2\right]-B\sigma\end{aligned}\tag{49}$$

where the bracketed expression here for r_{xx}/r was obtained in the first sentence that followed Equation (23). By the definition (22), and the definition of A^+ again, $v^+=\left(A^+/2\right)_x$. (49) is therefore the statement

$$0=\frac{1}{2}\left(A^+\right)_t-\frac{1}{2}\left(A^+\right)_{xx}-\frac{1}{4}\left[\left(A^+\right)_x\right]^2-B\sigma,\tag{50}$$

which is the H-J-B equation in (48).

At hand already we have a solution $\left(\sigma,A^+\right)$ of the H-J-B system (48), by formulas (27) and (28). (27) gives $\sigma(x,t)$, and we can plug the expression for $\rho\left(x,t/\beta\right)$ there into the first formula in (28) to get

$$\begin{aligned}A^+(x,t)&\overset{\text{def}}{=}2\log r(x,t)\\&=\log\left[\alpha_1+4a^2\beta^2dn^2\left(a(x-vt),\kappa\right)\right]-\log(-2\gamma)+2\phi(x,t)\\&=\log\sigma(x,t)+2\phi(x,t)\end{aligned}\tag{51}$$

with ϕ_x given in (31). Again we choose $B=-\gamma/\beta^2$.

The useful role of the reaction diffusion system (12) has been noted several times in this section. Typically in physics, chemistry, or biology, for example, a more general system of the form

$$\begin{aligned} r_t - d_r r_{xx} + F(r,s) &= 0 \\ s_t - d_s s_{xx} + G(r,s) &= 0 \end{aligned} \tag{52}$$

is encountered, where d_r, d_s are diffusion constants for r, s and where $F(u,v), G(u,v)$ are growth and interaction functions. r and s could be concentration functions for two chemicals, or prey and predator functions in a two-species ecological model, for example.

3. Further Remarks on the Case $\alpha_1 = 0$

It was pointed out in Section 2.1 that various formulas presented in this paper (and in the paper [10]) simplify drastically in case $\alpha_1 = 0$; in general $\alpha_1 \geq 0$. Here we find in this case, in particular, a concrete expression for the potential function $S(x,t)$ (and thus also for the function $\phi(x,t)$) appearing in some of these formulas.

For $\alpha_1 = 0$, $u(x,t) = u_0 = \beta v$, by (9) and (10), is a constant function: $C = 0$. By (11), $S_x = -\beta v/2$, $\gamma e^{2R} \overset{\text{def}}{=} -\rho/2$, and

$$R_{xx} + R_x^2 = \frac{1}{2}\left[\frac{\rho_{xx}}{2} - \frac{1}{2}\left(\frac{\rho_x}{\rho}\right)^2\right] \tag{53}$$

by straight-forward differentiation of R. By Maple, for example, the differentiation of ρ on the r.h.s. of (53) can be carried out. For ρ given by (10) and $w \overset{\text{def}}{=} a(x-\beta t)$, the result is that this r.h.s. is $a^2\kappa^2\left[2sn^2(w,\kappa)-1\right]$, or $a^2\left[-2dn^2(w,\kappa)+2-\kappa^2\right]$ by (29). As we have chosen δ in (1) to be β^2+1, we see that the second fluid equation in (4) therefore gives

$$\begin{aligned} 0 &= S_t - \beta^2 a^2\left[-2dn^2(w,\kappa)+2-\kappa^2\right] - \frac{\beta^2 v^2}{4} - \frac{\rho}{2} \\ &= S_t - \beta^2 a^2\left(2-\kappa^2\right) - \frac{\beta^2 v^2}{4} \end{aligned} \tag{54}$$

since $\rho/2 = 2a^2\beta^2 dn^2(w,\kappa)$ by (10), for $\alpha_1 = 0$. That is, $S_t(x,t)$ is the constant function $\beta^2 a^2\left(2-\kappa^2\right) + \beta^2 v^2/4$, or

$$S(x,t) = \left[\beta^2 a^2\left(2-\kappa^2\right) + \frac{\beta^2 v^2}{4}\right]t + f(x), \tag{55}$$

for a function of integration $f(x)$. Using again that $S_x = -\beta v/2$, we see that $f'(x) = -\beta v/2 \Rightarrow f(x) = -\beta v x/2 + c_0$, for some constant c_0. Thus, in the end, for $\alpha_1 = 0$ we can choose the potential function $S(x,t)$ and the associated function $\phi(x,t)$ in (13) to be given by

$$\begin{aligned} S(x,t) &= \beta^2\left[a^2\left(2-\kappa^2\right) + \frac{v^2}{4}\right]t - \frac{\beta v x}{2} + c_0, \\ \phi(x,t) &\overset{\text{def}}{=} S(x,t/\beta)/\beta = \left[a^2\left(2-\kappa^2\right) + \frac{v^2}{4}\right]t - \frac{vx}{2} + \frac{c_0}{\beta} \end{aligned} \tag{56}$$

for a constant c_0.

These expressions for $S(x,t)$ and $\phi(x,t)$ can be plugged into formulas (14), (15), and (51), for example—taking $\alpha_1 = 0$ there, to further explicate the solutions r, s, ψ, A^+; keep in mind the assumption $\gamma < 0$:

$$\begin{aligned} r(x,t) &= \frac{2a\beta}{\sqrt{-2\gamma}} dn\left(a(x-vt),\kappa\right) \mathrm{e}^{\phi(x,t)} \\ s(x,t) &= \frac{-2a\beta}{\sqrt{-2\gamma}} dn\left(a(x-vt),\kappa\right) \mathrm{e}^{-\phi(x,t)} \\ \psi(x,t) &= \frac{2a\beta}{\sqrt{-2\gamma}} dn\left(a(x-vt),\kappa\right) \mathrm{e}^{-iS(x,t)} \\ A^+(x,t) &= \log\left(\frac{\left[4a^2\beta^2 dn^2\left(a(x-vt),\kappa\right)\right]}{-2\gamma}\right) + 2\phi(x,t) \end{aligned} \tag{57}$$

for $\phi(x,t), S(x,t)$ given in (56). We also have the formulas for $\sigma(x,t)$ and $v^{\pm}(x,t)$ in (35) in case $\alpha_1 = 0$. In (57), $2\beta/\sqrt{-2\gamma} = \sqrt{2/B}$, by (13).

Some concluding remarks about the case $\alpha_1 = 0$ pertain to the conservation laws (16) and (17). These laws imply that *rs* and $r_x s_x + B(rs)^2/2$ are conserved quantities that give rise to constants of motion

$$I \stackrel{\text{def}}{=} \int_{-\infty}^{\infty} rs\,\mathrm{d}x, \quad J \stackrel{\text{def}}{=} \int_{-\infty}^{\infty} \left[r_x s_x + B(rs)^2/2\right]\mathrm{d}x. \tag{58}$$

In [16], for example, where $\alpha_1 = 0, \kappa = 1$ (and $\beta = 1$), the mass $M \stackrel{\text{def}}{=} -I$ and energy $E \stackrel{\text{def}}{=} 2J$ constants, in particular, are computed, where the notation e^+, e^- there (as in [5] [6] [11]) corresponds to r, s here; also $-\Lambda/4$ there corresponds to $B \stackrel{\text{def}}{=} -\gamma/\beta^2$ in (13) here. We state the results in terms of our notation, but we also express *M* and *E* in terms of the Gurevich-Krylov solution $\rho(x,t)$ in (10). First note that by (10), (29), (33), (36)

$$\begin{aligned} \left[\frac{\rho_x}{\rho}(x,t/\beta)\right]^2 &= \left[\frac{-8a^3\beta^2 \tanh\left(a(x-vt)\right)\mathrm{sech}^2\left(a(x-vt)\right)}{4a^2\beta^2 \mathrm{sech}^2\left(a(x-vt)\right)}\right]^2 \\ &= 4a^2 \tanh^2\left(a(x-vt)\right) = 4\left[\left(v^+v^-\right)(x,t) + \frac{v^2}{4}\right] \end{aligned} \tag{59}$$

for $\alpha_1 = 0, \kappa = 1$. Then by (18), (22), (27), (59) $r_x s_x = rv^+ sv^- = -\sigma v^+ v^-$, $(rs)^2 = \sigma^2 \Rightarrow$

$$\begin{aligned} \left[r_x s_x + B(rs)^2/2\right](x,t) &= -\sigma(x,t)\left[v^+v^- - \frac{B}{2}\sigma\right](x,t) \\ &= \frac{\rho(x,t/\beta)}{2\gamma}\left[\frac{1}{4}\left(\frac{\rho_x}{\rho}\right)^2(x,t/\beta) - \frac{v^2}{4} - \frac{B}{2}\frac{\rho(x,t/\beta)}{-2\gamma}\right]. \end{aligned} \tag{60}$$

The result is that

$$\begin{aligned} M &\stackrel{\text{def}}{=} -\int_{-\infty}^{\infty} (rs)(x,t)\,\mathrm{d}x \stackrel{\text{def}}{=} \int_{-\infty}^{\infty} \frac{\rho(x,t/\beta)}{-2\gamma}\,\mathrm{d}x = \frac{4a\beta^2}{-\gamma}, \\ E &\stackrel{\text{def}}{=} 2\int_{-\infty}^{\infty} \left[r_x s_x - \frac{\gamma}{2\beta^2}(rs)^2\right](x,t)\,\mathrm{d}x \end{aligned}$$

$$\begin{aligned} &= 2\int_{-\infty}^{\infty} \frac{\rho(x,t/\beta)}{-2\gamma}\left(\frac{1}{4}\left(\frac{\rho_x}{\rho}\right)^2(x,t/\beta)-\frac{v^2}{4}\right)-\frac{\rho(x,t/\beta)^2}{8\gamma\beta^2}\mathrm{d}x \\ &= -\frac{8a^3\beta^2}{3\gamma}-\frac{2a\beta^2v^2}{\gamma}, \end{aligned} \tag{61}$$

using that

$$\begin{aligned} &\int_{-\infty}^{\infty}\operatorname{sech}^2\left(a(x-vt)\right)\mathrm{d}x=\frac{2}{a},\quad \int_{-\infty}^{\infty}\operatorname{sech}^4\left(a(x-vt)\right)\mathrm{d}x=\frac{4}{3a}, \\ &\int_{-\infty}^{\infty}\left(\tanh^2\operatorname{sech}^2\right)\left(a(x-vt)\right)\mathrm{d}x=\frac{2}{3a}, \end{aligned} \tag{62}$$

where the latter integral formula in (62) is used to compute the integration of $r_x s_x$ in the definition of *E*. Namely, as we have just noted, $r_x s_x = -\sigma v^+ v^-$ so by (36) again

$$(r_x s_x)(x,t)=\frac{4a^2\beta^2}{2\gamma}\operatorname{sech}^2\left(a(x-vt)\right)\left[a^2\tanh^2\left(a(x-vt)\right)-\frac{v^2}{4}\right]. \tag{63}$$

4. Plasma Metric and Plasma Dilaton Fields

An exact connection of the cold plasma system (5) to a two-dimensional Jackiw-Teitelboim (J-T) black hole was investigated in [10], with the resonance NLS Equation (1) serving as a bridge. An explicit change of variables was set up which transformed a plasma metric associated with the system (5) to a J-T metric. This transformation, moreover, provided for a direct calculation of a plasma dilaton field, which with the plasma metric and an appropriate cosmological constant constitutes a solution of the J-T gravitational field equations [17] [18]. The results of [10] represent an extension to the non-trivial case $\alpha_1 \neq 0$ of results in [12]—a case discussed in Sections 2 and 3 here. As indicated in the introduction, two more plasma dilaton fields will be computed in this section, to obtain a set of three linearly independent ones altogether.

The J-T gravitational field equations are a system of equations

$$\begin{aligned} &R(g)+2\Lambda=0 \\ &\nabla_i\nabla_j\Phi+\Lambda\Phi g_{ij}=0,\quad 1\le i,j\le 2 \end{aligned} \tag{64}$$

of which a solution consists of a triple (g,Φ,Λ) where *g* is a pseudo Riemannian metric with local components g_{ij}, $R(g)$ is its Ricci scalar curvature, Φ is a real-valued function of the local coordinates (x_1,x_2) in which *g* is expressed (called a dilaton field), Λ is a cosmological constant (and therefore the scalar curvature is a constant), and where, locally, the Hessian $\nabla_i\nabla_j$ is given by

$$\nabla_i\nabla_j\Phi=\frac{\partial^2\Phi}{\partial x_i\partial x_j}-\sum_{k=1}^{2}\Gamma_{ij}^k\frac{\partial\Phi}{\partial x_k} \tag{65}$$

for the Christoffel symbols Γ_{ij}^k of *g*, of the second kind.

For example, the J-T (Lorentzian) black hole solution of the system (64) is given in the coordinates $(x_1,x_2)=(\tau,r)$ by g with

$$\begin{aligned} &\mathrm{d}s^2 \overset{\text{def}}{=} -\left(m^2r^2 - M\right)\mathrm{d}\tau^2 + \frac{\mathrm{d}r^2}{m^2r^2 - M}, \\ &\Phi(\tau, r) \overset{\text{def}}{=} mr, \ \ \Lambda \overset{\text{def}}{=} -m^2 \end{aligned} \tag{66}$$

for fixed real numbers m, M, $M > 0$ being a black hole mass parameter. Here $R(g) = 2m^2$, and we point out that the sign convention for scalar curvature that we adopt here (and in [10] [12]) is spelled out on page 182 of [19], for example. Thus, for example, our $R(g)$ is the negative of that employed in [17] [18]. We will also write g_{bh} for the J-T metric given in (66).

As a second example, we consider the plasma metric $g = g_{plasma}$ constructed in [10] by way of the G-K solution in (10) of the MAS (5). Here the local coordinates $(x_1, x_2) = (\tau, \rho)$, with the notation ρ here not to be confused with the same notation for the solution ρ in (10):

$$\begin{aligned} &g : \mathrm{d}s^2 \overset{\text{def}}{=} A(\rho)\mathrm{d}\tau^2 - \left[\frac{4a^4\beta^4\kappa^4}{\gamma^2 A(\rho)}\left(sn^2cn^2dn^2\right)(\rho,\kappa)\right]\mathrm{d}\rho^2, \\ &A(\rho) \overset{\text{def}}{=} 4a^2\beta^2\left[\frac{a^2\kappa^4}{-2\gamma}\left(sn^2cn^2\right)(\rho,\kappa) + \frac{v^2}{8\gamma}\mathrm{d}n^2(\rho,\kappa)\right] \\ &\qquad + \frac{16\alpha_1 a^4\beta^2\kappa^4\left(sn^2cn^2\right)(\rho,\kappa) + C^2/\beta^2}{8\gamma\left[\alpha_1 + 4a^2\beta^2 dn^2(\rho,\kappa)\right]} + \frac{\alpha_1 v^2}{8\gamma} - \frac{vC}{4\gamma\beta} \end{aligned} \tag{67}$$

where (again) C is given (9). Obviously this metric is more complicated in structure. For $\alpha_1 = 0$ (so that again $C = 0$) and for the choice $\gamma = -1/2$ (as in [5] [6]) it reduces to the metric (6) in [12], where the notation b there corresponds to 2β here. Some remarks herewith are offered to provide some clarification regarding the "raisons d'être" of the plasma metric formula (67).

The classical continuous Heisenberg model realized on a single sheeted hyperboloid

$$-S_1(x,t)^2 + S_2(x,t)^2 - S_3(x,t)^2 = -1 \tag{68}$$

with equations of motion

$$\mathcal{S}_t = \frac{1}{2i}[\mathcal{S}, \mathcal{S}_{xx}], \ \ \mathcal{S} \overset{\text{def}}{=} i\begin{bmatrix} S_3 & S_1 - S_2 \\ S_1 + S_2 & -S_3 \end{bmatrix} \tag{69}$$

is equipped with a canonical metric

$$\begin{aligned} &g_H : \mathrm{d}s^2 = g_{11}\mathrm{d}t^2 + 2g_{12}\mathrm{d}t\mathrm{d}x + g_{22}\mathrm{d}x^2 \\ &g_{11} \overset{\text{def}}{=} -\left(\frac{\partial S_1}{\partial t}\right)^2 + \left(\frac{\partial S_2}{\partial t}\right)^2 - \left(\frac{\partial S_3}{\partial t}\right)^2 \\ &g_{22} \overset{\text{def}}{=} -\left(\frac{\partial S_1}{\partial x}\right)^2 + \left(\frac{\partial S_2}{\partial x}\right)^2 - \left(\frac{\partial S_3}{\partial x}\right)^2 \\ &g_{12} \overset{\text{def}}{=} -\frac{\partial S_1}{\partial t}\frac{\partial S_1}{\partial x} + \frac{\partial S_2}{\partial t}\frac{\partial S_2}{\partial x} - \frac{\partial S_3}{\partial t}\frac{\partial S_3}{\partial x} \end{aligned} \tag{70}$$

of constant scalar curvature $R(g_H) = 2$. The bracket in (69) is just the commutator $[M_1, M_2] \overset{\text{def}}{=} M_1M_2 - M_2M_1$ of two matrices M_1 and M_2, and the g_{ij}

in (70) are simply Minkowski inner product expressions:
$\langle X,Y\rangle \overset{\text{def}}{=} -x_1y_1+x_2y_2-x_3y_3$ for $X=(x_1,x_2,x_3)$, $Y=(y_1,y_2,y_3)\in\mathbb{R}^3$.

On the other hand, one can construct Lax pairs $(J_0(\lambda),J_1(\lambda))$ for this Heisenberg model, and Lax pairs $(u_0(\lambda),u_1(\lambda))$ for the reaction diffusion system (12), and establish a gauge equivalence of these two nonlinear systems [16]. More precisely, in our specific setup,

$$\begin{aligned} &J_0(\lambda)\overset{\text{def}}{=}\frac{i\lambda^2\mathcal{S}}{8}+\frac{\lambda}{4}\mathcal{S}\mathcal{S}_x,\quad J_1(\lambda)\overset{\text{def}}{=}\frac{i\lambda\mathcal{S}}{4}\\ &u_0(\lambda)\overset{\text{def}}{=}\begin{bmatrix}\lambda^2/8-\tilde{r}\tilde{s} & -\tilde{s}_x+\lambda\tilde{s}/2\\ \tilde{r}_x+\lambda\tilde{r}/2 & -\lambda^2/8+\tilde{r}\tilde{s}\end{bmatrix},\quad u_1(\lambda)\overset{\text{def}}{=}\begin{bmatrix}\lambda/4 & \tilde{s}\\ \tilde{r} & -\lambda/4\end{bmatrix}\\ &\tilde{r}\overset{\text{def}}{=}\sqrt{\frac{B}{2}}r,\quad \tilde{s}\overset{\text{def}}{=}\sqrt{\frac{B}{2}}s,\end{aligned} \tag{71}$$

for a (complex) spectral parameter λ. The equations of motion assertion (69) is equivalent to the assertion that $(J_0(\lambda),J_1(\lambda))$ satisfies the zero curvature condition (zcc)

$$J_1(\lambda)_t-J_0(\lambda)_x+\left[J_0(\lambda),J_1(\lambda)\right]=0. \tag{72}$$

Similarly, a pair of functions $(r(x,t),s(x,t))$ is a solution of the RDS (12) if and only if $(u_0(\lambda),u_1(\lambda))$ satisfies the zcc

$$u_1(\lambda)_t-u_0(\lambda)_x+\left[u_0(\lambda),u_1(\lambda)\right]=0. \tag{73}$$

Gauge equivalence means that for some $M\in GL(2,\mathbb{R})$,

$$\begin{aligned} &u_0^M(\lambda)=J_0(\lambda),\quad u_1^M(\lambda)=J_1(\lambda),\\ &u_0^M(\lambda)\overset{\text{def}}{=}Mu_0(\lambda)M^{-1}-M_tM^{-1},\\ &u_1^M(\lambda)\overset{\text{def}}{=}Mu_1(\lambda)M^{-1}-M_xM^{-1},\end{aligned} \tag{74}$$

which in turn means that one can show that the Heisenberg metric g_H in (70) can be expressed in terms of *r* and *s*. The result (a key result) is that

$$g_{11}=2B(-r_xs_x),\quad g_{12}=B(r_xs-rs_x),\quad g_{22}=2Brs. \tag{75}$$

Since the scalar curvature $R(g_H)$ of g_H has the value 2, as we have noted, it is convenient to work with the metric $g_H/2B$ with scalar curvature $4B\overset{\text{def}}{=}-4\gamma/\beta^2$. Now $rs=-\sigma$ by definition (18), so by (27)

$$(g_H/2B)_{22}(x,t)\overset{\text{def}}{=}(rs)(x,t)=\left[\alpha_1+4a^2\beta^2dn^2\left(a(x-vt),\kappa\right)\right]/2\gamma. \tag{76}$$

By formulas (34) then

$$\left(v^+-v^-\right)(x,t)=\frac{-C/\beta}{2\gamma(rs)(x,t)}-v, \tag{77}$$

and by definition (22), $r_xs-rs_x=v^+rs-v^-sr=\left(v^+-v^-\right)rs=-C/2\gamma\beta-vrs$ by (77). That is, by (75), (76)

$$(g_H/2B)_{12}(x,t)=-\frac{C}{4\gamma B}-\frac{v}{4\gamma}\left[\alpha_1+4a^2\beta^2dn^2\left(a(x-vt),\kappa\right)\right]. \tag{78}$$

The computation of $\left(g_H/2B\right)_{11} \overset{\text{def}}{=} -r_x s_x$ (by (75)) is more involved. By (18) and (22) again, $-r_x s_x = \sigma v^+ v^-$, which can be computed by (27) and (34) again. The end result is that

$$\begin{aligned}\left(g_H/2B\right)_{11} &= 4a^2\beta^2\left[\frac{a^2\kappa^4}{-2\gamma}\left(sn^2cn^2\right)\left(a\left(x-vt\right),\kappa\right)+\frac{v^2}{8\gamma}dn^2\left(a\left(x-vt\right),\kappa\right)\right] \\ &+\frac{16\alpha_1 a^4\beta^2\kappa^4\left(sn^2cn^2\right)\left(a\left(x-vt\right),\kappa\right)+C^2/\beta^2}{8\gamma\left[\alpha_1+4a^2\beta^2 dn^2\left(a\left(x-vt\right),\kappa\right)\right]}+\frac{\alpha_1 v^2}{8\gamma}+\frac{vC}{4\gamma\beta}.\end{aligned} \tag{79}$$

In the very specialized case of $\alpha_1 = 0, \kappa = 1$, $-\left(g_H/2B\right)_{11}$ is given exactly by Equation (63). Formulas (76), (78), (79) (for C given in (9)), which give the structure of the metric $g_H/2B$ were also obtained in [10], by a different method. This metric is non-diagonal: $\left(g_H/2B\right)_{12} = \left(g_H/2B\right)_{21} \neq 0$. In Section 3 of [10] a suitable change of variables was constructed by which $g_H/2B$ was transformed exactly to the plasma metric g in (67), which is diagonal. For this, v^2 is required to be sufficiently large:

$$v^2 > 4a^2\kappa^4 \quad \text{and} \quad v^2 \geq \frac{4C^2}{\alpha_1^2\beta^2} \quad \text{for} \quad \alpha_1 > 0, \tag{80}$$

with the single condition

$$v^2 > 4a^2\kappa^4 \quad \text{for} \quad \alpha_1 = 0. \tag{81}$$

A clarification regarding how the plasma metric g_{plasma} in (67) arises is now established. Also $R\left(g_{plasma}\right) = R\left(g_H/2B\right) = -4\gamma/\beta^2$, as we have seen.

We move on now to the main result in [10], which will allow, in particular, for a direct computation of plasma dilaton fields and thus for solutions of the field Equations (64). That main result states that the change of variables $\left(\tau,\rho\right) \to \left(\tau, r = \psi\left(\rho\right)\right)$ for

$$\psi\left(\rho\right) \overset{\text{def}}{=} \frac{a^2\beta^2 dn^2\left(\rho,\kappa\right)}{-\gamma}+\frac{a^2\beta^2}{2\gamma}\left(2-\kappa^2\right)-\frac{\left(v^2\beta^2-\alpha_1\right)}{8\gamma} \tag{82}$$

transforms the cold plasma metric g_{plasma} in (67) precisely to the J-T black hole metric g_{bh} in (66), for m and M there given by

$$\begin{aligned} m &\overset{\text{def}}{=} +\frac{\left(-2\gamma\right)^{1/2}}{\beta}, \\ M &\overset{\text{def}}{=} \frac{-vC}{4\gamma\beta}+\frac{a^2\beta^2v^2}{2\gamma}-\frac{a^4\beta^2\kappa^4}{2\gamma}-\frac{a^2\beta^2\kappa^2v^2}{4\gamma}-\frac{\beta^2v^4}{32\gamma} \\ &+\frac{3\alpha_1v^2}{16\gamma}+\frac{3\alpha_1^2}{32\gamma\beta^2}-\frac{\alpha_1a^2\kappa^2}{4\gamma}+\frac{\alpha_1a^2}{2\gamma}. \end{aligned} \tag{83}$$

Another (more compact) expression is given in (99) for the black hole mass parameter M here, which is indeed positive for

$$v^2 > 8a^2\left(2-\kappa^2\right)+\frac{6\alpha_1}{\beta^2}, \quad v \geq \frac{\alpha_1}{C}\left[\frac{3\alpha_1}{8\beta}+2a^2\beta\right], \tag{84}$$

which we assume. Of course the second condition (84) is automatic for $\alpha_1 = 0$

and the first condition, in fact the condition $v^2 > 8a^2\left(2-\kappa^2\right)$, implies the first condition $v^2 > 4a^2\kappa^4$ in (80).

Going back to the earlier equations $R\left(g_{bh}\right) = 2m^2$ and $R\left(g_{plasma}\right) = -4\gamma/\beta^2$, we conclude from the equality of these scalar curvatures that m must be given by (83), and moreover that by the first field equation in (64) the cosmological constant Λ must be given by

$$\Lambda = \frac{-R\left(g_{plasma}\right)}{2} = \frac{2\gamma}{\beta^2} = -m^2. \tag{85}$$

$\gamma < 0$ throughout this paper, and we see that the cosmological constant is *negative*. The dilaton field $\Phi^{(1)}_{plasma}$ for the second set of equations in (64), for the plasma metric, can be derived immediately from the J-T dilaton field $\Phi(\tau, r) = mr$ in (66):

$$\begin{aligned}\Phi^{(1)}_{plasma}(\tau,\rho) &\overset{\text{def}}{=} \Phi\left(\tau,\psi(\rho)\right) \overset{\text{def}}{=} m\psi(\rho)\\ &\overset{\text{def}}{=} m\left[\frac{a^2\beta^2 dn^2(\rho,\kappa)}{-\gamma} + \frac{a^2\beta^2}{2\gamma}\left(2-\kappa^2\right) - \frac{v^2\beta^2-\alpha_1}{8\gamma}\right]\end{aligned} \tag{86}$$

as in [10]. There are, however, two other J-T dilaton fields $\Phi^{(j)}(\tau, r), j = 2,3$, that are also solutions of the second set of equations in (64) for the metric g_{bh}, and therefore by way of the transformation Ψ in (82) there are in addition plasma dilaton fields $\Phi^{(j)}_{plasma}(\tau,\rho), j = 2,3$, for the plasma metric which were not computed in [10], which we compute here.

In fact, one can take

$$\begin{aligned}\Phi^{(2)}(\tau, r) &\overset{\text{def}}{=} \sqrt{m^2r^2 - M}\,\sinh\left(m\sqrt{M}\,\tau\right),\\ \Phi^{(3)}(\tau, r) &\overset{\text{def}}{=} \sqrt{m^2r^2 - M}\,\cosh\left(m\sqrt{M}\,\tau\right)\end{aligned} \tag{87}$$

so that (as in (86))

$$\begin{aligned}\Phi^{(2)}_{plasma}(\tau,\rho) &\overset{\text{def}}{=} \Phi^{(2)}\left(\tau,\psi(\rho)\right) \overset{\text{def}}{=} \sqrt{m^2\psi(\rho)^2 - M}\,\sinh\left(m\sqrt{M}\,\tau\right),\\ \Phi^{(3)}_{plasma}(\tau,\rho) &\overset{\text{def}}{=} \Phi^{(3)}\left(\tau,\psi(\rho)\right) \overset{\text{def}}{=} \sqrt{m^2\psi(\rho)^2 - M}\,\cosh\left(m\sqrt{M}\,\tau\right)\end{aligned} \tag{88}$$

which means that we need to find expressions for $m^2\psi(\rho)^2 - M$ and $m\sqrt{M}$, given the definitions (82), (83). For convenience, write for now sn, cn, dn for $sn(\rho,\kappa), cn(\rho,\kappa), dn(\rho,\kappa)$. Let

$$\begin{aligned}w(\rho) = w &\overset{\text{def}}{=} 16a^4\beta^4 + 16a^4\beta^4\kappa^2 dn^2 + 4a^2\beta^4 v^2 dn^2 - 16a^4\beta^4\kappa^2\\ &\quad + 16a^4\beta^4 dn^4 - 32a^4\beta^4 dn^2\end{aligned} \tag{89}$$

Then, as is easily checked, w has factorization $w = 16a^2\beta^4 B(\rho)$ for

$$B(\rho) \overset{\text{def}}{=} dn^2\left[\frac{a^2\left(1-\kappa^2\right)}{dn^2} + a^2\kappa^2 - 2a^2 + \frac{v^2}{4} + a^2 dn^2\right], \tag{90}$$

which, in turn, can be written as

$$B(\rho) = dn^2\left[\frac{v^2}{4} - a^2\kappa^4\frac{sn^2cn^2}{dn^2}\right]. \tag{91}$$

The argument in [12], for example, leading up to Equation (55) there verifies this assertion. Therefore

$$w = 16a^2\beta^4 dn^2\left[\frac{v^2}{4} - a^2\kappa^4\frac{sn^2cn^2}{dn^2}\right]. \tag{92}$$

On the other hand, given the definitions (82), (83), one has by Maple, for example, that

$$\begin{aligned} &m^2\psi(\rho)^2 - M \\ &= \left[w + \alpha_1^2 + \alpha_1\beta^2v^2 + 8\alpha_1a^2\beta^2 - 4\alpha_1a^2\beta^2\kappa^2 - 4\alpha_1a^2\beta^2dn^2 - 2v\beta C\right]\Big/\left(-8\gamma\beta^2\right) \end{aligned} \tag{93}$$

for C (as usual) in (9). Using that $dn^2 - 1 = -\kappa^2sn^2$ and $1 - sn^2 = cn^2$ (by (29)), one can write $8\alpha_1a^2\beta^2 - 4\alpha_1a^2\beta^2\kappa^2 - 4\alpha_1a^2\beta^2dn^2 = 4\alpha_1a^2\beta^2\left[1 - \kappa^2cn^2\right]$. In the end,

$$\begin{aligned} &m^2\psi(\rho)^2 - M \\ &= \left[w(\rho) + \alpha_1\left\{\alpha_1 + \beta^2\left(v^2 + 4a^2\left(1 - \kappa^2cn^2(\rho,\kappa)\right)\right)\right\} - 2v\beta C\right]\Big/\left(-8\gamma\beta^2\right) \end{aligned} \tag{94}$$

for

$$\begin{aligned} &w(\rho) = w = 16a^2\beta^4dn^2(\rho,\kappa)\left[\frac{v^2}{4} - a^2\kappa^4\frac{sn^2cn^2}{dn^2}(\rho,\kappa)\right], \\ &C \overset{\text{def}}{=} +\left(\alpha_1\alpha_2\alpha_3\right)^{\frac{1}{2}} = \left[\alpha_1\left(4a^2\beta^2\left(1-\kappa^2\right) + \alpha_1\right)\left(4a^2\beta^2 + \alpha_1\right)\right]^{1/2}. \end{aligned} \tag{95}$$

Next, note that in (83)

$$\begin{aligned} &\frac{a^2\beta^2v^2}{2\gamma} - \frac{a^4\beta^2\kappa^4}{2\gamma} - \frac{a^2\beta^2\kappa^2v^2}{4\gamma} - \frac{\beta^2v^4}{32\gamma} \\ &= \frac{-\beta^2}{2\gamma}\left[\frac{-a^2v^2}{2}\left(2-\kappa^2\right) + a^4\kappa^4 + \frac{v^4}{16}\right] = \frac{\beta^2}{-2\gamma}A \end{aligned} \tag{96}$$

for the same constant A in definition (11) of [12]:

$$A \overset{\text{def}}{=} -\frac{a^2v^2}{2}\left(2-\kappa^2\right) + a^4\kappa^4 + \frac{v^4}{16}. \tag{97}$$

Also in (83)

$$\frac{3\alpha_1v^2}{16\gamma} + \frac{3\alpha_1^2}{32\gamma\beta^2} - \frac{\alpha_1a^2\kappa^2}{4\gamma} + \frac{\alpha_1a^2}{2\gamma} = \frac{\alpha_1\beta^2}{-2\gamma}\left[-\frac{3v^2}{8\beta^2} - \frac{3\alpha_1}{16\beta^4} - \frac{a^2\left(2-\kappa^2\right)}{2\beta^2}\right]. \tag{98}$$

It follows that M can also be expressed as

$$M = \frac{\beta^2}{-2\gamma}\left[\frac{vC}{2\beta^3} + A - \alpha_1\left(\frac{3v^2}{8\beta^2} + \frac{3\alpha_1}{16\beta^4} + \frac{a^2\left(2-\kappa^2\right)}{2\beta^2}\right)\right], \tag{99}$$

where $\beta^2/-2\gamma \overset{\text{def}}{=} 1/m^2$. Then

$$m\sqrt{M} = \left[\frac{vC}{2\beta^3} + A - \alpha_1\left(\frac{3v^2}{8\beta^2} + \frac{3\alpha_1}{16\beta^4} + \frac{a^2\left(2-\kappa^2\right)}{2\beta^2}\right)\right]^{1/2} \tag{100}$$

for C and A in (95) and (97), respectfully. In summary, the formulas for $m^2\psi(\rho)^2 - M$ and $m\sqrt{M}$ in (94) and (100) provide for the computation of the plasma dilaton fields $\Phi^{(j)}_{plasma}(\tau,\rho), j = 2,3$, in (88) for the plasma metric g_{plasma} in (67).

As usual, all formulas simplify considerably in case $\alpha_1 = 0$:

$$\begin{aligned} m^2\psi(\rho)^2 - M &= \frac{w(\rho)}{-8\gamma\beta^2} \overset{\text{def}}{=} \frac{16a^2\beta^4}{-8\gamma\beta^2} dn^2(\rho,\kappa)\left[\frac{v^2}{4} - a^2\kappa^4\frac{sn^2cn^2}{dn^2}(\rho,\kappa)\right], \\ m\sqrt{M} &= \sqrt{A} \overset{\text{def}}{=} \left[\frac{-a^2v^2}{2}\left(2-\kappa^2\right) + a^4\kappa^4 + \frac{v^4}{16}\right]^{1/2}, \end{aligned} \tag{101}$$

by (94), (95), (97), and (100), which gives

$$\begin{aligned} \Phi^{(1)}_{plasma}(\tau,\rho) &= \frac{m\beta^2}{-2\gamma}\left[2a^2dn^2(\rho,\kappa) - a^2\left(2-\kappa^2\right) + \frac{v^2}{4}\right], \\ \Phi^{(2)}_{plasma}(\tau,\rho) &= \sqrt{\frac{2}{-\gamma}}a\beta dn(\rho,\kappa)\left[\frac{v^2}{4} - a^2\kappa^4\frac{sn^2cn^2}{dn^2}(\rho,\kappa)\right]^{1/2}\sinh\left(\sqrt{A}\tau\right), \\ \Phi^{(3)}_{plasma}(\tau,\rho) &= \sqrt{\frac{2}{-\gamma}}a\beta dn(\rho,\kappa)\left[\frac{v^2}{4} - a^2\kappa^4\frac{sn^2cn^2}{dn^2}(\rho,\kappa)\right]^{1/2}\cosh\left(\sqrt{A}\tau\right). \end{aligned} \tag{102}$$

Apart from the constant factors $m\beta^2/-2\gamma = 1/m$ and $(2/-\gamma)^{1/2}a\beta$, the dilaton fields in (102) (obtained for $\alpha_1 = 0$) are exactly the ones computed in [12], by a different method; see Equation (10) and Equation (11) there.

5. A Plane Wave Solution of the Magnetoacoustic System

The traveling wave solution (ρ,u) in (10) of the magnetoacoustic system (5) has been of central interest, of course. Equation (15), with $S_x = -u/2$ as in (11), relates this solution to the solution ψ of the resonance NLS equation (1). There is another instance, or another sense, in which solutions of (5) and (1) are related, of which some brief remarks are added in this section.

The bond between the system (5) and Equation (1) is illustrated further in [20], for example, where it is shown that they share a dispersion relation. More precisely, in place of the traveling wave solution (ρ,u) in (10), consider a plane wave solution (ρ,u) of (5) of the form

$$\begin{aligned} \rho(x,t) &\overset{\text{def}}{=} \rho_0 + A_1 e^{i(kx-\omega t)} \\ u(x,t) &\overset{\text{def}}{=} A_2 e^{i(kx-\omega t)} \end{aligned} \tag{103}$$

for constants $\rho_0 \neq 0, A_1, A_2$, wave frequency ω, and wave number k. A proof of the dispersion relation

$$\omega^2 = k^2\rho_0\left(1 - \frac{k^2\beta^2}{\rho_0}\right) = k^2\rho_0 - k^4\beta^2 \tag{104}$$

for the system (5) is given in [20]. There it is also shown that this dispersion relation coincides exactly with the dispersion relation for the RNLS Equation (1), for a linearization of the latter equation about the ground state (condensate) solution

$$\psi_0(x,t) \stackrel{\text{def}}{=} a_0 \mathrm{e}^{i\gamma a_0^2 t}, \quad a_0 \in \mathbb{R} \tag{105}$$

of it, for the choice $\rho_0 = -2\lambda a_0^2 > 0$. The dispersion relation for Equation (1) is stated (without proof) in [6], for $\gamma = -1/2$.

6. Conclusions

The focal points of interest of this paper have been the nonlinear system (5), which describes the propagation of magnetoacoustic waves in a cold plasma in the presence of a transverse magnetic field, the particular traveling wave solution (ρ,u) of this system given by Gurevich-Krylov in (10), and the construction of new solutions of other nonlinear systems—elliptic function solutions that we have in fact expressed in terms of the solution (ρ,u). These other nonlinear systems considered were that of a Madelung fluid, a reaction diffusion system (which played a distinct, unifying role throughout the paper), systems of Broer-Kaup, Boussinesq, Hamilton-Jacobi-Bellman, and the Jackiw-Teitelboim system of gravitational field equations. An elliptic function solution of the resonance nonlinear Schrödinger Equation (1) is also expressed in terms of the solution (ρ,u) in Equation (11) and Equation (15).

Regarding the gravitational field equations (see (64)), in particular, some black hole solutions ($g_{plasma}, \Phi^{(j)}_{plasma}, \Lambda = -2B$) were presented where g_{plasma} is a pseudo-Riemannian metric (given in (67)) of constant Ricci scalar curvature $4B$ ($B \stackrel{\text{def}}{=} -\gamma/\beta^2$ for γ and β^2 in (1) and (5)), the $\Phi^{(j)}_{plasma}, j = 1,2,3$ are dilaton fields (given by (86), (88), (94), (100), (102)), and Λ is a (negative) cosmological constant. To obtain these solutions we used a fundamental result in [10] where an explicit change of variables was set up (which is given in definition (82) here) that transforms g_{plasma} precisely to the Jackiw-Teitelboim black hole metric g_{bh} in (66), for the values of m and M there given in (83).

Brief remarks in Section 5 further narrate a nexus between the magnetoacoustic system (5) and the resonance NLS Equation (1)—this by way of the dispersion relation (104).

The results presented here, generally speaking, provide for a non-trivial extension of a few selected results obtained in [11] [12], for example. On the other hand, as pointed out in Section 3, we have not considered an extension in the direction of two-soliton solutions of Broer-Kaup and Boussinesq systems, for example, as discussed in [11]; also see [5] [6] [16].

Acknowledgements

This paper, like that of reference [10], has drawn inspiration from the work of the authors in the references [5] [7], and [21].

Conflicts of Interest

The authors declare no conflicts of interest regarding the publication of this paper.

References

[1] Taniuti, T. and Washimi, H. (1996) *Physical Review Letters*, **17**, 996-998. https://doi.org/10.1103/PhysRevLett.17.996

[2] Gardner, C.S. and Morikawa, G.K. (1960) Similarity in the Asymptotic Behavior of Collision-Free Hydromagnetic Waves and Water Waves. Courant Institute of Mathematical Sciences Report No. NYO 9082 (Unpublished).

[3] Jeffrey, A. (1973) *The Quarterly Journal of the Royal Astronomical Society*, **14**, 183-189.

[4] Berezin, Y.A. and Karpman, V.I. (1964) *Soviet Physics Journal of Experimental & Theoretical Physics*, **19**, 1265-1271.

[5] Lee, J.-H., Pashaev, O.K., Rogers, C. and Schief, W.K. (2007) *Journal of Plasma Physics*, **73**, 257-272. https://doi.org/10.1017/S0022377806004648

[6] Lee, J.-H. and Pashaev, O.K. (2007) *Theoretical and Mathematical Physics*, **152**, 991-1003. https://doi.org/10.1007/s11232-007-0083-3

[7] Clarkson, P.A. and Rogers, C. (2018) *Journal of Nonlinear Mathematical Physics*, **25**, 247-261. https://doi.org/10.1080/14029251.2018.1452672

[8] Gurevich, A.V. and Krylov, A.L. (1988) *Doklady Akademii Nauk SSSR*, **298**, 608-611.

[9] Chandrasekharan, K. (1985) Elliptic Functions, Grundlehren der mathematischen Wissenschaften, Vol. 281. Springer-Verlag, Berlin. https://doi.org/10.1007/978-3-642-52244-4

[10] Williams, F. (2019) *Advances in Mathematical Physics*, **2019**, Article ID: 4810904. https://doi.org/10.1155/2019/4810904

[11] Pashaev, O.K. (2012) *Theoretical and Mathematical Physics*, **172**, 1147-1159. https://doi.org/10.1007/s11232-012-0103-9

[12] D'Ambroise, J. and Williams, F. (2017) *Advances in Mathematical Physics*, **2017**, Article ID: 2154784. https://doi.org/10.1155/2017/2154784

[13] Broer, L.J.F. (1975) *Applied Scientific Research*, **31**, 377-395. https://doi.org/10.1007/BF00418048

[14] Kaup, D.J. (1975) *Progress of Theoretical Physics*, **54**, 396-408. https://doi.org/10.1143/PTP.54.396

[15] Bellman, R. (1957) Dynamic Programming. Princeton Univ. Press, Princeton.

[16] Lee, J.-H. and Pashaev, O.K. (2002) *Modern Physics Letters A*, **17**, 1601-1619. https://doi.org/10.1142/S0217732302007995

[17] Jackiw, R. (1984) A Two-Dimensional Model of Gravity. In: Christensen, S., Ed., *Quantum Theory of Gravity*, Adam-Hilger Ltd., Hilger, 403-420.

[18] Teitelboim, C. (1984) The Hamiltonian Structure of Two-Dimensional Spacetime and Its Relation with the Conformal Anomaly. In: Christensen, S., Ed., *Quantum Theory of Gravity*, Adam-Hilger Ltd., Hilger, 327-344.

[19] Williams, F. (2014) Some Selected Thoughts Old and New on Soliton-Black Hole Connections in 2d Dilaton Gravity. In: Cuevas-Maraver, J., Kevrekidis, P. and Williams, F., Eds., *The Sine-Gordon Model and Its Applications: From Pendula and Josephson Junctions to Gravity and High-Energy Physics*, Springer Internat. Pub.,

Berlin, 177-205. https://doi.org/10.1007/978-3-319-06722-3_8

[20] Williams, F. (2020) Remarks on the Dispersion Relation for Long Magnetoacoustic Waves in a Cold Plasma: A 2d Black Hole Connection. In: Price, L., Ed., *The Wave Equation*: *An Overview*, Nova Science Publishers, Hauppauge, 171-182.

[21] Martina, L., Pashaev, O.K. and Soliani, G. (1998) *Physical Review D*, **58**, Article ID: 084025. https://doi.org/10.1103/PhysRevD.58.084025

Journal of Modern Physics, 2020, 11, 907-919
https://www.scirp.org/journal/jmp
ISSN Online: 2153-120X
ISSN Print: 2153-1196

Principles of Constructing a Correct Microscopic Theory

Boris V. Vasiliev

Dubna, Russia
Email: bv.vasiliev@yandex.com

How to cite this paper: Vasiliev, B.V. (2020) Principles of Constructing a Correct Microscopic Theory. *Journal of Modern Physics*, **11**, 907-919.
https://doi.org/10.4236/jmp.2020.116055

Received: May 21, 2020
Accepted: June 12, 2020
Published: June 15, 2020

Abstract

In our time, experimental physicists have obtained data on a very large number of phenomena and objects of the physical world. Very rarely there is a situation when theoretical physicists do not have enough experimental data to understand some known fundamental law of Nature. This situation arose almost a hundred years ago and sparked a discussion between A. Einstein and N. Bohr on the probabilistic nature of microcosm phenomena. From the time, it seemed that most physicists are inclined to believe that the proponents of a quantum explanation of the randomness of the phenomena of radioactive decay are right. Now this problem has been solved experimentally. The results of these measurements [1] show that A. Einstein and other proponents of determinism were right. In most cases, theoretical models are based on some already existing experimental data and are intended to explain them. At the same time, in the twentieth century, among microscopic, well-mathematically based models, there were several that raise doubts about their correctness, since they cannot explain a number of other experimental data that can be attributed to the fundamentally important properties of the studied objects [2] [3]. Therefore, the usual criterion for the correctness of the theory, which consists of its agreement with the measurement data, is ambiguous in this case. An additional criterion for the correctness of a microscopic theory can be formulated if it is assumed that the microscopic theory must be quantum one. The coefficients of quantum equations are world constants. Therefore, the solutions of these equations must be equalities made up of world constants only. For this reason, a correct microscopic model must rely on equalities consisting of world constants only. This criterion is shown to work successfully for models of superfluidity and superconductivity, for models of a number of particles, and models of the star interior.

Keywords

Beta-Decay, Neutrino, Nuclear Reactor, Superfluidity, Superconductivity,

Neutron, Hyperon, Meson, Star Interior

"A question that sometimes drives me hazy: am I or are the others crazy?...
...Do you think it's that easy? Yes, it's simple. But absolutely not so".

A. Einstein.

1. The Main Postulate of Natural Sciences

1.1. General Consideration

Einstein's statements in the epigraph can be attributed to a number of theories created by physicists in the twentieth century.

The twentieth century is a thing of the past. Now it is time to critically rethink some theories created by physicists during this period.

The need for this reinterpretation arises from the fact that theoretical physicists in the past century often are considered the most exciting and important task to build theoretical models for those phenomena and objects for which there was not yet enough experimental data collected for their unambiguous interpretation. To create such theories, in addition to knowledge, they needed intuition and a rich imagination. Therefore, the reliability of such models needs experimental confirmation, as required by the main principle of natural Science.

1.2. Gilbert's Postulate

The postulate, which eventually became the main principle of the natural Sciences, was formulated more than 400 years ago by William Gilbert (1544-1603) [4].

Its wording is simple:

All theoretical constructions that claim to be scientific must be tested and confirmed experimentally.

Today, Gilbert's postulate has become a basic principle of physics and experimental physics has created a reliable foundation for a building of theoretical models.

Only occasionally can occur ambiguous situation due to the fact that direct experiments do not indicate their decision.

This was the reason for the long-term debate of physicists at the beginning of the last century, who discussed the stochastic nature of microcosm phenomena.

1.3. The Nature of Beta-Decay

The question of the probabilistic nature of radioactive decay arose immediately after the discovery of this phenomenon.

Anti-determinists led by N. Bohr considered this decay as a purely random quantum mechanical tunneling phenomenon.

But the proponents of determinism in physics did not agree with this explanation. Einstein rejected the probabilistic interpretation of natural phenomena. In a letter to M. Born (1926) he wrote: "at any rate, I am convinced that the Lord

God does not roll the dice."

Still, the anti-determinists prevailed. The immaculate logic of the mathematics of the quantum-mechanical apparatus won over public opinion to their side.

Currently, the physical community generally believes that radioactive decay is a truly random process.

However, this problem should not be decided by voting.

In accordance with the Gilbert's principle, the solution is possible only on the basis of experimental data.

Einstein and his associates (for example, N. Tesla) believed that the cause of radioactive decay could be the impact of the unknown at the time external causes.

The neutrino flux fits the description of such external causes very well.

Therefore, it is natural that the assumption that the cause of beta-decay of radioactive nuclei may be their interaction with the neutrino flux, has been repeatedly expressed earlier by various researchers [5] [6] [7].

One can test this hypothesis by examining the reaction of a beta-source to changes in the neutrino flux incident on it. We can't reduce the cosmic neutrino flux, but we can increase it by adding the neutrino flux from the nuclear reactor.

The experiment used the IBR-2 pulse reactor (Dubna, Russsia) [1].

This reactor, after a short burst of activity, created a pulsed neutrino stream due to the beta-decay of fission fragments of nuclear fuel. Therefore, this neutrino flux decreased exponentially after each reactor flash.

The experiment [1] investigated the effect of this flow on the decay rate in an isolated beta-source ^{63}Ni. This source was located next to the reactor and was carefully protected from the effects of reactor neutrons and gamma-quanta. The isotope ^{63}Ni is characterized by having a very small energy of beta-electrons.

The result of these measurements is shown in **Figure 1**.

The effect of the same stream of reactor neutrinos on the beta-source ^{90}Sr/^{90}Y, which has almost a couple of orders of magnitude more beta-electron energy, was significantly weaker (**Figure 2**) [8].

From the obtained measurement data, it can be concluded that, as suggested by A. Einstein, the phenomenon of beta-decay is not a random phenomenon: "quantum mechanics speaks volumes, but it doesn't bring us any closer to solving the mystery of the Creator".

1.4. Clarifications of the Gilbert Principle

The first clarification was formulated shortly after Gilbert. It boils down to the statement that a scientific theoretical model should not have fundamentally immeasurable parameters inside it.

To a certain extent, this was a response to medieval ideas about angels. The very existence of angels was not questioned by anyone at that time. But they have attributed the property of complete undetectability, *i.e.* a kind of confinement, similar to that which was introduced into the theoretical concepts of non-observable quarks, which nevertheless have a well-defined fractional charge.

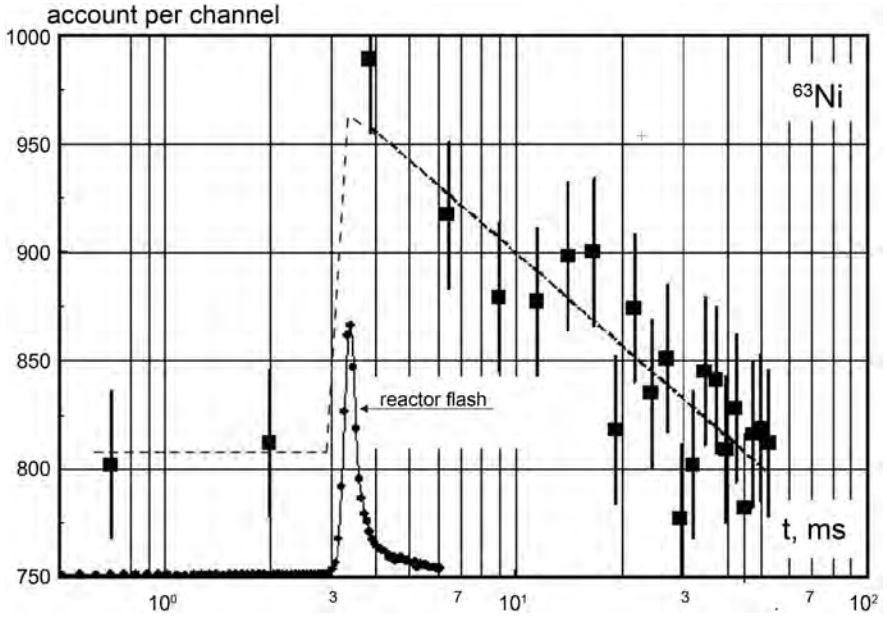

Figure 1. The result of the accumulating registration of beta-electrons emitted by ^{63}Ni. Measurement time is 1 day. The level of amplitude discrimination close to the boundary energy was chosen experimentally. On abscissa: time in ms in the logarithmic scale [1].

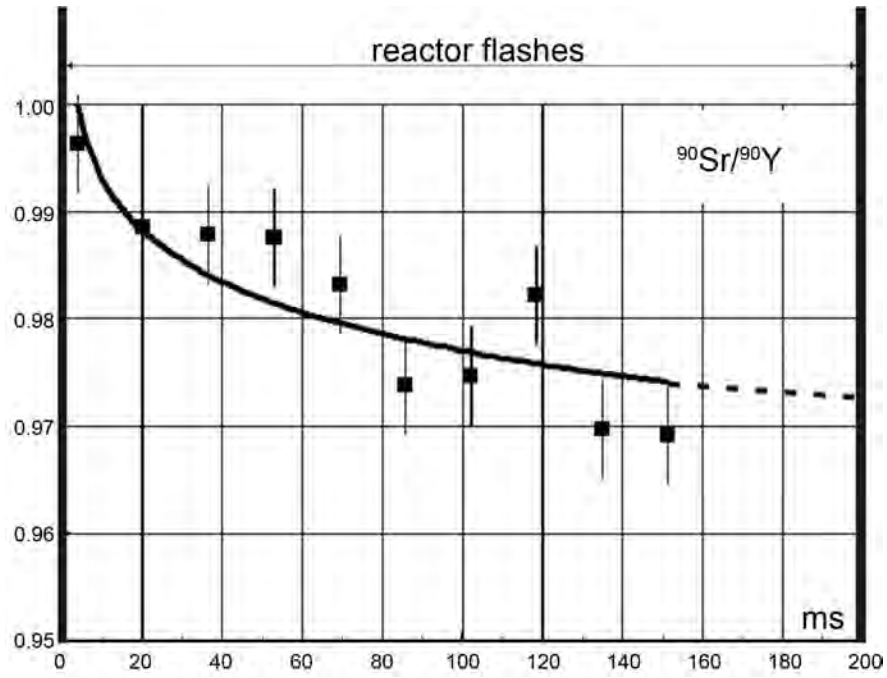

Figure 2. The result of the accumulation of registered beta-electrons emitted by the ^{90}Sr/^{90}Y source in the time interval between reactor flashes. The measurement time is 3 days [8]. On the ordinate axis the account in relative units.

Another important clarification is due to the fact that in our time, new theoretical constructions are created on the basis of any experimental facts and therefore automatically agree with them.

However sometimes, they do not provide an explanation for a number of oth-

er experimental data that can be attributed to the fundamentally important properties of the studied objects [2] [3].

Therefore, to test the correctness of some modern theoretical model, it is necessary to formulate an additional criterion that gives it an assessment from a fundamentally different point of view.

In applied physics, phenomenological theories play an important role, but this is not about them.

To understand the essence of physical objects and phenomena, it is necessary to develop fundamental theories that give them a microscopic theoretical description.

Due to the fact that these objects of the microcosm obey quantum laws, modern microscopic theories must be formulated in terms of quantum mechanics and its rules. Therefore, some basic formulas in modern microscopic theories must be expressed in ratios of world constants only.

There are no other solutions to the equations of quantum physics.

As an example, we can consider the model of the Bohr atom, in which all the main parameters are expressed only by world constants.

Of course, one can't put an identity mark between microscopic theory and quantum mechanical one. There may be exceptions. So a microscopic theory of Brownian motion should not be quantum. However, in the vast majority of cases, these two terms can be considered to coincide.

Therefore the modern formulation of requirements for microscopic physical theory must take this into account:

A correct microscopic theory must rely on basic relationships that consist of world constants only and are supported by measurement data.

Based on this formula, we can analyze the theoretical models of the twentieth century in order to determine the correctness of their understanding of the nature of the phenomena they study.

2. Investigating the Correctness of Some Twentieth-Century Physical Models

2.1. Superfluidity, Superconductivity and the Ordering of Zero-Point Oscillations

Modern microscopic theories of superfluidity and superconductivity are provided with well-developed mathematical justifications. Their authors were repeatedly awarded Nobel prizes. However, these theories do not satisfy the Gilbert principle in its modern formulation, since they cannot be called quantum.

They do not rely on equations made up only of world constants.

2.1.1. Superfluidity

In order to formulate a quantum mechanical model of superfluidity, it is necessary to take into account the mechanism for ordering of zero point oscillations of helium atoms, first considered by F. London almost a hundred years ago [9].

F. London showed that between atoms in the ground state, there is an interac-

tion of the type of Van-der-Waals forces, which has a quantum nature. Atoms in the ground state (at $T = 0$) make zero-point oscillations. He considered atoms as three-dimensional oscillating dipoles connected to each other by electromagnetic interaction and called this interaction of atoms in the ground state as a dispersional one.

If to take into account that different modes of zero-point oscillation are must order at different temperatures [10], we obtain an equality for the density of superfluid helium:

$$\gamma_4 = \frac{\alpha^2}{a_B^3}\sqrt{\frac{M_\alpha^3}{2m_e}} \cong 0.1443 \text{ g/cm}^3. \quad (1)$$

where $a_B = \frac{\hbar^2}{m_e e^2}$ is the Bohr radius,

M_α is the mass of He-4 nucleus,

m_e is the electron mass,

$\alpha = \frac{e^2}{\hbar c}$ is the fine structure constant.

This value is in good agreement with the measured density of liquid helium equal to 0.145 g/cm^3 at $T \simeq T_\lambda$.

Calculating the temperature at which helium goes into the superfluid state gives the equality [10]:

$$T_\lambda = \frac{1}{3}\frac{M_\alpha c^2 \alpha^6}{k} = 2.1772 \text{ K}, \quad (2)$$

which agrees very well with the measured value of $T_\lambda = 2.1768$ K.

2.1.2. Superconductivity

Consideration of zero-point oscillation in electron gas reveals the mode of these vibrations, in which attractive forces arise between the particles decreasing the ensemble energy. Comparing this energy decreasing of electron gas with its Fermi energy, we obtain the ratio of the transition temperature to the ordered superconducting state to the Fermi energy in the form of an equality that depends on the world constants only:

$$\frac{T_c}{T_F} = \frac{9\pi}{2}\alpha^3 \simeq 5.5\times 10^{-6} \quad (3)$$

Graphically, the dependence of the critical temperature T_c calculated in this way on its measured value for type I and II superconductors is shown in **Figure 3** [10].

2.2. Neutron and Its Excited States

Particle physics proceeds from the assumption that the neutron consists of three fractional-charged quarks of the lower level. This makes it easy to explain the reaction of converting a neutron into a proton. To do this, just one of the d-quarks of neutron must turn into a u-quark.

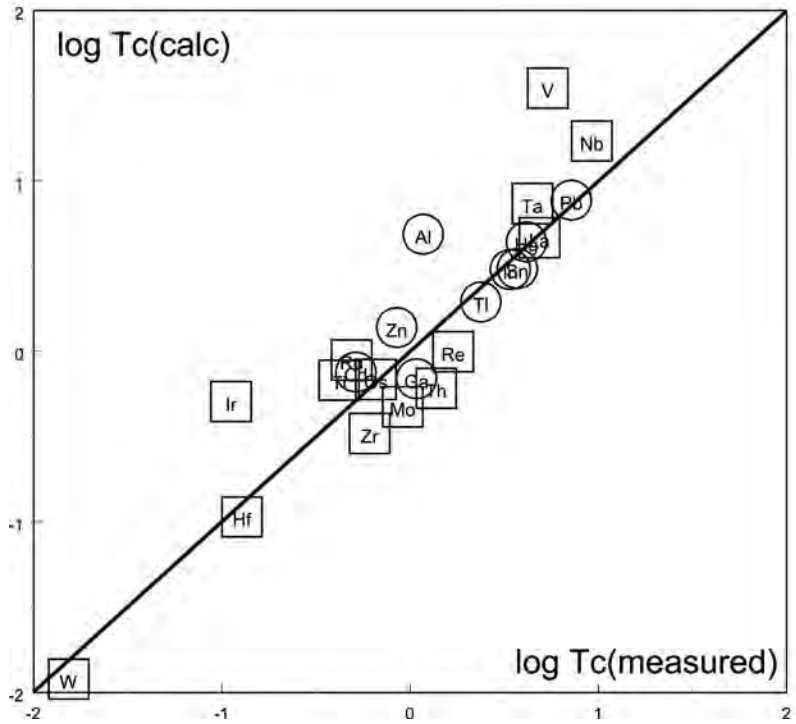

Figure 3. Comparison of calculated values of critical temperatures of superconductors with measurement data. Circles show the parameter values for type I superconductors, and squares show T_c for type II superconductors. The measured value of the critical temperature of superconductors is deposited on the abscissus axis, and the calculated critical temperature is deposited on the ordinate axis [10].

Formulas consisting of world constants do not arise in this theory.

According to another assumption, a neutron is a structure similar to a hydrogen atom, but with a relativistic electron [11] [12].

In this model, the process of converting neutron into proton does not require a complex explanation—it is a simple ionization.

Since electron and proton are bound by electromagnetic forces, the stable state of neutron can be found from the minimum energy condition.

This makes it possible to calculate the mass of the neutron, its magnetic moment, spin, and binding energy.

The results of these estimates are quite satisfactory in agreement with the data of measurements of neutron properties [11] [12].

There is another important property of this model [14].

A hydrogen atom can be in a stable state with minimal energy or in one of the excited states. In the ground state of the Bohr atom the electron orbit fits one de Broglie wavelength. The excited states realize at 2, 3 or more de Broglie waves.

By applying this condition to determine the excited states of neutron, we can calculate parameters characterizing these states. For example, calculated magnetic moments are shown in **Table 1**.

All these calculations are based on simple equalities consisting of world constants.

Table 1. Comparison of calculated values of magnetic moments with measured values. n denotes the number of de Broglie waves that fit in an electron orbit [14].

n	μ_{calc}	experimental data	Ref.
$n=1$	−1.9367	$\mu_{n_0} = -1.9130427 \pm 0.0000005$	[13]
$n=2$	−0.6247	$\mu_{\Lambda^0} = -0.613 \pm 0.004$	[13]
$n=3$	1.3779	$\mu_{\Sigma^0_{\Sigma\Lambda}} = 1.61 \pm 0.08$	[13]

It is generally assumed that there are two quantum values with length dimension.

This is the Bohr radius

$$a_B = \frac{\hbar^2}{m_e e^2} \approx 5 \times 10^{-9} \text{ cm}, \tag{4}$$

It characterizes non-relativistic quantum systems.

And Compton wavelength

$$\lambda_C = 2\pi\alpha a_B = 2\pi \frac{\hbar}{m_e c} \approx 2 \times 10^{-10} \text{ cm}, \tag{5}$$

It arises in quantum theories.

In accordance with the refined Gilbert principle, a new fundamental length appears in this model

$$R_* = \alpha^2 a_B = \frac{e^2}{m_e c^2} \approx 3 \times 10^{-13} \text{ cm}. \tag{6}$$

This radius determines the characteristic sizes of neutron and hyperons in order of magnitude and is included in the relations associated with them.

So the magnetic moment of neutron $\mu_n \approx \frac{eR_*}{2}$ coincides with the nuclear boron magneton in order of magnitude.

In this case, the theoretical and measured values of the deuteron binding energy differ by a numerical coefficient of the order of one.

The nature of nuclear forces in this case is described by a simple and well-known quantum mechanical effect, and there is no need to introduce gluons and the strong force (at least for light nuclei) [11] [12].

2.3. Neutrinos and Mesons

The characteristic feature of neutrino that distinguishes it from all other particles is its extremely weak interaction with matter. At the same time, neutrinos can carry away at the speed of light part of the energy released during beta-decay.

According to Thomson's theory, radiation scattering occurs due to the fact that the electric field of the incident electromagnetic wave accelerates electrons in the substance of a diffuser. As there are no magnetic monopoles in nature, only a particle that does not carry an electric field in its wave can avoid such scattering, transferring all its energy due to the magnetic component of its wave.

But is this magnetic wave possible?

It turns out that Maxwell's equations have a such solution [7].

This solution is usually not considered, probably because it is not technically feasible. However, in nature it is realized in reactions with relativistic particles.

A magnetic oscillation in the ether must occur as a result of a reaction in which a particle with a magnetic moment that did not exist before is born relativistically quickly.

Since beta-decay gives birth to a relativistic electron that carries the magnetic moment, according to Maxwell's equations, a magnetic gamma-quantum must be born that takes away part of the reaction energy. This gamma-quantum was called as neutrino in the twentieth century.

Since the excitation of a magnetic gamma-quantum is a purely electromagnetic process, it cannot be expected that neutrino physics should rely on equalities consisting only of world constants.

However, as a consequence of the existence of neutrinos, the occurrence of such equalities is possible.

So in the chain of reactions $\pi^{\pm} \to \mu^{\pm} \to e^{\pm}$ neutrino and two antineutrinos are born, which carry away some of the reaction energy. The fact that no other particles are born in these reactions allows us to estimate the masses of charged mesons, whose values are determined by the world constants (**Table 2**) [15].

3. Microscopic Models of the Star Interior and Measurement Data

Until last decades of the last century, measurement data that could shed light on the physical properties of the interior of stars was very poor. In the sense of such data simply almost did not exist.

But in recent decades, the technique of astronomical measurements has grown so much. The need data have appeared. On their basis, it has become possible to judge the state of the interior of stars.

Then it became clear that it was bad with the theory of the star interior. This is the result of the historical development of this theory.

One can assume that modern physics of stars appeared in the early twentieth century and an important milestone of this period was the work of R. Emden "Die Gaskugeln". It laid the foundation for describing stars as gas balls characterized by various equations of state.

Table 2. Results of calculations of the charged meson masses [15].

meson	measured meson mass m_{meas}	calculated meson mass m_{calc}	$\frac{m_{calc}-m_{meas}}{m_{meas}}$
$\pi^{\pm}$	$273.13m_e$	$2\frac{m_e}{\alpha}=274.1m_e$	3.5×10^{-3}
$\mu^{\pm}$	$206.77m_e$	$\frac{3}{2}\frac{m_e}{\alpha}=205.6m_e$	-5.8×10^{-3}

According to R. Emden, the equation of state of the gas that forms stars, determines their characteristics. It can be either a dwarf or a giant, or the main sequence star, etc.

In the 30s of the last century, I. Langmuir discovered a new state of matter-plasma. Soon the largest astrophysicist of that time A. Edington realized that the interior of stars must consists from plasma. He built the standard model of a plasma star, much like the model of a gas ball.

At the same time, the main difference between gas with any equation of state and a plasma fell out of the attention of the creators of new astrophysics.

Plasma is an electrically polarized medium. It must have the effect of gravitationally induced electric polarization (GIEP), which is absent in any gas.

The GIEP effect plays an important role in establishing the equilibrium state inside stars and therefore it determines many properties of stars.

3.1. Mass of Stars

Taking into account the GIEP effect, the mass of stars is determined by the equality [16]:

$$M_{\star} = 2\sqrt{\frac{13}{7}\frac{5^5}{\pi^3}}\frac{M_{Ch}}{\left(\frac{A}{Z}\right)^2} = 27.4\frac{M_{Ch}}{\left(\frac{A}{Z}\right)^2}. \tag{7}$$

where the constant M_{Ch} is called the Chandrasekhar mass, consists of world constants only:

$$M_{Ch} = \left(\frac{\hbar c}{Gm_p^2}\right)^{3/2} m_p, \tag{8}$$

A and Z are the mass and charge numbers of the nuclei that make up the plasma of the star's interior, G is gravitational constant, m_p is proton mass.

This equality is consistent with the mass distribution of stars obtained from measurements [17] (**Figure 4**).

3.2. Magnetic Moments of Cosmic Bodies

The existence of electric polarization in the plasma of cosmic bodies, which occurs under the influence of their own gravity, leads to the fact that due to their rotation, these bodies have magnetic moments. The ratio of magnetic moments thus induced $\boldsymbol{\mu}$ to their moments of rotation $\boldsymbol{\mathcal{L}}$ turns out to be equal to [16]:

$$\frac{\boldsymbol{\mu}}{\boldsymbol{\mathcal{L}}} = \frac{\sqrt{G}}{3c}. \tag{9}$$

This equality agrees well with the measurement data (**Figure 5**).

4. Conclusions

At our time, the goal of theoretical researches is always consistent with the Gilbert principle, since they are aimed at explaining some real physical phenomenon discovered by experimenters.

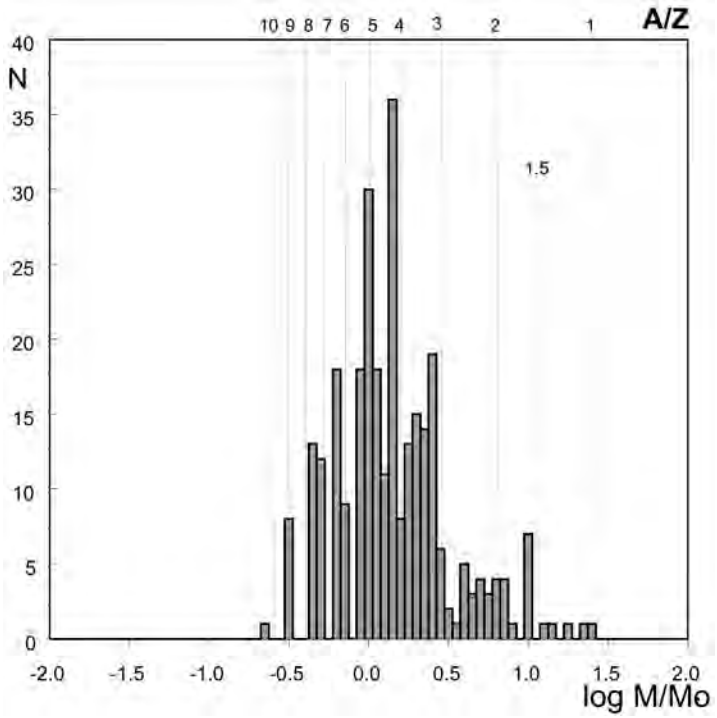

Figure 4. Mass distribution of double stars [17]. By the abscissa contains the logarithm of the mass in units of solar mass. Lines show separate values of A/Z from Equation (7).

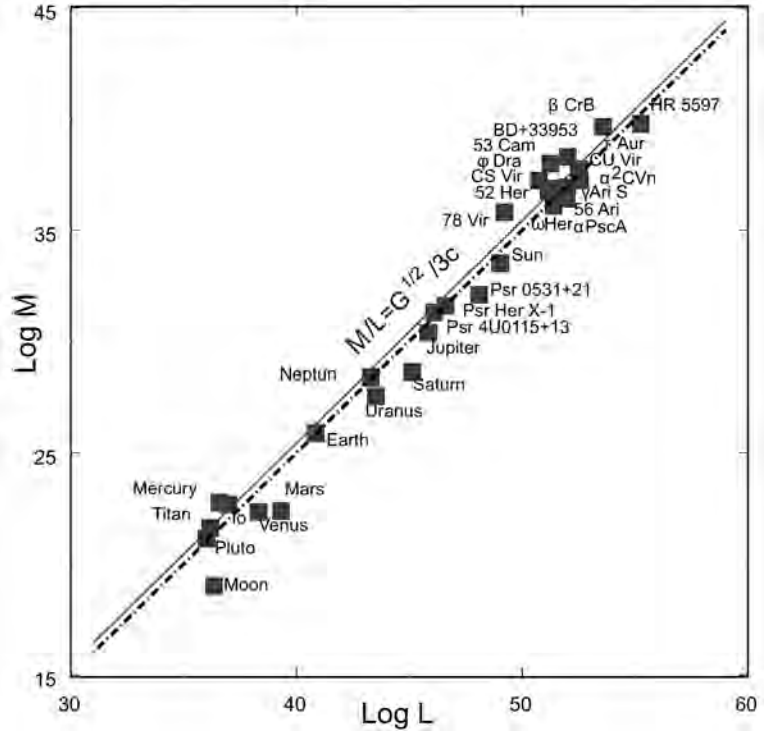

Figure 5: Measured values of magnetic moments space bodies depending on their moments of rotation. By ordinate, the logarithm of the magnetic moment (in Gs·cm^3) is shows, by the abscissa, the logarithm of the moment of rotation (in erg·s) is shown. The dashed line is obtained using the least squares method. Solid line illustrates the theoretical dependence Equation (9).

These theories are always correlated with measurement data without problems—they come from some actual experimental data.

Therefore, it is important to formulate the criterion of reliability of the theory so that it can be understood whether this theory has a scientific future.

The improved Gilbert principle stated above seems to satisfy this purpose. Indeed, the equations of quantum mechanics contain only world constants as coefficients. Therefore, combinations containing only world constants can be a solution to these equations.

Well, the fact that measurement data can confirm such decisions with amazing accuracy strengthens their role in theoretical physics.

Conflicts of Interest

The author declares no conflicts of interest regarding the publication of this paper.

References

[1] Vasiliev, B.V. (2020) *Journal of Modern Physics*, **11**, 608-615. https://doi.org/10.4236/jmp.2020.115040

[2] Vasiliev, B.V. (2015) *Journal of Pure and Applied Physics*, **3**, 1-10. http://www.rroij.com/open-access/on-the-disservice-of-theoretical-physics-work-on-the-bugs.php?aid=61047

[3] Vasiliev, B.V. (2018) *Journal of Modern Physics*, **9**, 2101-2124. https://www.scirp.org/Journal/PaperInformation.aspx?PaperID=87652 https://doi.org/10.4236/jmp.2018.912132

[4] Gilbert, W. (1600) De magneto magneticisque corporibus et de magno magnete tellure. London.

[5] Falkenberg, E.D. (2001) *Apeiron*, **8**, 32-45. https://pdfs.semanticscholar.org/3a21/346203f836847e60016770d931b324a46be9.pdf

[6] Jenkins, J.H., *et al.* (2008) *Astroparticle Physics*, **32**, 42-46. https://arxiv.org/abs/0808.3283 https://doi.org/10.1016/j.astropartphys.2009.05.004

[7] Vasiliev, B.V. (2017) *Journal of Modern Physics*, **8**, 338-348. https://doi.org/10.4236/jmp.2017.83023 http://www.scirp.org/Journal/PaperInformation.aspx?PaperID=74443

[8] Vasiliev, B.V. (2020) *Journal of Modern Physics*, **11**, 91-96. https://doi.org/10.4236/jmp.2020.111005 https://www.scirp.org/Journal/PaperInformation.aspx?PaperID=97775

[9] London, F. (1937) *Transactions of the Faraday Society*, **33**, 8. https://doi.org/10.1039/tf937330008b

[10] Vasiliev, B.V. (2015) Superconductivity and Superfluidity. Science Publishing Group, New York. http://www.sciencepublishinggroup.com/book/B-978-1-940366-36-4.aspx

[11] Vasiliev, B.V. (2017) *SciFed Journal of Nuclear Science*, **1**, 2. https://doi.org/10.23959/sfjns-1000013

[12] Vasiliev, B.V. (2015) *Journal of Modern Physics*, **6**, 648-659. http://www.scirp.org/Journal/PaperInformation.aspx?PaperID=55921

https://doi.org/10.4236/jmp.2015.65071

[13] Tanabashi, M., *et al.* (2018) *Physical Review D*, **98**, Article ID: 030001.

[14] Vasiliev, B.V. (2019) *Journal of Modern Physics*, **10**, 1487-1497. https://www.scirp.org/journal/paperinformation.aspx?paperid=96226 https://doi.org/10.4236/jmp.2019.1013098

[15] Vasiliev, B.V. (2019) *Journal of Modern Physics*, **10**, 1-7. http://www.scirp.org/pdf/JMP_2019011014591744.pdf https://doi.org/10.4236/jmp.2019.101001

[16] Vasiliev, B.V. (2014) *Universal Journal of Physics and Application*, **2**, 257-262.

[17] Heintz, W.D. (1978) Double Stars. Geophysics & Astrophysics Monographs: No. 15. D. Reidel, Dordrecht. https://doi.org/10.1007/978-94-009-9836-0

Journal of Modern Physics, 2020, 11, 920-927
https://www.scirp.org/journal/jmp
ISSN Online: 2153-120X
ISSN Print: 2153-1196

Quantization of Newton's Gravity

Mario C. Rocca[1,2,3*], Angelo Plastino[1,3,4]

[1]Departamento de Física, Universidad Nacional de La Plata, La Plata, Argentina
[2]Departamento de Matemática, Universidad Nacional de La Plata, La Plata, Argentina
[3]Consejo Nacional de Investigaciones Científicas y Tecnológicas (IFLP-CCT-CONICET), La Plata, Argentina
[4]SThAR-EPFL, Lausanne, Switzerland
Email: *rocca@fisica.unlp.edu.ar

How to cite this paper: Rocca, M.C. and Plastino, A. (2020) Quantization of Newton's Gravity. *Journal of Modern Physics*, **11**, 920-927.
https://doi.org/10.4236/jmp.2020.116056

Received: May 25, 2020
Accepted: June 14, 2020
Published: June 17, 2020

Abstract

In this work we will use a recently developed non relativistic (NR) quantization methodology that successfully overcomes troubles with infinities that plague non-renormalizable quantum field theories (QFTs). The ensuing methodology is here applied to Newton's gravitation potential. We employ here the concomitant mathematical apparatus to formulate the NR QFT discussed in the well known classical text-book by Fetter and Walecka. We emphasize the fact that we speak of non relativistic QFT. This is so because we appeal to Newton's gravitational potential, while in a relativistic QFT one does not employ potentials. Our main protagonist is the notion of propagator. This notion is of the essence in non relativistic quantum field theory (NR-QFT). Indeed, propagators are indispensable tools for both nuclear physics and condensed matter theory, among other disciplines. In the present work we deal with propagators for both fermions and bosons.

Keywords

Non-Relativistic Quantum Field Theory, Newton's Gravity, Schwartz' Distributions

1. Introduction

1.1. Preliminaries

In this work we will use a recently developed non relativistic quantization methodology that successfully overcomes all troubles of non-renormalizable QFT [1]. The essential result of such procedures is that we can dispense with renormalization and counter-terms. The reader can consult the recent references [1] [2] [3] [4] [5]. The proofs given there are conclusive.

The above claims are validated because infinities in Feynman diagrams, that arise in the convolution of quantum propagators (QP), disappear if one 1) represents QP by ultra-hyperfinctions (a generalization of Schwartz' distributions) and follows this technique with an appropriate Laurent expansion. The facts 1) and 2) above are clearly explained, with all kind of details, in [1] [2] [3] [4] [5]. Accordingly, no more mathematical aspects of the procedure need to be given in this paper.

The techniques of [1] [2] [3] [4] [5] are here applied to Newton's gravitation potential. We strongly emphasize the fact that, since we will be inserting a gravitational potential into a Schrödinger Equation (SE), the ensuing discussion is per force non-relativistic, and as such is the character of SE.

1.2. Organizing Our Material

In Section 2 we revisit Newton's gravity. Section 3 is devoted to an explicit display of results belonging to [6], concerning non relativistic quantum field theory (NR-QFT). In Section 4 we apply the results of Sections 2 and 3 so as to obtain the N-QFT of Newton's gravity. We discuss, as examples, the calculation of the self-energy for fermions and of the dressed propagator for both, bosons and fermions, to first order in perturbation theory. Some conclusions are drawn in Section 5.

2. Newton's Gravity

As stated above, r^{-1} is viewed here as

$$r^{-1}=\frac{1}{2}\left[\left(r-i0\right)^{-1}+\left(r+i0\right)^{-1}\right]=PV\frac{1}{r}. \tag{2.1}$$

Remember also that

$$\delta\left(r\right)=0. \tag{2.2}$$

We need now the Fourier transform of r^{-1}. We have

$$\begin{aligned}&\int r^{-1}\mathrm{e}^{ik\cdot x}\mathrm{d}^3x\\&=\lim_{\epsilon\to 0}\left[\int_0^{\infty}\int_0^{\frac{\pi}{2}}\int_0^{2\pi}\mathrm{e}^{i(k+i\epsilon)r\cos\theta}r\sin\theta\mathrm{d}r\mathrm{d}\theta\mathrm{d}\phi+\int_0^{\infty}\int_{\frac{\pi}{2}}^{\pi}\int_0^{2\pi}\mathrm{e}^{i(k-i\epsilon)r\cos\theta}r\sin\theta\mathrm{d}r\mathrm{d}\theta\mathrm{d}\phi\right].\end{aligned} \tag{2.3}$$

Integrating over ϕ one finds

$$\lim_{\epsilon\to 0}\left[2\pi\int_0^{\infty}\int_0^{\frac{\pi}{2}}\mathrm{e}^{i(k+i\epsilon)r\cos\theta}r\sin\theta\mathrm{d}r\mathrm{d}\theta+2\pi\int_0^{\infty}\int_{\frac{\pi}{2}}^{\pi}\mathrm{e}^{i(k-i\epsilon)r\cos\theta}r\sin\theta\mathrm{d}r\mathrm{d}\theta\right]. \tag{2.4}$$

Evaluating now for θ we reach

$$\lim_{\epsilon\to 0}2\pi\left\{\int_0^{\infty}\left[\frac{\mathrm{e}^{i(k+i\epsilon)r}}{i\left(k+i\epsilon\right)}-\frac{\mathrm{e}^{i(k-i\epsilon)r}}{i\left(k-i\epsilon\right)}\right]\mathrm{d}r\right\}. \tag{2.5}$$

Finally, dealing with the variable r we arrive at

$$2\pi \lim_{\epsilon\to 0}\left[\frac{1}{(k+i\epsilon)^2}+\frac{1}{(k-i\epsilon)^2}\right]. \tag{2.6}$$

As an example, consider now the anti transform of $4\pi k^{-2}$ and verify that it is $PV\frac{1}{r}$.

$$2\pi\left[\frac{1}{(k+i0)^2}+\frac{1}{(k-i0)^2}\right]=4\pi PV\frac{1}{k^2}\equiv 4\pi k^{-2}. \tag{2.7}$$

One has

$$\begin{aligned}&\frac{4\pi}{(2\pi)^3}\int k^{-2}\mathrm{e}^{-ik\cdot x}\mathrm{d}^3k\\&=\lim_{\epsilon\to 0}\left[\frac{1}{2\pi^2}\int_0^\infty\int_0^{\frac{\pi}{2}}\mathrm{e}^{-i(r-i\epsilon)k\cos\theta}\sin\theta\mathrm{d}k\mathrm{d}\theta+\frac{1}{2\pi^2}\int_0^\infty\int_{\frac{\pi}{2}}^{\pi}\mathrm{e}^{-i(r+i\epsilon)k\cos\theta}\sin\theta\mathrm{d}k\mathrm{d}\theta\right],\end{aligned} \tag{2.8}$$

so that

$$-\lim_{\epsilon\to 0}\frac{1}{\pi}\left\{\int_0^\infty\left[\frac{\mathrm{e}^{-i(r-i\epsilon)k}}{ik(r-i\epsilon)}-\frac{\mathrm{e}^{i(r+i\epsilon)k}}{ik(r+i\epsilon)}\right]\mathrm{d}k\right\}, \tag{2.9}$$

or

$$\frac{i}{\pi}PV\frac{1}{r}\int_\infty^\infty PV\frac{1}{k}\mathrm{e}^{-ikr}\mathrm{d}k=PV\frac{1}{r}, \tag{2.10}$$

where we used (see Ref. [7])

$$\int_\infty^\infty PV\frac{1}{k}\mathrm{e}^{-ikx}\mathrm{d}k=\frac{\pi}{i}Sgn(x), \tag{2.11}$$

together with $Sgn(r)=1$, where $Sgn(x)$ is the function sign of x.

3. Materials Needed from Fetter and Walecka's Book

3.1. Self Energies

The energy that a particle gains as the result of environment-modifications that it itself generates is called a self-energy Σ. This quantity denotes the contribution to the particle's effective mass due to interactions particle-surrounding medium (SM). Consider the particular (and common) condensed matter scenario: electrons moving in a material. Σ represents there the potential felt by a given electron due to the SM's interactions with it. Given that electrons repel each other, a moving electron does polarize the electrons in its vicinity, This, in turn, changes the potential of the moving electron fields. Such effects necessarily involve self-energy.

3.2. Fermion Dressed Propagators

The dressed propagator is defined to be the two-point function to all orders of the perturbation expansion. It changes the bare mass to the physical mass. We

will use this notion here. For an accessible discussion of the concept we recommend the book [8]. In Fetter and Walecka's (FW) [6] one, this idea is comprehensively discussed for a fermion's NR QFT. In the case of free fermions, FW defined the following (current) propagator

$$iG^0_{\alpha\beta}\left(\boldsymbol{x},t;\boldsymbol{x}',t'\right)=\left\langle 0\left|T\left[\psi_\alpha\left(\boldsymbol{x},t\right)\psi^+_\beta\left(\boldsymbol{x}',t'\right)\right]\right|0\right\rangle. \tag{3.1}$$

One has

$$\begin{aligned} &iG^0_{\alpha\beta}\left(\boldsymbol{x},t;\boldsymbol{x}',t'\right)\\ &=\frac{\delta_{\alpha\beta}}{\left(2\pi\right)^3}\int \mathrm{e}^{i\boldsymbol{k}\cdot\left(\boldsymbol{x}-\boldsymbol{x}'\right)}\mathrm{e}^{-\omega_k\left(t-t'\right)}\left[\Theta\left(t-t'\right)\Theta\left(k-k_F\right)-\Theta\left(t'-t\right)\Theta\left(k_F-k\right)\right]\mathrm{d}^3k. \end{aligned} \tag{3.2}$$

Θ is the Heaviside's step function. We appeal now to the very well known relation

$$\Theta\left(t-t'\right)=-\frac{1}{2\pi i}\int_{-\infty}^{\infty}\frac{\mathrm{e}^{-i\omega\left(t-t'\right)}}{\omega+i0}\mathrm{d}\omega, \tag{3.3}$$

and find

$$\begin{aligned} &iG^0_{\alpha\beta}\left(\boldsymbol{x},t;\boldsymbol{x}',t'\right)\\ &=\frac{\delta_{\alpha\beta}}{\left(2\pi\right)^3}\int\int_{-\infty}^{\infty}\mathrm{e}^{i\boldsymbol{k}\cdot\left(\boldsymbol{x}-\boldsymbol{x}'\right)}\mathrm{e}^{-\omega_k\left(t-t'\right)}\left[\frac{\Theta\left(k-k_F\right)}{\omega-\omega_k+i0}-\frac{\Theta\left(k_F-k\right)}{\omega-\omega_k-i0}\right]\mathrm{d}^3k\mathrm{d}\omega. \end{aligned} \tag{3.4}$$

Thus, the pertinent expression in momentum space reads

$$\hat{G}^0_{F\alpha\beta}\left(\boldsymbol{k},\omega\right)=\delta_{\alpha\beta}\left[\frac{\Theta\left(k-k_F\right)}{\omega-\omega_k+i0}+\frac{\Theta\left(k_F-k\right)}{\omega-\omega_k-i0}\right], \tag{3.5}$$

with

$$\frac{1}{\omega-\omega_k\pm i0}=PV\frac{1}{\omega-\omega_k}\mp i\pi\delta\left(\omega-\omega_k\right), \tag{3.6}$$

where $k=\left|\boldsymbol{k}\right|$ and $\omega_k=\sqrt{k^2/2m}$ We already stated above that PV signifies "principal value of a function". The system's interaction's Hamiltonian is defined by a two-body V_F potential such that

$$V_F\left(\boldsymbol{x}_1-\boldsymbol{x}_2\right)=V_F\left(\left|\boldsymbol{x}_1-\boldsymbol{x}_2\right|\right)\mathbf{1}(1)\mathbf{1}(2), \tag{3.7}$$

where $\mathbf{1}$ is the unity matrix. The dressed propagator here verifies

$$\hat{G}_{F\alpha\beta}=\delta_{\alpha\beta}\hat{G}_F, \tag{3.8}$$

so that the dressed propagator becomes diagonal. Then, ($\hat{G}^0_F\left(\boldsymbol{k},\omega\right)\equiv\hat{G}^0_F\left(k\right)$)

$$\hat{G}_F\left(k\right)=\hat{G}^0_F\left(k\right)+\hat{G}^0_F\left(k\right)\Sigma_F\left(k\right)\hat{G}^0_F\left(k\right), \tag{3.9}$$

with $\Sigma_F\left(k\right)$ the self-energy. We can pass now to its perturbative expansion at first order

$$\Sigma^{(1)}_F\left(k\right)\equiv\Sigma^{(1)}\left(\boldsymbol{k}\right)=\frac{n}{\hbar}\hat{V}\left(0\right)-\frac{1}{\left(2\pi\right)^3\hbar}\int\hat{V}_F\left(\boldsymbol{k}-\boldsymbol{k}'\right)\Theta\left(k_F-k'\right)\mathrm{d}^3k', \tag{3.10}$$

with $n=N/V$ and

$$\hat{V}_F(\boldsymbol{k}) = \int V_F(\boldsymbol{x}) \mathrm{e}^{-i\boldsymbol{k}\cdot\boldsymbol{x}} \mathrm{d}^3 x. \tag{3.11}$$

Consequently (up to first order),

$$\hat{G}_F^{(1)}(k) = \hat{G}_F^0(k) + \hat{G}_F^0(k)\Sigma_F^{(1)}(k)\hat{G}_F^0(k). \tag{3.12}$$

3.3. Bosons' Dressed Propagators from FW's Book

For free bosons FW introduce the propagator in momentum space as

$$iG^0(\boldsymbol{x},t;\boldsymbol{x}',t') = \langle 0 | T\left[\phi(\boldsymbol{x},t)\phi^+(\boldsymbol{x}',t')\right] | 0\rangle. \tag{3.13}$$

It reads

$$\hat{G}_B^0(k) = \frac{1}{k_0 - \omega_k + i0}, \tag{3.14}$$

with $\omega_k = \sqrt{k^2/2m}$. One has then

$$\hat{G}_B(k) = -(2\pi)^4 n_0 i\delta(k_0, k) + \hat{G}_B'(k), \tag{3.15}$$

where the primed part refers to the noncondensate ($n_0 = N_0/V$)

$$\hat{G}_B(k) = -(2\pi)^4 n_0 i\delta(k_0, k) + \hat{G}_B^0(k) + \hat{G}_B'^{(1)}(k), \tag{3.16}$$

$$\hat{G}_B'^{(1)}(k) = \frac{n_0}{h}\hat{G}_B^0(k)\left[\hat{V}_B(0) + \hat{V}_B(\boldsymbol{k})\right]\hat{G}_B^0(k), \tag{3.17}$$

and

$$\hat{V}_B(\boldsymbol{k}) = \int V_B(\boldsymbol{x}) \mathrm{e}^{-i\boldsymbol{k}\cdot\boldsymbol{x}} \mathrm{d}^3 x. \tag{3.18}$$

4. Non-Relativistic QFT of Newton's Gravity

4.1. Fermions

We wish to calculate $\Sigma^{(1)}$ for the potential $-\frac{Gm^2}{r}$.

$$V_F(r) = -\frac{Gm^2}{r}. \tag{4.1}$$

One has

$$\hat{V}_F(k) = \int V_F(x) \mathrm{e}^{ik\cdot x} \mathrm{d}^3 x, \tag{4.2}$$

and then

$$\hat{V}_F(k) = -\frac{4\pi Gm^2}{k^2}, \tag{4.3}$$

with

$$\hat{V}_F(0) = 0. \tag{4.4}$$

Starting here, a father lengthy manipulation leads to

$$-4\pi Gm^2 \int \frac{\Theta(k_F - k')}{|\boldsymbol{k} - \boldsymbol{k}'|^2} \mathrm{d}^3 k' = -8\pi^2 Gm^2 \frac{k_F^2 - k^2}{2k} \ln\left(\frac{k_F + k}{k_F - k}\right)^2, \tag{4.5}$$

so that the self energy reads

$$\Sigma^{(1)}(\boldsymbol{k}) = \frac{Gm^2}{\pi\hbar}\frac{k_F^2 - k^2}{2k}\ln\left(\frac{k_F + k}{k_F - k}\right)^2. \tag{4.6}$$

Accordingly, one writes for the dressed propagator

$$\hat{G}_F^{(1)}(k) = \hat{G}_F^0(k) + \frac{Gm^2}{\pi\hbar}\frac{k_F^2 - k^2}{2k}\ln\left(\frac{k_F + k}{k_F - k}\right)^2\left[\hat{G}_F^0(k)\right]^2, \tag{4.7}$$

noting that

$$\hat{G}_F^0(k) = \hat{G}_F^0(\boldsymbol{k},\omega) = \left[\frac{\Theta(k - k_F)}{\omega - \omega_k + i0} + \frac{\Theta(k_F - k)}{\omega - \omega_k - i0}\right]. \tag{4.8}$$

We recall at this stage that, in Ref. [9], it was been proved that

$$PV\frac{1}{x^n}\delta^{(m)}(x) = \frac{(-1)^n}{2}\frac{m!}{(m+n)!}\cdot\delta^{(m+n)}(x). \tag{4.9}$$

Then, using the result

$$PV\frac{1}{x^n}PV\frac{1}{x^m} = PV\frac{1}{x^{(n+m)}}, \tag{4.10}$$

we reach

$$\frac{1}{\omega - \omega_k - i0}\frac{1}{\omega - \omega_k - i0} = \frac{1}{(\omega - \omega_k - i0)^2}, \tag{4.11}$$

so that

$$\left[\hat{G}_F^0(\boldsymbol{k},\omega)\right]^2 = \left[\frac{\Theta(k - k_F)}{(\omega - \omega_k + i0)^2} + \frac{\Theta(k_F - k)}{(\omega - \omega_k - i0)^2}\right], \tag{4.12}$$

If $V \to \infty$, $k_F \to \infty$, n finite, we find

$$\int \frac{1}{|\boldsymbol{k} - \boldsymbol{k}'|^2}\mathrm{d}^3k' = 0, \tag{4.13}$$

so that

$$\Sigma_F^{(1)}(k) \simeq 0, \tag{4.14}$$

and thus

$$\hat{G}_F^{(1)}(k) \simeq \hat{G}_F^0(k). \tag{4.15}$$

4.2. Bosons' Potential $V_B(r)$

We calculate now the dressed propagator for

$$V_B(r) = -\frac{Gm^2}{r}. \tag{4.16}$$

Since

$$\hat{V}_B(k) = -\frac{4\pi Gm^2}{k^2}, \tag{4.17}$$

one has

$$\hat{V}_B(0)=0. \tag{4.18}$$

For this result, we have used the relation of [7] concerning the regularization of integrals that depend upon a power of *x*. Thus, for the dressed propagator we find, up to first order

$$\hat{G}_B'^{(1)}(k)=-\frac{n_0}{h}\frac{4\pi Gm^2}{k^2}\left[\hat{G}_B^0(k)\right]^2. \tag{4.19}$$

We must proceed from here as we did for the fermion case to obtain

$$\left[\hat{G}_B^0(k)\right]^2=\frac{1}{\left(k_0-\omega_k+i0\right)^2}, \tag{4.20}$$

and we obtain for the dressed propagator the relation

$$\hat{G}_B(k)=-in_0 2\pi^4\delta(k_0,k)+\hat{G}_B^0(k)-\frac{n_0}{h}\frac{4\pi Gm^2}{k^2}\left[\hat{G}_B^0(k)\right]^2. \tag{4.21}$$

5. Conclusions

We have here applied a recently developed non relativistic quantization methodology [2] [9] [10] [11] [12] to Newton's gravitation potential.

- We emphasize that our methodology successfully tackles all renormalization issues. We made full use ultra-hyperfunctions' theory, in particular the results reported in [2].
- With such tools we have been able to construct a non-relativistic quantum field theory (NR QFT) of Newton's gravitation (NG).
- This was done for pairs of fermions or bosons that interact between themselves via NG.
- Our manipulations were based on the results of the classical book [6].
- As special examples, we have obtained the dressed propagators for both types of particles, up to first order in perturbation theory, and also the fermions' self-energy.
- The examples indicate that we have indeed constructed, both for fermions and bosons, a viable non-relativistic quantum field theory of gravitation.
- Remark that we were here concerned only with Newton's gravitation.

Conflicts of Interest

The authors declare no conflicts of interest regarding the publication of this paper.

References

[1] Plastino, A. and Rocca, M.C. (2020) *Annals of Physics*, **412**, Article ID: 168013. https://doi.org/10.1016/j.aop.2019.168013

[2] Plastino, A. and Rocca, M.C. (2018) *Journal of Physics Communications*, **2**, Article No. 11. https://doi.org/10.1088/2399-6528/aaf186

[3] Plastino, A. and Rocca, M.C. (2020) *Journal of Modern Physics*, **11**, 565-580. https://doi.org/10.4236/jmp.2020.114037

[4] Plastino, A. and Rocca, M.C. (2020) *Journal of High Energy Physics*, *Gravitation and Cosmology*, **6** 298-311. https://doi.org/10.4236/jhepgc.2020.62023

[5] Plastino, A. and Rocca, M.C. (2020) *Journal of Physics Communications*, **4**, Article No. 3. https://doi.org/10.1088/2399-6528/ab8178

[6] Fetter, A.L. and Walecka, J.D. (1971) Quantum Theory of Many-Particle Systems. McGraw-Hill Book Company, New York.

[7] Guelfand, I.M. and Shilov, G.E. (1972) Les Distributions. Vol. 1, Dunod, Paris.

[8] Matttuck, R.D. (1996) A Guide to Feynman Diagrams in the Many Body Problem. 2nd Edition, McGraw Hill, NY.

[9] Bollini, C.G., Escobar, T. and Rocca, M.C. (1999) *International Journal of Theoretical Physics*, **38**, 2315-2332. https://doi.org/10.1023/A:1026623718239

[10] Bollini, C.G. and Rocca, M.C. (2004) *International Journal of Theoretical Physics*, **43**, 59-76. https://doi.org/10.1023/B:IJTP.0000028850.35090.24

[11] Bollini, C.G. and Rocca, M.C. (2004) *International Journal of Theoretical Physics*, **43**, 1019-1051. https://doi.org/10.1023/B:IJTP.0000048599.21501.93

[12] Bollini, C.G., Marchiano, P. and Rocca, M.C. (2007) *International Journal of Theoretical Physics*, **46**, 3030-3059. https://doi.org/10.1007/s10773-007-9418-y

Journal of Modern Physics, 2020, 11, 928-943
https://www.scirp.org/journal/jmp
ISSN Online: 2153-120X
ISSN Print: 2153-1196

Accurate Ground State Electronic and Related Properties of Hexagonal Boron Nitride (h-BN)

Y. Malozovsky, C. Bamba, A. Stewart, L. Franklin, D. Bagayoko

Department of Physics, Southern University and A&M College, Baton Rouge, LA, USA
Email: bagayoko@aol.com

How to cite this paper: Malozovsky, Y., Bamba, C., Stewart, A., Franklin, L. and Bagayoko, D. (2020) Accurate Ground State Electronic and Related Properties of Hexagonal Boron Nitride (h-BN). *Journal of Modern Physics*, **11**, 928-943.
https://doi.org/10.4236/jmp.2020.116057

Received: May 12, 2020
Accepted: June 15, 2020
Published: June 18, 2020

Abstract

We present an *ab-initio*, self-consistent density functional theory (DFT) description of ground state electronic and related properties of hexagonal boron nitride (h-BN). We used a local density approximation (LDA) potential and the linear combination of atomic orbitals (LCAO) formalism. We rigorously implemented the Bagayoko, Zhao, and Williams (BZW) method, as enhanced by Ekuma and Franklin (BZW-EF). The method ensures a generalized minimization of the energy that is far beyond what can be obtained with self-consistency iterations using a single basis set. The method leads to the ground state of the material, in a verifiable manner, without employing over-complete basis sets. We report the ground state band structure, band gap, total and partial densities of states, and electron and hole effective masses of hexagonal boron nitride (h-BN). Our calculated, indirect band gap of 4.37 eV, obtained with room temperature experimental lattice constants of $a = 2.504$ Å and $c = 6.661$ Å, is in agreement with the measured value of 4.3 eV. The valence band maximum is slightly to the left of the K point, while the conduction band minimum is at the M point. Our calculated, total width of the valence and total and partial densities of states are in agreement with corresponding, experimental findings.

Keywords

Density Functional Theory, Band Gap, Density and Partial Density of States, Electron and Hole Effective Masses

1. Introduction

The demand for compact ultraviolet laser devices has led many researchers to search for materials with band gaps larger than that of GaN (3.4 eV), a material presently utilized in the fabrication of high-power, blue-ray laser devices [1].

Properties of hexagonal boron nitride (h-BN), with a graphite-like crystal structure, provide a basis for many applications. It is employed as a good electrical insulator, with excellent thermal conductivity, for crystal growth and molecular beam epitaxy. It has several applications in electronics and nuclear energy industries and serves as an excellent lubricant [2]. Recently, its outstanding catalyst properties have attracted much attention, for potential applications in oxygen reduction reactions [3] [4] [5]. Hexagonal boron nitride (h-BN) is a wide band gap material with high chemical and thermal stability. Despite the above attributes of h-BN, a survey of the literature shows a lack of consensus on the experimentally determined band gap of the material. Measured, direct and indirect band gaps have been reported, with values ranging from 3.6 to 7.1 eV. Its electronic structure and band gap have been studied experimentally using x-ray photoemission [6] [7] [8] [9], optical absorption [10], UV absorption [11], optical reflectivity [12] [13], luminescence spectra [14] [15], photoconductivity [16] [17], and temperature dependence of the electrical resistivity [18]. The various experimentally measured band gaps are summarized in **Table 1**. From the content of the table, we infer a lack of consensus not only on the direct or indirect nature of the band gap, but also on its numerical value—notwithstanding some of the discrepancies may be due to differences in sample purity, thickness (for films) and measurement temperature.

As shown in **Table 2**, the theoretical studies of h-BN disagree on the value of the band gap and particularly on the locations of the valence band maximum (VBM) and of the conduction band minimum (CBM), respectively. Specifically, the table shows that previous LDA and GGA calculations [22]-[32] led to seven (7) different pairs of VBM and CBM: M-H (1), H-M (5), K-M (2), M-K (1), H-K (1), Γ-H (1) and Γ-K (2), where the numbers between parentheses represent the respective frequencies of the concerned VBM-CBM pair. The two Green function and dressed Coulomb approximation (GW) calculations in the table found the gap to be from H to M. With an LDA potential, Ma *et al.* [23] employed the

Table 1. Experimental values of the band gap (E_g) of h-BN, in eV. The results in this table are reportedly for bulk h-BN. We note that some authors believe the measured indirect band gap of 4.3 eV [9] [10] [11] best represents the true band gap of h-BN.

Experimental method	E_g (eV)
X-ray photoemission spectra	3.6 [a], 3.85 [b]
Optical and UV absorption	3.9 [c], 4.3 [d]
Laser-induced fluorescence (LIF)	4.02 [e]
Optical reflectivity spectra	4.5 [f], 5.2 [g]
Luminescence optical spectra	>5.5 [h], 5.89 [i], 5.95 [j]
Photoconductivity, and absorption spectra	5.8 [k], 5.83 [l]
Temperature dependence of electrical resistivity	7.1 [m]

[a]Ref. [6], [b]Ref. [7] [8] [9], [c]Ref. [10], [d]Ref. [11] [12] [13], [e]Ref. [14], [f]Ref. [15], [g]Ref. [16], [h]Ref. [17], [i]Ref. [18], [j]Ref. [19], [k]Ref. [20], [l]Ref. [21], [m]Ref. [22].

Table 2. Illustrative, previously calculated values of the band gap (E_g) of h-BN, in eV. They include results from LDA, GGA, and GW calculations.

Computational method	Potentials	E_g (eV)
Linear Combination of Pseudoatomic Orbitals (LCPAO)	LDA	3.7 (M-H) [a]
FP-LAPW	LDA	3.9 (H-M) [b] 4.3 (H-H) [b]
Ab-initio Pseudopotential	LDA	3.9 (K-M) [c]
OLCAO	LDA	4.07 (M-K) [d]
Ultra soft Pseudopotential	LDA	4.1 (H-M) [e] 4.5 (M-M) [e]
FP-LAPW	LDA	4.0 (H-M) [f] 4.5 (M-M) [f]
FP-LAPW	LDA	4.58 (H-K) [g]
FP-LAPW	PW91-GGA	4.53 (Γ-K) [g]
FP-LAPW	PBE-GGA	4.54 (Γ-K) [g]
Projected-Augmented-Wave (PAW)	LDA	4.02 (K-M) [h]
PAW (VASP)	LDA	4.21 (H-M) [i]
PAW (VASP)	GGA	4.39 (H-M) [i]
PAW	GGA	4.47 (K-M) [j]
GW	GGA	5.4 (H-M) [c]
GW	LDA	5.95 (K-M) [h]
GW	LDA	5.95 (H-M) [k]

[a]Ref. [23], [b]Ref. [24], [c]Ref. [25], [d]Ref. [26], [e]Ref. [27], [f]Ref. [28], [g]Ref. [29], [h]Ref. [30], [i]Ref. [31], [j]Ref. [32], [k]Ref. [33].

linear combination of pseudo-atomic-orbitals (PAO) method to calculate properties of h-BN. Their calculated, indirect band gap, from H to M, was 3.7 eV [23]. The calculated direct (H-H) and indirect (H-M) band gaps, obtained by using the Full Potential Linearized Augmented Plane Wave (FP-LAPW) method, were respectively 4.3 eV and 3.9 eV [24]. The LDA pseudopotential calculations of Blasé *et al.* [25] resulted in an indirect (K-M) band gap of 3.9 eV while their GW quasiparticle calculations produced an indirect (H-M) band gap of 5.4 eV. Xu and Ching [26], using orthogonalized linear combination of atomic orbitals (OLCAO), found an indirect (K-M) band gap of 4.07 eV. The optimized ultra-soft (Vanderbilt-type) LDA pseudopotential calculations of Furthmüller *et al.* [27] predicted an indirect (H-M) band gap of 4.1 eV and a direct (M-M) gap of 4.5 eV. **Table 2** shows the above referenced results and several other theoretical findings [28]-[33].

Clearly, this range of theoretical results for the band gap of h-BN, including the seven (7) different pairs of VBM-CBM, points to the need for further work. Additionally, and unlike the cases for most semiconductors, the experimental results in **Table 1** also disagree. These discrepancies constitute a major motiva-

tion for this work. This motivation is partly predicated on previous, theoretical results of our group, in agreement with corresponding experimental ones, for more than 30 semiconductors [34].

2. Method and Computational Details

We succinctly provide below the essential features of our computational approach. Extensive details on it are available in the literature [34]-[41]. As with most other calculations, we employed a density functional theory (DFT) potential and the linear combination of atomic orbitals (LCAO). Our specific DFT potential for this work is the local density approximation (LDA) one by Ceperley and Alder, with the parameterization of Vosko *et al.* [42] [43] [44] [45]. A major difference between our method and most others in the literature stems from our performance of a generalized minimization of the energy functional to attain the ground state of the system, without utilizing over-complete basis sets. The first [46] [47] [48] and the enhanced [49] [50] [51] versions of this generalized minimization of the energy are respectively expounded upon in the literature.

As per the second DFT theorem, self-consistent iterations with a single basis set lead to a stationary solution among an infinite number of such solutions. This fact resides in the reality that the ground state charge density (*i.e.* basis set) is not *à priori* known, as far as we can determine. Consequently, the chances are extremely small for a calculation with a single basis set to lead to the ground state of the system or to avoid over-complete basis sets.

We have described in previous publications a straightforward way to search for and to reach the ground state of the system. Beginning with a small basis set that is large enough to account for all the electrons in the system, we perform successive self-consistent calculations, where the basis set of a calculation, except for the first one, is that of the preceding calculation augmented with one orbital. The first and second versions of our method, known as BZW and BZW-EF method, differ as follows. For the first one, we add orbitals in the order of increasing energy of the excited states they represent. In the second, we heed the "arbitrary variations" clause of the second DFT theorem and add orbitals so as to recognize the primacy of polarization orbitals (p, d, and f) over the spherical symmetry of s orbitals for valence electrons. Indeed, for diatomic and any other multi-atomic system, valence electrons do not possess any full, spherical symmetry known to us, unlike the core electrons. The above referenced, successive calculations continue until three (3) consecutive ones produce the same occupied energies. This criterion guarantees the attainment of the absolute minima of the occupied energies (*i.e.* the true ground state). With just two (2) consecutive calculations leading to the same occupied energies, these energies could represent a local minima and not the absolute ones. The first of the referenced three (3) consecutive calculations [34] is the one providing the DFT description of the material. The basis set for this calculation is dubbed the optimal basis set, *i.e.* the smallest basis set leading to the ground state charge density and energies.

In this study, we utilized the program package developed at the US Department of Energy's Ames Laboratory, in Ames, Iowa. B and N are light enough to neglect relativistic corrections. Self-consistent calculations of the electronic energies and wave functions for the atomic or ionic species provided input data for the solid-state calculations. Specifically, for hexagonal BN, the species we considered were B^{3+} and N^{3-}. Preliminary calculations for neutral atoms (B and N) pointed to a charge transfer larger than 2, from B to N.

We provide below computational details to enable the replication of our work. Hexagonal BN (h-BN) belongs to the D_{6h}^{4} space group, with a space group number of 194, a Pearson symbol of hP4, and Patterson space group $P6_3/mmc$ [17]. There are two atoms of each kind in the unit cell, with the boron (B) atoms occupying sites $(0,0,\frac{1}{2})$ and $(\frac{1}{3},\frac{2}{3},0)$ while the nitrogen (N) atoms are at (0, 0, 0) and $(\frac{1}{3},\frac{2}{3},\frac{1}{2})$. Our self-consistent calculations were performed with the experimental lattices constants for hexagonal BN with a = 2.504 Å = 4.7319 a.u. is a lattice constant in atomic units (1 a.u. = 1 Å/a_B, where a_B is the Bohr radius) and c = 6.661 Å = 12.5875 a.u. at room temperature. We expanded the radial parts of the orbitals in terms of even-tempered Gaussian functions. The s and p orbitals for the cation B^{3+} were each described with 16 even-tempered Gaussian functions with the respective minimum and maximum exponents of 0.2658 and 1.655×10^4 for the atomic potential and 0.1242 and 1.365×10^4 for the atomic wave functions. The self-consistent calculations for B^{3+} led to the total charge of 2.0005, which is also the valence charge, with an error per electron of 2.5×10^{-4}. Similarly, the s and p orbitals for N^{3-} were described with 20 even-tempered Gaussian functions with the respective minimum and maximum exponents of 0.1600 and 1.600×10^4 for the atomic potential and 0.1000 and 1.300×10^4 for the atomic wave functions. These exponents led to the convergence of the atomic calculations for N^{3-} with the total, core and valence charges of 10.00004, 2.00002, and 8.00002, respectively. The error per electron was therefore 4×10^{-6}. We utilized a 24 k-point mesh with proper weights, in the irreducible Brillouin zone, for the self-consistency iterations. The criterion for the convergence of the iterations was a difference of 10^{-5} or less between the potentials from two consecutive ones. We used 140 k points in the irreducible Brillouin zone for the production of the final, self-consistent bands.

3. Results

Table 3 contains information on the successive calculations performed with the purpose of reaching the absolute minima of the occupied energies. The band gap generally can decrease or increase before one reaches the optimal basis set. As shown farther below, with the graphs of the bands, Calculations IV, V, and VI led to the same occupied energies indicating that these energies have reached their absolute minima, *i.e.* the ground state. As per the BZW-EF method, Calculation IV, the first of the three (3) is the one providing the DFT description of the

Table 3. Successive calculations with the BZW-EF method, for h-BN (Calculations I-VI). In these calculations, the lattice constants are a = 2.504 Å and c = 6.661 Å, at room temperature. Calculation IV led to the absolute minimum of the occupied energies, given that Calculations V and VI produced occupied energies identical to corresponding ones from Calculation IV. The calculated indirect band gap, from near K to M, is 4.369 eV (or 4.37 eV).

Calculation No.	Valence Orbitals for B^{3+}	Valence Orbitals for N^{3-}	No. of Functions	Band Gaps (eV) (near K-M)
I	$1s^2 2p^0 2s^0$	$2s^2 2p^6$	36	7.499
II	$1s^2 2p^0 2s^0$	$2s^2 2p^6 3p^0$	48	5.767
III	$1s^2 2p^0 2s^0 3p^0$	$2s^2 2p^6 3p^0$	60	4.370
IV	$\mathbf{1s^2 2p^0 2s^0 3p^0}$	$\mathbf{2s^2 2^6 3p^0 3s^0}$	**64**	**4.369**
V	$1s^2 2p^0 2s^0 3p^0 3s^0$	$2s^2 2^6 3p^0 3s^0$	68	4.365
VI	$1s^2 2p^0 2s^0 3p^0 3s^0$	$2s^2 2p^6 3p^0 3s^0 4p^0$	80	4.210

material. The basis set for this calculation is the *optimal basis set*, *i.e.* the smallest basis set leading to the ground state of the material, without being over-complete.

Figures 1(a)-(e) provide a graphical illustration of the generalized minimization of the energy, as the basis set is methodically augmented for successive, self-consistent calculations. Every pair of bands from consecutive calculations is shown below. In Figure 1(c), Calculations III may appear to reach the minima of the occupied energies, given that these occupied energies are mostly the same as corresponding ones from Calculation IV. However, a close examination of the occupied energies around −18.50 eV, at the Γ point, shows that both bands have been lowered by Calculation IV from their values from Calculation III. The occupied energies from Calculation IV are identical to the corresponding ones from Calculations V and VI. This perfect superposition of the occupied energies from three (3) consecutive calculations is the robust criterion for the attainment of the absolute minima of the occupied energies, *i.e.* the ground state of the material. As such, these occupied energies possess the full, physical content of DFT. From Figure 1(d) and Figure 1(e), it is apparent that the referenced superposition of the occupied energies does not hold for the all the unoccupied ones. It is instructive to note, however, that the low laying, unoccupied energies from the three (3) calculations, up to 8 eV, are also superimposed. This gratifying feature, notwithstanding, it is clear from the graphs that higher, unoccupied energies tend to be lowered as the size of the basis set increases.

The top of the valence band (VBM) is between K and Γ, at equally 10% of the K-Γ separation, to the left of K. Its distance from K is $\Delta K = (4\pi/3a) \times 0.1 = 0.0885$, where a = 4.7319 a.u. is a lattice constant in atomic units. Hence, the location of the VBM is at $K^* = K - \Delta K = (0, 0.7965, 0)$, to the left of K.

Even though the occupied energies in Table 4 and the graph of the bands from Calculation IV (in Figure 1(d)) provide an adequate description of the ground state electronic properties of hexagonal BN, we discuss farther below

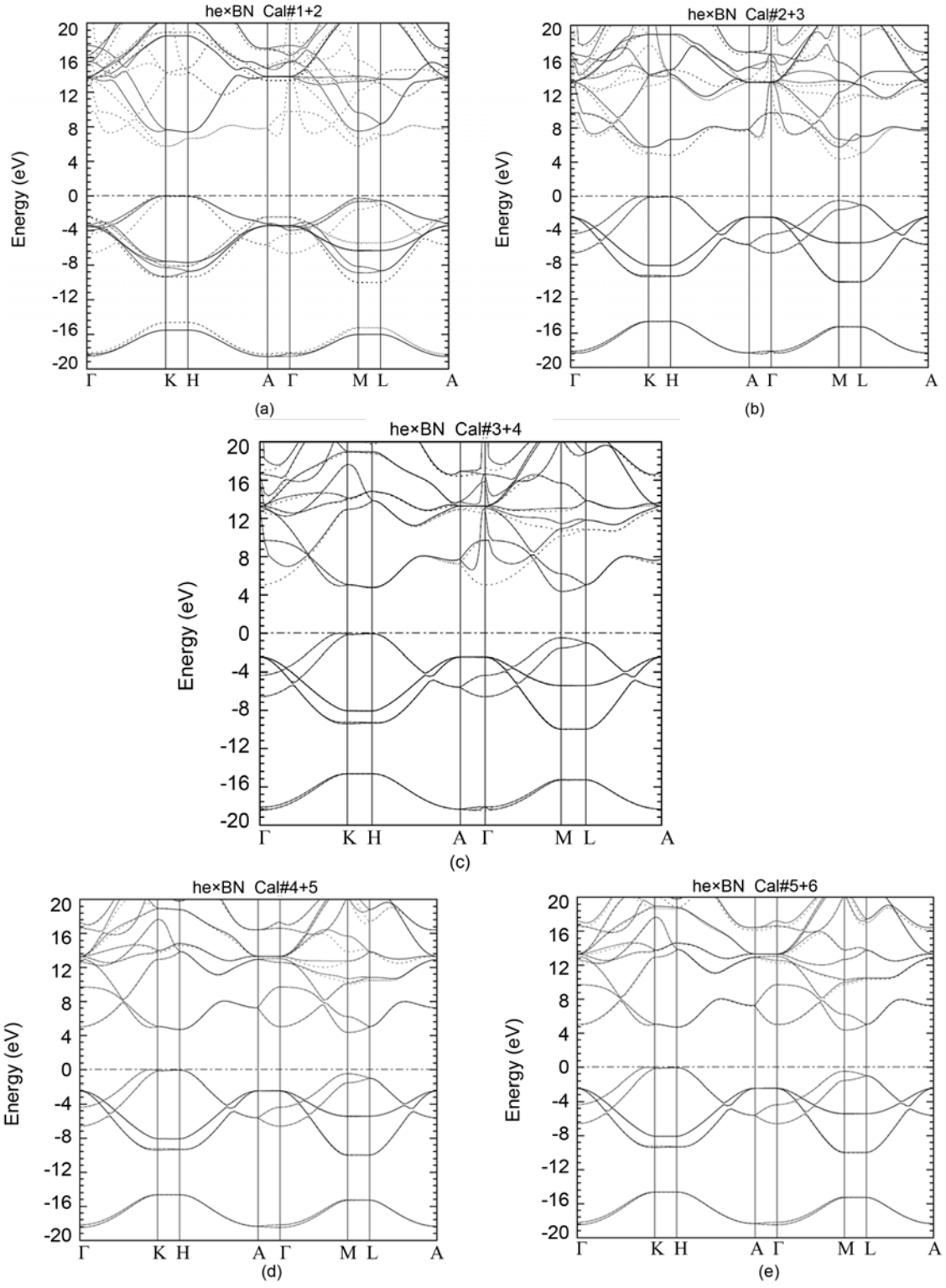

Figure 1. Energy bands of hexagonal BN (h-BN) as obtained in Calculations I-VI of the BZW-EF method. These figures show the bands for pairs of consecutive calculations, with solid lines for bands of a calculation and dashed lines for the bands of the calculation immediately following it. The progressive lowering of the occupied energies, upon setting the Fermi levels to zero, is apparent, up to Calculation IV-VI, which produced the same absolute minima of the occupied energies, *i.e.* the ground state. (a) Calculations I and II; (b) Calcualtions II and III; (c) Calculations III and IV. Calculation IV is optimal basis set; (d) Calculations IV and V; (e) Calculations V and VI.

Table 4. Calculated, electronic energies (in eV) of h-BN, at high symmetry points in the Brillouin zone, obtained from Calculation IV. The Fermi energy is set equal to zero. The calculated band gap is 4.37 eV.

Γ-point	K-ΔK-point	K-point	H-point	A-point	M-point	L-point
17.357	21.116	20.759	19.791	16.4508	21.593	21.745
16.617	20.969	20.759	19.791	16.4508	21.259	21.745
13.322	19.793	18.939	18.802	13.320	21.033	18.820
13.321	18.613	18.939	18.802	13.320	20.236	18.820
13.305	16.896	17.668	14.843	13.319	15.699	13.856
13.304	14.445	13.994	14.843	13.319	12.780	13.856
13.056	13.656	13.994	13.878	12.958	10.689	10.824
12.592	12.309	12.957	13.878	12.958	10.163	10.824
9.714	5.445	5.064	4.715	7.263	6.222	5.040
5.049	4.953	5.064	4.715	7.263	**4.369**	5.040
−2.419	**0.000**	−0.138	**−0.048**	−2.435	−0.482	−1.007
−2.420	−0.614	−0.138	−0.048	−2.435	−1.552	−1.007
−2.453	−7.827	−8.067	−8.082	−2.436	−5.399	−5.423
−2.453	−7.833	−8.067	−8.082	−2.436	−5.452	−5.423
−4.365	−9.241	−9.242	−9.322	−5.606	−9.960	−9.990
−6.593	−9.366	−9.400	−9.322	−5.606	−10.012	−9.990
−18.206	−14.748	−14.653	−14.653	−18.368	−15.254	−15.283
−18.509	−14.801	−14.653	−14.653	−18.368	−15.313	−15.283

subtilities relative to the valence band maximum (VBM) and the conduction band minimum (CBM). In particular, our close examination of the bands hints at a possible explanation of the multitude of VBM-CBM pairs reported by previous density functional theory calculations. These calculations, as far as we can determine, did not perform the generalized minimization of the energy as dictated by the second DFT theorem.

Figure 2 and Figure 3 respectively show the calculated, total and partial densities of states (DOS, pDOS). We derived them from the bands produced by Calculation IV, with the optimal basis set. Short, vertical segments indicate the locations of major peaks, whose values are provided on the graph of the total density of states. The calculated valence band width of 18.58 eV is in agreement with the calculated valence band width (18.5 eV) from Ma *et al.* [23] and from Castellani *et al.* [24]. While this value is smaller than the experimental finding of 20.7 ± 1.5 eV obtained by J. Barth *et al.* [7] and by Tegeler *et al.* [8] in their XPS measurements, we note that, according to these authors [7] [8] [23] [24], the real total width of the valence bands may be smaller than the measured value by l - 3 eV, due to significant Auger broadening of the XPS spectrum at energies corresponding to the s band.

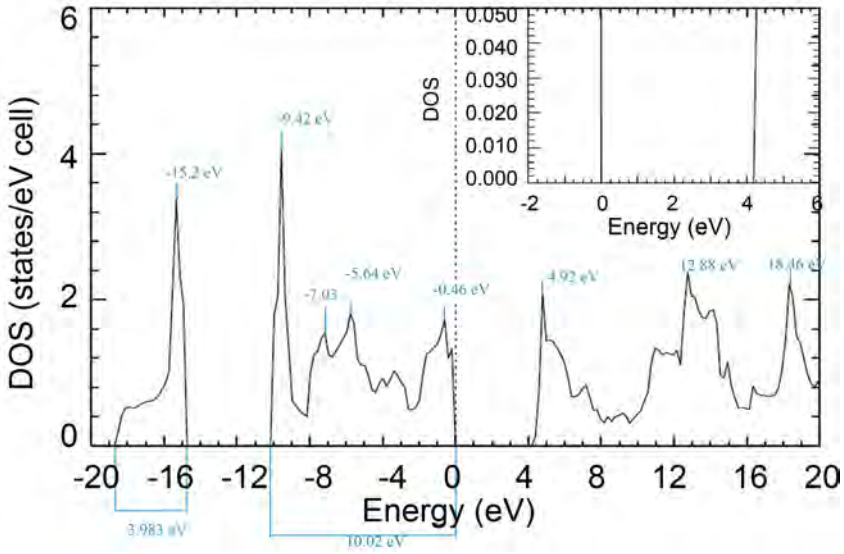

Figure 2. Calculated, total density of states (DOS) for hexagonal boron nitride (h-BN), obtained with the bands from Calculation IV.

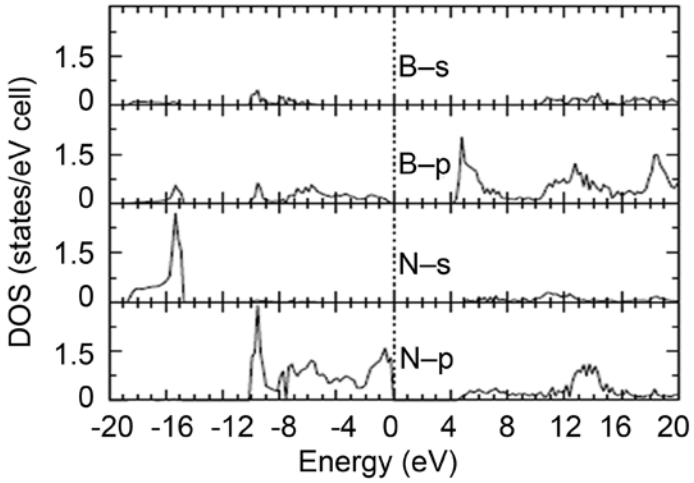

Figure 3. Calculated, partial densities of states (p-DOS), as derived from bands resulting from Calculation IV.

The lower and upper groups of valence bands have widths of 3.98 eV and 10.02 eV, respectively. Three major peaks in the density of states for the conduction bands are located at 4.92 eV, 12.88 eV, and 18.46 eV. The above characteristics of the total density of states (DOS), for h-BN, will be hopefully confirmed by future experimental measurements. Additionally, the eigenvalues in **Table 4** lend themselves to comparison with some X-Ray and UV spectroscopic measurements. From **Figure 3**, for the partial densities of state (pDOS), we clearly observe a net dominance by nitrogen s state in the lowest group of valence bands, with a tiny contribution from boron p state. In the upper group of valence bands, N p dominates, with small contributions from boron p and minuscule ones from boron s. This hybridization of nitrogen p and boron p should be observable in X-Ray spectroscopic measurements. While the largest contribution

to the conduction bands comes from nitrogen p, particularly around the absorption edge, that of boron p is also significant. Both N s and B s have evanescent contributions to the conduction bands.

Several transport properties, including various mobilities for electrons or holes, depend on the inverse of the electron or hole effective masses, respectively. For this reason, we have calculated the electron and hole effective masses shown in Table 5, in units of the electron mass m_0. With values of $0.205m_0$, $2.250m_0$, and $1.730m_0$ in the M to Γ, M to K, and M to L directions, respectively, the electron effective mass at the bottom of the conduction band is clearly anisotropic. The same is true for the electron effective mass at H, even though its values from H to A and H to Γ are identical.

The hole effective masses from K* to Γ, K* to H, and K* to M are respectively 0.534, 0.569, and 1.48, in units of m_0. The calculated hole effective masses at the H symmetry point, along H-A, H-Γ, H-K, and H-L axes, are 0.822, 0.822, 3.468, and 1.671, respectively, in units of m_0. These hole effective masses are anisotropic, despite the equality of the ones from H to A and H to Γ.

4. Discussion

A discussion of our results, particularly in relation to findings from previous DFT calculations, rests on the following fact. None of the previous calculations

Table 5. Calculated effective masses for hexagonal BN, in units of free electron mass m_0: M_e indicates an electron effective mass in the conduction bands and M_h represents a hole effective mass. The top of the valence band is at K*, to the left of the K symmetry point, as defined above.

Types and Directions of Effective Masses	Values of Effective Masses (m_0)
M_e (M-Γ)	0.205
M_e (M-K)	2.250
M_e (M-L)	1.730
M_e (H-A)	0.588
M_e (H-Γ)	0.588
M_e (H-K)	1.102
M_e (H-L)	3.129
M_e (K-Γ)	0.387
M_e (K-H)	0.433
M_h (K*-Γ)	0.534
M_h (K*-H)	0.569
M_h (K*-M)	1.480
M_h (H-A)	0.822
M_h (H-Γ)	0.822
M_h (H-K)	3.468
M_h (H-L)	1.671

appear to have performed a generalized minimization of the energy. The minimization obtained following self-consistent iterations, with a single basis set, produces the minimum of the energy relative to that basis set. Such solutions are stationary ones whose number is practically infinite. None should be *à priori* assumed to provide a description of the ground state of the material. Consequently, the computational results should not be expected to possess the full, physical content of DFT or to agree with experimental measurement. Our generalized minimization, as thoroughly explained above, verifiably leads to the absolute minima of the occupied energies, *i.e.* the ground state, as required by the second DFT theorem. Explicitly searching for the ground state and avoiding basis sets that are overcomplete for the description of the ground state are two requirements for a correctly performed DFT calculation. We address below plausible, negative consequences use of over-complete basis sets.

With the second corollary of the first DFT theorem, *i.e.* that the spectrum of the Hamiltonian is a unique functional of the ground state charge density [34], we avoid over-complete basis sets. While these larger basis sets lead to the ground state energies, they also lower some unoccupied energies from their values obtained with the optimal basis set. As per the above corollary, any unoccupied energy, different from (*i.e.* lower than) its corresponding value obtained with optimal basis set, no longer belongs to the spectrum of the Hamiltonian. This rigorous conclusion also results from the fact that, with these larger basis sets, the charge density and the Hamiltonian do not change from their respective values obtained with the optimal basis set. Consequently, the unoccupied eigenvalues, different from their corresponding values obtained with the optimal basis set, cannot rationally be physically meaningful ones. The Rayleigh theorem for eigenvalues, as elaborated upon elsewhere [34] [49] [50], trivially explains the spurious lowering of unoccupied energies in calculations employing larger basis sets that contain the optimal one. We should note the spuriously lowered, unoccupied energies, including some lowest laying ones, provide one plausible explanation of the widespread underestimation of band gaps in the literature. This contention stems in part from the fact that single basis set calculations tend to employ large basis sets in order to avoid incompleteness.

With the above understanding, we discuss the fine structures of the bands using the enlarged graphs in **Figure 4** and **Figure 5**. While **Figure 4** shows the entire band structure, **Figure 5** only exhibits the drastically enlarged uppermost and lowest valence and conduction bands, respectively, around and between the K and H symmetry points. In **Figure 4**, the highest and degenerate valence bands are visibly close to the Fermi level, from K to H. **Figure 5** is needed to ascertain the location of the valence band maximum. To do so, one is guided by the fact that, at the location of the VBM, the band is superimposed on a short segment at the Fermi level. **Figure 5** shows that the VBM is at the K* point defined above. At the H point, the degenerated valence band is only 0.048eV below the Fermi level. The top of the valence band at M is 0.482 eV below the Fermi level. The direct band gap at M is therefore 4.369 eV + 0.482 eV = 4.851 eV. It

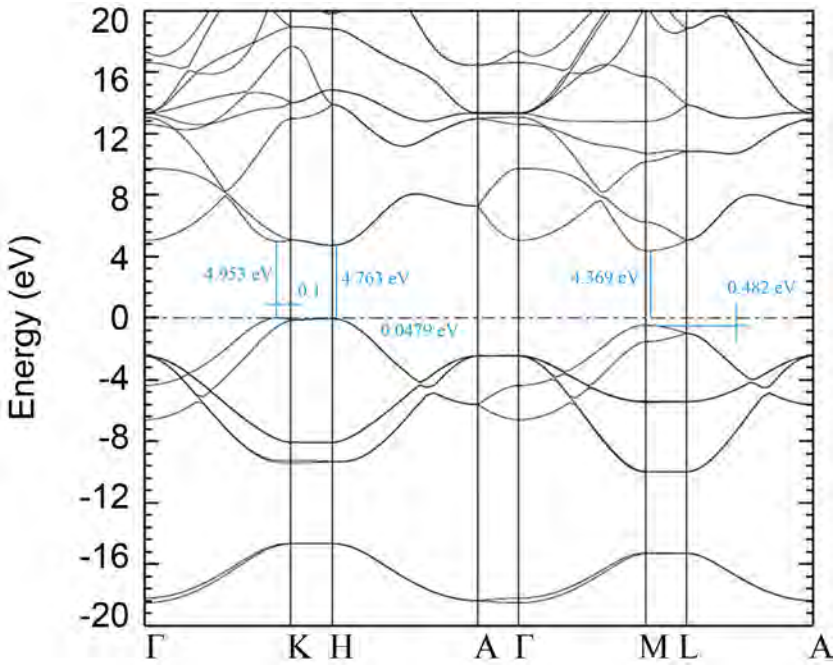

Figure 4. The enlarged graph of the band structure of hexagonal BN, produced by Calculation IV, with the optimal basis set.

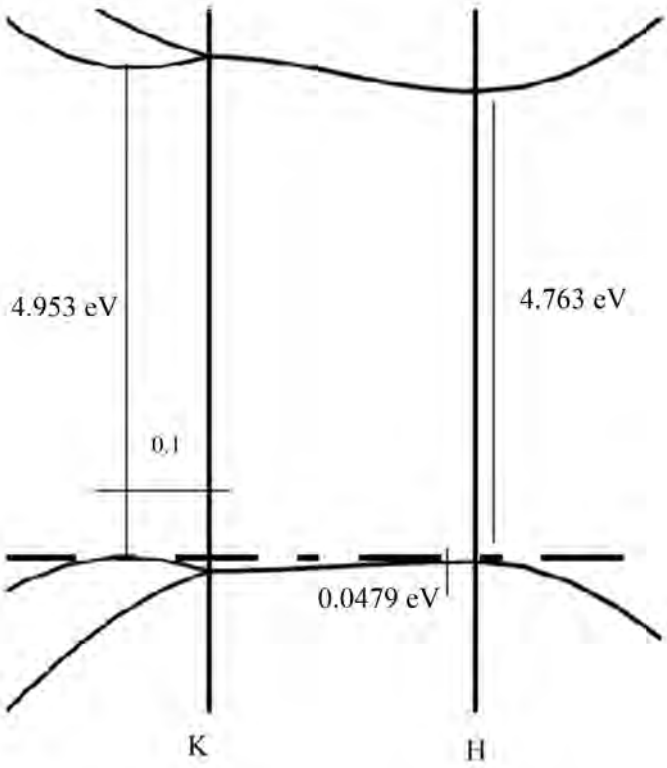

Figure 5. The further enlarged parts of highest and lowest valence and conduction bands, respectively, in **Figure 4**, between and around the K and H high symmetry points. Clearly, the top of the valence band is the only part that is superimposed on the Fermi level; this top is at K* as defined above, to the left of K, and 0.1 is the one tenth of the distance between Γ and K points.

is slightly larger than the one at H which is 4.763 eV + 0.048 eV = 4.811 eV.

The above fine structures of the bands hint to a possible explanation of the report of seven (7) different VBM-CBM pairs by previous DFT calculations. Indeed, while the presumed single basis sets in these calculations may be close to or contain the corresponding optimal basis sets, with the above subtle features of the band structure, the slightest deviation of these basis sets from the one describing the ground state could explain the differences between the resulting bands and between them and the ones reported here. Additionally, without the generalized minimization, it is practically hopeless to have the basis set complete for the description of the ground state, without being over-complete.

5. Conclusion

We have presented the description of electronic and related properties of the ground state of h-BN, as obtained from *ab-initio*, self-consistent density functional theory (DFT) calculations. Our generalized minimization of the energy, following the BZW-EF method, verifiably led to the ground state and avoided over-complete basis sets. Our findings possess the full, physical content of DFT. Our calculated indirect band gap from K* to M is 4.37 eV. This value is practically in agreement with the experimental finding of 4.30 eV which is the most accepted one in the literature. The density of states (DOS) and partial densities of states (p-DOS) are in good agreement with those from electron momentum spectroscopy (EMS) [6] [7] [8] [9]. To the best of our knowledge, no measurements of the electron effective masses are available for comparison with our calculated ones. In light of our previous success, partly through accurate predictive capabilities, we expect future experiments to confirm our findings.

Acknowledgements

This work was funded in part by the National Science Foundation [NSF, Award Nos. EPS-1003897, NSF (2010-2015)-RH SUBR, and HRD-1002541], the US Department of Energy, National Nuclear Security Administration (NNSA, Award No. DE-NA0002630), LaSPACE and LONI-SUBR.

Conflicts of Interest

The authors declare no conflicts of interest regarding the publication of this paper.

References

[1] Fasol, G. (1996) *Science*, **272**, 1751. https://doi.org/10.1126/science.272.5269.1751

[2] Pouch, J.J. and Alterovitz, S.A. (1990) Synthesis and Properties of Boron Nitride. Trans-Tech, Zurich.

[3] Venegas, J.M., Grant, J.T., McDermott, W.P., Burt, S.P., Micka, J., Carrero, C.A. and Hermans, I. (2017) *ChemCatChem*, **9**, 2118. https://doi.org/10.1002/cctc.201601686

[4] Tang, S., Wang, H., Zhang, Y., Li, A., Xie, H., Liu, X., Liu, L., Li, T., Huang, F., Xie, X. and Jiang, M. (2013) *Science Reports*, **3**, Article No. 2666.

https://doi.org/10.1038/srep02666

[5] Khan, A.F., Randviir, E.P., Brownson, D.A.C., Ji, X., Smith, G.C. and Banks, C.E. (2017) *Electroanalysis*, **29**, 622. https://doi.org/10.1002/elan.201600462

[6] Fomichev, V.A. and Rumsh, M.A. (1968) *Journal of Physics and Chemistry of Solids*, **29**, 1015. https://doi.org/10.1016/0022-3697(68)90237-0

[7] Barth, J., Kunz, C. and Zimkina, T.M. (1980) *Solid State Communications*, **36**, 453. https://doi.org/10.1016/0038-1098(80)90932-1

[8] Tegeler, E., Kosuch, N., Wiech, G. and Faessler, A. (1979) *Physica Status Solidi*, **91**, 223. https://doi.org/10.1002/pssb.2220910123

[9] Fossard, F., Sponza, L., Schué, L., Attaccalite, C., Ducastelle, F., Barjon, J. and Loiseau, A. (2017) *Physical Review B*, **96**, Article ID: 115304. https://doi.org/10.1103/PhysRevB.96.115304

[10] Rand, M.J. and Roberts, J.F. (1968) *Journal of the Electrochemical Society*, **115**, 423. https://doi.org/10.1149/1.2411238

[11] Zupan, J. and Kolar, D. (1972) *The Journal of Physical Chemistry*, **5**, 3097. https://doi.org/10.1088/0022-3719/5/21/014

[12] Leapman, R.D. and Silcox, J. (1972) *Physical Review Letters*, **42**, 1361. https://doi.org/10.1103/PhysRevLett.42.1361

[13] Leapman, R.D., Fejes, P.L. and Silcox, J. (1983) *Physical Review B*, **28**, 2361. https://doi.org/10.1103/PhysRevB.28.2361

[14] Solozhenko, V.L., Lazarenko, A.G., Petitet, J.-P. and Kanaev, A.V. (2001) *Journal of Physics and Chemistry of Solids*, **62**, 1331. https://doi.org/10.1016/S0022-3697(01)00030-0

[15] Mamy, R., Thomas, J., Jezequel, G. and Lemomnnier, J.C. (1981) *Journal of Physics Letters*, **42**, 473. https://doi.org/10.1051/jphyslet:019810042022047300

[16] Hoffman, D.M., Doll, G.L. and Ecklund, P.C. (1984) *Physical Review B*, **30**, 6051. https://doi.org/10.1103/PhysRevB.30.6051

[17] Larac, S. and Shrader, R.E. (1956) *Physical Review B*, **104**, 68. https://doi.org/10.1103/PhysRev.104.68

[18] Lukomskii, A.J., Shipilo, V.B. and Gameza, L.M. (1993) *Journal of Applied Spectroscopy*, **57**, 607. https://doi.org/10.1007/BF00667655

[19] Watanabe, K., Taniguchi, T. and Kanda, H. (2004) *Nature Materials*, **3**, 404. https://doi.org/10.1038/nmat1134

[20] Katzir, A., Zunger, A. and Halperin, A. (1976) *Bulletin of the American Physical Society*, **21**, 246.

[21] Baronian, W. (1972) *Materials Research Bulletin*, **7**, 119. https://doi.org/10.1016/0025-5408(72)90268-1

[22] Carpenter, L.G. and Kirby, P.Y. (1982) *Journal of Physics D*, **15**, 1143. https://doi.org/10.1088/0022-3727/15/7/009

[23] Ma, H., Lin, S.H., Carpenter, W., Rice, P. and Sankey, O.F. (1993) *Journal of Applied Physics*, **73**, 7422. https://doi.org/10.1063/1.353983

[24] Catellani, A., Posternak, M., Baldereschi, A. and Freeman, A.J. (1987) *Physical Review B*, **36**, 6105. https://doi.org/10.1103/PhysRevB.36.6105

[25] Blasé, X., Rubio, A., Louie, S.G. and Cohen, M.L. (1995) *Physical Review B*, **51**, 6868. https://doi.org/10.1103/PhysRevB.51.6868

[26] Xu, Y. N. and Ching, W.Y. (1991) *Physical Review B*, **44**, 7789.

[27] Furthmuller, J., Hafner, J. and Kresse, G. (1994) *Physical Review B*, **50**, 15606. https://doi.org/10.1103/PhysRevB.50.15606

[28] Park, K.T., Terakura, K. and Hamada, N.J. (1987) *Journal of Physics C: Solid State Physics*, **20**, 1241. https://doi.org/10.1088/0022-3719/20/9/014

[29] Catellani, A., Posternak, M., Baldereschi, A., Jansen, H.J.F. and Freeman, A.J. (1985) *Physical Review B*, **32**, 6997. https://doi.org/10.1103/PhysRevB.32.6997

[30] Arnaud, B., Lebegue, S., Rabiller, P. and Alouani, M. (2006) *Physical Review Letters*, **96**, Article ID: 026402. https://doi.org/10.1103/PhysRevLett.96.026402

[31] Ooi, N., Rainkar, A., Lindsley, L. and Adams, J.B. (2006) *Journal of Physics: Condensed Matter*, **18**, 97. https://doi.org/10.1088/0953-8984/18/1/007

[32] Topsakal, M., Akturk, E. and Ciratci, S. (2009) *Physical Review B*, **79**, Article ID: 115442. https://doi.org/10.1103/PhysRevB.79.115442

[33] Arnaud, B., Lebegue, S. and Alouani, M. (2005) *Physical Review B*, **71**, Article ID: 035308. https://doi.org/10.1103/PhysRevB.71.035308

[34] Bagayoko, D. (2014) *AIP Advances*, **4**, Article ID: 127104. https://doi.org/10.1063/1.4903408

[35] Bagayoko, D., Zhao, G.L., Fan, J.D. and Wang, J.T. (1998) *Journal of Physics: Condensed Matter*, **10**, 5645. https://doi.org/10.1088/0953-8984/10/25/014

[36] Bagayoko, D., Zhao, G.L. and William, T.D. (1999) *Physical Review B*, **60**, 1563-1572. https://doi.org/10.1103/PhysRevB.60.1563

[37] Ekuma, C.E., Bagayoko, D., Jarell, M. and Moreno, J. (2012) *AIP Advances*, **2**, Article ID: 032163. https://doi.org/10.1063/1.4751260

[38] Ekuma, C.E., Franklin, L., Jarell, M., Moreno, J., Zhao, G.L., Wang, J.T. and Bagayoko, D. (2012) *Materials Chemistry and Physics*, **136**, 1137-1142. https://doi.org/10.1016/j.matchemphys.2012.08.066

[39] Franklin, L., Zhao, G.L. and Bagayoko, D. (2004) *Journal of Applied Physics*, **96**, 4297-4301. https://doi.org/10.1063/1.1790064

[40] Jin, H., Zhao, G.L. and Bagyoko, D. (2007) *Journal of Applied Physics*, **101**, Article ID: 033123. https://doi.org/10.1063/1.2435802

[41] Bagayoko, D., Franklin, L., Zhao, G.L. and Jin, H. (2008) *Journal of Applied Physics*, **103**, Article ID: 096101. https://doi.org/10.1063/1.2908179

[42] Ceperley, D.M. and Alder, B. (1980) *Physical Review Letters*, **45**, 566. https://doi.org/10.1103/PhysRevLett.45.566

[43] Vosko, S.H., Wilk, L. and Nusair, M. (1980) *Canadian Journal of Physics*, **58**, 1200. https://doi.org/10.1139/p80-159

[44] Feibelman, P.J., Appelbaum, J.A. and Hamann, D.R. (1979) *Physical Review B*, **20**, 1433. https://doi.org/10.1103/PhysRevB.20.1433

[45] Harmon, B.N., Weber, W. and Hamann, D.R. (1982) *Physical Review B*, **25**, 1109. https://doi.org/10.1103/PhysRevB.25.1109

[46] Bagayoko, D. and Franklin, L. (2005) *Journal of Applied Physics*, **97**, Article ID: 123708. https://doi.org/10.1063/1.1939069

[47] Bagayoko, D. and Zhao, G.L. (2000) *New Journal of Physics*, **2**, 16. https://doi.org/10.1088/1367-2630/2/1/316

[48] Bagayoko, D. and Zhao, G.L. (2004) *Journal of Applied Physics*, **96**, 4297-4301. https://doi.org/10.1063/1.1790064

[49] Bagayoko, D., Ekuma, C.E., Jarrel, M. and Morreno, J. (2013) *Physics Letters A*, **337**,

2172-2176. https://doi.org/10.1016/j.physleta.2013.05.043

[50] Bagayoko, D., Zhao, G.L., Franklin, L. and Ekuma, C.E. (2013) *Journal of Physics and Chemistry of Solids*, **74**, 729-736. https://doi.org/10.1016/j.jpcs.2013.01.013

[51] Stewart, A., Hart, D., Khamala, B., Malovzosky, Y. and Bagayoko, D. (2015) *Journal of Advances in Physics*, **9**, 2277-2286.

Journal of Modern Physics, 2020, 11, 944-951
https://www.scirp.org/journal/jmp
ISSN Online: 2153-120X
ISSN Print: 2153-1196

Relativistic Reduction of the Electron-Nucleus Force in Bohr's Hydrogen Atom and the Time of Electron Transition between the Neighbouring Quantum Energy Levels

Stanisław Olszewski

Institute of Physical Chemistry, Polish Academy of Sciences, Warsaw, Poland
Email: olsz@ichf.edu.pl

How to cite this paper: Olszewski, S. (2020) Relativistic Reduction of the Electron-Nucleus Force in Bohr's Hydrogen Atom and the Time of Electron Transition between the Neighbouring Quantum Energy Levels. *Journal of Modern Physics*, **11**, 944-951.
https://doi.org/10.4236/jmp.2020.116058

Received: May 7, 2020
Accepted: June 21, 2020
Published: June 24, 2020

Abstract

The aim of the paper is to get an insight into the time interval of electron emission done between two neighbouring energy levels of the hydrogen atom. To this purpose, in the first step, the formulae of the special relativity are applied to demonstrate the conditions which can annihilate the electrostatic force acting between the nucleus and electron in the atom. This result is obtained when a suitable electron speed entering the Lorentz transformation is combined with the strength of the magnetic field acting normally to the electron orbit in the atom. In the next step, the Maxwell equation characterizing the electromotive force is applied to calculate the time interval connected with the change of the magnetic field necessary to produce the force. It is shown that the time interval obtained from the Maxwell equation, multiplied by the energy change of two neighbouring energy levels considered in the atom, does satisfy the Joule-Lenz formula associated with the quantum electron energy emission rate between the levels.

Keywords

Hydrogen Atom, The Bohr Model, Lorentz Transformation Done with the Aid of the Electron Orbital Speed, Maxwell Equation Applied to Calculate the Time Interval of Electron Transitions between Two Quantum Energy Levels, Comparison with the Joule-Lenz Law for Energy Emission

1. Introduction

In an application of the Bohr model to the energy spectrum of the atomic hydrogen, the electric field—acting between the electron and nucleus—plays a do-

minant role; see e.g. [1]. Nevertheless the magnetic field—due to circulation of the electron along its orbit—though it does not enter the spectral calculations, can be important for the Lorentz transformations of different kind applied to the vector fields active in the atom. For, in some previous paper [2], we noticed that quantum properties of the magnetic field

$$B_n = \frac{e^3 m^2 c}{\hbar^3 n^3} \tag{1}$$

can be also applied in calculating the energy quanta of the electron in the hydrogen atom. These quanta of energy can be obtained when the magnetic moments associated with the circulating electron particle are interacting with corresponding quanta of the magnetic field. In effect of that interaction the spectrum of the energy levels identical to that known from the Bohr atom can be calculated.

Another application of B_n in (1)—taken into account together with the quanta E_n of the electric field acting between the nucleus and electron—concerns the calculation of the drift velocity of electron possessed in the hydrogen atom; see [2] [3].

Evidently E_n—when multiplied by the electron charge $-e$—gives the attractive force between the nucleus of charge e and the electron having charge $-e$:

$$-eE_n = -\frac{mv_n^2}{r_n}; \tag{2}$$

see [4]. The right-hand side of (2) is the centripetal force which provides us with an equilibrium of the electron motion along a circular orbit having the radius [4]

$$r_n = \frac{n^2\hbar^2}{me^2} \tag{3}$$

and the speed [4]

$$v_n = \frac{e^2}{n\hbar}. \tag{4}$$

In the result of (2)-(4) we obtain the electric field

$$E_n = \frac{mv_n^2}{er_n} = m\frac{e^3}{n^2\hbar^2}\frac{me^2}{n^2\hbar^2} = \frac{m^2e^5}{n^4\hbar^4}. \tag{5}$$

In [5] we have shown that a classical Lorentz force—which combines both E_n and B_n at the same time—can attain zero on condition both electric and magnetic fields are represented by parameters characteristic for some electron orbit n. The first aim of the present paper—being a supplement of [5]—is to point out that E_n can be reduced to zero due to a suitable Lorentz transformation done in the presence of B_n. In effect we find with the use of one of the Maxwell equations that the time interval seeked for the electron transition can be obtained in terms of both the electric and magnetic field intensities characte-

ristic for some quantum state in the atom.

2. Lorentz Transformation of the Electric and Magnetic Field Present in the Hydrogen Atom

If the velocity v_L entering the Lorentz transformation is relatively small in comparison with the speed of light c [6], so

$$v_L \ll c, \tag{6}$$

the components of the transformation matrix which are [6]

$$\left(F_{ik}\right)=\begin{pmatrix} 0 & B_z & -B_y & -iE_x \\ -B_z & 0 & B_x & -iE_y \\ B_y & -B_x & 0 & -iE_z \\ iE_x & iE_y & iE_z & 0 \end{pmatrix} \tag{7}$$

can be simplified into the approximate expressions

$$\begin{aligned} &E_x = E_x', \quad E_y = E_y' + \frac{v_L}{c}B_z', \quad E_z = E_z' - \frac{v_L}{c}B_y', \\ &B_x = B_x', \quad B_y = B_y' - \frac{v_L}{c}E_z', \quad B_z = B_z' + \frac{v_L}{c}E_y', \end{aligned} \tag{8}$$

The primes indicate the components of the transformed field.

The formulae entering (8) and (9) can be combined into the vector relations

$$\boldsymbol{E} = \boldsymbol{E}' + \frac{1}{c}\left[\boldsymbol{B}' \times \boldsymbol{v}_L\right], \tag{9}$$

$$\boldsymbol{B} = \boldsymbol{B}' - \frac{1}{c}\left[\boldsymbol{E}' \times \boldsymbol{v}_L\right]. \tag{10}$$

Formally there exist two kinds of the transformation possibilities which reduce the external fields to zero [6]:

$$\left(\mathrm{a}\right) \qquad \boldsymbol{B}' = 0 \tag{11a}$$

which implies

$$\boldsymbol{B}^{(\mathrm{a})} = \frac{1}{c}\left[\boldsymbol{v}_L \times \boldsymbol{E}\right], \tag{11b}$$

or

$$\left(\mathrm{b}\right) \qquad \boldsymbol{E}' = 0 \tag{12a}$$

which implies

$$\boldsymbol{E}^{(\mathrm{b})} = -\frac{1}{c}\left[\boldsymbol{v}_L \times \boldsymbol{B}\right]. \tag{12b}$$

From the calculations done in Sec. 3 it becomes evident that

$$\left|\boldsymbol{B}\right| \gg \left|\boldsymbol{E}\right|, \tag{13}$$

so we examine solely the case of (b) in (12a).

As the size of the transformation speed v_L we assume

$$\left|v_L\right| = \left|v_n\right| = \frac{e^2}{n\hbar} \tag{14}$$

given in (4). Because the direction of $\boldsymbol{v}_n$ is normal to that of B_n, we obtain in this case from (12b) the result

$$E_n^{(\mathrm{b})} = -\frac{1}{c} v_n B_n = -\frac{1}{c}\frac{e^2}{n\hbar}\frac{e^3 m^2 c}{\hbar^3 n^3} = -\frac{e^5 m^2}{n^4 \hbar^4} \tag{15a}$$

which is the size of the electric field acting on the electron located on the orbit n, but having an opposite sign than E_n in (5). In effect the field in (5) added to the correcting term in (15a) give the Lorentz force equal to zero:

$$e\boldsymbol{E}_n - \frac{e}{c}\left[\boldsymbol{B}_n \times \boldsymbol{v}_n\right] = 0. \tag{15b}$$

3. Equation for the Field Invariants and Its Solution

The matrix (6) can be applied in solving the equation

$$\left|F_{ik} - \lambda\delta_{ik}\right| = 0 \tag{16}$$

the solution of which gives the invariants λ; see [6]. A substitution of the components F_{ik} entering (7) into (16) provides us with the equation

$$\lambda^4 + \lambda^2\left(\boldsymbol{B}^2 - \boldsymbol{E}^2\right) - \left(\boldsymbol{B}\cdot\boldsymbol{E}\right)^2 = \lambda^4 + \lambda^2\left(\boldsymbol{B}^2 - \boldsymbol{E}^2\right) = 0. \tag{17}$$

The last step on the left of (17) holds because the field $\boldsymbol{B}$ is normal to $\boldsymbol{E}$.

Evidently a substitution of

$$\boldsymbol{B}^2 = B_n^2 = \frac{e^6 m^4 c^2}{n^6 \hbar^6}, \tag{18}$$

and of $E_n = E_n^{(\mathrm{b})}$ from (15a), so

$$\boldsymbol{E}^2 = E_n^2 = \frac{e^{10} m^4}{n^8 \hbar^8}, \tag{19}$$

gives

$$\boldsymbol{B}^2 - \boldsymbol{E}^2 = B_n^2 - E_n^2 = \frac{e^6 m^4 c^2}{n^6 \hbar^6} - \frac{e^{10} m^4}{n^8 \hbar^8} = \frac{e^6 m^4 c^2}{n^6 \hbar^6}\left(1 - \frac{e^4}{n^2 c^2 \hbar^2}\right). \tag{20}$$

Since the atomic constant is equal to

$$\frac{e^2}{c\hbar} \cong \frac{1}{137.04}, \tag{21}$$

we obtain in (20) the relation

$$B_n^2 \gg E_n^2. \tag{22}$$

For example for $n = 1$ the first term entering the bracket expression in (20) is more than 10^4 times larger than the second term.

This makes (17) transformed into the expression

$$\lambda^2 = -\left(B_n^2 - E_n^2\right) < 0 \tag{23}$$

equal to a negative number which implies an imaginary λ.

4. Reduction of the Lorentz Force and Its Effect on the Electromotive Force Acting on the Electron in the Hydrogen Atom

A basic content of the Maxwell equation which provides us with a combination

of the electric field, magnetic field and an interval of time is [7]

$$\oint \boldsymbol{E}_c \mathrm{d}\boldsymbol{l} = -\frac{\partial}{c\partial t}\int \boldsymbol{B}\mathrm{d}\boldsymbol{f}. \tag{24}$$

On the left-hand side of (24) there is presented the integral of a non-vanishing electric field $\boldsymbol{E}_c$ performed along a closed contour line which—in the present case—is the cross-section line of the electron orbit normal to the orbit axis; on the right-hand side we have a time derivative of the integral concerning the magnetic field vector $\boldsymbol{B}$ enclosed by the contour mentioned on the left-hand side of (24); t is time and c is a speed of light.

We assume that field $\boldsymbol{B}$ for some quantum state n is a constant equal to (1). On the other hand, $\boldsymbol{E}_c$ is a non-vanishing electric field along the contour; the field size

$$\left|\boldsymbol{E}_c\right| = \left|\boldsymbol{E}^{(\mathrm{b})}\right| = E_{cn} = \frac{e^5 m^2}{n^4 \hbar^4} \tag{25}$$

is given in (15a). The contour, being a cross-section line of the electron orbit, can be identified with a circumference of the electron microparticle; see below (27).

The only simplification we apply in (24) is the replacement

$$\frac{\partial}{\partial t} \to \frac{1}{\Delta t}, \tag{26}$$

so Δt becomes the time interval dividing the integral given on the right-hand side of (24).

The electron particle is moving about the atomic nucleus along a circular orbit n, but for any n we have the same length of the cross-section line of the orbit namely

$$\oint \mathrm{d}\boldsymbol{l} = 2\pi r_{el} \cong 2\pi \frac{e^2}{mc^2} \tag{27}$$

where r_{el} is the radius of the electron particle given in [7]:

$$r_{el} \cong \frac{e^2}{mc^2}. \tag{28}$$

In effect the area enclosing the electron orbit becomes

$$\int \mathrm{d}\boldsymbol{f} = 2\pi r_{el} 2\pi r_n. \tag{29}$$

The expression on the right of (29) is approximately equal to a surface of a cylinder having its length equal to the orbit length equal to

$$2\pi r_n \tag{30}$$

and the circumference of the cylinder is assumed to be equal to (27).

In effect, by neglecting the negative sign in (24), we obtain from the Maxwell equation the formula

$$E_{cn} 2\pi r_{el} \cong \frac{1}{c\Delta t} B_n 2\pi r_{el} 2\pi r_n, \tag{31}$$

or

$$E_{cn} \cong \frac{1}{c\Delta t} B_n 2\pi r_n. \tag{32a}$$

This relation, because of (1) and (25), is equivalent to

$$\frac{e^5 m^2}{n^4 \hbar^4} \cong \frac{1}{c\Delta t} \frac{e^3 m^2 c}{\hbar^3 n^3} 2\pi \frac{n^2 \hbar^2}{me^2}. \tag{32b}$$

Therefore

$$\Delta t \cong \frac{e^3}{\hbar^3 n^3} \frac{n^4 \hbar^4}{e^5} 2\pi \frac{n^2 \hbar^2}{me^2} = 2\pi \frac{n^3 \hbar^3}{me^4}. \tag{33}$$

This result is identical to the time interval associated with the electron transition between neighbouring quantum levels obtained earlier (see [8]) on the basis of an examination of the dynamical properties characteristic for the electron particle moving in the Bohr's hydrogen atom.

5. Comparison with the Joule-Lenz Law Coupling the Time and Energy of the Quantum Transitions

The energy ΔE emitted between two quantum levels $n+1$ and n is coupled with the emission time Δt (see [9] [10] [11]) by the formula

$$\Delta E \Delta t = h \tag{34}$$

derived with the aid of the quantum reasoning applied to the Joule-Lenz law of the energy emission in classical thermodynamics [12].

The size of the time emission interval Δt in case of the hydrogen atom is calculated in (33). In the next step, the energy interval between two neighbouring quantum levels becomes

$$\begin{aligned} \Delta E = E_{n+1} - E_n &= -\frac{me^4}{2\hbar^2}\left[\frac{1}{(n+1)^2} - \frac{1}{n^2}\right] \\ &\cong \frac{me^4}{2\hbar^2} \frac{(n+1)^2 - n^2}{n^2 (n+1)^2} \cong \frac{me^4}{2\hbar^2} \frac{2n}{n^4} = \frac{me^4}{\hbar^2 n^3}. \end{aligned} \tag{35}$$

Therefore we obtain for the product entering (34) the result

$$\Delta E \Delta t = \frac{me^4}{\hbar^2 n^3} 2\pi \frac{\hbar^3 n^3}{e^4 m} = 2\pi\hbar = h \tag{36}$$

which is identical to that given in (34). Evidently the energy symbols E_{n+1} and E_n in (35) should not be confused with the electric field strength in (5), (15a) and (25).

6. Summary

The aim of the paper was to get an insight into the time interval connected with the electron transition between two neighbouring quantum energy levels in the hydrogen atom. To this purpose a non-probabilistic approach to the quantum atomic levels characteristic for the Bohr semiclacssical theory became useful.

This is so because such approach allowed us to apply the classical Maxwell electrodynamics in describing the electron behaviour on the orbits present in the atom.

In result, in the first step, the paper demonstrates that when the size of the velocity v_L entering the Lorentz transformation amounts the size v_n of the electron speed along some orbit n in the hydrogen atom, the effect of transformation reduces the electric field E_n by the term $-E_n$ making the electric field between the electron and nucleus equal to zero. The presence of a corresponding magnetic field in the atom normal to the orbit n [see (1)] is essential for the effect.

In the second step of the paper the Maxwell equation for the electromotive force joining the electric and magnetic field with the time interval of the electron transition is taken into account. In this case the presence of a non-zero electric field active along the cross-section line of the electron orbit is assumed. A characteristic point is that the size of this field, obtained with the aid of the Lorentz transformation making the electrostatic interaction between the electron and atomic nucleus equal to zero, is equal to the size of E_n; see (5) and (15a). The new electric field active along the cross-section of the orbit is much smaller than the magnetic field normal to the orbit plane.

When a substitution of the both—electric and magnetic—fields to the Maxwell equation is done, the time interval for the electron transition due to the electromotive force is found. This interval is very close to the time intervals obtained earlier from an analysis of the dynamical properties of the electron in the hydrogen atom (see [8]), or on the basis of an examination of the Ehrenfest adiabatic invariants; see [11]. In a final step it is shown that the product of intervals of transition time and that of energy between two neighbouring states in the hydrogen atom does satisfy the quantum formula for the Joule-Lenz energy emission in that atom; see (34) and (36).

Conflicts of Interest

The author declares no conflicts of interest regarding the publication of this paper.

References

[1] Bohr, N. (1922) The Theory of Spectra and the Atomic Constitution. Cambridge University Press, Cambridge, UK.

[2] Olszewski, S. (2016) *Reviews in Theoretical Science*, **4**, 336-352. https://doi.org/10.1166/rits.2016.1066

[3] Olszewski, S. (2014) *Journal of Modern Physics*, **5**, 2022-2029. https://doi.org/10.4236/jmp.2014.518198

[4] Sommerfeld, A. (1931) Atombau und Spektrallinien. Vol. 1, 5th Edition, Braunschweig.

[5] Olszewski, S. (2019) *Journal of Modern Physics*, **10**, 717-724. https://doi.org/10.4236/jmp.2019.107051

[6] Landau, L.D. and Lifshitz, E.M. (1948) The Field Theory. 2nd Edition, OGIZ, Mos-

cow. (In Russian)

[7] Landau, L.D. and Lifshitz, E.M. (1969) Lifshits, Mechanics. Electrodynamics, Izd. Nauka, Moscow. (In Russian)

[8] Olszewski, S. (2019) *Journal of Modern Physics*, **10**, 1522-1531. https://doi.org/10.4236/jmp.2019.1013101

[9] Olszewski, S. (2015) *Journal of Modern Physics*, **6**, 1277-1288. https://doi.org/10.4236/jmp.2015.69133

[10] Olszewski, S. (2017) *Journal of Modern Physics*, **7**, 162-174. https://doi.org/10.4236/jmp.2016.71018

[11] Olszewski, S. (2020) *Journal of Quantum Information Science*, **10**, 1-9. https://doi.org/10.4236/jqis.2020.101001

[12] Lass, H. (1950) Vector and Tensor Analysis. McGraw-Hill, New York. https://doi.org/10.1119/1.1932684

Journal of Modern Physics, 2020, 11, 952-966
https://www.scirp.org/journal/jmp
ISSN Online: 2153-120X
ISSN Print: 2153-1196

There Also Can Be Fuzziness in Quantum States Itself—Breaking through the Framework and the Principle of Quantum Mechanics

Wenbing Qiu

Department of Physics, Faculty of Science, Shihezi University, Shihezi, China
Email: 2962546794@qq.com

How to cite this paper: Qiu, W.B. (2020) There Also Can Be Fuzziness in Quantum States Itself—Breaking through the Framework and the Principle of Quantum Mechanics. *Journal of Modern Physics*, **11**, 952-966.
https://doi.org/10.4236/jmp.2020.116059

Received: April 9, 2020
Accepted: June 29, 2020
Published: June 30, 2020

Abstract

In this paper, an attempt is made to synthesize fuzzy mathematics and quantum mechanics. By using the method of fuzzy mathematics to blur the probability (wave) of quantum mechanics, the concept of fuzzy wave function is put forward to describe the fuzzy quantum probability. By applying the non-fuzzy formula of fuzzy quantity and Schrödinger wave equation of quantum mechanics, the membership function equation is established to describe the evolution of the fuzzy wave function. The concept of membership degree amplitude is introduced to calculate fuzzy probability amplitude. Some important concepts in fuzzy mathematics are also illustrated.

Keywords

Fuzzy Quantum Probability, Fuzzy Wave Function, Membership Function, Membership Degree Amplitude, Fuzzy Probability Amplitude

1. Introduction

The research on combining fuzzy mathematics and quantum mechanics has been done in the prior work [1]-[8]. These theories, which are using fuzzy mathematics to understand quantum mechanics, can be regarded as the equivalent theory of quantum mechanics. They do not break through quantum mechanics.

In order to be able to break through quantum mechanics and find a deeper principle of the universe, in this article a mathematical theory named "fuzzy quantum probability" is proposed. Different from the prior theories, the theory in this paper is not using fuzzy mathematics to understand quantum mechanics, but using fuzzy mathematics to fuzzify the state function of quantum mechanics so that a fuzzy (unsharp) probability can be obtained. This work is not

the equivalent theory of quantum mechanics but a breaking through quantum mechanics.

In a sense, quantum mechanics is a theory of probability (so-called "quantum probability"). This kind of probability is different from the classical probability in the traditional mathematical probability and statistics theory. It is a kind of probability associated with volatility and calculated by wave function.

After the birth of fuzzy mathematics, people use the method of fuzzy mathematics to fuzzify classical probability to obtain fuzzy probability (the probability of uncertain and imprecise values, also called "language probability"). Then, can we use the method of fuzzy mathematics to also blur quantum probability to obtain fuzzy quantum probability (see Figure 1)?

In fuzzy mathematics there are two directions for developing classical probability into fuzzy probability: one is to introduce fuzziness into the event, whereas the probability is clear or determined, so as to obtain the probability of fuzzy event. The other is to introduce fuzziness into the probability, while the event is clear, so as to obtain the fuzzy probability of the event. Similarly, we also can try to develop quantum probability into fuzzy quantum probability along these two directions. This article is dedicated to the work in the second direction, *i.e.* doing the work of "the fuzzification of quantum probability" with the method of fuzzy mathematics (the work of the first direction will be done in another paper).

The calculation of the quantum probability of the event is realized by means of a wave function, and the value of the quantum probability is obtained by squaring the modulus of the (normalized) wave function. Therefore, it can be assumed that the fuzzification of the quantum probability should first be the fuzzification of the wave function (state function), and the value of the fuzzy quantum probability can be obtained by the square of the modulus of the fuzzy wave function. The concept of fuzzy wave function was first put forward by Markus Müller [9], but he did not conduct in-depth research. In this paper I will discuss the mathematical description of fuzzy wave function in detail and how to calculate out a fuzzy quantum probability of the event from fuzzy wave function. In addition, the evolution equation of fuzzy wave function also is established.

As the Russian mathematician Lobachevsky said, any branch of mathematics, no matter how abstract it is, will one day find applications in the real world. As the application of fuzzy mathematical methods to quantum mechanical probabilities, the theory of fuzzy quantum probabilities will eventually be applied in

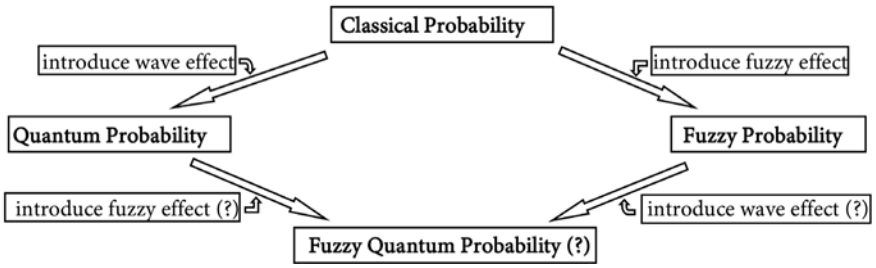

Figure 1. This figure shows the logical clues to the development of probability theory.

reality one day even though now we cannot find its specific application. Fuzzy quantum probability is mainly used to describe and compute the probability that is difficult to accurately estimate. Then, where could there be such a kind of probability? Maybe in the field of particle decay, maybe in the field of economics and finance, maybe in small closed regions of space as proposed by Markus Müller in his paper, ... One day, we will find a place where fuzzy quantum probability comes into play.

In this paper, fuzzy wave function and fuzzy quantum probability (density) are discussed in Section 2. The equation of the membership function of the fuzzy wave function is established in Section 3. In Section 4, the concept of membership degree amplitude is introduced and discussed. Fuzzy probability amplitude is also discussed in this Section. Lastly, in **Appendix 1** the list of the used variables in the paper is provided, whereas in **Appendix 2** some important concepts pertaining to the fuzzy mathematics are illustrated.

2. Fuzzy Wave Function

Usually, in quantum mechanics it is thought that the value of the probability for the event $(\vec{r},t)$ is clear and certain, correspondingly, the probability wave $\psi(\vec{r},t)$ also is clear and certain. However, if the probability value is unsharp or imprecise, this kind of probability should be described by fuzzy number. Correspondingly, the probability wave also should be depicted by fuzzy plural. Such a fuzzy wave function is denoted by $\tilde{\psi}(\vec{r},t)$ (fuzzification plural function). According to fuzzy mathematics, $\tilde{\psi}(\vec{r},t)$ is depicted by a membership function $\lambda_{\tilde{\psi}}(\psi,\vec{r},t)\in[0,1]$, where ψ is one of all possible values of $\tilde{\psi}(\vec{r},t)$. Here it should be pointed out that ψ is an independent variable, the variety of which no longer depends on the event $(\vec{r},t)$ because the value of fuzzy wave function is uncertain. This is similar to the case in quantum mechanics, where the coordinate $\vec{r}$ is an independent variable, the variety of which no longer relies on the time t because the value of the coordinate is uncertain. From classical mechanics to quantum mechanics, and then to fuzzy quantum probability, the relationship between variables and the changes in the status of variables can be seen in **Figure 2**.

The membership function $\lambda_{\tilde{\psi}}(\psi,\vec{r},t)$ tells us about the distribution of the membership degrees of all possible values of the fuzzy probability wave about the event $(\vec{r},t)$. The meaning of the fuzzy wave function depicted by the membership function is showed in **Figure 3**.

$\tilde{\psi}(\vec{r},t)$ can be represented as

$$\tilde{\psi}(\vec{r},t)=\int_{\psi\in C}\lambda_{\tilde{\psi}}(\psi,\vec{r},t)\Big/(\psi,\vec{r},t).$$

Here C is the plural set. The symbol "$\int$" does not represent integration but a sign, whereas "/" does not represent division but a kind of corresponding symbol.

The normalization problem of $\tilde{\psi}(\vec{r},t)$ will be discussed in Section 4.

Now it should be considered how to calculate fuzzy probability from $\tilde{\psi}(\vec{r},t)$. This is by means of the membership function. The specific approach is considered as follows:

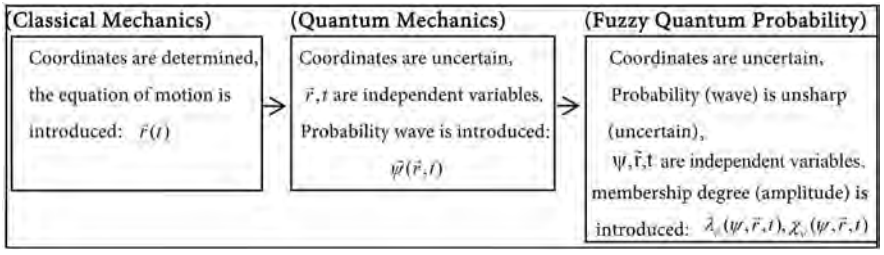

Figure 2. This figure shows that quantum mechanics breaks through the principle of classical mechanics by replacing certainty with probability, while fuzzy quantum probability breaks through the principle of quantum mechanics by replacing clarity with ambiguity (using the uncertainty of probability (wave) to replace the certainty of probability (wave)).

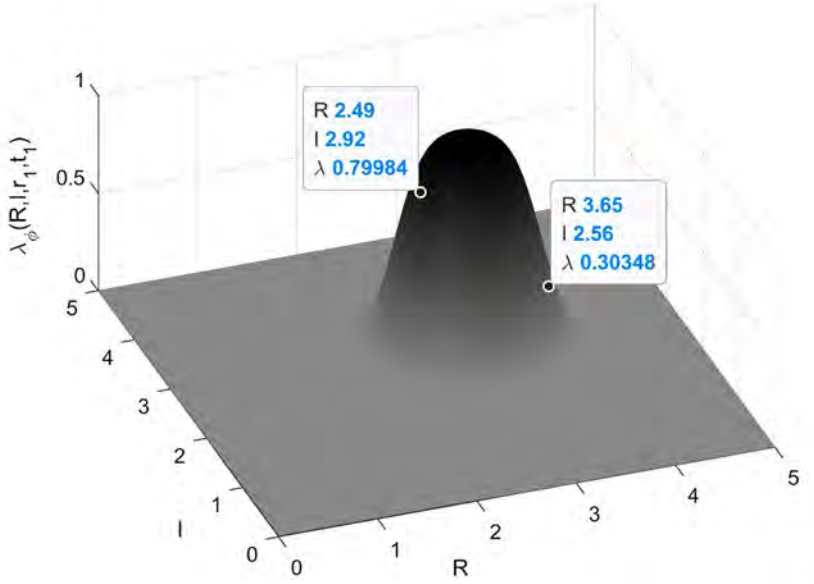

Figure 3. This figure shows that the normalized fuzzy probability wave of a specific event $(\vec{r}_1,t_1)$ takes much possible plural values, and each value has a (generally different) degree of membership (credibility or truth). For instance, if $\tilde{\psi}(\vec{r}_1,t_1)$ is depicted by such a membership function with the form as follow:

$$\lambda_{\tilde{\psi}}(R,I,\vec{r},t) = \frac{1}{2\pi\sigma^2}\exp\left\{-\frac{1}{2\sigma^2}\left[\left(R^2-I^2-R_0^2(\vec{r},t)+I_0^2(\vec{r},t)\right)^2+4\left(RI-R_0(\vec{r},t)I_0(\vec{r},t)\right)^2\right]\right\},$$

the credibility of $\tilde{\psi}(\vec{r}_1,t_1)$ taking one value $2.49+i2.92$ is 0.79984, while that of $\tilde{\psi}(\vec{r}_1,t_1)$ taking another value $3.65+i2.56$ is 0.30348.

Calculating the fuzzy quantum probability of the event $(\vec{r},t)$ is by computing $\left|\tilde{\psi}(\vec{r},t)\right|^2$;

Calculating $\left|\tilde{\psi}(\vec{r},t)\right|^2$ is by computing $\left|\tilde{\psi}(\vec{r},t)\right|$;

Order $\tilde{\rho}=\left|\tilde{\psi}(\vec{r},t)\right|$, *i.e.* $\tilde{\rho}$ represents the (fuzzy) modulus of the fuzzy wave function of the event $(\vec{r},t)$. Then calculating $\left|\tilde{\psi}(\vec{r},t)\right|$ is by determining the membership function $\alpha(\rho,\vec{r},t)$ of $\tilde{\rho}$. Here ρ, the membership degree of which is α, represents a possible value of $\tilde{\rho}$.

$\alpha(\rho,\vec{r},t)$ can be computed from $\lambda_{\tilde{\psi}}(\psi,\vec{r},t)$, and the specific method is as

follows:

Order $\psi = \rho e^{i\varphi}$ (or $\psi = R + iI$), then $\lambda_{\tilde{\psi}}(\psi, \vec{r}, t)$ can be equivalently rewritten as $\lambda_{\tilde{\psi}}(\rho, \varphi, \vec{r}, t)$ (or $\lambda_{\tilde{\psi}}(R, I, \vec{r}, t)$). Thus, $\alpha(\rho, \vec{r}, t)$ is determined from $\lambda_{\tilde{\psi}}(\rho, \varphi, \vec{r}, t)$. Then how to determine the value of $\alpha(\rho, \vec{r}, t)$? About $\lambda_{\tilde{\psi}}(\rho, \varphi, \vec{r}, t)$, it is usually such a case that for the specified event $(\vec{r}, t)$, one value of ρ corresponds to much different values of membership degree because of the variation of φ. $\alpha(\rho, \vec{r}, t)$ should take the maximal value of membership degree according to the assignment rule of the membership degree of the possible value of fuzzy number in fuzzy mathematics. For instance, suppose when $\varphi = \varphi_0$, $\lambda_{\tilde{\psi}}(\rho, \varphi, \vec{r}, t)$ takes maximum value $\lambda_{\tilde{\psi}}^{\max}(\rho, \varphi_0, \vec{r}, t)$. Then, $\alpha(\rho, \vec{r}, t)$ can be assigned the value $\lambda_{\tilde{\psi}}^{\max}(\rho, \varphi_0, \vec{r}, t)$, *i.e.*

$$\alpha = \alpha(\rho, \vec{r}, t) = \lambda_{\tilde{\psi}}^{\max}(\rho, \varphi_0, \vec{r}, t). \quad \text{(see Figure 4)}$$

Thus, the membership function of $\tilde{\rho}$ has been got.

By using $\alpha(\rho, \vec{r}, t)$, the membership function of the fuzzy wave strength $\tilde{I}(\vec{r}, t) = |\tilde{\psi}(\vec{r}, t)|^2$ can be obtained

$$\alpha = \alpha(\rho, \vec{r}, t) = \alpha\left(\sqrt{I}, \vec{r}, t\right) = f(I, \vec{r}, t),$$

where I, the membership degree of which is α, represents a possible value of the fuzzy wave strength $\tilde{I}$ of the event $(\vec{r}, t)$.

By using $f(I, \vec{r}, t)$, the fuzzy quantum probability (density) of the event $(\vec{r}, t)$ can be obtained. The specific method is as follows:

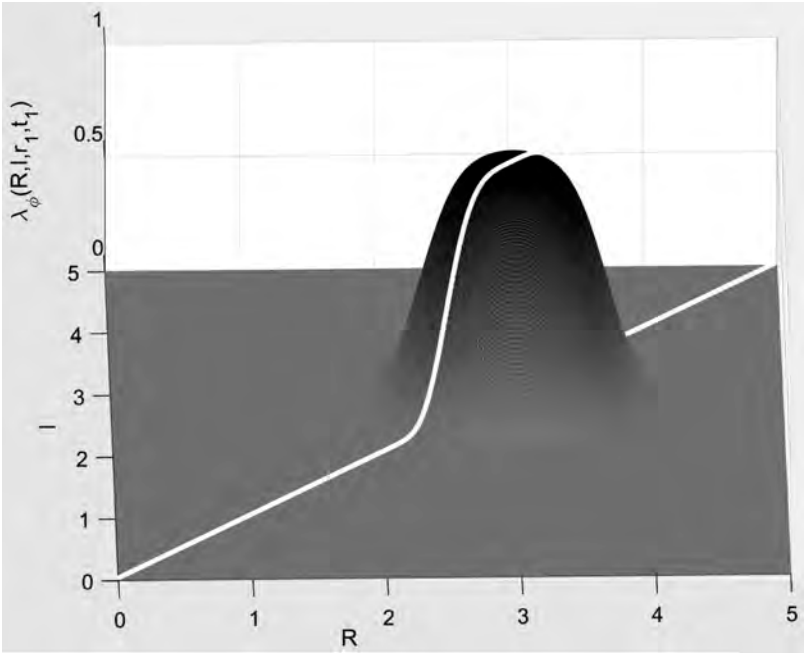

Figure 4. This figure shows how the membership function of $|\tilde{\psi}(\vec{r}_1, t_1)|$ of a specific event $(\vec{r}_1, t_1)$ is determined from that of $\tilde{\psi}(\vec{r}_1, t_1)$ (this fuzzy wave function is mentioned in Figure 3). This is by finding the maximum value of $\lambda_{\tilde{\psi}}(\rho, \varphi, \vec{r}_1, t_1)$ in the case of a fixed value of ρ. The bright white line in the figure is the function curve of $\alpha(\rho, \vec{r}_1, t_1)$.

$$\alpha = f\left(I,\vec{r},t\right) \to I = f^{-1}\left(\alpha,\vec{r},t\right) = I_\alpha\left(\vec{r},t\right).$$

This is a possible function form (the membership degree of this form is α) of the fuzzy wave strength $\tilde{I}\left(\vec{r},t\right)$.

From $I_\alpha\left(\vec{r},t\right)$, one possible quantum probability (density) (the membership degree of this quantum probability (density) is α) of the event $\left(\vec{r},t\right)$ can be derived

$$\omega_\alpha\left(\vec{r},t\right) = C_\alpha I_\alpha\left(\vec{r},t\right).$$

where C_α is the normalization constant.

Thus, the fuzzy quantum probability (density) of the event $\left(\vec{r},t\right)$ has been obtained

$$\tilde{\omega}\left(\vec{r},t\right) = \int_{\alpha\in[0,1]} \alpha/\omega_\alpha\left(\vec{r},t\right),$$

In addition, the membership function of $\tilde{\omega}\left(\vec{r},t\right)$ can be easily solved as follows:

Order $\omega = \omega_\alpha\left(\vec{r},t\right) = \omega\left(\alpha,\vec{r},t\right)$, then one can have $\alpha = \omega^{-1}\left(\omega,\vec{r},t\right) = \alpha\left(\omega,\vec{r},t\right)$. This is the membership function for $\tilde{\omega}\left(\vec{r},t\right)$. Thus, $\tilde{\omega}\left(\vec{r},t\right)$ can be rewritten as

$$\tilde{\omega}\left(\vec{r},t\right) = \int_{\alpha\in[0,1]} \alpha\left(\omega,\vec{r},t\right)/\omega.$$

3. The Membership Function Equation

Next, an equation will be established for the membership function $\lambda_{\tilde{\psi}}\left(R,I,\vec{r},t\right)$. The membership function can be normalized, *i.e.* it should satisfy

$$\int_\infty \mathrm{d}R\mathrm{d}I\, \lambda_{\tilde{\psi}}\left(R,I,\vec{r},t\right)/u\left(\vec{r},t\right) = 1, \tag{1}$$

where $u\left(\vec{r},t\right) = \int_\infty \mathrm{d}R\mathrm{d}I\lambda_{\tilde{\psi}}\left(R,I,\vec{r},t\right)$. The normalized membership function reads as

$$\mu_{\tilde{\psi}}\left(R,I,\vec{r},t\right) = \lambda_{\tilde{\psi}}\left(R,I,\vec{r},t\right)/u\left(\vec{r},t\right).$$

Schrödinger equation is $i\hbar\partial_t\overline{\psi} = H\overline{\psi}$. Order $\overline{\psi} = \overline{R} + i\overline{I}$, $H = H_R + iH_I$. Then Schrödinger equation turns into real form

$$\begin{cases} \partial_t\overline{R} = \left(H_I\overline{R} + H_R\overline{I}\right)/\hbar, & (2) \\ \partial_t\overline{I} = \left(-H_R\overline{R} + H_I\overline{I}\right)/\hbar. & (3) \end{cases}$$

As we know, the deterministic mechanical quantity in classical mechanics can be considered as a statistical average of the corresponding indeterministic mechanical quantity in quantum mechanics. Similarly, here one can regard the clear or deterministic wave function in quantum mechanics as the result of the non-fuzzification [10] [11] of fuzzy wave function

$$\begin{cases} \overline{R} = \int_\infty R\mu_{\tilde{\psi}}\left(R,I,\vec{r},t\right)\mathrm{d}R\mathrm{d}I, & (4) \\ \overline{I} = \int_\infty I\mu_{\tilde{\psi}}\left(R,I,\vec{r},t\right)\mathrm{d}R\mathrm{d}I. & (5) \end{cases}$$

Putting (4), (5) into (2) and shifting items, one can obtain

$$\int_{\infty} \mathrm{d}R\mathrm{d}I\left[R\partial_t \mu_{\tilde{\psi}}(R,I,\vec{r},t)-\left(RH_I+IH_R\right)\mu_{\tilde{\psi}}(R,I,\vec{r},t)/\hbar\right]=0.$$

Therefore, the integrand in the bracket is a function whose integral is zero about *R, I.*

Order

$$R\partial_t \mu_{\tilde{\psi}}(R,I,\vec{r},t)-\left(RH_I+IH_R\right)\mu_{\tilde{\psi}}(R,I,\vec{r},t)/\hbar=g_1(R,I,\vec{r},t). \tag{6}$$

Then $g_1(R,I,\vec{r},t)$ satisfies

$$\int_{\infty} \mathrm{d}R\mathrm{d}I g_1(R,I,\vec{r},t)=0.$$

Similarly, by bringing (4) and (5) into (3), one can derive

$$I\partial_t \mu_{\tilde{\psi}}(R,I,\vec{r},t)-\left(IH_I-RH_R\right)\mu_{\tilde{\psi}}(R,I,\vec{r},t)/\hbar=g_2(R,I,\vec{r},t). \tag{7}$$

where $g_2(R,I,\vec{r},t)$ satisfies

$$\int_{\infty} \mathrm{d}R\mathrm{d}I g_2(R,I,\vec{r},t)=0.$$

Order

$$\mu_1(R,I,\vec{r},t)=R\mu_{\tilde{\psi}}(R,I,\vec{r},t),\mu_2(R,I,\vec{r},t)=I\mu_{\tilde{\psi}}(R,I,\vec{r},t).$$

Then (6), (7) can be written as

$$\begin{cases}\partial_t \mu_1(R,I,\vec{r},t)=H_I\mu_1(R,I,\vec{r},t)/\hbar+H_R\mu_2(R,I,\vec{r},t)/\hbar+g_1(R,I,\vec{r},t),\\ \partial_t \mu_2(R,I,\vec{r},t)=H_I\mu_2(R,I,\vec{r},t)/\hbar-H_R\mu_1(R,I,\vec{r},t)/\hbar+g_2(R,I,\vec{r},t).\end{cases}$$

Again order

$$\boldsymbol{\mu}=\begin{pmatrix}\mu_1(R,I,\vec{r},t)\\ \mu_2(R,I,\vec{r},t)\end{pmatrix},\quad \boldsymbol{g}=\begin{pmatrix}g_1(R,I,\vec{r},t)\\ g_2(R,I,\vec{r},t)\end{pmatrix},\quad \boldsymbol{H}=\begin{pmatrix}H_I & H_R\\ -H_R & H_I\end{pmatrix}.$$

Then the above equations about $\mu_1(R,I,\vec{r},t),\mu_2(R,I,\vec{r},t)$ can be simply written in a matrix form

$$\partial_t \boldsymbol{\mu}=\boldsymbol{H}\boldsymbol{\mu}/\hbar+\boldsymbol{g}. \tag{8}$$

This is the membership function equation, which determines the evolution of the fuzzy wave function $\tilde{\psi}(\vec{r},t)$, accompanied by constraints:

$$\begin{cases}I\mu_1(R,I,\vec{r},t)=R\mu_2(R,I,\vec{r},t),\\ \int \mathrm{d}R\mathrm{d}I g_1(R,I,\vec{r},t)=0,\\ \int \mathrm{d}R\mathrm{d}I g_2(R,I,\vec{r},t)=0.\end{cases} \tag{9}$$

Equation (8) is a nonhomogeneous equation. The nonhomogeneous item $\boldsymbol{g}$ can be interpreted as fuzzy source which leads to the blurring and uncertainty of probability and probability wave. If there is no fuzzy source, there is no fuzziness of probability and probability wave, and Equation (8) loses meaning. This point can be proved as follows:

In fact, by ordering $\boldsymbol{g}=0$ in Equation (8), one can obtain

$$\begin{cases} R\partial_t \mu_{\tilde{\psi}}(R,I,\vec{r},t) - (RH_I + IH_R)\mu_{\tilde{\psi}}(R,I,\vec{r},t)/\hbar = 0, \\ I\partial_t \mu_{\tilde{\psi}}(R,I,\vec{r},t) - (IH_I - RH_R)\mu_{\tilde{\psi}}(R,I,\vec{r},t)/\hbar = 0 \end{cases}$$

$$\Rightarrow (RIH_I + I^2 H_R)\mu_{\tilde{\psi}}(R,I,\vec{r},t) = (RIH_I - R^2 H_R)\mu_{\tilde{\psi}}(R,I,\vec{r},t)$$

$$\Rightarrow (I^2 + R^2)H_R \mu_{\tilde{\psi}}(R,I,\vec{r},t) = 0$$

$$\Rightarrow \begin{cases} \mu_{\tilde{\psi}}(R,I,\vec{r},t) = 0, & (\text{when } I^2 + R^2 \neq 0) \\ \mu_{\tilde{\psi}}(R,I,\vec{r},t) \neq 0. & (\text{when } I = R = 0) \end{cases}$$

It can been seen that $\tilde{\psi}(\vec{r},t)$ has only one value $\tilde{\psi}(\vec{r},t) = 0$. This is a meaningless result. Thereby, Equation (8) without fuzzy source is meaningless. So, the equation of the membership function of the fuzzy wave function only can be a nonhomogeneous one.

4. The Membership Degree Amplitude and Fuzzy Probability Amplitude

In order to discuss the normalization of fuzzy wave function and the calculation of fuzzy probability amplitude, a new concept is now introduced, named "membership degree amplitude" $\chi_{\tilde{\psi}}(\psi,\vec{r},t) \in C$ (C is the plural set), the square of the modulus of which denotes the membership degree, *i.e.*

$$\left|\chi_{\tilde{\psi}}(\psi,\vec{r},t)\right|^2 = \lambda_{\tilde{\psi}}(\psi,\vec{r},t) \in [0,1],$$

From $\chi_{\tilde{\psi}}(\psi,\vec{r},t)$, it can be derived that

$$\chi = \chi_{\tilde{\psi}}(\psi,\vec{r},t) \to \psi = \chi_{\tilde{\psi}}^{-1}(\chi,\vec{r},t) = \psi_\chi(\vec{r},t).$$

This is one possible form (the membership degree of this form is $|\chi|^2$) of $\tilde{\psi}(\vec{r},t)$. And $\tilde{\psi}(\vec{r},t)$ can be denoted as

$$\tilde{\psi}(\vec{r},t) = \int_{\forall \chi \in C, |\chi|^2 \in [0,1]} |\chi|^2 / \psi_\chi(\vec{r},t).$$

If for $\forall \chi \in C$, the wave function $\psi_\chi(\vec{r},t)$ is normalized (multiplying by the normalization constant C_χ)

$$\psi_\chi(\vec{r},t) \to \phi_\chi(\vec{r},t) = C_\chi \psi_\chi(\vec{r},t),$$

then the fuzzy wave function $\tilde{\psi}(\vec{r},t)$ is normalized

$$\tilde{\psi}(\vec{r},t) \to \tilde{\phi}(\vec{r},t) = \int_{\forall \chi \in C, |\chi|^2 \in [0,1]} |\chi|^2 / \phi_\chi(\vec{r},t).$$

The membership degree amplitude of $\tilde{\phi}(\vec{r},t)$ can be derived

$$\phi = \phi_\chi(\vec{r},t) = \phi(\chi,\vec{r},t) \to \chi = \phi^{-1}(\phi,\vec{r},t) = \chi_{\tilde{\phi}}(\phi,\vec{r},t).$$

The membership degree of $\tilde{\phi}(\vec{r},t)$ is $\left|\chi_{\tilde{\phi}}(\phi,\vec{r},t)\right|^2 = \lambda_{\tilde{\phi}}(\phi,\vec{r},t)$. From $\lambda_{\tilde{\phi}}(\phi,\vec{r},t)$, the fuzzy quantum probability (density) $\tilde{\omega}(\vec{r},t)$ can be derived with the train of thought in Section 2 of this paper.

Now one can discuss the calculation problem of fuzzy probability amplitude $\tilde{c}_n(t)$ which is defined by

$$\tilde{\phi}(\vec{r},t) = \sum_n \tilde{c}_n(t)\psi_n(\vec{r}), \tag{10}$$

or

$$\int\limits_{\forall\chi\in C,|\chi|^2\in[0,1]} |\chi|^2 \Big/ \phi_\chi(\vec{r},t) = \int\limits_{\forall\chi\in C,|\chi|^2\in[0,1]} |\chi|^2 \Big/ \sum_n c_{n\chi}(t)\psi_n(\vec{r}),$$

i.e.

$$\begin{cases} \phi_\chi(\vec{r},t) = \sum\limits_n c_{n\chi}(t)\psi_n(\vec{r}), \\ \tilde{c}_n(t) = \int\limits_{\forall\chi\in C,|\chi|^2\in[0,1]} |\chi|^2 \Big/ c_{n\chi}(t) = \int\limits_{\forall\chi\in C,|\chi|^2\in[0,1]} \dfrac{|\chi|^2}{\int \mathrm{d}\tau \psi_n^*(\vec{r})\phi_\chi(\vec{r},t)}. \end{cases}$$

where $\psi_n(\vec{r})$ is the normalized eigenfunction of the mechanical quantity operator $\hat{F}$, satisfying $\hat{F}\psi_n(\vec{r}) = F_n\psi_n(\vec{r})$.

It should be pointed out that the sum rule in Equation (10) about the fuzzy plurals is different from the general that of fuzzy plurals, the operation rule in (10) need ensure the normalization of $\tilde{\phi}(\vec{r},t)$.

The fuzzy probability from $\tilde{c}_n(t)$ can be solved as follows:

$$c = c_{n\chi}(t) = c(\chi, F_n, t) \to \chi = c^{-1}(c, F_n, t) = \chi_{\tilde{c}_n}(c, F_n, t).$$

The membership degree of $\tilde{c}_n(t)$ is $\left|\chi_{\tilde{c}_n}(c,F_n,t)\right|^2 = \lambda_{\tilde{c}_n}(c,F_n,t)$. From $\lambda_{\tilde{c}_n}(c, F_n,t)$, the fuzzy quantum probability $\left|\tilde{c}_n(t)\right|^2 = \tilde{P}(F=F_n)$ can be derived with the train of thought in Section 2 of this paper.

Next, an equation will be established for the normalized membership degree amplitude function $\chi_{\tilde{\phi}}(\phi,\vec{r},t)$ which satisfies

$$\left|\chi_{\tilde{\phi}}(\phi,\vec{r},t)\right|^2 = \mu_{\tilde{\phi}}(\phi,\vec{r},t).$$

where $\mu_{\tilde{\phi}}(\phi,\vec{r},t)$ is the normalized membership function which satisfies Equation (1).

For simplicity, the real number form is adopted. Order $\phi = R + iI$, then $\chi_{\tilde{\phi}}(\phi,\vec{r},t)$ can be equivalently rewritten as

$$\chi_{\tilde{\phi}}(R,I,\vec{r},t) = u(R,I,\vec{r},t) + iv(R,I,\vec{r},t),$$

here u and v are the real and imaginary parts of $\chi_{\tilde{\phi}}(\phi,\vec{r},t)$ respectively.

And then

$$\mu_{\tilde{\phi}}(\phi,\vec{r},t) = u^2 + v^2. \tag{11}$$

Putting (11) into (8), one can derive out

$$\begin{cases} 2R(u\dot{u}+v\dot{v}) - (RH_I + IH_R)(u^2+v^2)/\hbar = g_1(R,I,\vec{r},t), & (12) \\ 2I(u\dot{u}+v\dot{v}) - (IH_I - RH_R)(u^2+v^2)/\hbar = g_2(R,I,\vec{r},t). & (13) \end{cases}$$

By $(12)\times R + (13)\times I$, $(13)\times R - (12)\times I$, one can respectively obtain

$$\begin{aligned} &2(R^2+I^2)(u\dot{u}+v\dot{v}) - (R^2+I^2)H_I(u^2+v^2)/\hbar \\ &= Rg_1(R,I,\vec{r},t) + Ig_2(R,I,\vec{r},t), \\ &(R^2+I^2)H_R(u^2+v^2)/\hbar = Rg_2(R,I,\vec{r},t) - Ig_1(R,I,\vec{r},t). \end{aligned}$$

By sorting out the above two formulas, an equation set is established for $\chi_{\tilde{\phi}}(\phi,\vec{r},t)$

$$\begin{cases} u\dot{u}+v\dot{v}-H_I\left(u^2+v^2\right)\Big/\left(2\hbar\right)=f_1\left(R,I,\vec{r},t\right), \\ H_R\left(u^2+v^2\right)\Big/\hbar=f_2\left(R,I,\vec{r},t\right). \end{cases} \tag{14}$$

Here

$$\begin{cases} f_1\left(R,I,\vec{r},t\right)=\dfrac{Rg_1\left(R,I,\vec{r},t\right)+Ig_2\left(R,I,\vec{r},t\right)}{2\left(R^2+I^2\right)}, \\ f_2\left(R,I,\vec{r},t\right)=\dfrac{Rg_2\left(R,I,\vec{r},t\right)-Ig_1\left(R,I,\vec{r},t\right)}{R^2+I^2} \end{cases}$$

can be regarded as the fuzzy source.

Now let me prove the rationality of the above designing fuzzy probability amplitude. This only need prove that the result of the non-fuzzification of fuzzy probability amplitude satisfies the equation of probability amplitude in quantum mechanics. A derivation as follows can be done:

1) The equation of probability amplitude in quantum mechanics is

$$i\hbar\dot{\overline{c}}_n=\sum_m H_{nm}\overline{c}_m. \tag{15}$$

Order $\overline{c}_n=\overline{X}_n+i\overline{Y}_n$, $H_{nm}=H_{nmR}+iH_{nmI}$. Then (15) turns into real form

$$\begin{cases} \hbar\dfrac{\mathrm{d}}{\mathrm{d}t}\overline{X}_n=\sum_m\left(H_{nmR}\overline{Y}_m+H_{nmI}\overline{X}_m\right), \\ \hbar\dfrac{\mathrm{d}}{\mathrm{d}t}\overline{Y}_n=\sum_m\left(-H_{nmR}\overline{X}_m+H_{nmI}\overline{Y}_m\right). \end{cases} \tag{16}$$

Here

$$\begin{cases} H_{nmR}=\int\mathrm{d}\tau\left[R_n\left(H_RR_m-H_II_m\right)+I_n\left(H_RI_m+H_IR_m\right)\right], \\ H_{nmI}=\int\mathrm{d}\tau\left[R_n\left(H_RI_m+H_IR_m\right)-I_n\left(H_RR_m-H_II_m\right)\right]. \end{cases}$$

2) By solving (14), it can be obtain that

$$\begin{cases} u=u\left(R,I,\vec{r},t\right), \\ v=v\left(R,I,\vec{r},t\right). \end{cases} \tag{17}$$

By solving (17), one can obtain

$$\begin{cases} R=R\left(u,v,\vec{r},t\right), \\ I=I\left(u,v,\vec{r},t\right). \end{cases}$$

Thus, $\phi_\chi\left(\vec{r},t\right)=R\left(u,v,\vec{r},t\right)+iI\left(u,v,\vec{r},t\right)$.

So,

$$\begin{aligned} c_{n\chi}\left(t\right)&=\int\mathrm{d}\tau\psi_n^*\left(\vec{r}\right)\phi_\chi\left(\vec{r},t\right) \\ &=\int\mathrm{d}\tau\psi_n^*\left(\vec{r}\right)R\left(u,v,\vec{r},t\right)+i\int\mathrm{d}\tau\psi_n^*\left(\vec{r}\right)I\left(u,v,\vec{r},t\right). \end{aligned} \tag{18}$$

Order

$$\begin{cases} c_{n\chi}\left(t\right)=X_n\left(u,v,t\right)+iY_n\left(u,v,t\right), \\ \psi_n\left(\vec{r}\right)=R_n\left(\vec{r}\right)+iI_n\left(\vec{r}\right). \end{cases}$$

Bringing them into (18), one can derive

$$\begin{cases} X_n(u,v,t) = \int \mathrm{d}\tau R_n(\vec{r}) R(u,v,\vec{r},t) + \int \mathrm{d}\tau I_n(\vec{r}) I(u,v,\vec{r},t), \\ Y_n(u,v,t) = \int \mathrm{d}\tau R_n(\vec{r}) I(u,v,\vec{r},t) - \int \mathrm{d}\tau I_n(\vec{r}) R(u,v,\vec{r},t). \end{cases} \tag{19}$$

By using (19), the real part of the non-fuzzification of $\tilde{c}_n(t)$ can be obtained

$$\begin{aligned} \overline{X}_n(t) &= \int \mathrm{d}u\mathrm{d}v\left(u^2+v^2\right) X_n(u,v,t) \\ &= \int \mathrm{d}\tau R_n(\vec{r}) \int \mathrm{d}u\mathrm{d}v\left(u^2+v^2\right) R(u,v,\vec{r},t) \\ &\quad + \int \mathrm{d}\tau I_n(\vec{r}) \int \mathrm{d}u\mathrm{d}v\left(u^2+v^2\right) I(u,v,\vec{r},t) \\ &= \int \mathrm{d}\tau \left[R_n(\vec{r}) \overline{R}(\vec{r},t) + I_n(\vec{r}) \overline{I}(\vec{r},t) \right], \end{aligned} \tag{20}$$

Similarly, the imaginary part of the non-fuzzification of $\tilde{c}_n(t)$ is

$$\overline{Y}_n(t) = \int \mathrm{d}u\mathrm{d}v\left(u^2+v^2\right) Y_n(u,v,t) = \int \mathrm{d}\tau \left[R_n(\vec{r}) \overline{I}(\vec{r},t) - I_n(\vec{r}) \overline{R}(\vec{r},t) \right].$$

3) By differentiating the variable t at both sides of (20), and by using (2) and (3), it can be derived out that

$$\hbar \dot{\overline{X}}_n(t) = \int \mathrm{d}\tau \left[\left(R_n H_I - I_n H_R \right) \overline{R} + \left(R_n H_R + I_n H_I \right) \overline{I} \right]. \tag{21}$$

In quantum mechanics

$$\begin{aligned} \overline{\phi}(\vec{r},t) &= \overline{R}(\vec{r},t) + i\overline{I}(\vec{r},t) = \sum_m \overline{c}_m(t) \psi_m(\vec{r}) = \sum_m \left(\overline{X}_m + i\overline{Y}_m \right) \left(R_m + iI_m \right) \\ &\rightarrow \begin{cases} \overline{R}(\vec{r},t) = \sum_m \left(\overline{X}_m R_m - \overline{Y}_m I_m \right), \\ \overline{I}(\vec{r},t) = \sum_m \left(\overline{X}_m I_m + \overline{Y}_m R_m \right). \end{cases} \end{aligned} \tag{22}$$

Substituting (22) into (21), one can get

$$\begin{aligned} \hbar \dot{\overline{X}}_n(t) = \sum_m \int \mathrm{d}\tau \Big\{ &\left[R_n \left(H_I R_m + H_R I_m \right) - I_n \left(H_R R_m - H_I I_m \right) \right] \overline{X}_m \\ &+ \left[R_n \left(H_R R_m - H_I I_m \right) + I_n \left(H_R I_m + H_I R_m \right) \right] \overline{Y}_m \Big\}. \end{aligned}$$

Similarly, it can be derived that

$$\begin{aligned} \hbar \dot{\overline{Y}}_n = \sum_m \int \mathrm{d}\tau \Big\{ &-\left[R_n \left(H_R R_m - H_I I_m \right) + I_n \left(H_R I_m + H_I R_m \right) \right] \overline{X}_m \\ &+ \left[R_n \left(H_R I_m + H_I R_m \right) - I_n \left(H_R R_m - H_I I_m \right) \right] \overline{Y}_m \Big\}. \end{aligned}$$

These two results are completely consistent with (16), so the above design of fuzzy probability amplitude is rational.

5. Conclusions

The subject of this paper is to do the work of "the fuzzification of quantum probability" with the method of fuzzy mathematics. The mathematical framework of fuzzy quantum probability has been established. It includes fuzzy wave function depicted by a membership function, the equation of the membership function of deciding the evolution of fuzzy wave function, fuzzy probability amplitude computed by a membership degree amplitude, the equation of the membership degree amplitude, the method of obtaining fuzzy probability from fuzzy wave function and fuzzy probability amplitude.

Unlike the work on using fuzzy mathematics to understand quantum mechanics is equivalent to quantum probability in a certain sense, my work on bluring quantum probability with the method of fuzzy mathematics in this paper is not equivalent to quantum probability. Quantum probability theory only advocates the uncertainty of events, while probability and probability waves are determined. Fuzzy quantum probability theory advocates not only the uncertainty of events, but also the uncertainty (fuzziness, unclearness) of probability and probability wave. The core concepts of quantum probability theory are probability wave and wave equation, while the core concepts of fuzzy quantum probability theory are membership degree (membership degree amplitude) and membership degree equation (membership degree amplitude equation).

Acknowledgements

I sincerely express my heartfelt thanks to Wang Suyun from the Department of Physics, College of Science, Shihezi University for his technical support for the work of this paper!

Conflicts of Interest

The author declares no conflicts of interest regarding the publication of this paper.

References

[1] Gudder, S. (2005) *Foundations of Probability and Physics*, **3**, 114-127. https://doi.org/10.1063/1.1874565

[2] Pykacz, J. (1998) *International Journal of Theoretical Physics*, **37**, 281-290.

[3] Ishikawa, S. (1997) *Fuzzy Sets and Systems*, **90**, 277-306. https://doi.org/10.1016/S0165-0114(96)00114-5

[4] Seising, R. (2006) Can Fuzzy Sets Be Useful in the (Re) Interpretation of Uncertainty in Quantum Mechanics? *Fuzzy Information Processing Society. NAFIPS* 2006-2006 *Annual Meeting of the North American Fuzzy Information Processing Society*, Montreal, 3-6 June 2006, 414-419. https://doi.org/10.1109/NAFIPS.2006.365445

[5] Gudder, S. (1989) *Foundations of Physics*, **19**, 293-317. https://doi.org/10.1007/BF00734561

[6] Tzara, C. (1987) *Nuovo Cimento B*, **98**, 131-144. https://doi.org/10.1007/BF02721475

[7] Pykacz, J. (2009) Quantum Probability Calculus as Fuzzy-Kolmogorovian Probability Calculus. *Foundations of Probability and Physics—5 Series: AIP Conference Proceedings*, Vol. 1101, Vaxjo, Sweden, 1 January 2008, 161-166. https://doi.org/10.1063/1.3109936

[8] Riečan, B. (2007) *Kybernetika Praha*, **4**, 481-490.

[9] Markus, M. (2009) *Physics Letters B*, **673**, 166-167. https://doi.org/10.1016/j.physletb.2009.02.017

[10] Sugeno, M. (1985) *Information Sciences*, **36**, 59-83. https://doi.org/10.1016/0020-0255(85)90026-X

[11] LEE, C.C. (1990) *IEEE Transactions on Systems Man & Cybernetics*, **20**, 419-435. https://doi.org/10.1109/21.52552

Appendix 1: The Main Used Variables in the Paper

Sign of the variable	Name of the variable	Meaning of the variable
$\tilde{\psi}(\vec{r},t)$	fuzzy wave function	Describing the fuzziness or inaccuracy of the values of the wave function
$\lambda_{\tilde{\psi}}(\psi,\vec{r},t)$	membership function	Describing the distribution of the credibility or truth value of the fuzzy probability wave taking all the possible values about the event $(\vec{r},t)$
$\lambda_{\tilde{\psi}}(\rho,\varphi,\vec{r},t)$	the equivalent form of membership function	ditto
$\lambda_{\tilde{\psi}}(R,I,\vec{r},t)$	ditto	ditto
$\tilde{\omega}(\vec{r},t)$	fuzzy quantum probability (density)	Describing the fuzziness or inaccuracy of the values of the quantum probability (density)
$\mu_{\tilde{\psi}}(R,I,\vec{r},t)$	the normalized membership function	Describing the relative distribution of the credibility or truth value of the fuzzy probability wave taking all the possible values about the event $(\vec{r},t)$
$\boldsymbol{g}$	fuzzy source	Describing the distribution of the factors which lead to the fuzziness or inaccuracy of quantum probability
$\chi_{\tilde{\psi}}(\psi,\vec{r},t),\chi_{\tilde{\phi}}(R,I,\vec{r},t)$	membership degree amplitude	There is no physical meaning in itself, and the square of its modulus represents the degree of membership. This is similar to probability wave or probability amplitude
$u(R,I,\vec{r},t),v(R,I,\vec{r},t)$	real and imaginary parts of $\chi_{\tilde{\phi}}(R,I,\vec{r},t)$	
$\psi_{\chi}(\vec{r},t)$	one possible form with a membership degree amplitude χ of $\tilde{\psi}(\vec{r},t)$	Representing that the credibility or truth value of $\tilde{\psi}(\vec{r},t)$ taking such a form $\psi_{\chi}(\vec{r},t)$ is $\lvert\chi\rvert^2$
$\tilde{\phi}(\vec{r},t)$	the normalized fuzzy wave function	Being similar to the above explanation
$\phi_{\chi}(\vec{r},t)$	being similar to the name of $\psi_{\chi}(\vec{r},t)$	Being similar to the above explanation
$\tilde{c}_n(t)$	fuzzy probability amplitude	Being similar to the above explanation
$c_{n\chi}(t)$	being similar to the name of $\psi_{\chi}(\vec{r},t)$	Being similar to the above explanation
$X_n(u,v,t),Y_n(u,v,t)$	real and imaginary parts of $c_{n\chi}(t)$	
$\tilde{P}(F=F_n)$	the fuzzy probability for $F=F_n$	Describing the fuzziness or inaccuracy of the values of the quantum probability for $F=F_n$
$R_n(\vec{r}),I_n(\vec{r})$	Real and imaginary parts of $\psi_n(\vec{r})$	
$\overline{X}_n(u,v,t),\overline{Y}_n(u,v,t)$	Real and imaginary parts of $\overline{c}_n(t)$	
H_{nmR},H_{nmI}	real and imaginary parts of H_{nm}	

Appendix 2: The Important Concepts in Fuzzy Mathematics

Since famous American automatic control expert Zadeh, L.A. pioneered the theory of fuzzy sets. Fuzziness has caused widespread concern and research. Its application has become increasingly widespread and in-depth. Here several pairs of important concepts are introduced.

1) Fuzziness and clarity

This pair of concepts is used to describe the property and state of things. "Clarity" refers to an unequivocal and certain property-state, whereas "Fuzziness" to an equivocal and uncertain one. For instance, "far larger than 5", "pretty girl", "tall man" etc. are all fuzzy conceptions and there is no categorical or unambiguous boundary about them. "Larger than 5", "Chinese people", "round table" etc. are all clear concepts with distinct or certain boundaries about them.

2) Fuzziness and chance

These two concepts both refer to uncertainty. However, the former means uncertain property-state of things, whereas the latter means uncertain the results of the event. The most critical quantity to depict fuzziness is "membership degree" (look below), whereas the most critical quantity describing chance is "probability".

3) General set and fuzzy set

There is a categorical boundary about classical set: an object either belongs to a classic set or does not belong to this classic set, whereas there is not a clear boundary about fuzzy set: the membership relation about an object belongs to a fuzzy set is uncertain, and we only can say how large is the degree of membership of an object for a fuzzy set? Order U represents a collection of some objects, called "discussion domain". For a classical set $A \subseteq U$, we may use a characteristic function $\chi_A(x)$ to indicates the membership degree for $x \in A$. When $\chi_A(x)=1$, x belongs to A. When $\chi_A(x)=0$, x does not belong to A. From this we may define a fuzzy set $\tilde{A}$. On the discussion domain U, $\tilde{A}$ is depicted using a real-valued function $\mu_{\tilde{A}}: U \to [0,1]$.

For $x \in U$, $\mu_{\tilde{A}}(x)$ is called the membership degree for $x \in \tilde{A}$, whereas the function $\mu_{\tilde{A}}(x)$ is named "membership function" of $\tilde{A}$. Because of $\mu_{\tilde{A}}(x) \in [0,1]$, it means that x does not Completely absolutely belong to $\tilde{A}$, *i.e.* x belongs to $\tilde{A}$ only in a certain of degree. This membership relation is inexplicit. A fuzzy set is entirely depicted by its membership function.

If U is the finite set, $\tilde{A}$ is marked in the form

$$\tilde{A} = \frac{\mu_{\tilde{A}}(x_1)}{x_1} + \frac{\mu_{\tilde{A}}(x_2)}{x_2} + \cdots + \frac{\mu_{\tilde{A}}(x_n)}{x_n} = \sum_{i=1}^{n} \frac{\mu_{\tilde{A}}(x_i)}{x_i}.$$

when U is the infinite set, $\tilde{A}$ can be expressed as $\tilde{A} = \int_{x \in U} \mu_{\tilde{A}}(x)/x$. Here $\sum, \int, /$ respectively is not summation, integration and division.

4) Fuzzy number and fuzzy plural

Normal fuzzy set: For a fuzzy set $\tilde{A}$, if there is at least one element $x \in \tilde{A}$, satisfying $\mu_{\tilde{A}}(x)=1$. Then $\tilde{A}$ is called "normal fuzzy set".

Convex fuzzy set: For a fuzzy set $\tilde{A}$, if $\forall x < y < z$, always satisfying

$\mu_{\tilde{A}}(x_2) \geq \left[\mu_{\tilde{A}}(x_1), \mu_{\tilde{A}}(x_3)\right]$. Then $\tilde{A}$ is called "convex fuzzy set".

Fuzzy number: A normal convex fuzzy set $\tilde{A}$ on real domain is called "fuzzy number".

Fuzzy plu-set: A fuzzy set $\tilde{Z}$ on plural domain is called "fuzzy plu-set".

Normal fuzzy plu-set: For a fuzzy plu-set $\tilde{Z}$, if there is at least one element $z \in \tilde{Z}$, satisfying $\mu_{\tilde{Z}}(z) = 1$. Then $\tilde{Z}$ is called "normal fuzzy plu-set".

Convex plu-set: For a classical set Z on plural domain (plural plane), if the connection of any two points in the set Z is entirely inside this set. Then Z is called "convex plu-set".

Convex fuzzy plu-set: For a fuzzy plu-set $\tilde{Z}$, if its any cut set is Convex plu-set. Then $\tilde{Z}$ is called "convex fuzzy plu-set".

Fuzzy plural: A normal convex fuzzy plu-set $\tilde{Z}$ is called "fuzzy plural".

5) Modulus of fuzzy plural $\tilde{Z}$: Modulus of fuzzy plural $\tilde{Z}$ is written as $\left|\tilde{Z}\right|$. Its membership function is $\lambda_{\left|\tilde{Z}\right|}(r) = \sup\limits_{z \in C, |z|=r} \mu_{\tilde{Z}}(z)$, *i.e.* the supremum of $\mu_{\tilde{Z}}(z)$.

6) Fuzzification and non-fuzzification

Fuzzification: Fuzzification is a process which blurs the clear, certain amount. We can have such a concise understanding: many quantities, which are thought to be clear and certain ones, factually are not uncertain at all. They have great uncertainty. If the uncertainty results from inaccuracy, ambiguity, the variable may be fuzzy and should be depicted using fuzzy number.

Non-fuzzification: Non-fuzzification is a process of converting the fuzzy amount into a certain one. The most popular non-fuzzification method is "centroid method" with the equation [10] [11]

$$\tilde{A} \xrightarrow{\text{non-fuzzification}} \overline{x} = \int_{x \in U} x \mu_{\tilde{A}}(x) \mathrm{d}x \Big/ \int_{x \in U} \mu_{\tilde{A}}(x) \mathrm{d}x.$$

7) Fuzzy probability

After the fuzzification of classical probability, one can obtain fuzzy probability, whereas classical probability can be regarded as the result of the non-fuzzification of fuzzy probability.

8) Fuzzification function and fuzzification plural function

Fuzzification function from X to Y is the ordinary function from X to $\tilde{\Re}(Y)$, $\tilde{f}: x \rightarrow \tilde{f}(x)$. Where X, Y are the two real number fields, whereas $\tilde{\Re}(Y)$ is the set of all fuzzy numbers on Y.

Fuzzification plural function from X to C is the ordinary function from X to $\tilde{\Re}(C)$, $\tilde{g}: x \rightarrow \tilde{g}(x)$. Where C is the plural field, whereas $\tilde{\Re}(C)$ is the set of all fuzzy plurals on C.

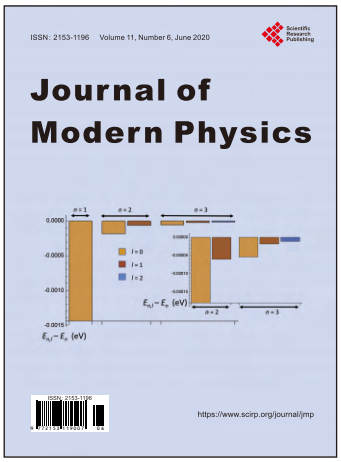

Call for Papers

Journal of Modern Physics

ISSN: 2153-1196 (Print) ISSN: 2153-120X (Online)
https://www.scirp.org/journal/jmp

Journal of Modern Physics **(JMP)** is an international journal dedicated to the latest advancement of modern physics. The goal of this journal is to provide a platform for scientists and academicians all over the world to promote, share, and discuss various new issues and developments in different areas of modern physics.

Editor-in-Chief

Prof. Yang-Hui He City University, UK

Subject Coverage

Journal of Modern Physics publishes original papers including but not limited to the following fields:

Biophysics and Medical Physics
Complex Systems Physics
Computational Physics
Condensed Matter Physics
Cosmology and Early Universe
Earth and Planetary Sciences
General Relativity
High Energy Astrophysics
High Energy/Accelerator Physics
Instrumentation and Measurement
Interdisciplinary Physics
Materials Sciences and Technology
Mathematical Physics
Mechanical Response of Solids and Structures
New Materials: Micro and Nano-Mechanics and Homogeneization
Non-Equilibrium Thermodynamics and Statistical Mechanics
Nuclear Science and Engineering
Optics
Physics of Nanostructures
Plasma Physics
Quantum Mechanical Developments
Quantum Theory
Relativistic Astrophysics
String Theory
Superconducting Physics
Theoretical High Energy Physics
Thermology

We are also interested in: 1) Short Reports—2-5 page papers where an author can either present an idea with theoretical background but has not yet completed the research needed for a complete paper or preliminary data; 2) Book Reviews—Comments and critiques.

Notes for Intending Authors

Submitted papers should not have been previously published nor be currently under consideration for publication elsewhere. Paper submission will be handled electronically through the website. All papers are refereed through a peer review process. For more details about the submissions, please access the website.

Website and E-Mail

https://www.scirp.org/journal/jmp **E-mail: jmp@scirp.org**

What is SCIRP?

Scientific Research Publishing (SCIRP) is one of the largest Open Access journal publishers. It is currently publishing more than 200 open access, online, peer-reviewed journals covering a wide range of academic disciplines. SCIRP serves the worldwide academic communities and contributes to the progress and application of science with its publication.

What is Open Access?

All original research papers published by SCIRP are made freely and permanently accessible online immediately upon publication. To be able to provide open access journals, SCIRP defrays operation costs from authors and subscription charges only for its printed version. Open access publishing allows an immediate, worldwide, barrier-free, open access to the full text of research papers, which is in the best interests of the scientific community.

- High visibility for maximum global exposure with open access publishing model
- Rigorous peer review of research papers
- Prompt faster publication with less cost
- Guaranteed targeted, multidisciplinary audience

Scientific Research Publishing

Website: https://www.scirp.org

Subscription: sub@scirp.org

Advertisement: service@scirp.org